The Characterisation of Rock Masses from Laboratory and Field Studies of the Velocity and Attenuation of Seismic Waves

by

Dominic Robert Pearce

Submitted in accordance with the requirements for the degree of
Doctor of Philosophy

University of Leeds
Department of Mining and Mineral Engineering

October, 1996

The candidate confirms that the work submitted is his own and that appropriate credit has been given where reference has been made to the work of others.

Abstract

This thesis addresses the concept of non-destructive rock mass characterisation using in-situ measurements of the velocity and attenuation of seismic waves. The thesis is divided in to two sections, the first of which considers a comprehensive laboratory study of the phenomena of stress-induced velocity and attenuation anisotropy, whilst the second documents a number of field case studies.

In the first section, a review is given of the current experimental evidence and theoretical explanations of the factors that affect the propagation of seismic waves. A description is given of the spectral ratio technique for the laboratory determination of P-wave attenuation in rock core samples. The section concludes with the presentation of the results of an investigation of stress-induced velocity and attenuation anisotropy in intact samples, samples induced to failure, and fractured samples. Experimental results show that in-situ measurements of the change in velocity and attenuation could be used to predict stress change in a homogenous rock mass which contains infrequent, isolated fractures. The prediction would be based on laboratory measurements of stress-induced attenuation anisotropy in intact samples.

In the second section, a new variant of seismic tomography called Combined Transmission and Reflection Tomography (CTRT) is fully described. In the chapters following this, a number of field cases are documented to show how the technique can be used to identify geological structure such as general stratigraphy, faults, orebody volumes, and man-made features such as old workings and blast induced fracture zones. The technique is shown to be ideal for surveying inaccessible areas and improving tomograms above those that can be produced by the popular transmission tomography algorithms. A final case study considers the use of seismic measurements in the prediction of rock mass behaviour in the footwall of a mine stope. The simple technique described successfully identified fault zones in two stopes before mining commenced, one of which resulted in the subsequent loss of a stope half way through mineral extraction.

In conclusion this thesis comprehensively describes how seismic measurements can be used to characterise a rock mass and lays the foundations for using the same measurements for monitoring and predicting rock mass behaviour in active environments.

Contents

I dedicate this thesis to my mother and father without whom none of this would have been possible.

Acknowledgements

A number of people have been a source of help and inspiration throughout the last three years. Whilst it would be impossible to mention everyone that has helped, I am deeply indebted to the following,

The members of the Department of Mining and Mineral Engineering. In particular, members of the technical staff, Bob Willan for his never ending help with all the field work in this thesis and his expertise with a sledge hammer! Andy for his electronic expertise with laboratory and field equipment, Peter for his help and advice in the laboratory, and Jim, Paul and Clive for their assistance with metalwork. Members of staff, especially Rob Farnfield for introducing me to the concepts of the Fast Fourier Transform, for his help with computer code and various discussions throughout the period of this work. My colleagues in the post-graduate room, for their help with many aspects of this work, in particular, Richard Goodchild for risking his life in the name of Geophysics!

The members of the Geophysics section of the department of Earth Sciences. In particular, Weijan Mao for supplying and adapting his inversion and forward modelling software for all the tomographic calculations and for all his time in discussions and tomogram interpretation over the last two years. Graham Stuart, Roger Clark and Phil Murphy for their advice and loan of field equipment.

The members of the British Geological Survey's Engineering Geology and Geophysics Group. In particular, Laurance Donnelly, Steve Shedlock and Peter Jackson for their help with the field work and useful discussion for interpretation of results in chapters 7 and 8 of this thesis, loan of equipment and access to borehole information at the Morley Quarry site. Thanks to Martin Culshaw for authorising the use of the BGS facilities. I hope that the new co-operation and links between the BGS and the Department will continue to prosper.

All the staff at Laporte Minerals, in particular, Nick Hardie for allowing access to Milldam Mine for the field work sites in Chapter 8 and Clint White for all his help and input throughout all the work at the mine.

Finally, I would like to thank my supervisor, Lindsay Wade for all his help and guidance throughout the last three years, providing support when I needed it, all his efforts in proof reading this thesis and for giving me the opportunity to present our joint paper in China, a fitting end to my work!

Published Work

Donnelly, L. J. & Pearce, D. R. (1996) A 4-D seismic tomography investigation at Laportes Milldam Mine, Derbyshire : A strata control investigation to locate sedimentary horizons associated with the orebody and fault zones, British Geological Survey, Engineering Geology & Geophysics Group, Report WN/96/37.

Pearce, D. R. & Wade, L. (1995) Rock mass characterisation through the velocity and attenuation of seismic waves - a project overview, LUMA, pp. 13-22.

Pearce, D. R. & Wade, L. (1996a) Laboratory and in-situ assessment of rock mass quality, APCOM '96, Penn State University.

Pearce, D. R. & Wade, L. (1996b) The application of seismic velocity and attenuation tomography in mining, Int. Conf. Mining Science & Technology, Xuzhou, China.

List of Figures

List of Tables

CHAPTER 1

1. Introduction

1.1 Laboratory Samples versus the In-Situ Rock Mass

In the design of underground excavations, rock mechanics investigations have always relied on rock mass properties estimated from intact sample, geomechanical laboratory tests. The problem is that whilst these tests may accurately determine the intact rock materials engineering properties they fail to describe how the same rock is likely to behave in-situ. The in-situ rock mass is not an intact homogenous entity but is characterised by discontinuities such as faults, joints and fractures. Distinct from the laboratory intact sample, this rock mass is also usually highly stressed due to the mass of the overlying rock sequences and the site specific tectonic stress regime, dependent on the geographical location. Discontinuities provide pathways through the rock mass for the movement of fluids and the deposition of infill materials, such as clays. The overall rock mass is therefore in effect only as strong as the weakest links within its structure. The engineering property values obtained in the laboratory for intact samples are therefore over-estimations of an in-situ rock mass's properties. It is for this reason that intact rock engineering values need to be scaled down for input in to computer models or simulations for excavation design. These scale factors are in many cases site specific and need to be carefully 'massaged' to create a model or design that is a reasonable reflection of the real case scenario.

The approach of this thesis will be one of direct in-situ rock mass characterisation, as an aid to excavation design, using seismic geophysics. Seismic geophysics does of course cover a vast area of research and commercial usage, most notably in the oil industry. This thesis will focus only on the velocity and attenuation of the compressional wave. The reasons for this are simple. Whilst it is relatively easy to create shear waves in the laboratory environment, current technology is not available to simply and easily create a pure vertically or horizontally aligned high frequency shear wave ideal for the characterisation of a rock mass in an underground environment. The development of such a source is beyond the scope of this work. A P-wave is the easiest of the wave modes to initiate, and therefore the simplest to implement in the field environment. The vision of this thesis is to develop the concepts and tools for direct rock mass characterisation using P-wave velocity and attenuation as part of the site

investigation process and provide the design engineer with extra or alternative information with minimum effort or cost.

The implications of a successful conclusion to this work are far ranging and are not restricted to the mining industry. Some of the perceived applications might be,

- The short term monitoring of mining excavations to identify regions deemed vulnerable to failure, unsafe or production threatening, for example, within a mine stope, longwall section or pillar structures.
- The long-term monitoring of civil engineering excavations to routinely monitor excavation walls or pillars, to check for localised stress concentration or variation throughout its working life. Examples where this might be applied include, nuclear waste repositories, tunnels, gas or water storage caverns, underground power stations and hydroelectric excavations.
- Other applications need not be based underground and could potentially include the monitoring of surface civil engineered structures constructed from homogenous materials such as concrete, where accurate measurements and prediction of stress change is possible with greater resolution. For example, dams (stress change as water levels fluctuate and indications of concrete fatigue), bridges, building foundations, railway and other embankments, or concrete pipelines and other structures.

1.2 Seismic Geophysics

Seismic techniques have over and over again proved their worth in the exploration for oil, gas or other extractable products. A simple seismic wave is affected throughout its propagation by the medium through which it is travelling. Seismic geophysics is therefore the process of extracting the history stored in a received waveform and inferring from that the properties or structure of the medium through which that wave has propagated.

For inferring geological structure from a seismic waveform, the interpreter is interested in identifying primary reflections from geological interfaces. Seismic waves are reflected at such boundaries due to the difference in acoustic impedance between two geological units. The larger the difference, the greater the reflected energy.

On a more fundamental basis, the traveltime of a direct or reflected seismic wave, or the velocity calculated from this, can reveal a multitude of information about a rock mass's internal properties, from the type of lithology, the porosity, the pore fluid,

through to the fracture state or stress regime. Similarly, the amount of energy that the wave loses to its surroundings by geometric spreading, intrinsic losses or scatter from discontinuities provides another aspect for property interpretation.

1.3 Geophysical Field Technique

There are several branches of seismic field work techniques, each concentrating on individual specific aspects of the seismic waveform. The oil industry is most interested in the geological structure of a survey area and therefore processes data with a view to maximising the appearance of primary reflections within the seismic section. Whilst a knowledge of geological structure is vitally important to the excavation engineer, plots of seismic velocity or attenuation can provide information on the engineering condition of the rock mass as well as its internal geological structure. The simplest way to determine velocity structure in a shallow surface environment is the use of seismic refraction. This method is simple to use, but is really only appropriate for shallow, near surface, two or three layer geological environments. To get a more comprehensive and accurate image of the velocity or attenuation structure of complex geological environments, more sophisticated methods are needed. Most of the seismic geophysical techniques used in the field studies described in this thesis aim to reconstruct the velocity structure of a rock mass by the measurement of seismic traveltimes through many paths within that rock mass. The technique employed comes under the general pseudonym of combined field measurement and numerical reconstruction methods known as 'seismic tomography'. Seismic tomography was developed from the medical imaging technique known as X-ray tomography, whereby a property of a 2-D or 3-D object can be estimated by the mathematical inversion of 1-D line integral measurements through various angular pathways within that object. With medical tomography, the property that is usually measured is the degree of absorption of X-rays within the human body. Seismic tomography, on the other hand, usually involves measuring seismic P-wave traveltimes across a number of theoretical angular raypaths that connect a seismic source to an array of receivers. Medical tomography enjoys the luxury of complete 360 degree access to an objects surface area. Additionally, the relationship between the distance of propagation of the X-ray and the degree of absorption within the human body is linear. In seismic tomography neither of the above apply. At best, a 2-D tomographic survey may have access to four sides of the rock mass to be imaged. This limited geometrical access causes mathematical difficulties in resolving the velocity or attenuation image. The symptom of this difficulty is a non-unique solution. That is, given one dataset of traveltimes through a body, there

are an infinite number of potential solutions that fit or nearly fit the available data. The problem of non-uniqueness can only be helped by increasing the number and angular coverage of the 1-D integral measurements across a body. Seismic tomography is a non-linear problem. This is because the length of a particular theoretical raypath depends on the velocity structure through which that raypath is propagating, which is of course itself an unknown. Therefore it should be pointed out that seismic tomography is a subjective technique and is dependent on the ability and experience of the user to control the mathematical process to produce the most likely result from the possible infinite number of solutions. Given this limitation, however, it is still one of the most powerful geophysical interpretation tools to be developed in recent times and, in the opinion of the author, provides one of the best methods for non-destructively characterising a rock mass.

This thesis will address the problems of limited surface area access on seismic tomography. Traditionally, seismic tomography only reconstructs a velocity image based on the measurement of the direct P-wave arrival along a number of raypaths. For instance, to reconstruct a 2-D image of a square or rectangular rock mass, the method needs a minimum access to two parallel sides of that square or rectangle. It is not, for example, possible to successfully image that square or rectangle from two adjacent sides. This is a very simple case scenario. Many potential sites where seismic tomography could be used to great effect, such as in mining or civil engineering rock mass evaluation, do not have these idealised geometries. Seismic tomography is therefore not a viable proposition without the need for the expensive drilling of longholes or the excavation of new galleries in order to site measurement points in more favourable locations. This is why the method has not been used extensively in either industry. As has already been pointed out, a seismic wave contains much more information than this simple first arrival with respect to reflections from and refractions along geological boundaries or discontinuities. This thesis will show that it is possible to use this extra traveltime information along with the more traditionally used direct arrival traveltimes to produce quality images for poor geometry sites. By using this new variant technique, seismic tomography suddenly becomes much more accessible to the mining and civil engineering industries with all the direct rock mass assessment advantages that the method has to offer.

1.4 Geophysical Laboratory Technique

Although the ultimate goal of this work is to achieve direct rock mass characterisation free from the problems mentioned in the first section, the author does

recognise the importance of laboratory work to accomplish this aim. The laboratory provides a controlled environment where specific factors can be isolated and restrained to establish the process and mechanisms involved. This process is really not possible within an in-situ rock mass with the exception of a very few rare cases.

A comprehensive laboratory study is described in this thesis which aims to expand current knowledge of the influence of a changing stress regime on the velocity and attenuation of a seismic wave propagating through rock. This laboratory work has been inspired by rock physics research within the literature and focuses on a phenomenon known as stress-induced velocity or attenuation anisotropy. The 'intact' laboratory sample will be taken as a starting point for this study. The study will then go one step further to encompass controlled consideration of the effects of rock mass failure on seismic properties. Once under a condition of failure, the study will consider how the seismic properties can help characterise the fractured sample as it is re-subjected to varying stress regimes. This type of study will give an indication of the sensitivity of velocity or attenuation measurements to changes within a rock mass that may be induced by mining or civil excavation.

1.5 Thesis Structure

The thesis is split in to two sections. The first section is laboratory based, with a review of pertinent experimental work investigating the in-situ factors affecting seismic wave propagation, consideration of the techniques for measuring seismic properties in the laboratory, and a comprehensive analysis of laboratory results. The second section is field work based. A description of the numerical basis of the variant of seismic tomography adopted throughout this work is followed by specific field applications of the technique. Both inactive and active mining environments will be considered, and a variety of seismic measurements and numerical methods used to improve the characterisation of the rock masses under investigation. Finally, the two sections will be drawn together to discuss where comparisons are possible, and indicate where there is scope for further work.

1.5.1 Chapter 2, Rock Physics

The seismic properties considered in this study are comprehensively defined. A review is given of the current theories within the science of rock physics which describe the factors that affect the velocity and attenuation of seismic waves. A large body of literature is reviewed, from experimental work to discover the factors, through to the current theories describing the mechanisms in play. The fundamental understanding of

the processes that affect wave propagation is the key to extracting information about a rock mass's properties from a seismic wave.

1.5.2 Chapter 3, The Laboratory Determination of Velocity and Attenuation

The methods for the pulse transmission determination of ultrasonic attenuation in laboratory rock core samples are reviewed. The advantages and disadvantages of each of the methods are carefully considered and the Spectral Ratio method is selected. A full theoretical mathematical treatment of the method is described. The description of a specially written computer program called AUTOQ is given for the automatic determination of attenuation from laboratory acquired ultrasonic waveform data. A new numerical approach is given to robustly improve calculated values of the quality factor from spectral ratio slopes.

1.5.3 Chapter 4, Laboratory Results.

The properties of stress-induced velocity and attenuation anisotropy will be fully investigated in a laboratory study encompassing intact and fractured rock core samples. Velocity and attenuation are also measured in confined samples which are subjected to failure. In the light of experimental results, conclusions are drawn for the measurement of velocity and attenuation in the field, and the possible interpretation of these measurements for differing situations.

1.5.4 Chapter 5, Seismic Tomography

A literature review examines some field studies which have employed seismic tomography in the mining and civil engineering industries. The studies are appraised and key gaps identified in the literature. The variant of seismic tomography, known as 'combined transmission and reflection tomography' or CTRT inversion is mathematically defined.

1.5.5 Chapter 6, Combined Transmission and Reflection Traveltime Tomography in Rock Mass Characterisation.

The first of the field studies, this chapter considers a tomographic survey site at the University-managed Gillfield Mine. The site displays poor geometry for traditional transmission traveltime seismic tomography, where a near square rock mass is to be imaged from two adjacent sides. The discussion first shows the kind of results that are obtained from the traditional method. Following this, the CTRT method is applied and the differences compared.

1.5.6 Chapter 7, Cross-hole Tomography at Morley Quarry

The second of the field case studies considers a two dimensional tomographic survey carried out between two boreholes at a disused quarry. Different tomographic reconstruction algorithms are compared with respect to the way the processing technique affects the final result. The chapter shows how the tomographic technique can identify a man-induced fracture zone and identifies an antithetic fault zone which crosses the survey area.

1.5.7 Chapter 8, Seismic Velocity and Attenuation in the Prediction of Rock Mass Behaviour in an Active Mining Environment

The last of the case studies, this chapter considers a working Fluorspar Mine called Milldam Mine, owned and run by Laporte Minerals. A description is given of a number of calibration tests to determine the propagation properties of various seismic sources and receivers. A description is then given of two tomographic surveys of producing stope footwalls. The study considers the use of seismic profiles in an unmined block to help predict how the rock mass will react when the stope commences production. Some comparisons are drawn between the in-situ and laboratory results.

1.5.8 Conclusion and Suggestions for Further Work

Both of the sections of this thesis are summarised and comparisons drawn between field and laboratory findings. The final section suggests areas which deserve further work and are a natural continuation of the work of this thesis.

CHAPTER 2

2. Rock Physics

Since the late 1960's the area of research named 'Rock Physics' has been increasing in popularity. Rock physics is the study on a microscopic scale of the processes involved in the propagation of seismic waves through a porous rock matrix. A large body of research is available, mostly nurtured by the demands of oil exploration to identify methods of determining in-situ rock properties from the seismic parameters of wave propagation, velocity and attenuation. Firstly this chapter defines seismic attenuation. Secondly, the chapter provides an overview of the experimental observations of previous authors in identifying the main factors that affect the velocity and attenuation of compressional waves through rock. These observations are all laboratory based and were conducted at various frequency ranges from seismic (< 250 Hz) to ultrasonic (kHz to MHz). Where the frequency range is important with respect to the particular factor this is indicated. Finally, attention is focused on the current theories which have been developed in light of experimental evidence and which attempt to identify the mechanisms or basic processes which modify wave propagation in rock.

2.1 Definition of Attenuation.

Attenuation is the broad term that is used to describe the energy lost to the surrounding medium when an elastic wave propagates in a solid. Attenuation is a measure of the anelasticity of a material and is characterised by the mechanical quality factor Q which is inversely proportional to the fractional decrease in wave energy density per cycle of harmonic loading.

$$Q = \frac{2\pi E}{dE} \tag{2.1}$$

where,

E = total elastic energy of a wave cycle.

dE = energy dissipated per wave cycle.

An alternative measure of attenuation which describes the exponential decrease in amplitude of a propagating wave at a specific frequency with distance is termed the attenuation coefficient α, commonly quoted in terms of nepers/cm or dB/cm.

It is also usual to describe attenuation mathematically in terms of a complex wavenumber K, a complex velocity V and a complex elastic modulus M, (Futterman, 1962).

From the average energy density and loss per cycle of a complex plane wave it can be shown that,

$$\frac{1}{Q} = \frac{M_i}{M_r} \tag{2.2}$$

where M_r and M_i are the real and imaginary parts of the complex elastic modulus M. This modulus being defined by,

$$M = \rho V^2 \quad = \frac{\rho \omega^2}{K^2} \tag{2.3}$$

where,

ρ = density

ω = angular frequency.

In reality, no material is perfectly elastic and therefore $\frac{1}{Q}$ is a representation of the usually small perturbation to this perfect elasticity.

2.1.1 Intrinsic and Extrinsic Attenuation.

When considering the propagation of seismic waves it is important to distinguish between two types of attenuation, intrinsic and extrinsic.

The intrinsic attenuation is defined as the energy lost as heat and internal friction during the passage of an elastic wave. The microscopic mechanisms responsible will be considered later on in this chapter.

Extrinsic attenuation encompasses the phenomena of geometric spreading and scattering from inhomogeneities. Geometric spreading is simply the energy density decrease that occurs as an elastic wavefront expands. Scattering is not true energy loss but the redistribution of elastic energy in angular directions away from the receiver or its conversion to wave types arriving in different time windows at the receiver. Scattering processes include reflection, refraction and mode conversion by irregularities in the rock medium.

Intrinsic attenuation can be measured in the laboratory by choosing samples of suitable geometry and by only considering the first arrival wavelets of the wave type of interest. However, the differentiation of extrinsic and intrinsic attenuation in field data is

very difficult and the measured value of Q from such data should be considered to be the sum of the two components,

$$Q = Q_i + Q_e \tag{2.4}$$

where,

Q = actual measured value.

Q_i = intrinsic attenuation component.

Q_e = extrinsic attenuation component.

2.2 Factors Affecting Compressional Wave Velocity

2.2.1 Stress

It is an accepted fact that intact sedimentary rocks contain imperfections such as randomly distributed and orientated microcracks, open grain boundaries and pores. In most cases, there may be natural aligning of these imperfections depending on the original diagenesis conditions and the in-situ stress regime.

2.2.1.1 Hydrostatic Stress

The effect of hydrostatic stress on velocity has been studied extensively and is a well understood phenomenon, (King, 1966, 1969), (Simmons & Brace, 1965), (Birch, 1960, 1961) and (Christensen, 1965). Subject a rock matrix containing microcracks and pores to hydrostatic stress and the effect is to close the cracks and collapse pores, thereby increasing the stiffness of the rock.

In low porosity rocks, cracks that are open at low confining pressures close with pressure to yield large increases in compressional wave velocity, increases that are anomalous with respect to those expected from mineral constituents alone. A typical result for Westerley Granite is shown in figure 2.4

In higher porosity rocks, pore collapse and crack closure has the same effect although generally the effect of pore collapse takes place over a wider pressure range, (Wyllie et al, 1958), (King, 1966) since pores are generally stronger than cracks, (Walsh, 1965).

2.2.1.2 Anisotropic Stress Regimes

If we subject a rock to a non-hydrostatic stress regime it is sensible to assume that a random distribution of cracks will yield differently. The effect will be to close cracks

in some directions and leave cracks open or even dilate cracks in others. This has been directly observed by Batzle et al (1980) using a scanning electron microscope. They observed that microcracks orientated perpendicular to the maximum principal stress closed and those parallel tended to remain open or dilated further. If we now measure compressional wave velocity across various orientations, differences will be observed and this is known as stress induced velocity anisotropy.

The simplest case of non-hydrostatic stress is uniaxial compression. Experiments monitoring velocity normal and parallel to a varying axial load have been carried out by Tocher (1957), Nur and Simmons (1969) and more recently, Wu et al (1991). They all observed that the increase in velocity parallel to the applied axis of stress was much greater than the increase in the normal direction. This observation suggests that cracks aligned normal to the axis of loading were preferentially closed with the onset of stress. The effect is graphically illustrated in figure 2.1 taken from Nur & Simmons (1969) depicting the change in velocity in Barre Granite with angle of propagation θ from the loading axis at various constant axial loads.

The experiment carried out by Nur & Simmons (1969) was at relatively low stress levels compared to the failure strength of Barre Granite. Work by Sayers et al (1990) on Berea sandstone illustrates anisotropy at greater stress levels. Their experimental set-up and results are depicted in figures 2.2 and 2.3 respectively for a cube sample subjected to a 'true' triaxial stress regime provided by a specially designed loading frame.

At an initial hydrostatic stress of 4.1 MPa it is clear that the sample is already anisotropic due to the presence of lenticular cracks parallel to the bedding plane. With the increase in σ_{x_3}, below 30 MPa all velocities rise due to the closure of pre-existing cracks and open grain boundaries. Above 30 MPa, anisotropy increases due to the growth of new microcracks and extension and coalescing of pre-existing cracks.

2.2.2 Saturation

When an elastic wave propagates through a saturated porous rock an increment of pore pressure is induced which in turn resists wave compression and effectively stiffens the rock. The pore fluid increases the effective density of the rock and since velocity is dependant on the effective bulk modulus and density, an increase in velocity should accompany saturation. Any net increase or decrease in velocity will depend on which is larger, an increase or decrease in rock stiffness or effective density.

The increase in effective bulk modulus was shown experimentally by Nur & Simmons (1969) on low porosity rocks, the results of which are shown graphically in

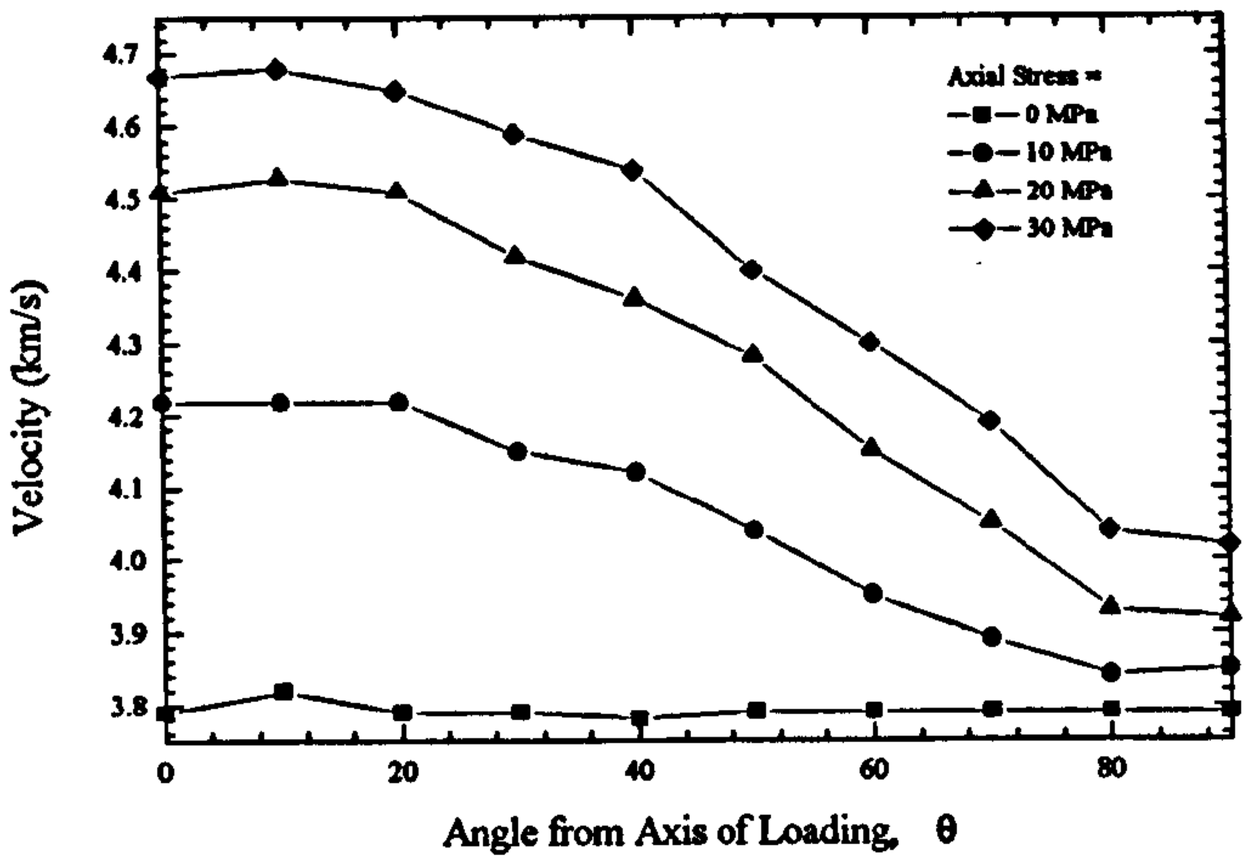

FIGURE 2.1 Velocity versus Angle from loading axis in Barre Granite, after Nur & Simmons (1969)

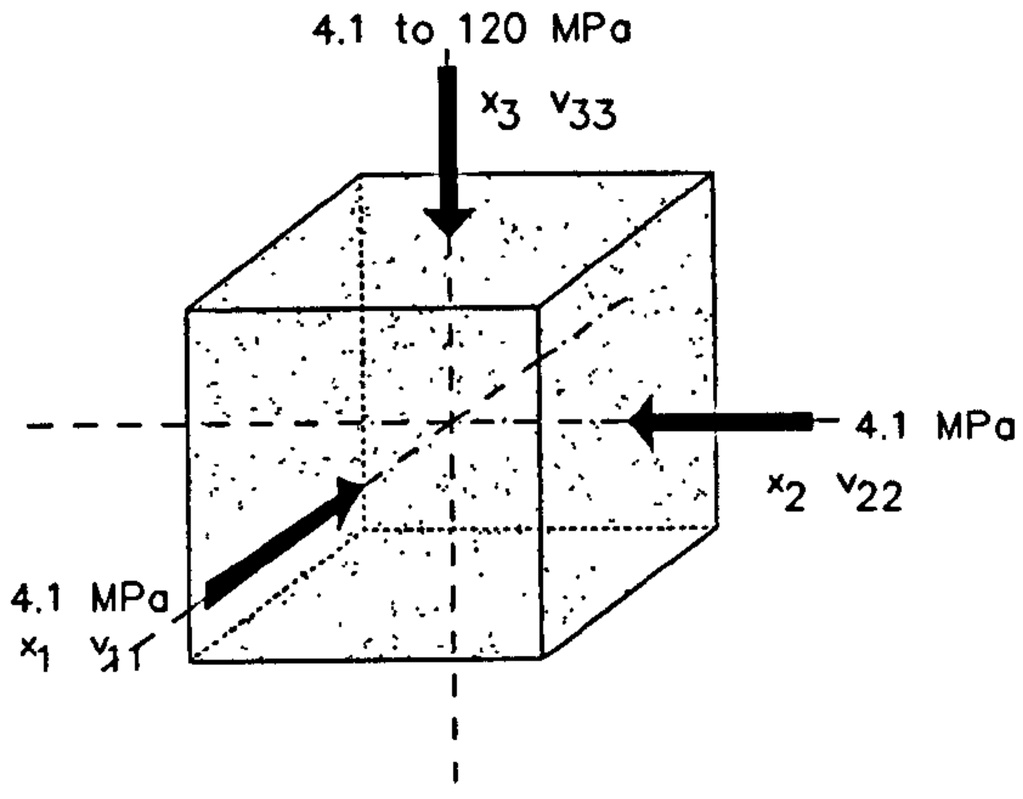

FIGURE 2.2 Experimental set-up for measurement of stress induced anisotropy, after Sayers et al (1990)

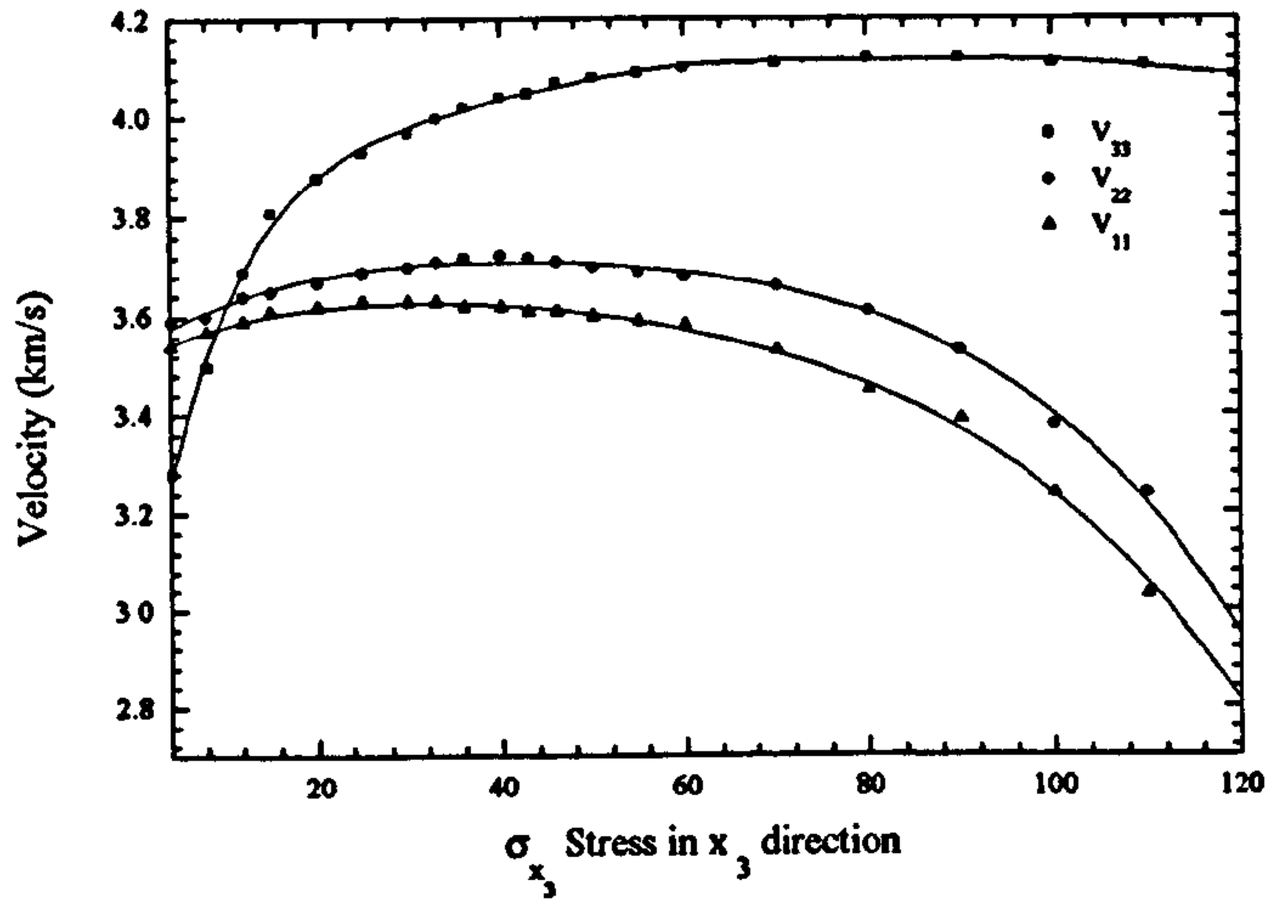

FIGURE 2.3 Velocities measured across three axis of a cube of Berea Sandstone versus axial stress in the x_3 direction (see Figure 2.2), after Sayers et al (1990).

figures 2.4 and 2.5. Figure 2.4 shows that with increasing confining pressure velocities are consistently higher in the saturated Westerly granite.

At 0 MPa, K_{dry} and K_{sat} are significantly different, showing that the water present in microcracks and pores increases the bulk modulus and the P-wave velocity. With the onset of pressure above 100 MPa the two sets of curves start to converge. At this point cracks start to close and the effect of saturation is reduced to a point where the saturated bulk modulus approaches the bulk modulus of the mineral material alone represented by the dry bulk modulus under high hydrostatic loads. Similarly the two velocities approach the same 'terminal' state.

The increase in effective bulk modulus is predicted by Biot-Gassmann-Domenico theory. Gassmann (1951) and Biot (1956a,b) predict that,

$$\frac{K_{sat}}{K_0 - K_{sat}} = \frac{K_{dry}}{K_0 - K_{dry}} + \frac{K_{pf}}{\phi\left(K_0 - K_{pf}\right)} \tag{2.4}$$

where,

K_0 = bulk modulus of the mineral material.

K_{pf} = bulk modulus of the pore fluid.

K_{dry} = bulk modulus of the dry rock.

K_{sat} = bulk modulus of the saturated rock.

ϕ = porosity.

Equation 2.5 can be used to determine the bulk modulus of the pore fluid for a partially saturated rock and predicts a similar increase in the bulk modulus but only when the effective bulk modulus of the gas-liquid mixture K_{pf} is appreciably larger than that of the gas alone, (Domenico, 1976).

$$\frac{1}{K_{pf}} = \frac{1-S}{K_g} + \frac{S}{K_f} \tag{2.5}$$

where,

K_g = gas bulk modulus.

K_f = fluid bulk modulus.

S = liquid saturation.

Murphy (1982) showed for reasons that will be explained later that equation 2.5 is only relevant at frequencies < 1 kHz in highly porous rocks. At these low frequencies, pore fluid is able to flow in and out of pores and cracks and pressures can be

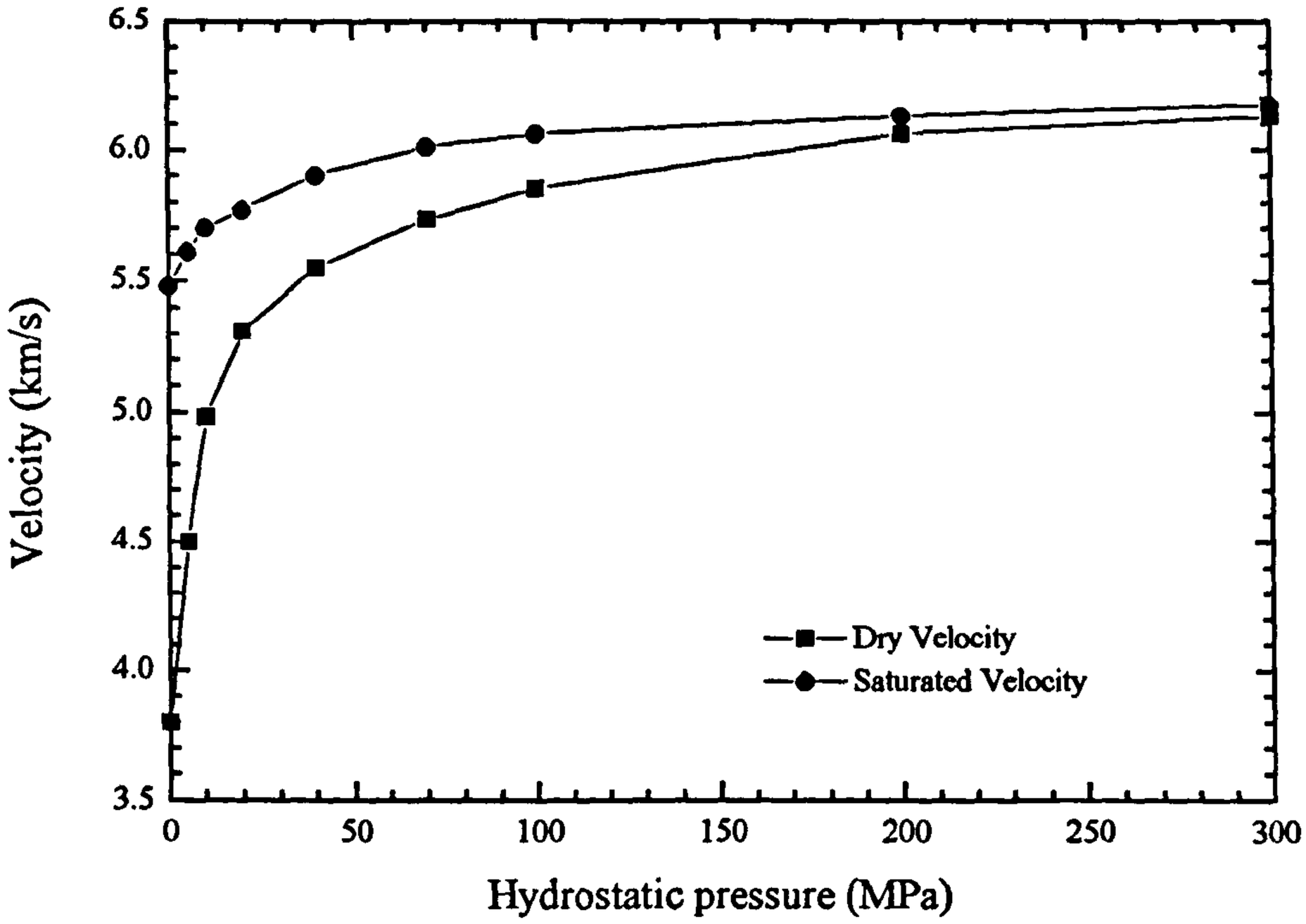

FIGURE 2.4 Velocities in dry and saturated Westerley Granite at confining pressure up to 300 MPa, after Nur & Simmons (1969).

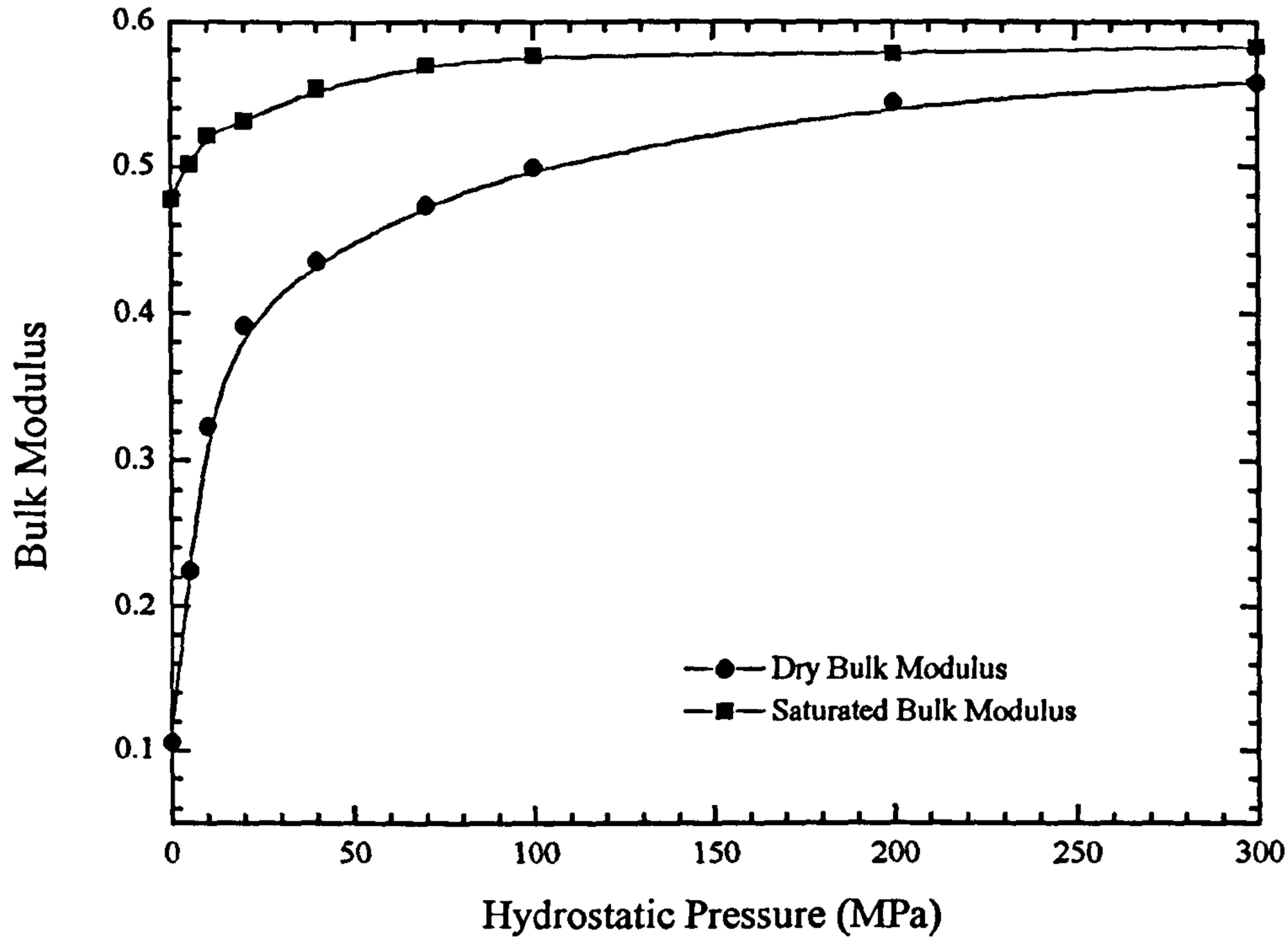

FIGURE 2.5 Bulk Modulus versus Hydrostatic Pressure for dry and saturated Westerley Granite, after Nur & Simmons (1969).

equilibrated within the pore space. Such a state is termed 'relaxed'. At higher frequencies, viscous and inertial effects prevent fluid flow into the thinnest pores. The system becomes 'unrelaxed' with the inducement of unequilibrated pressures in the pore space. Biot-Gassmann-Domenico theory does not successfully predict velocities under these conditions. A number of other theories to predict velocities at ultrasonic frequencies have been proposed by O'Connell & Budiansky (1977), Kuster & Toksov (1974), Mavko & Nur (1979), Endres & Knight (1991) and Mavko & Nolen-Hoeksema (1994).

2.2.3 Porosity and Clay Content

Porosity can be related to velocity by the Wyllie equation (Wyllie et al, 1958),

$$\frac{1}{V_p} = \frac{(1-\phi)}{V_m} + \frac{\phi}{V_f} \tag{2.6}$$

where,

V_m = P-wave velocity of the rock matrix

V_f = P-wave velocity of the pore fluid.

ϕ = porosity.

Alternatively the equation of Raymer et al (1980) which gives a better statistical fit to the data predicts,

$$V_p = (1-\phi)^2 V_m + \phi V_f \tag{2.7}$$

Both equations adequately predict the porosity in clean sandstones with porosities in the range of 10 to 25%. Both relationships have been shown to be inadequate for shaly sandstones and shales (Tosaya & Nur, 1982), (Han et al, 1986).

Klimentos (1991) reported that P-wave velocity decreases with increasing clay content. This agrees with the findings of other authors (Tosaya & Nur, 1982), (Kowalis et al, 1984), (Han et al, 1986). Similarly, for a constant clay content, P-wave velocity decreases with increasing porosity. The following empirical relationships were derived for the dependence of P-wave velocity on porosity, ϕ , and clay content, C,

$$V_p = 5.87 - 6.99\,\phi - 3.33\,C \qquad \text{Klimentos (1991)} \tag{2.8}$$

$$V_p = 5.59 - 6.93\,\phi - 2.18\,C \qquad \text{Han et al (1986)} \tag{2.9}$$

The two equations are very close, discrepancies in the clay content term being accounted for by the different experimental methods used to determine the clay content.

2.2.4 Temperature

In general, velocity decreases with increasing temperature, probably because of the expansion of existing cracks and the propagation of new cracks due to thermal stress. However these effects are only observed above 100 ^{0}C and little or no effect on velocity occurs below this temperature. Above 100^{0}C water evaporates and is lost as steam for a sample at atmospheric pressure. Therefore under these conditions, the pore fluid consists of a partial gas fluid mixture. After the description in section 2.2.2 one would expect a reduction in the bulk modulus of the overall system which would be accompanied by a reduction in the compressional wave velocity.

2.3 Factors affecting Compressional Wave Attenuation.

2.3.1 Stress

2.3.1.1 Hydrostatic Stress

P-wave attenuation closely follows the trend of velocity when a rock is subjected to hydrostatic stress. Attenuation decreases rapidly with the onset of stress and reaches a low plateau at higher stress levels. The most important factor causing change in velocity is the change of porosity with pressure, in particular, the closing of thin microcracks. The same is true for attenuation. In both dry and saturated cases and all rock types described in the literature, attenuation is seen to decrease with hydrostatic stress. Some of the experimental data verifying this is shown graphically in figures 2.6 to 2.8 for various different rock types under dry and saturated conditions and for differing frequency ranges.

The rate of increase of Q with pressure varies depending on the rock type, saturation and the crack porosity and distribution. For dry rocks the rate of increase is usually greater than that for saturated rocks. A possible explanation is that with the onset of pressure, pore fluid opposes the closing of cracks and grain contacts by reducing the net intergranular stress. This leads to reduced effective moduli, lower velocity and higher attenuation.

2.3.1.2 Anisotropic Stress Regimes

Section 2.2.1.2 considered the effect of an anisotropic stress regime on seismic velocity. Considering the large amount of work done on this topic, surprisingly little published work exists documenting the study of attenuation under a non-hydrostatic stress regime.

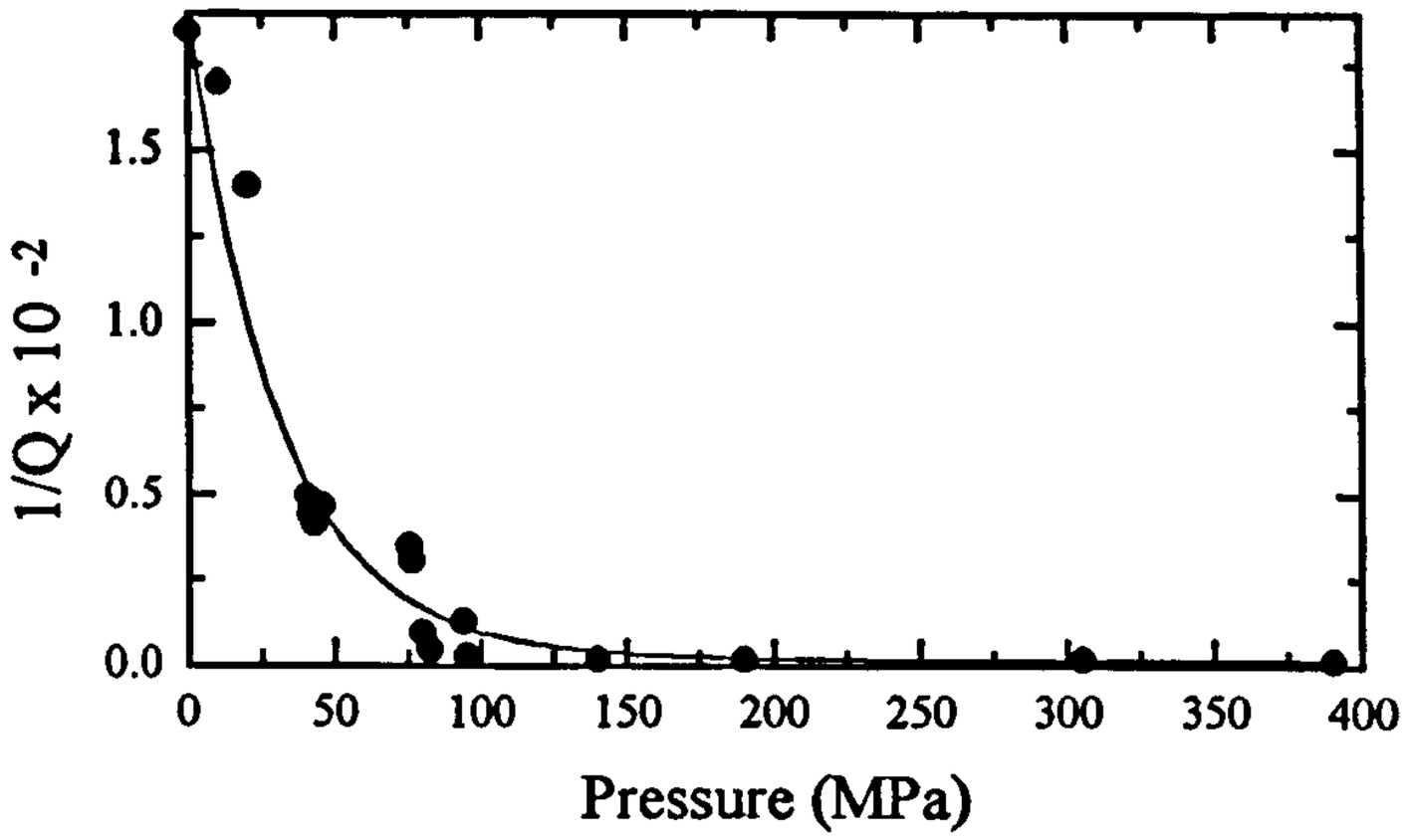

FIGURE 2.6. Pressure dependence of 1/Q in granite, after Gordon & Davis (1968).

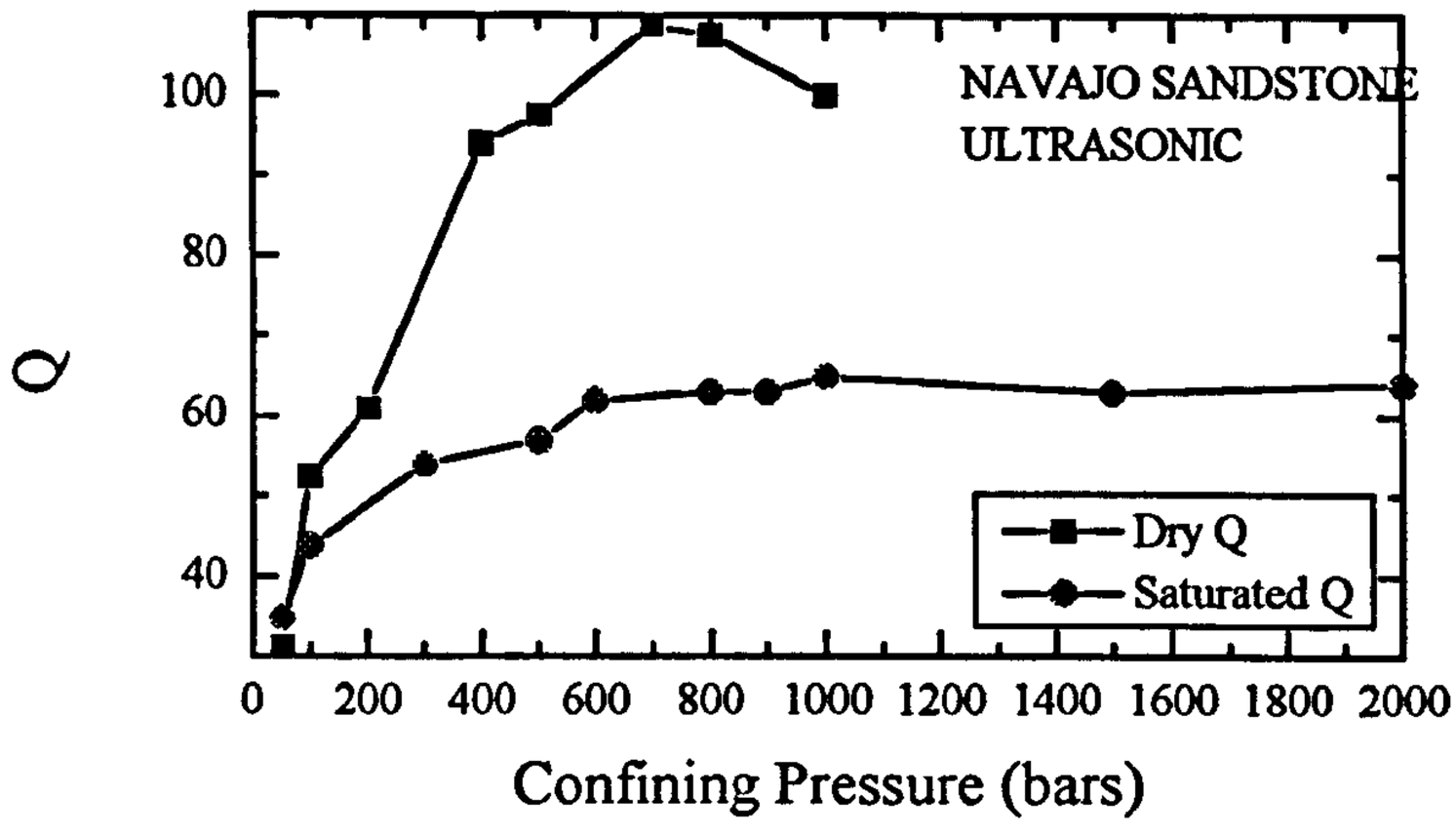

FIGURE 2.7. Pressure dependence of Q in dry and saturated Navajo Sandstone, after Johnston & Toksov (1980)

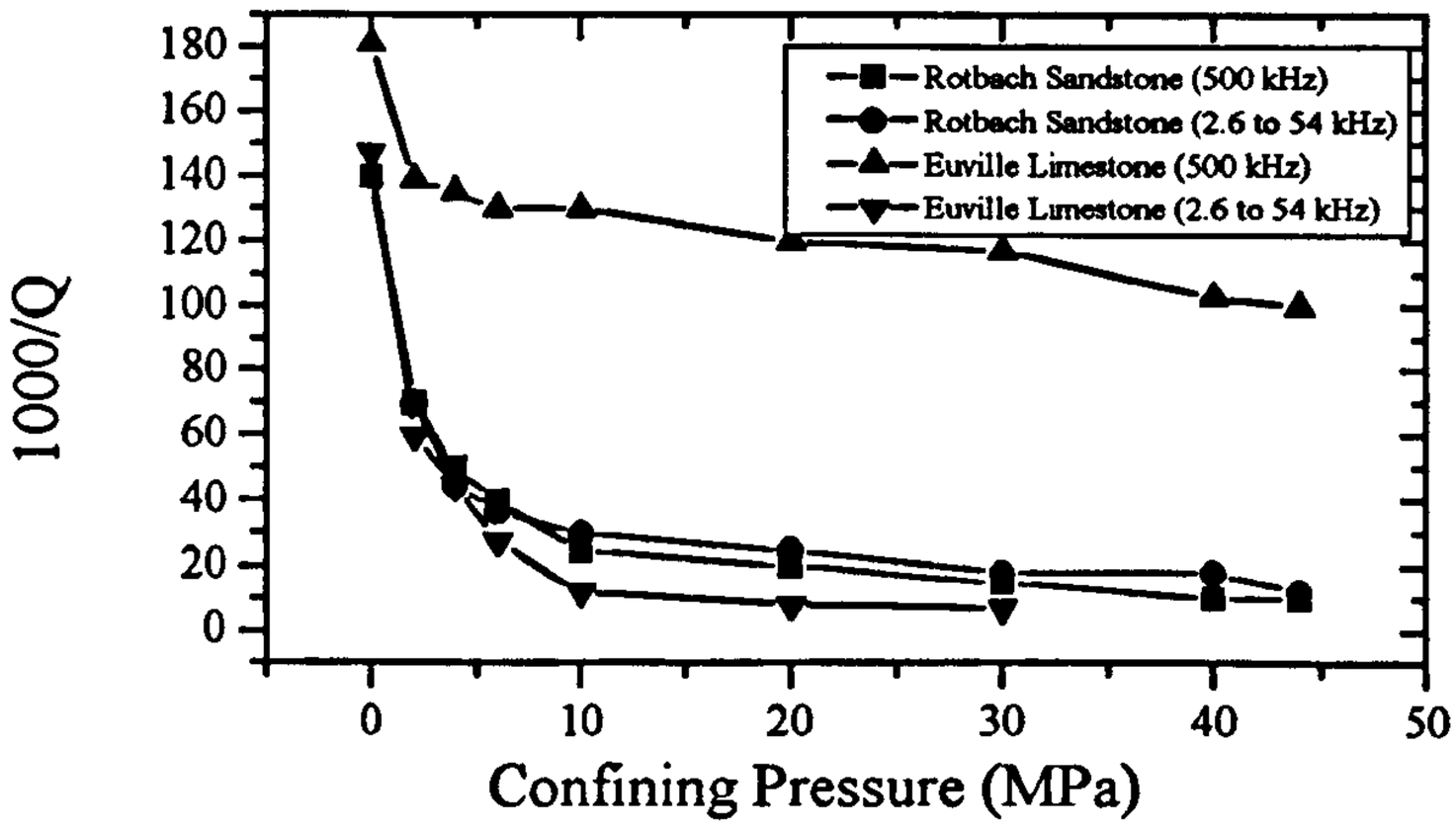

FIGURE 2.8. Pressure dependence of 1000/Q in Rotbach Sandstone and Euville Limestone at 2.6 kHz to 54 kHz and 500 kHz, after Lucet & Zinszner (1992)

The last section showed that attenuation follows a similar trend to seismic velocity when a rock is subjected to a hydrostatic stress regime for apparently same reasons of crack closure and pore collapse. It therefore seems sensible to assume that stress-induced attenuation anisotropy should occur for a state of anisotropic stress.

Lockner et al (1977) measured amplitude ratios for the first and second arriving peaks as a function of the percentage failure strength in axially loaded granite samples. Propagation paths were normal to the axial loading axis. Peak P-wave amplitudes were seen to gradually decrease with increasing axial load and dropped more sharply at around 80% of the sample failure strength. Lockner et al.(1977) deduced from this observation that P-wave attenuation was relatively insensitive to the initial closure of cracks parallel to the direction of propagation (i.e. initial closure of cracks due to the increasing axial load). However, the initiation of new cracks and the probable dilation of existing cracks perpendicular to the propagation path that accompanied the onset of sample failure had a larger effect on the peak amplitudes.

As far as the author is aware, no published accounts of true triaxial loading stress induced attenuation anisotropy experiments exist and this remains a large unexplored area in the literature today.

2.3.2 Saturation

Attenuation in fully or partially saturated rocks is higher than for dry rocks. The processes involved are complicated, depending on the degree of saturation, the frequency range of interest and the type of pore fluid. This discussion will be restricted to the case of water saturation. A limited number of authors have investigated the change in attenuation with increasing percentage water saturation (Murphy, 1982), (Jones, 1986). Figures 2.9 and 2.10 show the effect of partial saturation on Q of 0 to 10% and 10 to 100% respectively in sandstone.

Lunar rock studies have revealed that completely moisture free rocks under a condition of vacuum have very low attenuations. Work by Tittmann et al (1981) and Pandit and King (1979) shows a significant increase in attenuation occurs on the addition of small amounts of water from the completely dry state. Pandit and King (1979) observed a sharp fall in Q from 200 to 50 during the initial increase (about 0.01% by mass) in moisture content in Berea sandstone. Further increase in moisture content up to a cut-off of approximately 10% saturation produced no further significant change in Q.

Murphy (1982) explains this effect in terms of the lining of pore walls with a film of water 1 to 10 nm thick with the onset of moisture increase. The moisture is drawn

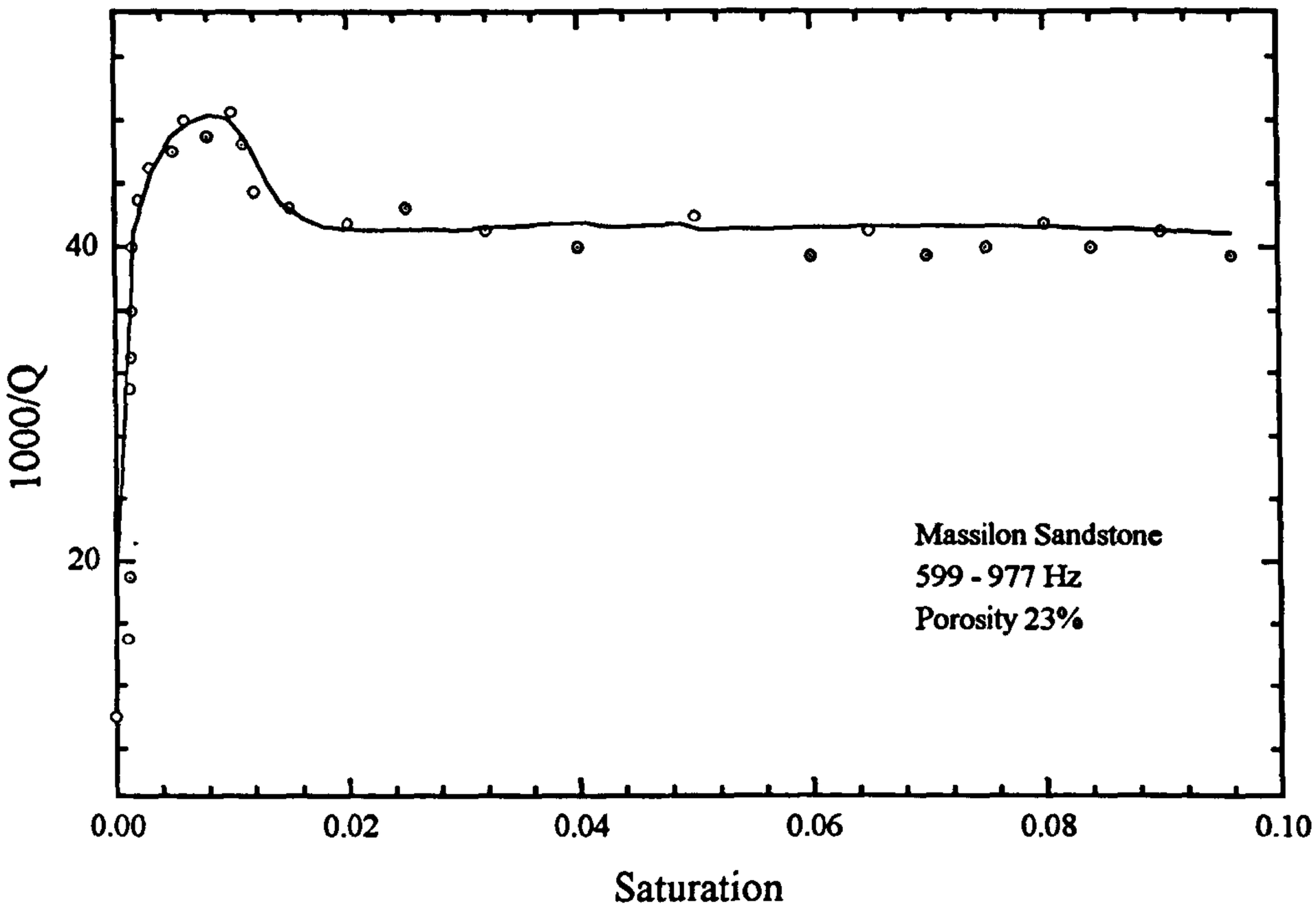

FIGURE 2.9 Low water saturation effect on Q, after Murphy (1982).

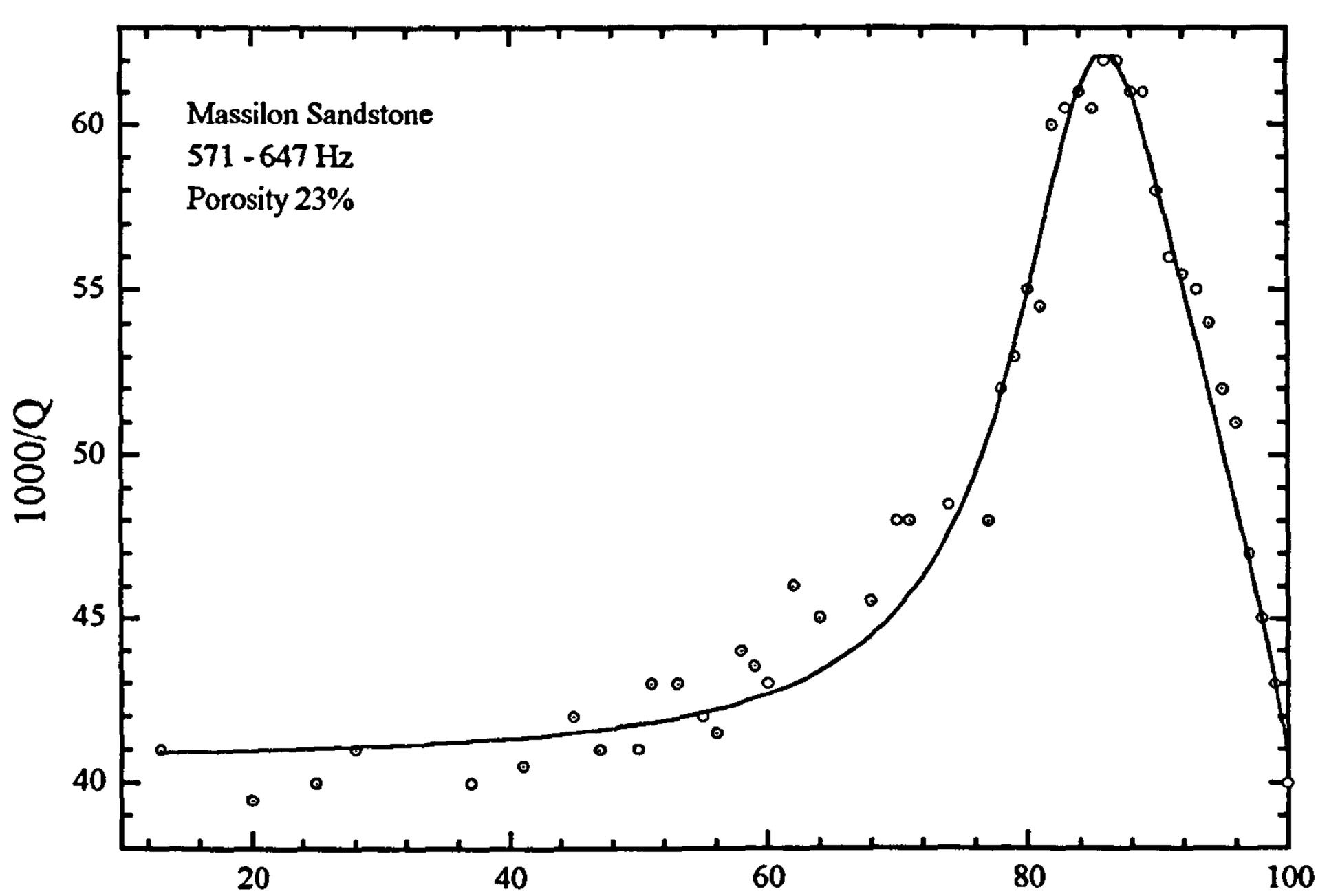

FIGURE 2.10 Partial to complete saturation effect on 1000/Q after Murphy (1982).

into and held in the capillaries by strong capillary pressure. This develops an adhesive force sufficient to densify the material. When subjected to a compressional wave front the film must deform as pores are compressed and energy loss occurs by overcoming either breaking the bond between the water film and the pore wall or capillary interface, or viscous dissipation induced in the film as it moves across the pore surface.

Between the saturations of 0.2 and 0.5 no significant change is observed in Q. Above 0.5 a broad peak occurs for compressional waves. The process responsible has been called 'fluid flow'. Between 0.2 and 0.5 saturation, sample crack porosity, such as small pores and tubes, is becoming fluid filled. At a state of 50% saturation, only larger pores remain undersaturated and it is assumed that certain regions of the sample will be fully saturated whereas other regions remain dry, depending on the distribution of cracks (Walsh, 1995). Subject this state to a compressional wave front and fluid pressure will rise in the saturated regions due to decreasing pore volume forcing fluid to flow to unsaturated regions. This process results in energy loss in the form of viscous dissipation. The process is frequency dependent since at very high frequencies, no fluid flow occurs and no energy is dissipated due to the small compressional front cycle times. At low frequencies flow may occur but viscous stresses are low and flows can be considered to be lamina in nature. In the intermediate frequency zone, loss is not negligible and this bell shaped peak is observed. Further discussion of this phenomenon can be found under the sections of the frequency dependence of attenuation and theoretical mechanisms.

2.3.3 Porosity and Clay Content

Klimentos & McCann (1990) derived an empirical relationship to show that attenuation coefficient, α at 1 MHz in sandstones is linearly dependant on the percentage of intrapore clay minerals. Han et al (1986) derived a similar relationship, showing a weak relationship between pulse amplitude, clay content and porosity. The empirical relationship given by Klimentos & McCann (1990) shows that in sandstones, at 1 MHz and 40 MPa confining pressure, clay content, C, has an order of magnitude greater effect than porosity, ϕ,

$$\alpha = 0.0315\,\phi + 0.241\,C - 0.132 \qquad (2.10)$$

The presence of clay in sandstones causes the following effects (Klimentos & McCann, 1990)

- Reduces the diameters of pores
- Increases the specific surface area.

- Fills pores with small diameter particles.
- Creates microporosity with pores of diameter less than 1μm.

2.3.4 Frequency Dependence

Laboratory evidence indicates that Q may be independent of frequency (i.e. the attenuation coefficient, α, is proportional to frequency) over a broad frequency range in dry rocks. Toksov et al (1979), Johnston et al (1979), Johnson & Toksov (1980) all suggest that Q is independent of frequency for the range 10 Hz to 1 MHz. Attewell & Ramana (1966) analysed P-wave attenuation data from 14 authors, encompassing 120 data points in the frequency range $1<f<10^8$ Hz and concluded that the attenuation coefficient, α, is described by the equation,

$$\alpha = 10^{-5} f^{0.911} \qquad (2.11)$$

More recent work by Klimentos and McCann (1990), Molina and Wack (1982), Peacock et al (1994) and Tutuncu et al (1994) confirm these findings for dry rocks.

Q^{-1} in liquids is proportional to frequency and therefore fluid saturated and partially melted rocks should show a weak dependence on frequency, $Q^{-1} \propto f^n$, where n is between 0 and 1.

In the laboratory, Tittmann et al (1981) measured Q for fully saturated Berea sandstone at 7 kHz and 200 Hz across a range of different effective pressures and found attenuation to be greater at the higher frequency range. Winkler and Nur (1982) observed an apparent peak in Q^{-1} for saturated Massillon sandstone at about 4 kHz, but reported Q^{-1} independent of frequency in the dry case. Other workers have shown that attenuation is strongly affected by fluid saturation and the seismic frequency (Spencer, 1981), (Jones and Nur, 1983), (Jones, 1986) and the process is considered to be related to local scale fluid flow (see section 2.4.2)

Kan et al (1983) claim to have observed frequency dependent Q from spectral ratio analysis of Vertical Seismic Profile (VSP) data. However, many authors studying similar VSP datasets claim constant Q wave propagation (Ganley and Kanesewich, 1980), (Spencer et al, 1982). To detect statistically significant frequency dependence of Q in-situ is inherently difficult because of the relatively short bandwidths for surveys and the presence of noise, as well as the problems of distinguishing between the intrinsic and extrinsic components of attenuation (see section 2.1.1)

Such ambiguity about the frequency dependence of Q has led to the general acceptance that for investigations involving limited bandwidths it is reasonable and mathematically simpler to adopt an approximation of constant Q propagation

(Kjartansson, 1979a). For the interpolation of high frequency laboratory results to low frequency seismic field frequencies this is an invalid assumption and a better understanding of the attenuation mechanisms in play at the different frequencies is necessary to attempt such a transition.

2.3.5 Grain Size and Density Heterogeneities

Grain size can have an effect on attenuation at higher frequencies, where the ratio of the wavelength to the grain or homogeneity diameter is close or equal to 1. Winkler (1985) observed a large increase in attenuation at frequencies greater than 1 MHz in large grained rocks, indicating that grain scattering was a significant source of attenuation. Almossawi (1988) carried out attenuation studies on highly porous synthetic sandstones and concluded that the attenuation coefficient increases with increasing grain and pore size. He deduced that the increasing grain or pore size distorts the signal due to preferential attenuation of high frequency components. The rock effectively acts as a low pass filter with properties linearly related to the pore or grain size.

Blair (1990) concluded, from his measurements on granite blocks at two different frequency ranges, that the discrepancy between the two values of Q was due to scattering from grains at the higher frequency range. However, the wavelengths involved were greater than the grain diameter and he attributes the attenuation to scattering from grain clusters or density heterogeneities rather than single grains. Lucet & Zinszner (1992) made similar observations in limestone core samples at two different frequency ranges. They attributed the higher attenuation values at the higher frequency range (as seen in figure 2.8) to scattering from density heterogeneities, the existence of which, they proved using X-ray scanner tomography.

2.3.6 Temperature.

In general Q is independent of temperature at temperatures low relative to the melting point, Gordon & Davis (1968). Anomalies to this were noted by Gordon & Davis (1968) in quartzite at 150 ^{0}C where an increase was observed in attenuation which they attributed to thermal cracking of the sample.

Conversely, at low temperatures where pore fluids freeze, a large increase in Q is observed (Toksov et al, 1979), (Remy et al, 1994).

2.3.7 Strain Amplitude.

Q is roughly independent of strain amplitude provided that this amplitude is low enough. Beyond a certain strain threshold, Q becomes amplitude dependent (Peselnick & Outerbridge, 1961), (Winkler et al, 1979), (Gordon & Davis, 1968). The accepted strain threshold has been determined experimentally and its value is around 10^{-6} for a variety of rock types in dry, partially saturated and saturated states. This value is higher than those expected in seismic studies and hence strain dependent effects can be ignored. However, strain amplitude dependence provides clues to likely attenuation mechanisms, discussed in the next section.

2.4 Intrinsic Attenuation Mechanisms.

2.4.1 Frictional Sliding Model

Rocks are essentially polycrystals, made up from single crystals of their constituent minerals. However, experimental observations of Q for rocks are always much lower than values determined for the single crystal components. A possible mechanism responsible for this discrepancy is known as frictional sliding. The mechanism involves the frictional dissipation of energy as heat due to the relative motions at grain boundaries and across crack surfaces induced by wave propagation. The increase in Q with pressure is consistent with a frictional mechanism, pressure closing cracks and decreasing the number of surfaces available for frictional dissipation. However, a rock subjected to a confining pressure sufficient to close all cracks still exhibits non-zero attenuation. This residual attenuation is attributed to the small perturbations to elasticity present in the single crystal matrix.

Other evidence for a frictional mechanism comes from studies in lunar rocks, where Q is found to be very high in totally dry rocks under hard vacuum conditions. Coulomb forces are very strong and friction coefficients are high which prevent sliding motion occurring.

Walsh (1966) derived expressions for internal friction based on distributions of 'critical' cracks. The 'critical' crack is one whose faces are barely touching, cracks whose faces are completely open or closed are unable to contribute to attenuation by frictional dissipation.

Mavko (1979) showed that a frictional mechanism must yield attenuation directly proportional to the strain amplitude of the passing wave. However, observations by numerous authors have revealed that Q^{-1} is independent of strain amplitude below a

certain threshold value (see section 2.3.7). Some experimental results for Berea sandstone are reproduced from Winkler & Nur (1982) in figure 2.11. The threshold amplitude for onset of the non-linear behaviour shifts upwards with increasing pressure. Seismic strains are generally less than this threshold and a conclusion to be drawn from this is that although sliding friction may contribute to attenuation above strain levels of around 10^{-6}, this mechanism cannot be responsible for the observed frequency independent Q values found at lower strains.

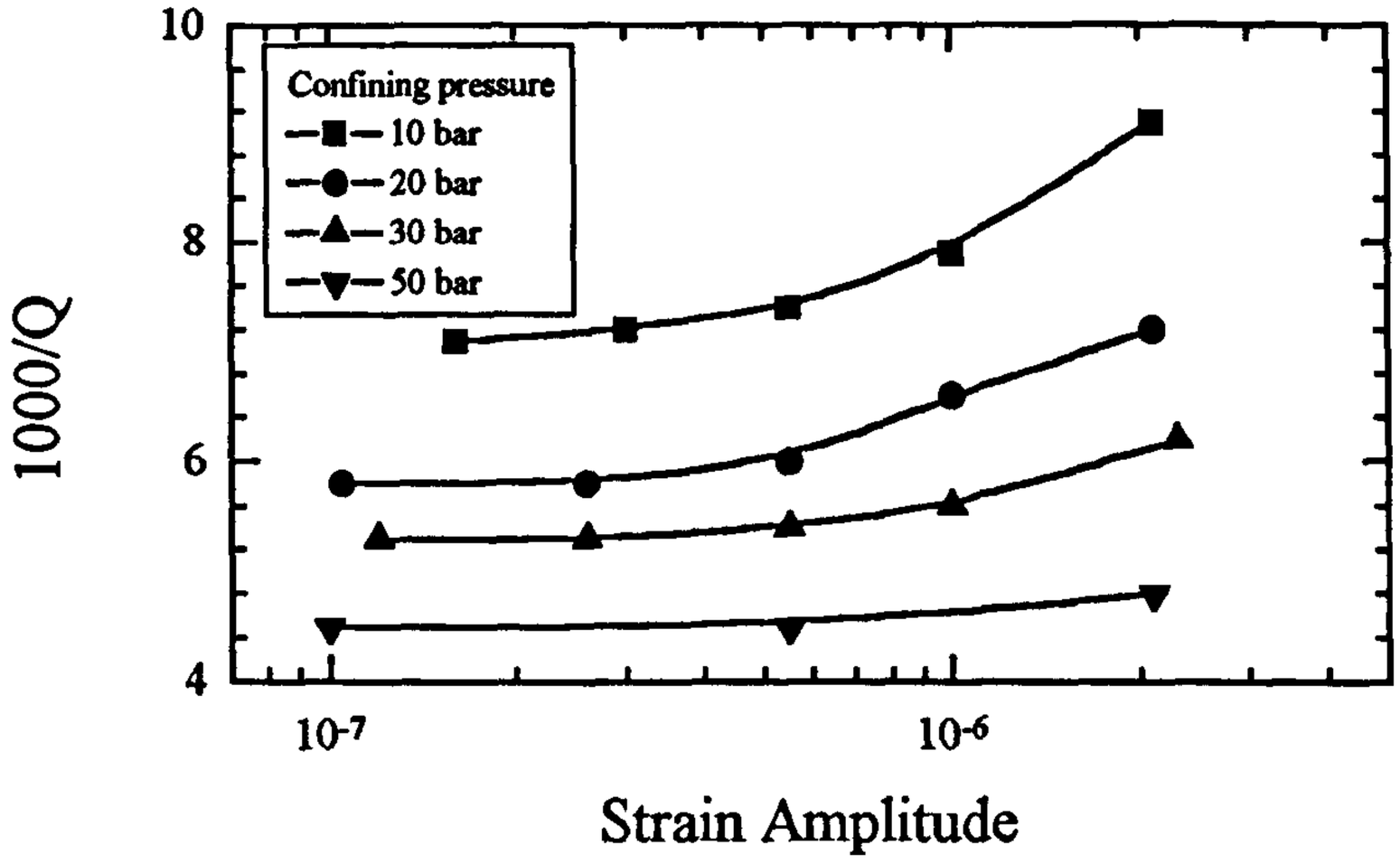

FIGURE 2.11 Q^{-1} versus strain amplitude with differing hydrostatic confining pressures, after Winkler & Nur (1982).

2.4.2 Pore fluid-rock matrix interaction models

So far, the discussion on mechanisms has only considered dry rocks. All rocks in the confines of in-situ conditions are partially or completely saturated with a pore fluid such as water or brine. In the case of partial saturation, the remaining pore void is occupied by a gas. Section 2.3.2 showed that pore fluids have very strong effects on attenuation in rocks even at very low strain amplitudes. Winkler et al (1979) showed that the addition of small amounts of water lowered the strain amplitude threshold for non-linear behaviour presumably due to the lubrication of cracks and surfaces, making sliding easier. On the addition of more water no significant increase in the lubricating effect is observed but the increased saturation is accompanied by a drastic reduction in Q. Obviously another mechanism, or combination of mechanisms, is responsible for this increase in attenuation relating to the pore fluid. The type of mechanism thought to be operating with the greatest dominance differs according to whether the rock is fully or partially saturated and the frequency range of wave propagation. Winkler and Nur

(1982) provide a good qualitative overview of many of the proposed mechanisms as follows,

- Effects of wetting on grain boundary friction (Johnston et al, 1979)
- Macroscopic fluid flow (Biot, 1956a,b)
- Intercrack squirt flow (Mavko and Nur, 1975), (O'Connell and Budiansky, 1977)
- Intercrack flow (Mavko and Nur, 1979)
- Thermoelastic effects (Kjartansson 1979b)
- Flow between macroscopic regions of total and partial saturation (White, 1975), (Dutta and Seriff, 1979).

Biot (1956a,b) formulated a comprehensive theory to describe acoustic wave propagation in porous rock based on the interaction of the rock matrix frame with the pore fluid. By subjecting rock to an acoustic wave the effect is to accelerate the rock matrix which generates shear stresses within the pore fluid. These stresses decay exponentially away from the pore wall within a viscous skin depth that decreases with increasing frequency. Biot's theory predicts three scenarios dependant upon the frequency range of wave propagation.

- At low frequencies the viscous skin depth is larger than the pore diameter and hence induced shear stresses are small and energy dissipation is minimal.
- At high frequencies the viscous skin depth is very small which results in large shear stresses but concentrated in a small volume near the pore wall. The resulting energy dissipation is still small.
- At intermediate frequencies where the skin depth is comparable to the pore diameter, moderate shear stresses exist throughout the entire pore volume, imparting maximum resistance to wave propagation and resulting in maximum energy dissipation.

Biot's theory predicts macroscopic flow in the direction of wave propagation and derives equations for velocity dispersion and attenuation. However, in many cases, the theory greatly underestimates these values, indicating that other mechanisms may account for the apparent discrepancies. The Biot theory falls down in its prediction of the viscoelastic behaviour of rocks with fluids. For example, Nur and Simmons (1969) observed an increase in compressional wave velocity with increasing pore fluid viscosity, but the Biot theory, on its own, predicts an opposite trend.

Apart from this macroscopic 'Biot flow', another mechanism that has been proposed is entitled 'Squirt flow'. Squirt flow is the movement of fluid laterally out of pores and cracks as the pores are compressed by a propagating P-wave. The process is graphically illustrated in figure 2.12. This squirt mechanism seems best able to explain experimental attenuation data for partially saturated rocks (Winkler & Nur, 1979), (Mavko & Nur, 1979), (Palmer & Traviola, 1980). Every crack in the rock matrix is partially saturated, with the liquid phase wetting the crack surfaces and accumulating at crack tips or at constrictions along the crack length. This process is illustrated in figure 2.13. Under the action of a compressional wave, the grain surfaces are pushed together, causing fluid to flow toward the pressure release areas of the air pockets. This mechanism could explain why P-wave attenuation in partially saturated rock is much greater than in the fully saturated case (see figure 2.10). Theoretical models predict that at low frequencies attenuation varies as the square of frequency and its magnitude is most greatly affected by the thinnest cracks, those being the ones that take up the pore fluid first by capillary action.

A combined Biot / Squirt flow mechanism model known as the BISQ model has been presented by Dvorkin et al (1994) which allows the pore fluid to simultaneously participate in the Biot type flow and the squirt flow. This model is an improved attempt to quantitatively relate the features of the squirt flow and Biot flow mechanisms to macroscopically measurable rock and fluid properties and frequency.

2.5 Conclusion

This chapter has reviewed experimental evidence and current theoretical explanations for the factors that affect the propagation of compressional waves. What is obvious from this discussion is that the number and variety of these factors is large. This potentially makes the process of identifying specific rock properties from seismic field measurements difficult because of the data's reliance on a number of interrelated factors depending on the in-situ conditions. The controlled conditions of the laboratory attempt to isolate one or two variables of interest where this is not possible in the field. What this chapter has done is define the influence (at current levels of knowledge) of a number of factors and therefore arms the interpreter with a set of rules. The interpreter can then, in the light of laboratory findings, deduce the most likely field conditions based on what is available from the seismic data. A typical example of this type of application is in the exploration for natural gas. A gas bearing horizon is usually characterised by a 'flat spot' in the seismic data, that is a region where reflections cease to exist or are severely reduced in size across the section. Laboratory analysis indicates

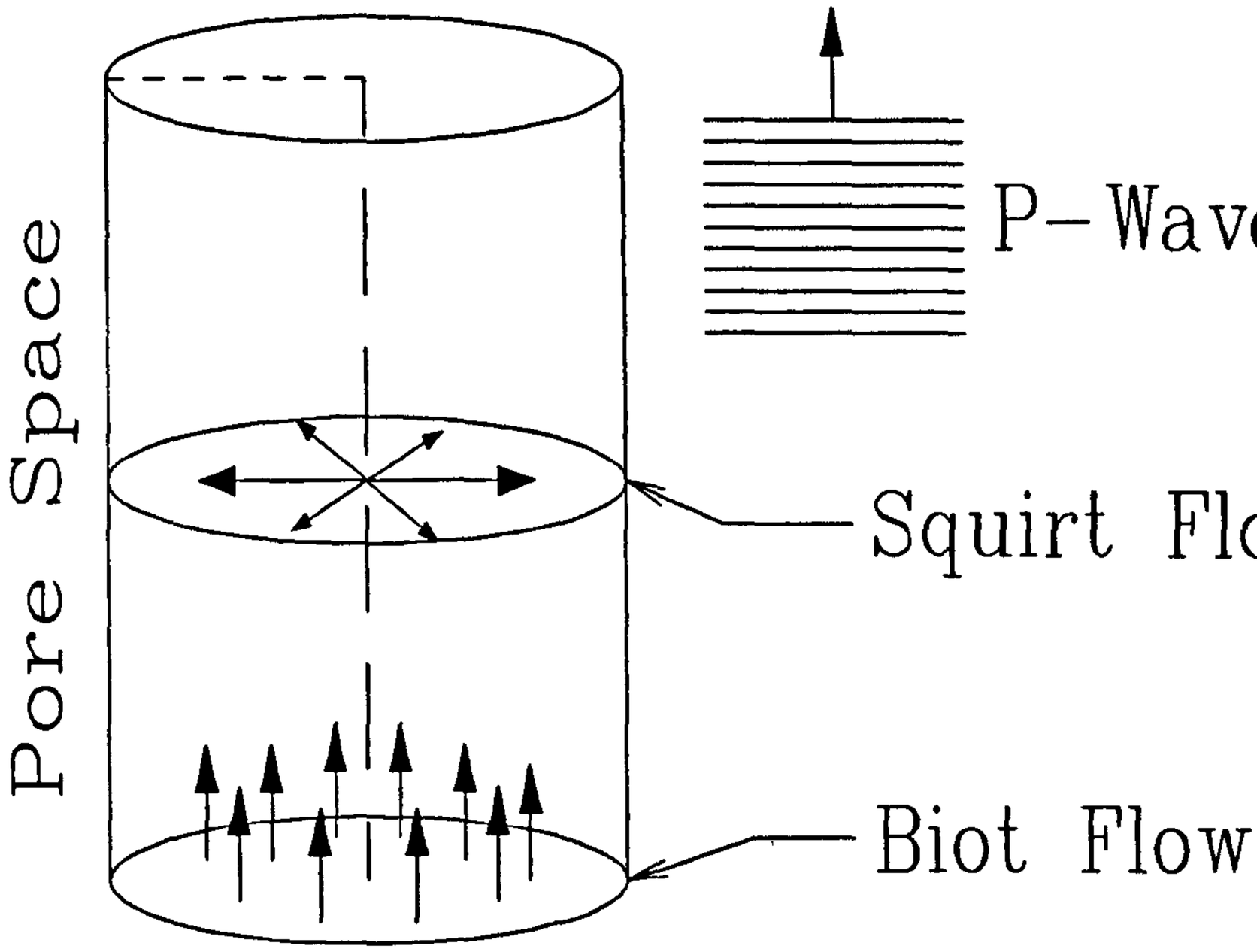

FIGURE 2.12 Graphical representation of Biot and Squirt flow mechanisms when a rock matrix is subjected to a compressional wave front.

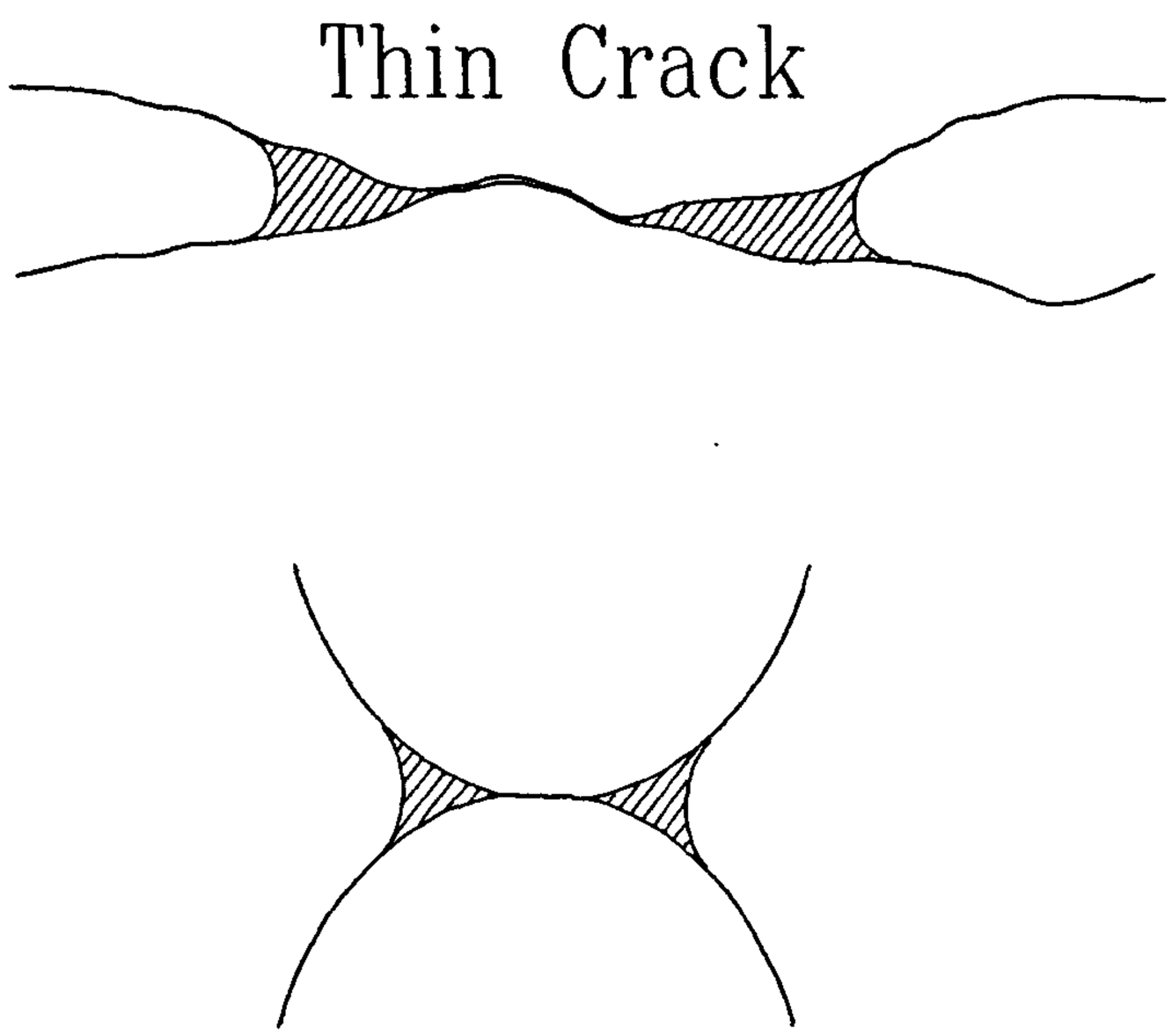

FIGURE 2.13 Pore space occupation in partially saturated rock, with the liquid phase (represented by hatching) at crack or pore tips or at constrictions along the length of the crack.

that partially saturated rocks have unusually high attenuation due to the squirt flow mechanism. Therefore the presence of gas in that layer is the most likely cause for the 'flat spot'.

This chapter has set a reference point for the rest of the thesis when discussing rock properties or conditions inferred from seismic velocity and attenuation and will be referred to again on a number of occasions for clarification of specific points.

CHAPTER 3

3. The Laboratory Determination of Velocity and Attenuation.

3.1 Introduction

This chapter describes the experimental techniques used to determine P-wave velocity and attenuation on rock core samples. Velocity was determined using the ISRM standard. No standard however exists for the measurement of attenuation and the merits and disadvantages of three methods described in the literature are discussed.

The aims of the laboratory study were to investigate the effects on velocity and attenuation of :

- 'triaxial' stress on saturated and 'room dry' samples.
- fracturing on saturated and 'room dry' samples.
- frequency on saturated and 'room dry' samples.

In this case, 'room dry' is a term used to describe a sample state under normal laboratory conditions, where the sample has been left on an open bench to equilibrate with the surrounding atmosphere for a period of at least 2 weeks.

'Triaxial' stress was simulated using a uniaxial compression loading frame in conjunction with a Hoek cell, so in effect the confinement was biaxial ($\sigma_2 = \sigma_3$ controlled by the cell pressure), and the loading was uniaxial (σ_1 controlled by the press).

Frequency dependence was investigated by using two sets of P-wave transducers. One set was centred at 1MHz with a usable range of 0.6 to 1.2 MHz. The other set was centred at approximately 29 kHz with a usable range of 18 to 65 kHz.

3.2 Attenuation Measurement.

Three methods are described and have been used by previous authors for the laboratory measurement of attenuation in rock samples by pulse transmission. The three methods are:

- Rise Time - Gladwin & Stacey (1974), Blair (1982), Blair & Spathis (1982 & 1984), Tariff & Bourbie (1987), Kavetsky et al (1990).

- Spectral Ratios - Toksov et al (1979), Sears and Bonner (1981), Tarif & Bourbie (1987), Almossawi (1988), Lucet & Zinszner (1992), Remy et al (1994), Tutuncu et al (1994).
- Buffer Rod - Papadakis et al (1973), Winkler & Plona (1982), Klimentos (1988), Klimentos & McCann (1990), Green et al (1993), Peacock et al (1994).

3.2.1 The Methods Outlined:

3.2.1.1 Rise time

The rise time refers to the time difference between the P-wave arrival and its first peak amplitude according to one of the following definitions:

- Gladwin & Stacey (1974) define the rise time τ, as the time difference between the intercept of a tangent to the point of maximum slope extrapolated to zero amplitude and the first peak amplitude.
- Blair & Spathis (1982) define the rise time as the time difference between 10% and 90% amplitude levels of the first peak.

Experimental evidence presented by Gladwin & Stacey (1974) shows a linear relation for the variation of rise time with distance of wave propagation in rock, a phenomenon known as pulse broadening, according to the following equation,

$$\tau = \tau_0 + CT/Q \qquad (3.1)$$

τ = rise time.

τ_0 = rise time of the source.

C = source dependant constant.

T = traveltime.

Q = Rock Quality Factor.

3.2.1.2 Spectral Ratios

The Spectral Ratio technique was adapted for the laboratory by Toksov et al (1979) and is essentially a comparison technique between the rock sample and a reference sample of identical dimension with very low attenuating properties. Aluminium is usually used, it having a Q value estimated by Zamanek & Rudnick (1961) at over 150000. Two measurements are made using identical procedures, one with the rock specimen and the other with the reference sample. The spectral ratio is

calculated in the frequency domain and a best fit line used to determine the slope, which is proportional to Q.

3.2.1.3 Buffer Rod

Papadakis et al (1973) first pioneered this method for measurement of attenuation in metals. Spectral ratios are calculated from the frequency spectra of an input pulse reflected from the front face of the sample and the same pulse reflected from the base face. A perspex buffer separates the transducer from the sample, effectively 'slowing down' the reflected arrivals so that they can be separately distinguished on the received waveform. The attenuation coefficient can be calculated with frequency by taking into account the reflection coefficients of the perspex buffer and the sample interfaces.

3.2.2 Discussion of the Three Methods

The accuracy of the rise time method is purely dependant upon the ability of the rise time law to successfully describe wave propagation according to equation 3.1. Kjartansson (1979a) proved the relation theoretically and showed that the constant C is source and Q range dependant. Blair & Spathis (1982) observed differences in the calculated value of Q of up to 200% using two different sources on the same sample of rock. They concluded that equation 3.1 is not valid for short traveltimes, such as those expected in the laboratory, since τ_0 is source dependant, but is not strictly equal to the rise time at $T = 0$.

Tarif & Bourbie (1987) propagated experimental and theoretical source wavelets using Kjartanssons constant Q transfer function for various values of T/Q and found a two stage linear relationship. They concluded that if this relationship is known, either by theoretical or experimental determination, then it could be used to determine Q from a real data set. However, Blair & Spathis (1984) showed that the constant Q model of Kjartansson (1979a) can produce erroneous results despite the real data showing a linear relationship. They concluded from this that C and τ_0 are also dependant on the response characteristics of the source and receiver and their coupling functions to the surrounding medium.

Tonn (1991) investigated the use of rise time on VSP data, both synthetic with variable amounts of noise and real, and concluded that the method was strongly dependant on the sampling rate and the data quality. The results were generally poor.

The main assumption with the spectral ratio technique is that Q is independent of frequency over the range of investigation. This matter has already been discussed in chapter 2. The method itself confirms whether this assumption is correct. An identical

geometry reference sample and good coupling between samples and transducers is required to eliminate any geometrical dependant effects from the experiment. These samples are difficult to make, particularly because of the limitations when working with rock to produce samples to match existing reference samples. Toksov et al (1979) suggested using the same rock sample frozen as the reference since attenuation should be very low. This may however irreversibly damage the sample for any subsequent analysis.

Tarif & Bourbie (1987) and Tonn (1991) investigated the effect of noise on the spectral ratio estimate of Q. Tarif & Bourbie (1987) concluded that the method was still accurate even in the presence of 20% noise. Tonn (1991) compared 10 different methods for the determination of Q and concluded that spectral ratios was amongst the top three in terms of reliability in the presence of 'minor' noise. He does not however define this level. By stacking signals in the laboratory we can significantly reduce if not negate altogether the effect of noise. The other two reliable methods were numerical waveform modelling techniques only suitable for field determinations of attenuation.

The Buffer Rod method is an attractive method as there is no need for a reference sample. However, the experiment is technically more difficult to set up since ultrasonic source pulse lengths need to be very short requiring expensive hardware for transducer excitation and trace acquisition, and the pressures to which samples can be confined are limited by the strength of the perspex buffers.

With consideration of the above factors and the available resources, it was opted to use the spectral ratio method for all determinations of Q. Both the Buffer Rod Method and the Spectral Ratio Method have gained acceptance in recent literature. The reference sample problem was solved by producing a set of aluminium samples increasing in length in steps of 0.05 mm over the length range of rock samples under investigation. This meant that a reference sample was always available for each sample with a maximum length difference of 0.025 mm or approximately 0.2 % of the wavelength at 1 MHz.

For absolute measurement of Q, results from all three methods need to be corrected for diffraction or geometrical spreading effects using the method described by Papadakis et al (1976). We were however only concerned with the relative changes in attenuation and therefore the extra complexity introduced by diffraction corrections was not deemed necessary.

3.3 Description of the Spectral Ratio Method.

3.3.1 Theoretical Background.

Consider a plane wave travelling in an absorptive medium. The amplitude in the frequency domain $A(\omega)$ may be described by the following equation,

$$A(\omega) = A_0(\omega)\exp\left[i\left(\omega t - K(\omega)x\right)\right] \tag{3.2}$$

where,

$i = \sqrt{-1}$

$$K(\omega) = \frac{\omega}{c(\omega)} - i\,\alpha(\omega) \tag{3.3}$$

$K(\omega)$ = complex wavenumber represented by equation 3.3 and,

$c(\omega)$ = phase velocity

$\alpha(\omega)$ = attenuation coefficient

ω = angular frequency

x = distance of propagation.

$A_0(\omega)$ = frequency response at time t = 0 (source).

Now consider the laboratory case. The propagation of a plane seismic wave through a reference sample and rock sample can be described by the two following equations, including a term G to account for the effects of spreading, reflection and transducer coupling and the source frequency response.

$$A_1(\omega) = G_1(x)e^{i(\omega t - K_1 x)} \tag{3.4}$$

$$A_2(\omega) = G_2(x)e^{i(\omega t - K_2 x)} \tag{3.5}$$

The subscripts 1 and 2 refer to the aluminium reference and specimen respectively.

Figures 3.1 and 3.2 show some typical experimental results for an aluminium reference and a dry sandstone specimen respectively in the time and frequency domains. Taking the spectral ratio of the two frequency spectra by dividing eqn 3.4 by 3.5 and taking the natural logarithm the following expression is obtained,

$$\ln\left(\frac{A_1}{A_2}\right) = i(K_2 - K_1)x + \ln\left(\frac{G_1}{G_2}\right) \tag{3.6}$$

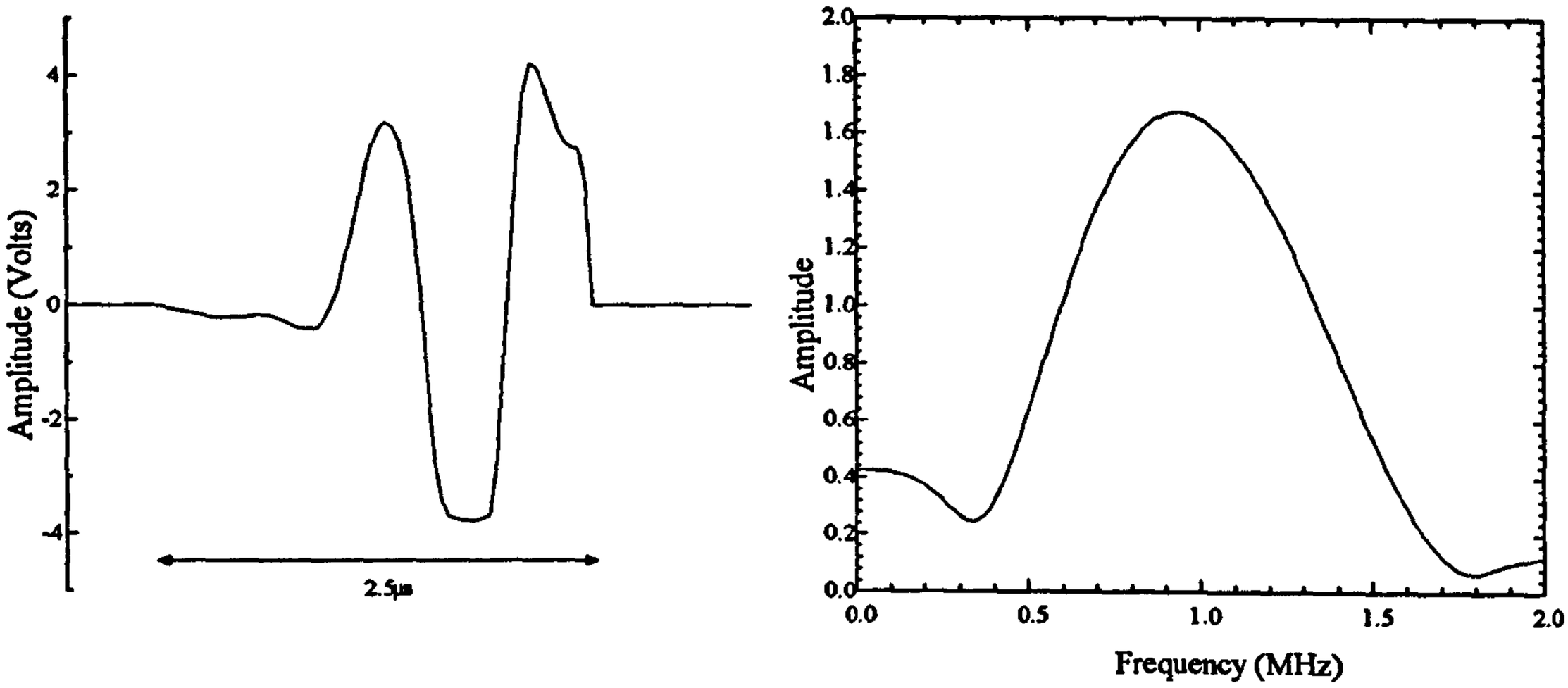

FIGURE 3.1 Aluminium reference time and frequency domain characteristics

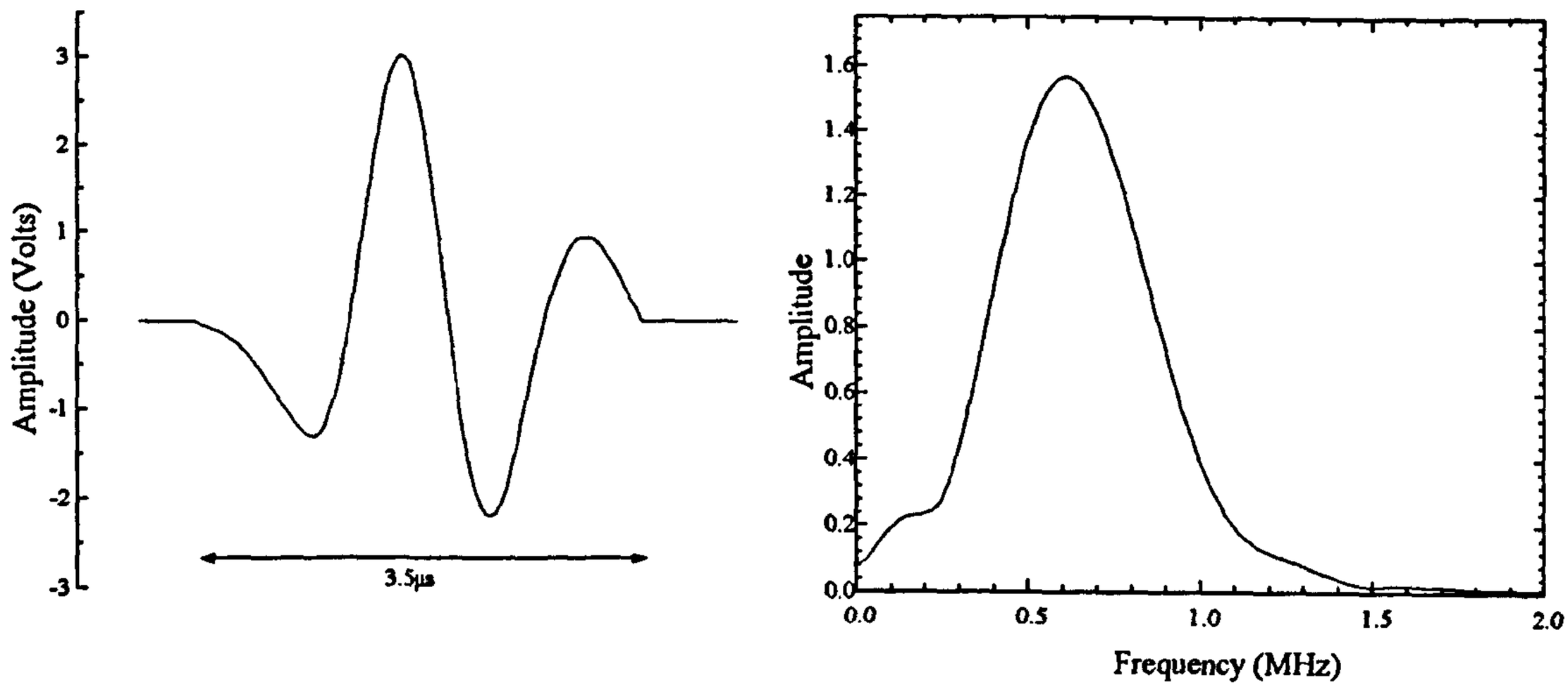

FIGURE 3.2 Dry sandstone time and frequency domain characteristics

Since the reference and specimen have the same geometry and coupling conditions the geometric term can be ignored, i.e. $G_1 = G_2$. Expanding equation 3.6 by substituting equation 3.3, the following expression is obtained,

$$\ln\left(\frac{A_1}{A_2}\right) = \left[\alpha_2(\omega) - \alpha_1(\omega)\right]x + i\left[\frac{\omega}{c_2(\omega)} - \frac{\omega}{c_1(\omega)}\right]x \qquad (3.7)$$

Since the attenuation of a plane wave through aluminium is very low, it is sensible to assume $\alpha_1(\omega) \approx 0$ and the amplitude of $\ln\left(A_1/A_2\right)$ can be used to estimate the attenuation change with frequency, and the phase of $\ln\left(A_1/A_2\right)$ can be used to estimate the phase dispersion.

A second assumption that attenuation is frequency independent over the range of investigation defines that the attenuation coefficient $\alpha(f)$ is proportional to frequency, i.e.,

$$\alpha(f) = \gamma f \qquad (3.8)$$

where γ is a constant and is related to the Quality Factor Q by,

$$Q = \frac{\pi}{\gamma v} \qquad (3.9)$$

where,

v = velocity

γ can be found from the slope of the fitted line to $\ln\left(A_1/A_2\right)/x$ versus frequency.

Figure 3.3 shows the spectral ratio calculated from the two frequency spectra in figures 3.1 and 3.2 and the least squares best fit line.

Figure 3.4 shows the spectral ratio calculated for a sample with very high attenuation. In this case a poor signal to noise ratio introduces erroneous peaks and oscillation into the ratio and the least squares line is badly affected by outlying data points.

This problem has been addressed by Oliver (1992) and Dasgupta (1994). Oliver (1992) showed that simple least squares slope estimation was not reliable when applied to VSP first arrival spectral ratios. He showed that the variance in spectral ratios is not normally distributed and hence least squares is not an appropriate method. He applied a robust M-Norm method to determine the slopes and found it gave much better results. Similarly Dasgupta (1994) encountered problems with noisy spectral ratios and resorted to the use of a robust method.

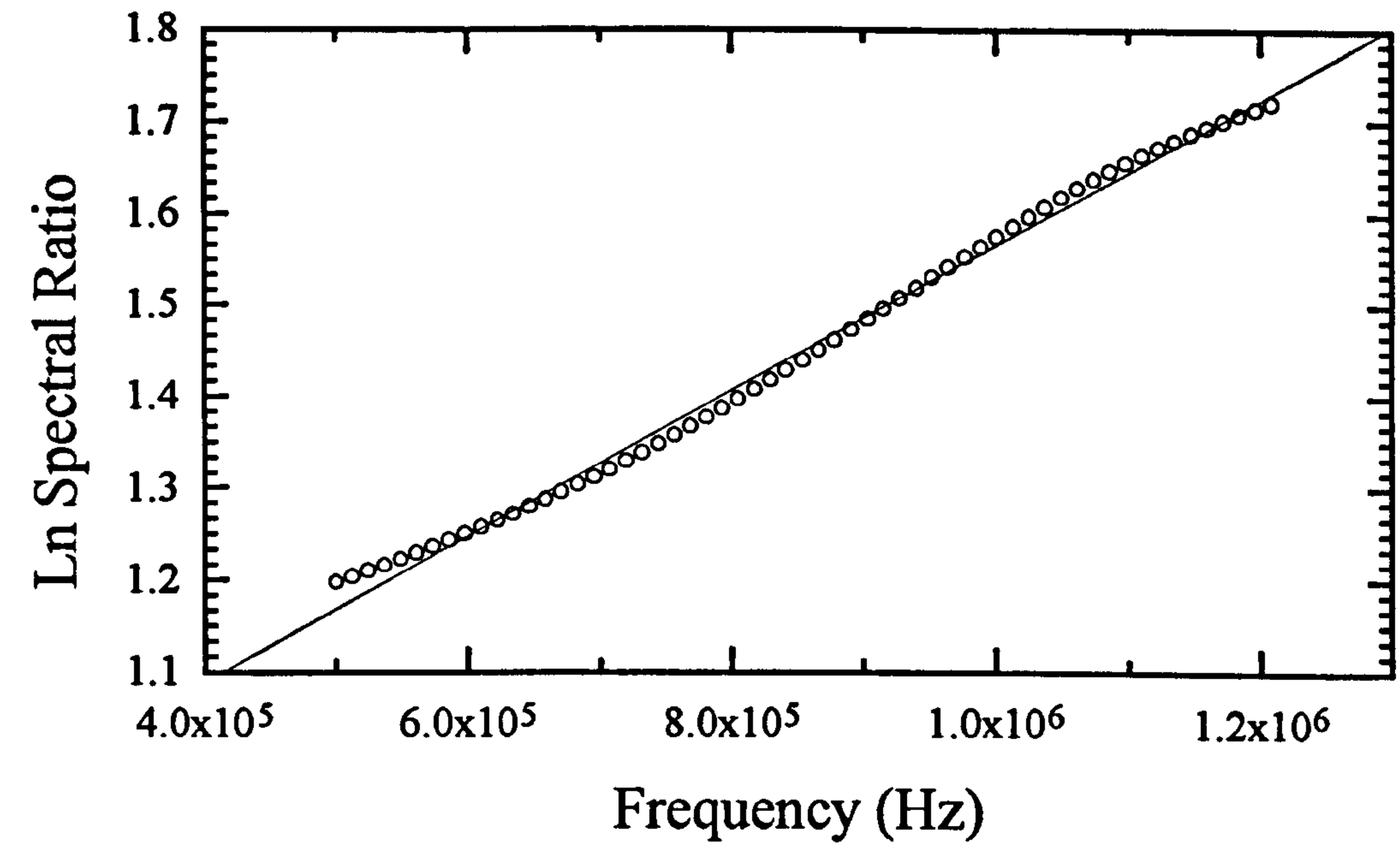

FIGURE 3.3 Spectral ratio calculated from the frequency spectra in figures 3.1 and 3.2 according to equation 3.7

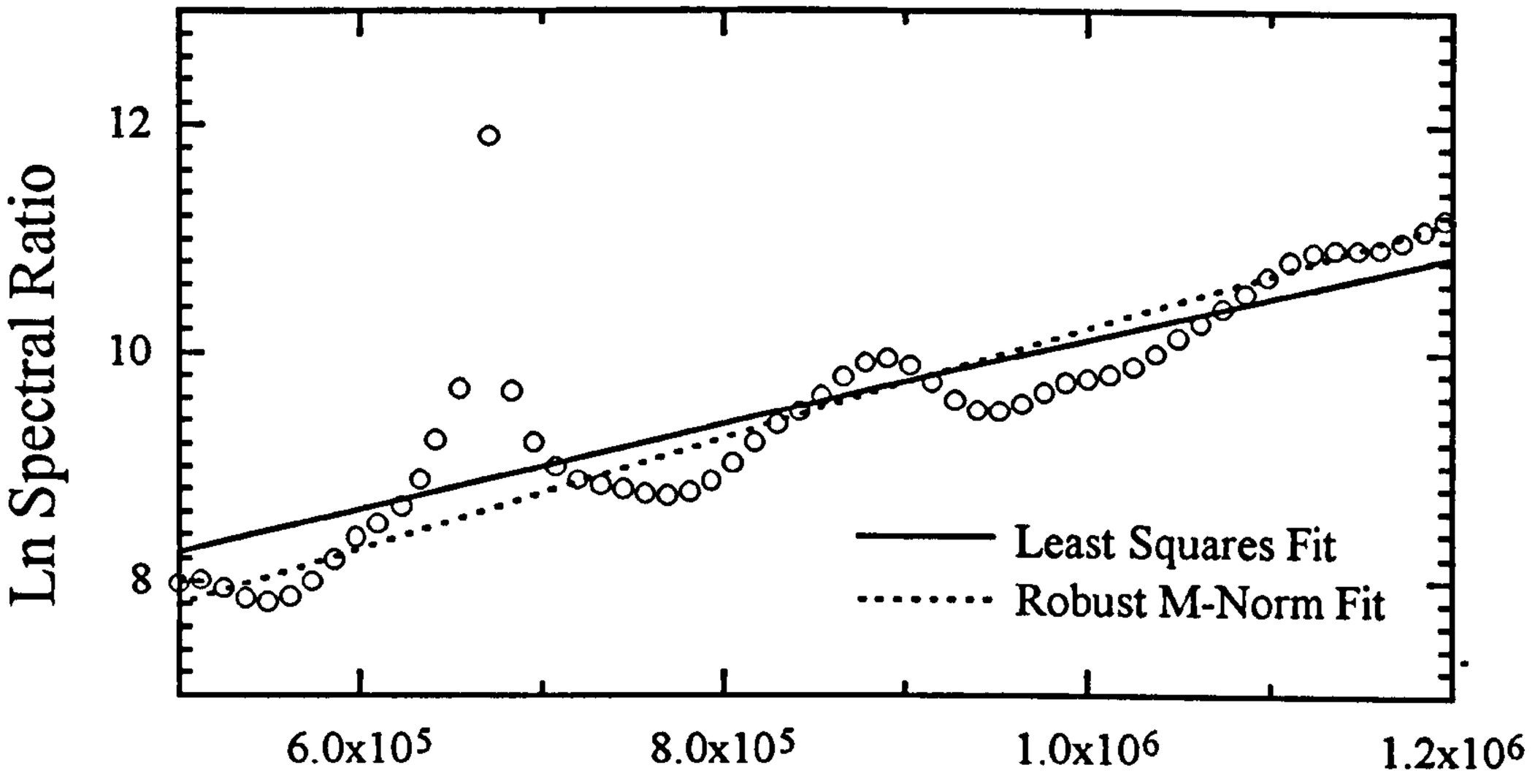

FIGURE 3.4 Spectral ratio for poor signal to noise ratio data due to high attenuation in a coarse grained sandstone. The peak may be due to resonance within the sample at 700 kHz.

For these reasons a robust method of slope estimation is adopted here based on the fitting algorithm of Williamson (1969). The method is intrinsically superior to simple least squares because it takes into account the uncertainties in both variables, rather than assuming that the uncertainty resides only in the 'y' value. The method assumes that the spectral ratio line consists of pairs of points (X_i, Y_i) where i runs from 1 to N, the number of points between the limits of our frequency range. Each point has a variance $\mathrm{var}(X_i) = u_i$ and $\mathrm{var}(Y_i) = v_i$. The data is to be fitted by a straight line of the form $y_i = a + b x_i$. The solution is obtained by iteratively minimising,

$$S = \sum_i \frac{(x_i - X_i)^2}{u_i} + \frac{(a + b x_i - y_i)^2}{v_i} \qquad (3.10)$$

Referring to figure 3.4 again it is obvious that the robust line is less affected by erroneous peaks and gives a more likely estimate of the gradient for Q calculation.

3.3.2 Experimental Set-up

Figure 3.5 is a pictorial representation of the components making up the experimental system for the high frequency transducers. The low frequency transducer experiment follows the same set-up without the need for two stage amplification of received signals.

Transducers are mounted in specially designed platens depicted in figure 3.6 which protect them from axial and horizontal loads. A spring provides sufficient force to ensure a good contact between the transducer and platen inside face.

3.3.2.1 Sample Preparation.

Two different sizes of rock core were used depending on the frequency range under investigation. For the 1 MHz transducers, samples were approximately 50 mm in length and 25 mm diameter. For the 29 kHz transducers, samples were approximately 130 mm in length and 54 mm diameter. These sizes were chosen on the basis of the realistic propagation distance that could be supported by the transducers and the sizes of the available Hoek Cells. All sample ends were flat bed ground parallel to within 0.02 mm. Samples were wrapped in a plastic sleeve to prevent penetration of oil leakage from the Hoek cell and assembled in the loading frame as indicated in figure 3.5.

3.3.2.2 Transducer - Sample Coupling and Traveltime Correction.

Two types of coupling have been used by previous authors:

- Viscous Liquid based coupling

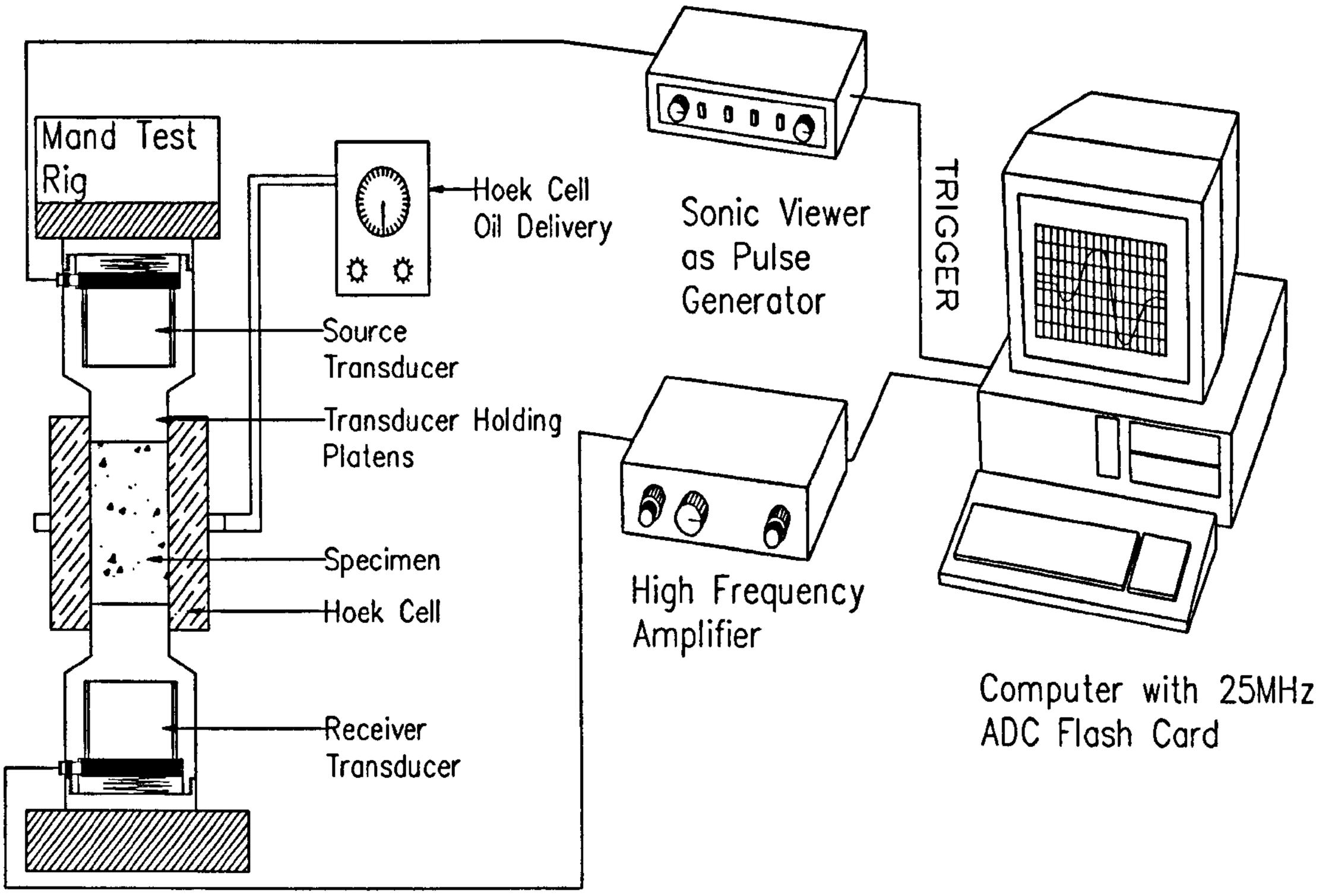

FIGURE 3.5 Spectral ratio experimental set-up for high frequency range transducers.

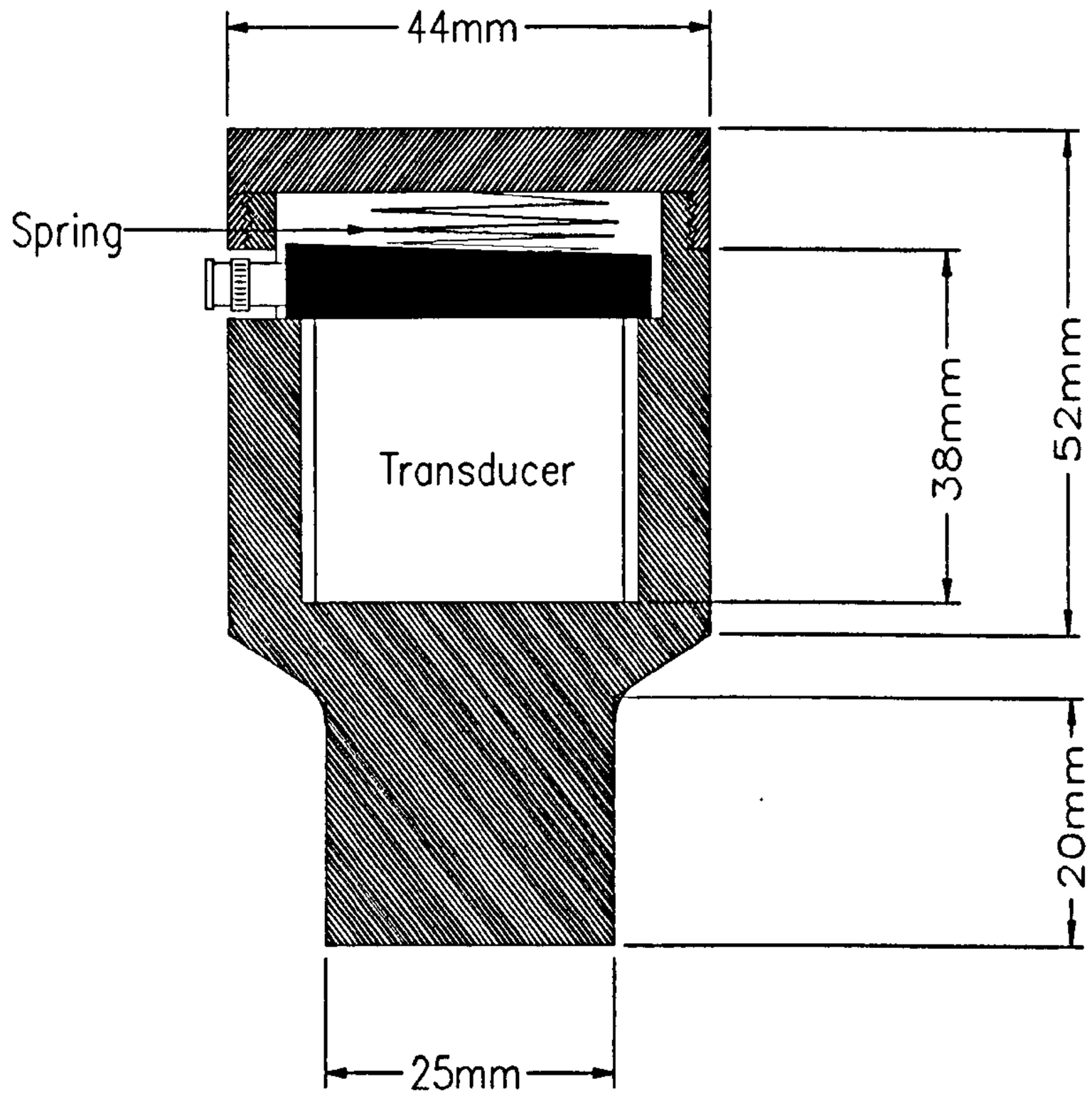

FIGURE 3.6 Transducer holding platens

- Metal Foil coupling

Li & Norland (1993) investigated the effects of coupling on P-wave transmission and concluded that viscous liquids are better than metal foils as acoustic couplants. The amplitude transmission ratio of a liquid couplant is greater than that of a metal foil and the traveltime through the liquid interface is shorter. The metal foil interface was found to be much more pressure dependant in its coupling properties with changes occurring up to axial pressures of 7MPa as opposed to no observed change above 3 MPa for a fluid contact.

A vaseline coupling was used here and the coupling characteristics of the transducers were checked by measuring face plate traveltimes versus axial pressure. The result is shown in figure 3.7 and it can be clearly seen that above 3 MPa no further contact pressure dependence is observed, the face plate traveltimes being unchanged within experimental error. This effectively set the lower axial stress limit for accurate velocity and attenuation measurement using the pulse method with the available transducers at 3 MPa assuming that the sample - transducer contacts are similar to the transducer - transducer contacts. This assumption is of course incorrect, since it is difficult to machine rock to the same specifications as aluminium especially in coarse grained samples. To check the rock transducer interface, figure 3.8 shows some Q value results for a coarse sandstone from low axial stress levels. The error bars show that below 3 MPa errors are relatively big and Q values vary widely. Between 3 and 5 MPa error values are smaller, but consistently small errors are only achieved after 7 MPa axial stress. The most likely explanation for this change in errors at this level is that the best contact conditions between the rock and transducers has been achieved. This is for a coarse sandstone which potentially has the worst contact conditions for any of the samples used in this study. Therefore by setting the cut-off level for Q measurements at 7MPa axial stress throughout the study, the results will be free from changes within the transducer-rock contact.

3.3.2.3 Data Acquisition.

A seismic pulse is initiated in the source transducer using an OYO Sonic Viewer as a pulse generator. The OYO unit produces a very stable pulse of about 10 μs duration which rises sharply to 400 V and decays slowly.

The attenuated pulse is received by an identical transducer. The signal undergoes 2 stage amplification before sampling at 25MHz by a programmable Analogue to Digital storage flash card installed in a normal PC. Acquisition is triggered by the Sonic Viewer. For high speed cycling, contents of the ADC on-board buffer after each trigger

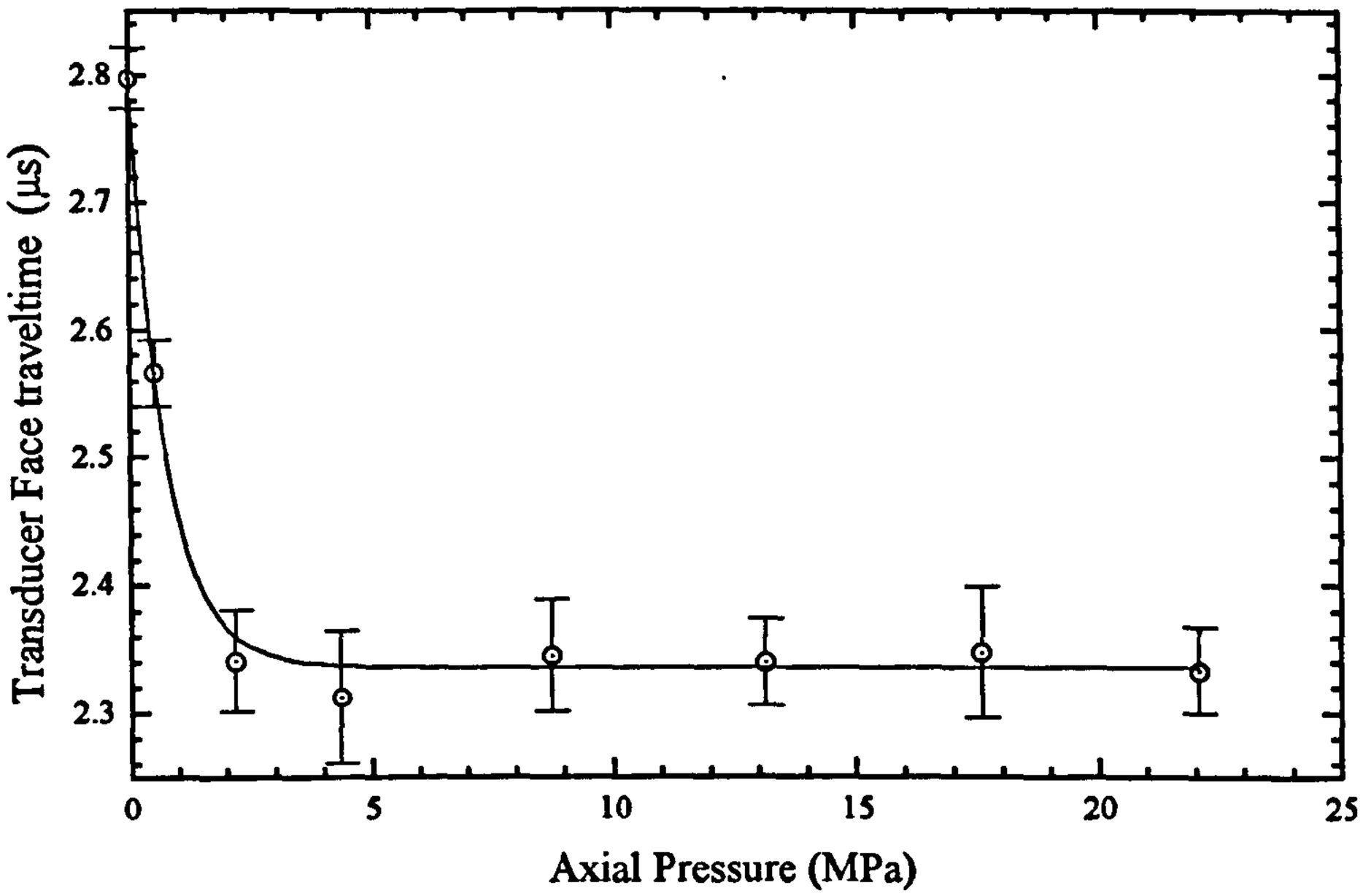

FIGURE 3.7 Platens face traveltime versus axial pressure

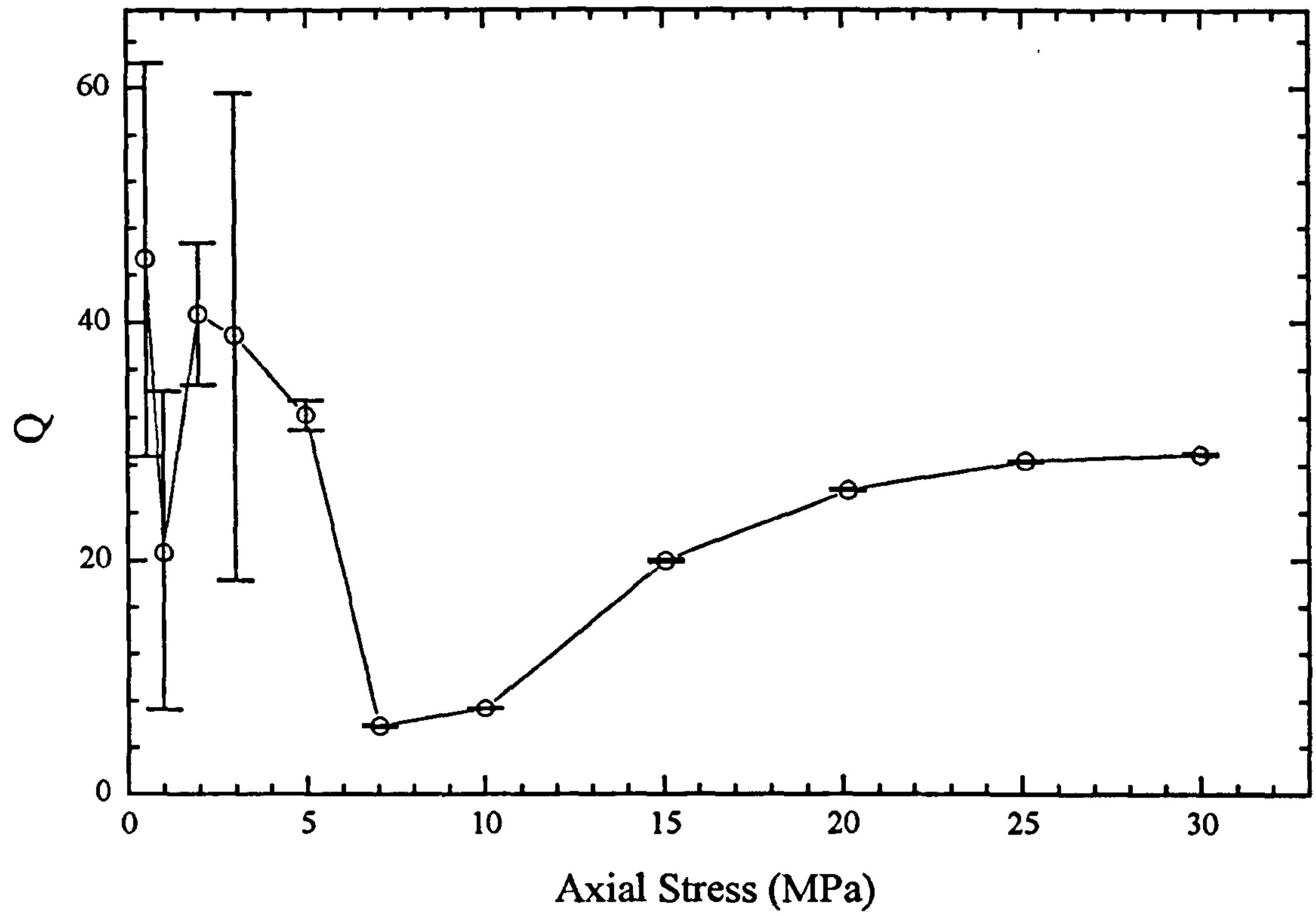

FIGURE 3.8 Q versus axial stress in a coarse sandstone, showing large errors in values below 7MPa.

event are continuously transferred to PC memory where the traces are stacked a user defined number of times before being saved to disk.

3.3.2.4 Data Processing.

3.3.2.4.1 Velocity Determination.

The first arrival time for each trace was determined manually. All first arrivals were very pronounced and easy to identify accurately. Traveltimes were measured to within 0.04 μs and velocity was determined from the simple relation,

$$= \frac{l}{(t - t_f)} \qquad \text{m/s}$$

where,

l = sample length in metres.

t = measured traveltime in seconds.

t_f = traveltime across the platens in seconds.

3.3.2.4.2 Attenuation Determination.

For a typical experimental run, traces were acquired for various different sample stress regimes. A program was written, called AUTOQ, to calculate Q values for an entire experimental run in one go using the following steps. The program structure is depicted in flowchart form in figure 3.9

STEP 1. AUTOQ Initiation.

The program reads an input file containing the following information,

- Number of stress regimes or traces, n.
- Sample details, mass, length, diameter, dry or saturated, sampling rate, number of samples per trace.
- Aluminium reference sample details, length, sampling rate, number of samples per trace, file name.
- For each stress regime,
  - Axial Load (kN)
  - Horizontal Stress (MPa)
  - Traveltime (μs)

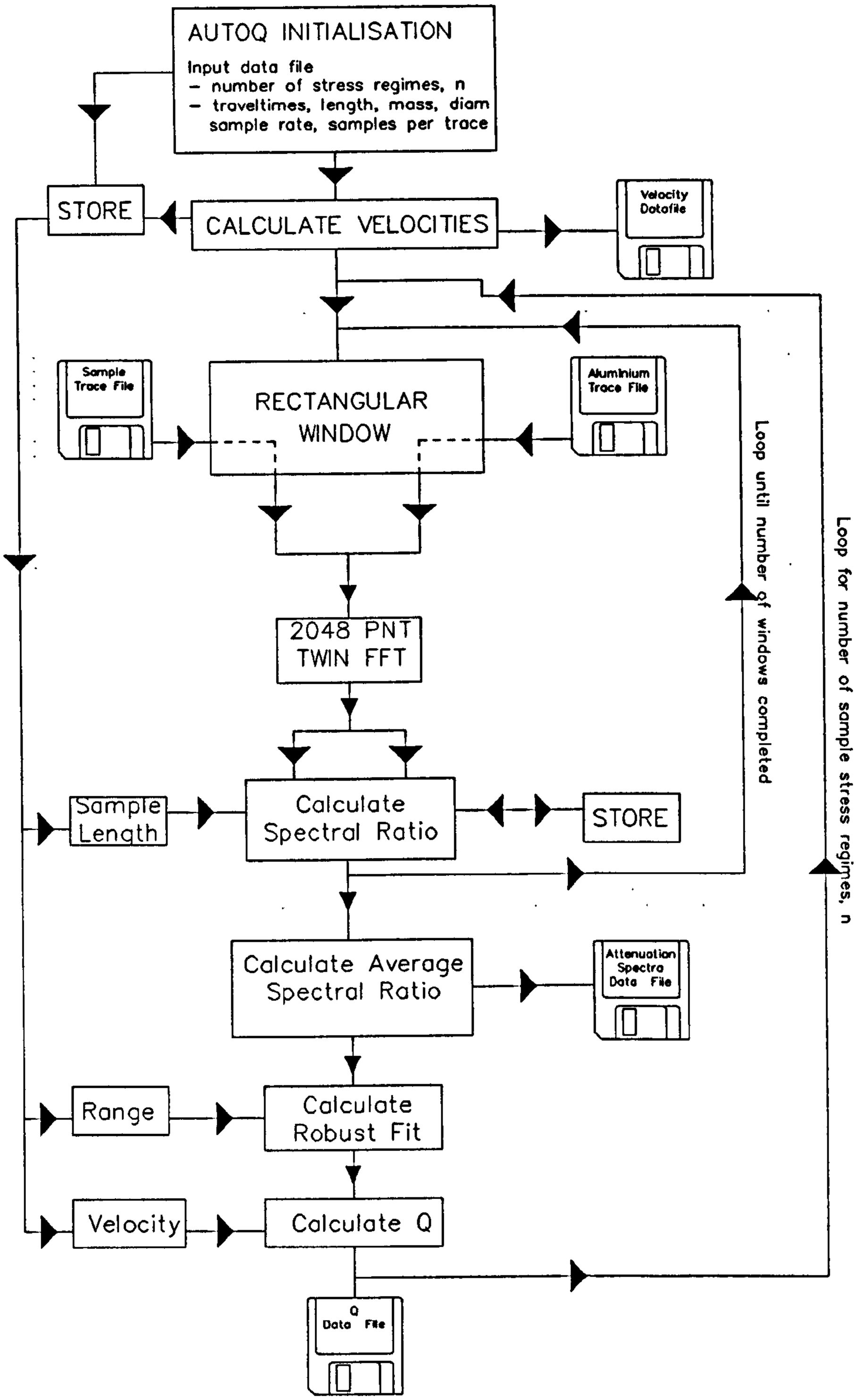

FIGURE 3.9 AUTOQ program flow diagram.

- Platen face traveltime correction (μs)

- Traveltime error

- Trace file name

- Frequency range for Q calculation and number of rectangular windows.

STEP 2. Velocity calculation and output results to velocity datafile.

STEP 3. Windowing Subroutine and Spectral Ratio calculation and stacking.

The sample trace and aluminium trace are read from file. A rectangular window is then applied to the first complete wavelet of each trace. A 2048 point forward fast fourier transform is taken simultaneously on both traces by a wrapping and unwrapping FFT routine and the spectral ratio calculated. This is then stored. The rectangular window is then moved to the next complete wavelet and the process repeated, the spectral ratio being stacked in the store. This cycling is continued until the user defined number of rectangular window loops is completed (normally 2 or 3)

STEP 4. Q Calculation.

An average spectral ratio is calculated over the number of windows and the best fit straight line is calculated using the robust M-norm method over the user defined range. The gradient is then used to calculate Q according to eqn 3.9 and associated error is calculated based on the 95% confidence limits estimate of the gradient and the error in the velocity. These values are then appended to a master Q datafile.

Steps 3 & 4 are repeated for the number of stress regimes, n. A complete code listing of AUTOQ is given in Appendix A.

3.3.2.5 Further Improving Q Estimates.

Q estimates from just a single determination of the spectral ratio slope tend to be widely variable. Improvement can be gained by using a robust statistical estimate of the slope. However, it is the author's opinion that Q values should be averaged wherever possible in an attempt to eliminate or significantly reduce the effect of small changes in the slope on the determination of Q. This is particularly apparent when attempting to measure high values of Q using the spectral ratio technique. Figure 3.10 shows that for higher values of Q the spectral ratio slope rapidly exponentially decreases with minimal effect from the velocity and therefore Q becomes increasingly more difficult to estimate accurately. A small local change in the gradient for a single estimation of Q can produce wildly variable results, particularly for high values of Q.

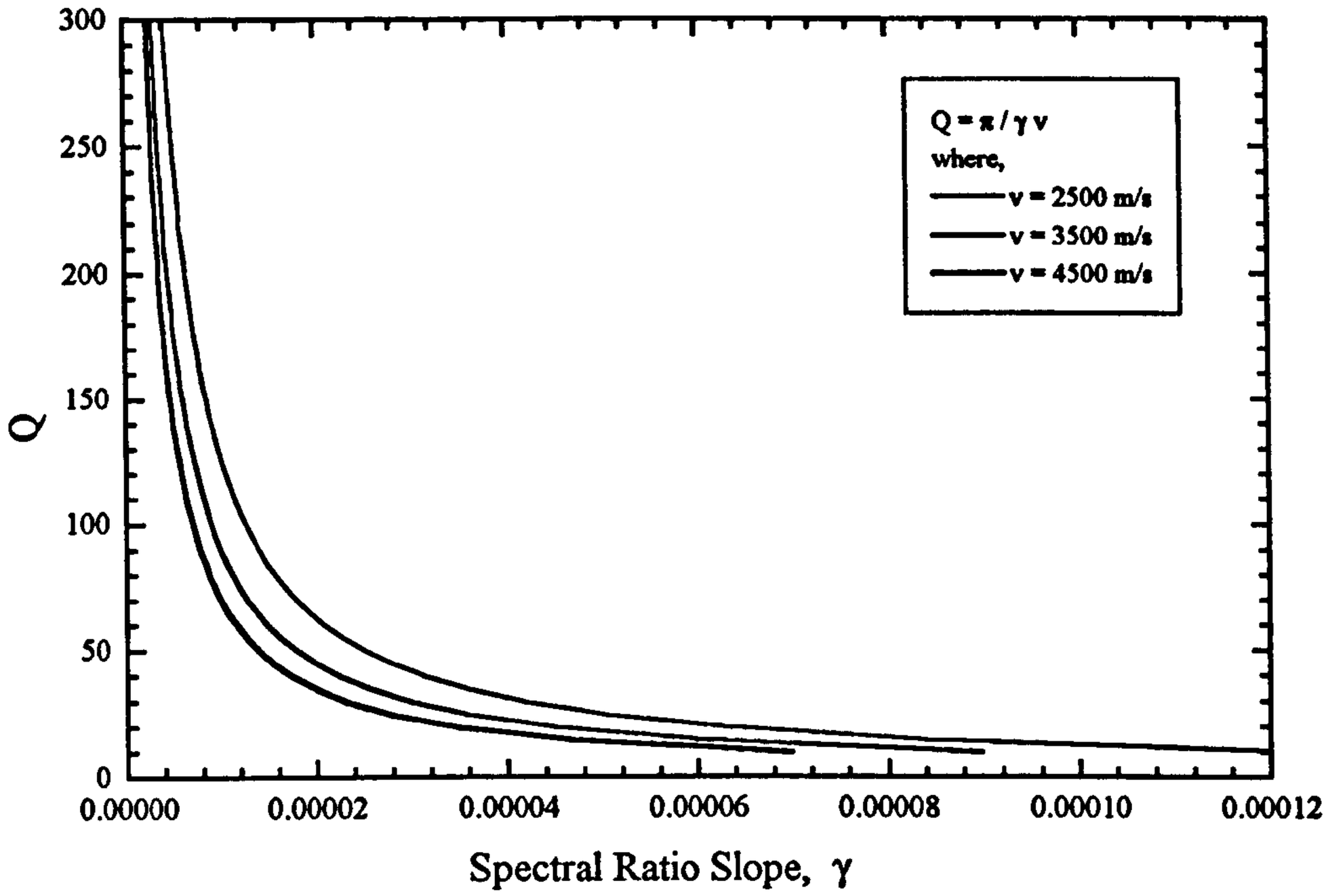

FIGURE 3.10 Q versus spectral ratio slope for varying velocity from equation 3.9. Shows that Q becomes more difficult to calculate above 100 due to the rapid exponential decrease in the spectral slope

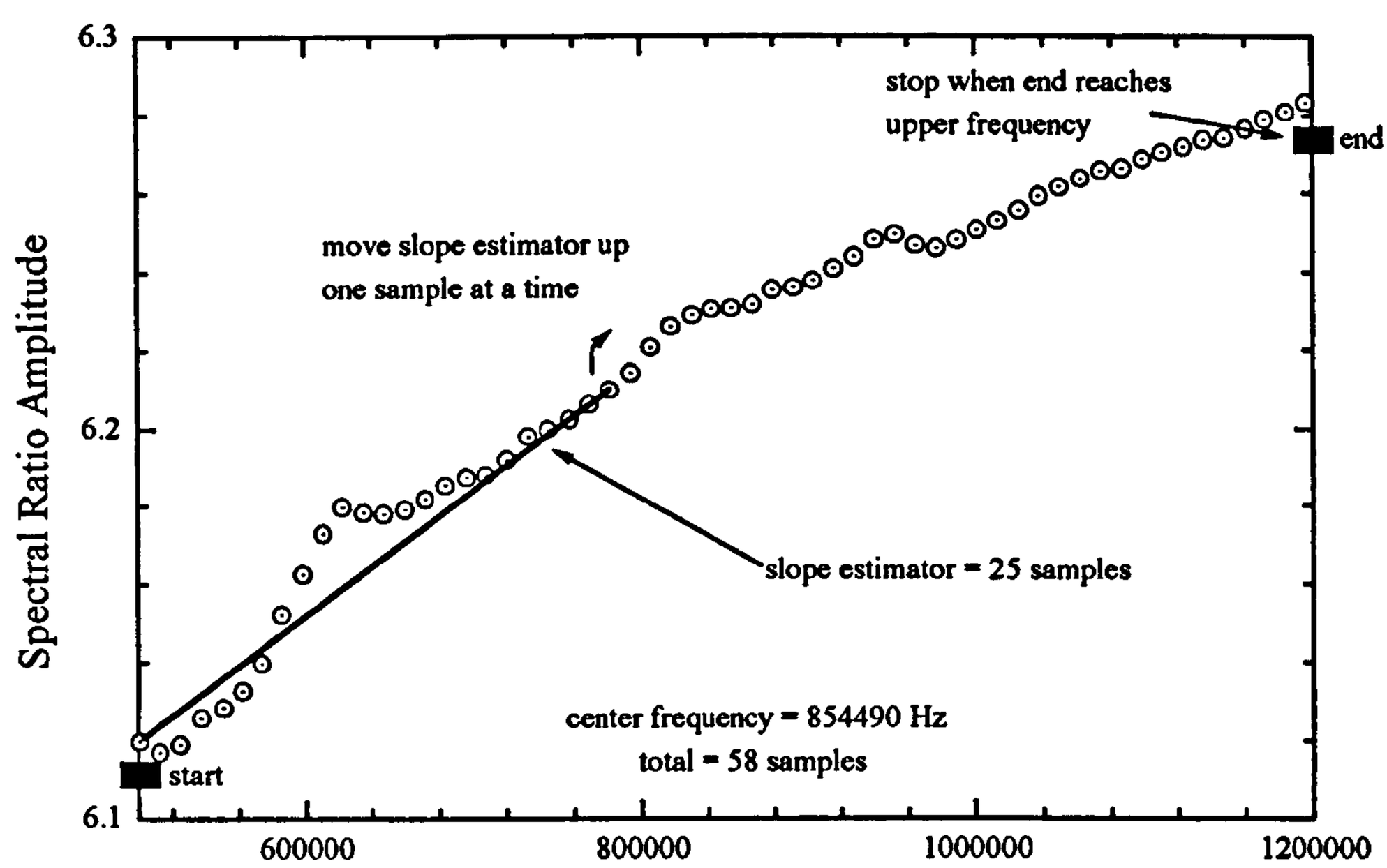

FIGURE 3.11 Method of scanning the spectral slope using a small length slope estimator to produce a subset of Q values.

A subset of Q values can be obtained for each trace or sample state by 'scanning' the spectral ratio between the frequency range of interest by determining the slope in smaller fixed overlapping portions. The process is illustrated in figure 3.11. In this example, a spectral ratio consisting of 58 points is scanned using a slope estimator of length 25 points. The slope estimator is first positioned at the start of the user defined frequency range and Q is determined. Then the slope estimator is moved one sample up the spectral slope and Q re-determined. This is continued until the end of the slope estimator has reached the end of the user defined frequency range. The example shown produces 34 separate estimates of Q for a single sample state. This process can be carried out using either a least squares or robust statistical slope determination method. The method has the advantage that the most frequently estimated portion of the spectral ratio slope is based around the center of the user defined frequency range which can be set to coincide with the central energy band of the transducers used in the experiment.

For each trace an average Q can now be calculated using the following aids based on,

a) the maximum upper level cut-off for Q

b) the maximum percentage error for Q

c) a combination of both of the above.

a) eliminates any extreme values of Q from the average, above a user defined maximum level, which are unrealistic and subject to the problems depicted in figure 3.10. b) eliminates any values from the average with error above a user defined maximum percentage which could be caused by the problems in figure 3.10 or by a noisy spectral ratio. c) eliminates Q values above the maximum value defined in a) and values less than this cut-off with errors greater than the percentage value defined in b). These measures help to eliminate widely incorrect values from the average and reduces the distribution of Q values at specific sample states to produce more reliable estimates of Q. Selection of upper cut-off values and percentage errors are helped by using histogram and probability plots such as that depicted in figure 3.12 to identify obvious outliers.

3.4 Conclusions

In summary, this chapter has reviewed three methods for the laboratory determination of compressional wave attenuation. It was shown that of the three

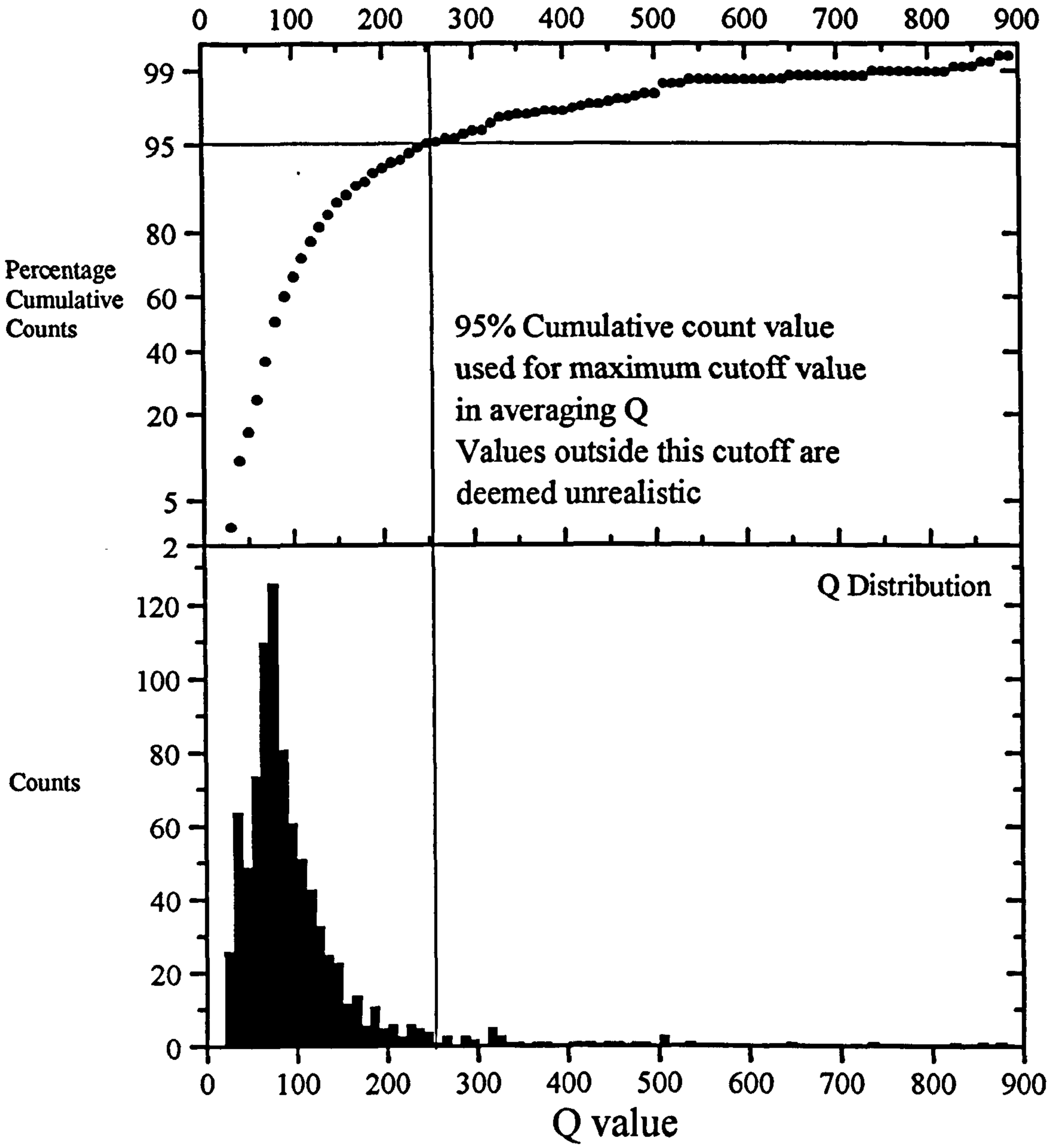

FIGURE 3.12 Typical Q distribution for a complete experiment trace set. The cumulative percentage count can be used to help decide the upper cut-off level for rejection of Q values from the average. In this case the upper cut-off level is set at 250. Beyond this level, values of Q are deemed to be unrealistic and subject to errors in calculation due to the inability to estimate the spectral ratio slope accurately (see figure 3.10).

methods, the spectral ratio technique was the easiest to implement for this study. The rise time method was shown to be too inaccurate for laboratory samples, whilst the buffer rod method was beyond the resources of this study and was difficult to use in triaxial confinement experiments.

The theory behind the spectral ratio was mathematically defined and illustrated using real data. The problems of applying the technique to very high attenuation or poor signal to noise ratio data were discussed and the use of robust statistics for spectral ratio slope estimation suggested to improve Q calculations.

The practicalities of the transducer to sample interface were addressed with the conclusion that attenuation results at axial stress conditions of less than 7 MPa are unreliable and are dependent on the contact conditions.

A new computer program was described for easy and quick analysis of complete experimental result sets. A new method was introduced to improve Q estimates by scanning the spectral ratio slope and using a series of confidence limits to remove widely inaccurate data.

In conclusion, this chapter has defined the complete set-up for the repeatable experimental determination of velocity and attenuation in laboratory rock core samples.

CHAPTER 4

4. Laboratory Results

4.1 Introduction

This chapter will consider the findings of a comprehensive laboratory study, looking at the suitability of measurements of compressional wave velocity and attenuation for the prediction of rock mass conditions. A number of different experiments are documented relating to different rock core sample states in an attempt to discover the 'sensitivity' of velocity or attenuation measurements to various simulated varying in-situ stress regimes, Pearce & Wade (1996a). The experimental methods have already been discussed in chapter 3. This chapter will look at the measurements of velocity and attenuation in samples with a changing triaxial stress regime for samples under the following conditions,

- Intact core samples
- Triaxialy confined intact core sample loaded to failure
- Fractured core samples

As well as considering the individual cases, the chapter then goes on to investigate the inter-relationships between sample states, and the expected changes that occur between them. To allow good interrelation between each state, the experiments have been designed to follow the sequence stated above for a single core sample. For example, a core would first be measured intact, then measured whilst being subjected to failure and re-measured after failure. This process allows for meaningful comparison of the sample states and removes the variability that would be introduced by using separate samples for each experiment. Some of the results indicated in chapter 2 are reproduced to check the scientific method used in this study and verify the findings of other workers.

4.2 Laboratory Dataset

The laboratory study was carried out in two distinct phases. The main concern of the first phase was to implement and refine the spectral ratio method and ensure that it successfully determined attenuation values under a triaxial stress regime. This phase considered a variety of rock types taken from a suite of borehole cores which were

accompanied by the corresponding geophysical borehole logs. The second phase was conducted on samples taken from the field sites outlined in chapters 6 and 8. A summary of the rock types considered in this study and some of the pertinent seismic properties is given in table 4.1. All listed seismic parameters in table 4.1 were measured at a hydrostatic stress of 10 MPa.

4.2.1 Characteristics of the complete dataset.

Figures 4.1, 4.2, 4.3 and 4.4 show the variation of velocity, robust calculated Q, least squares calculated Q and attenuation coefficient respectively with density in room dry samples. These results were plotted to investigate the suitability of each of the seismic parameters as a lithology indicator. Velocity shows an increase with increasing density, a well known phenomenon, and the plot has been split into distinct areas based upon lithological identification. In the case of the sandstone region, the plot can be further subdivided according to relative grain size. At higher densities any subdivision based upon grain size becomes impossible. The Q plots show little or no relationship with density. This shows that the absolute measurement of quality factor is difficult and in reality values are very sample specific. However, relative values of attenuation measured on the same sample under different stress regimes for the purpose of the investigation of stress induced attenuation anisotropy are reliable, since comparisons are being carried out under identical sample conditions. Attenuation coefficient shows a marginal decreasing trend with increasing density but the spread of the data points is considerable, indicating a very weak relation.

4.3 Intact Sample Behaviour

4.3.1 Change in velocity with hydrostatic stress

Figure 4.5 shows the change in P-wave velocity with increasing hydrostatic stress for the same dry and water saturated limestone sample. Consistent with section 2.1.1.1, an increase in velocity is observed for both cases with increasing hydrostatic stress. The dry case approaches a plateau region at a pressure of around 15 MPa whilst the saturated case reaches the same plateau earlier at around 7 MPa. This results suggests that above 15 MPa hydrostatic stress substantial microcrack closure has taken place. Similarly consistent with section 2.2.2, the presence of water in the saturated case increases the initial bulk modulus of the sample and hence the P-wave velocity (Nur and Simmons, 1969). The saturated and room dry curves converge at higher pressures (25 to 30 MPa) indicating further crack closure has occurred. At these higher stress levels

Description	Saturated / Dry	Density Range (kg/m^3)	Velocity Range (km/s)	Attenuation coefficient (dB/cm)	Q Range
Coarse Sandstone	Dry	1841-1940	2.99-3.03	7.48-9.74	10-22
	Saturated	2155-2230	3.04-3.14	10.25-13.93	5-15
Medium Sandstone	Dry	2100-2427	2.97-3.72	6.02-7.40	11-33
	Saturated	2278-2498	3.28-3.65	9.87-11.94	9-26
Fine Sandstone	Dry	2227-2530	3.48-4.05	5.12-6.02	20-39
	Saturated	2369-2585	3.42-4.17	6.53-7.37	15-30
Medium Siltstone	Dry	2407-2465	3.45-3.75	2.85-3.17	42-53
Fine Siltstone	Dry	2458-2556	3.11-3.37	4.59-5.24	55-68
Laportes Limestone	Dry	2611-2695	5.56-6.52	0.19-0.65*	55-73*
	Saturated	2683-2694	6.35-6.59	0.40-0.91*	35-57*
Gillfield Limestone	Dry	2653-2664	5.51-6.29	5.05-7.87	39-92
	Saturated	2659-2690	6.02-6.42	5.97-8.57	32-75
Diorite	Dry	2666-2889	5.20-5.60	1.79-2.29	78-110

TABLE 4.1 Rock types considered in the laboratory study and the typical values for density, velocity, attenuation coefficient and quality factor. All seismic parameters were measured at a hydrostatic stress of 10 MPa. (* At 29 kHz, all other values of attenuation coefficient and Q at 1MHz)

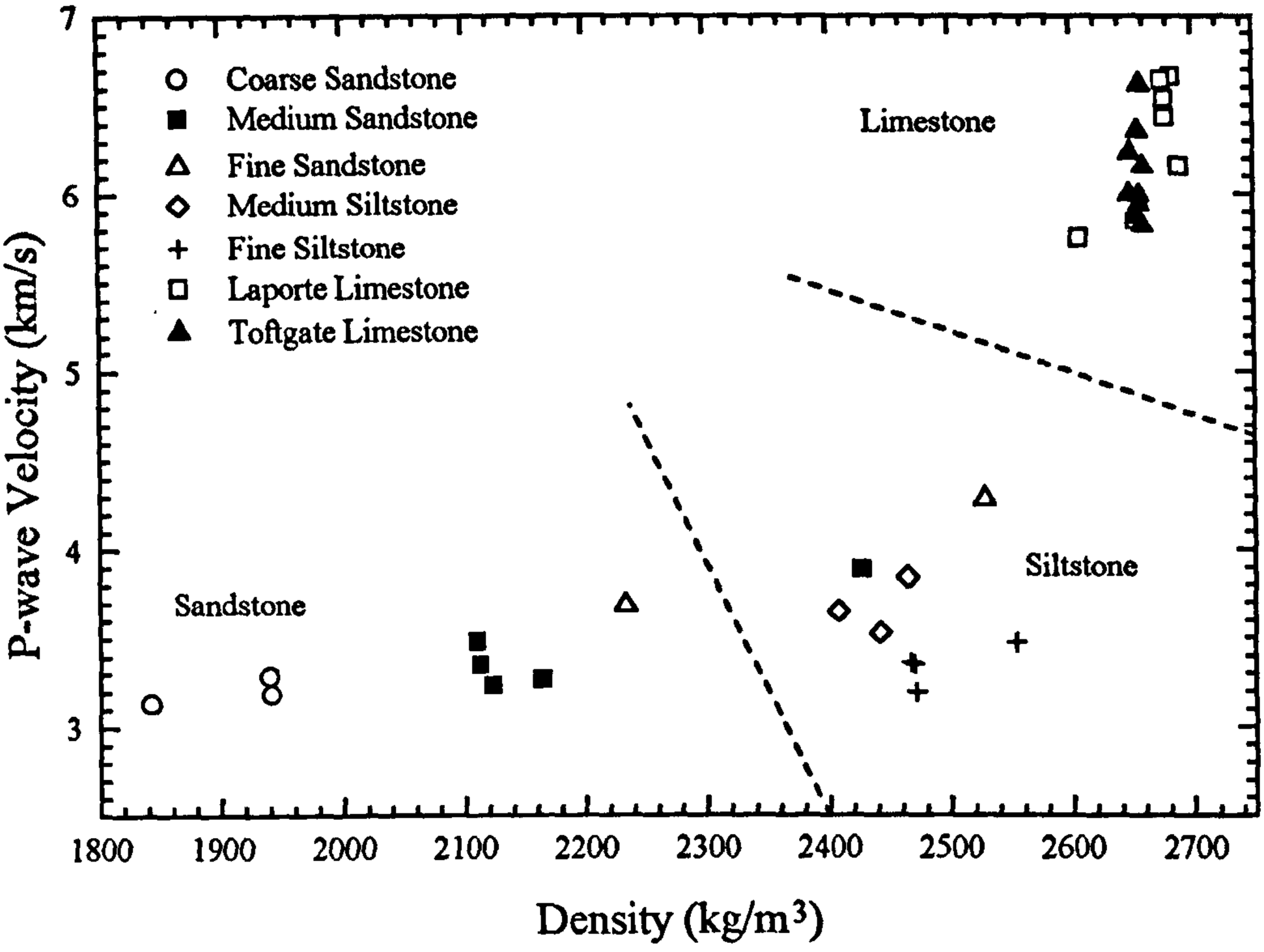

FIGURE 4.1 P-wave velocity versus density for a range of room dry rock types.

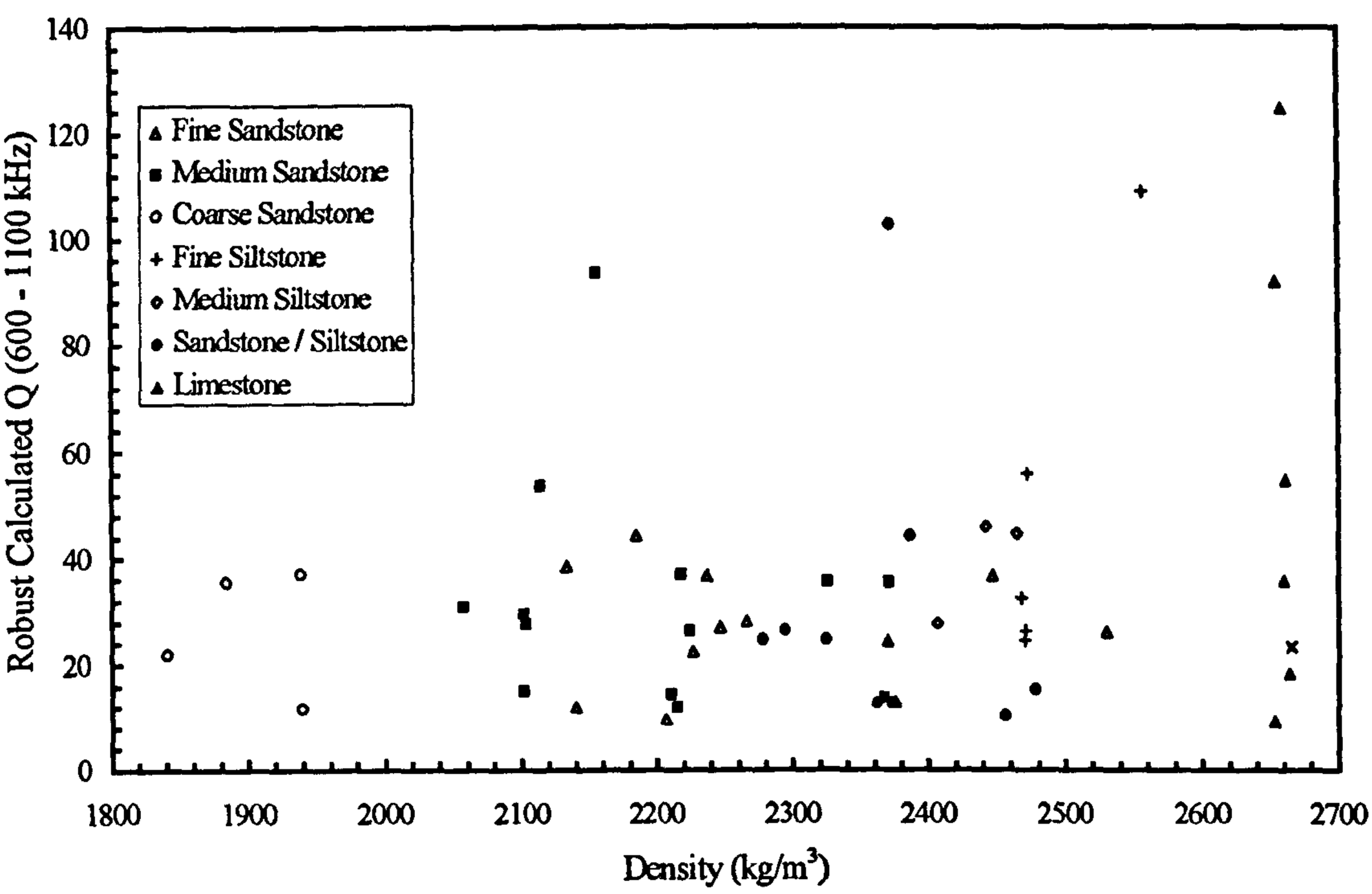

FIGURE 4.2 Robust calculated Q versus density in the range 600 to 1100 kHz for the same rocktypes.

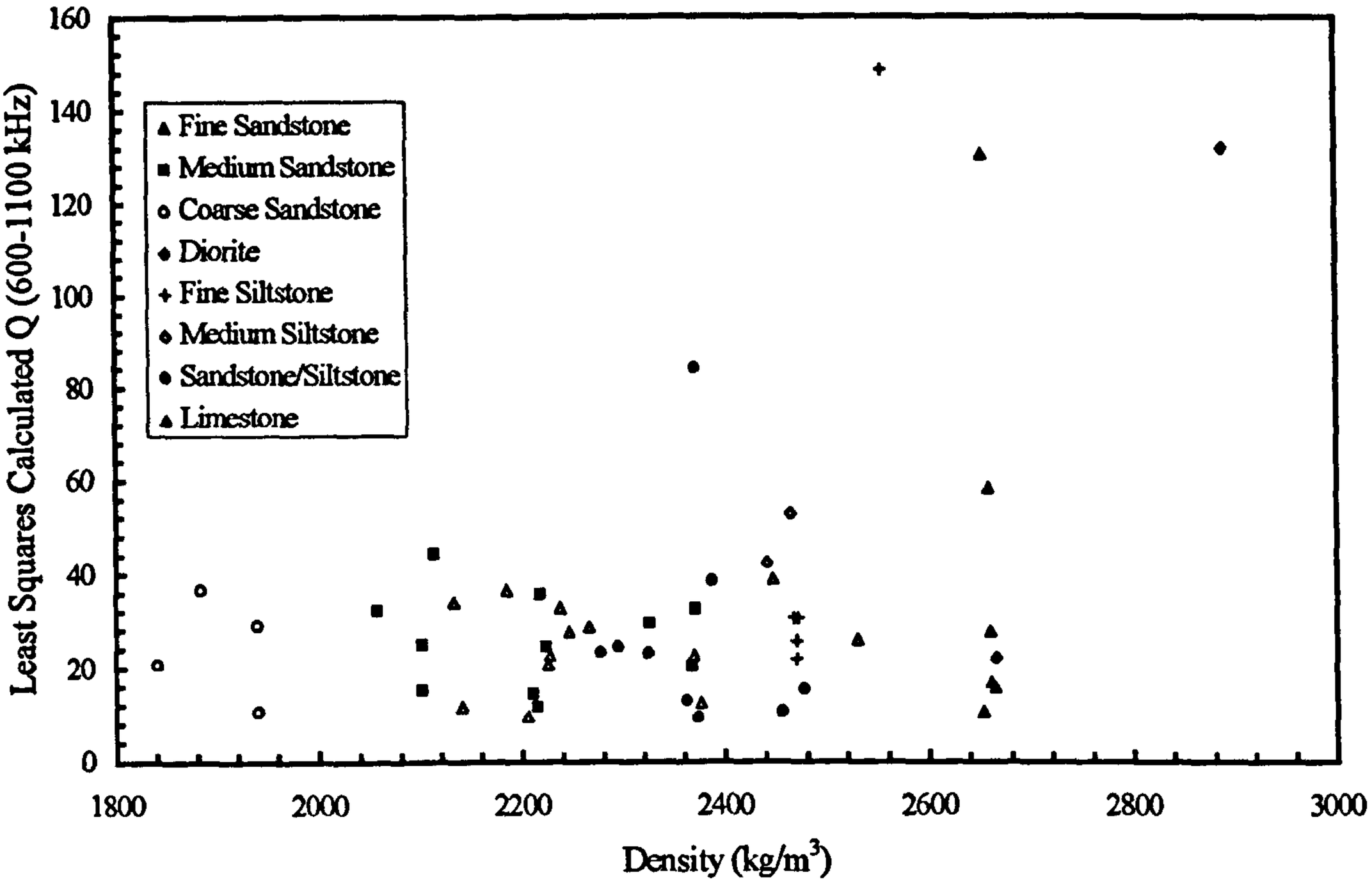

FIGURE 4.3 Least squares calculated Q versus density in the range 600 to 1100 kHz for the same rocktypes.

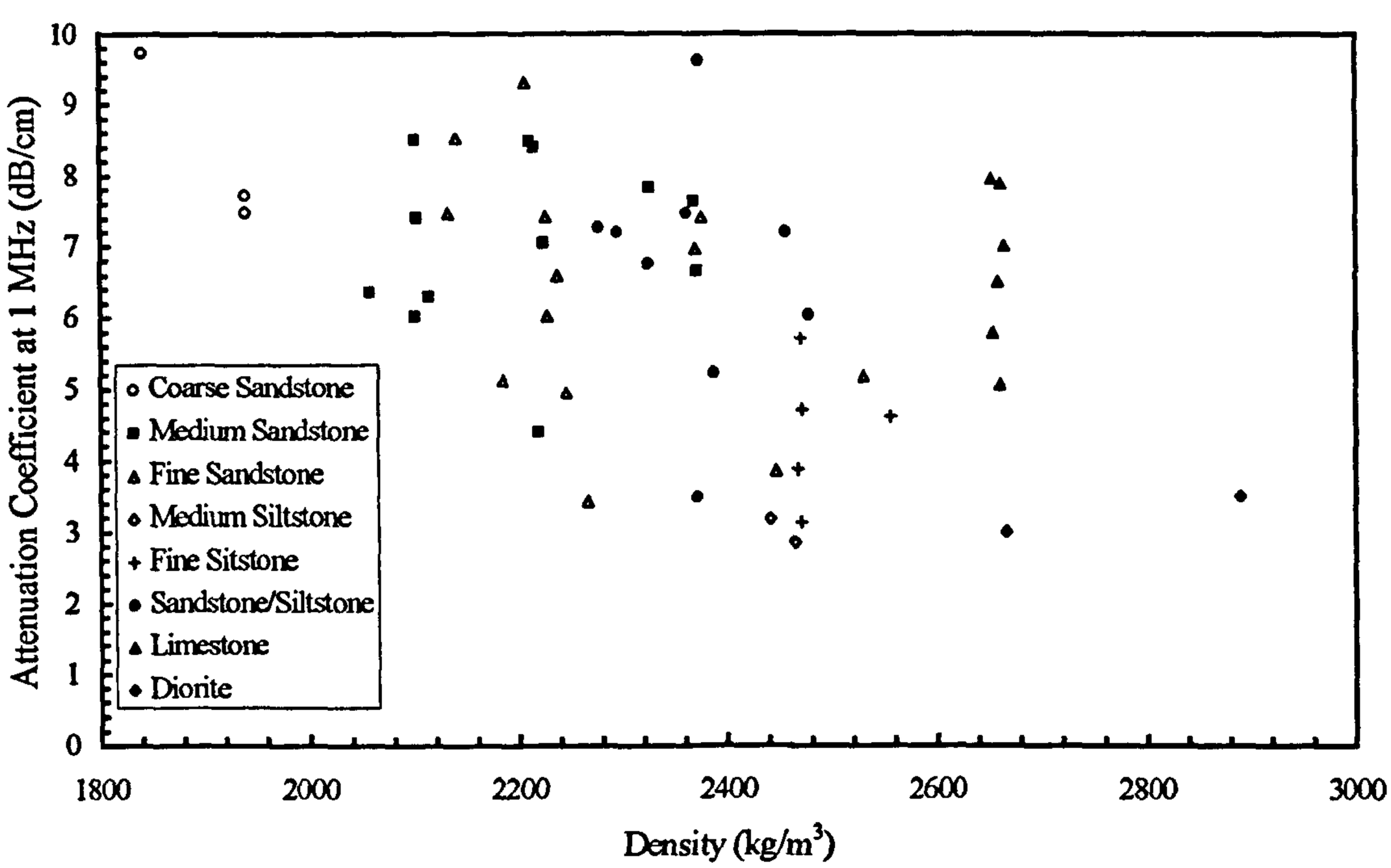

FIGURE 4.4 Attenuation coefficient versus density calculated at 1 MHz for the same rocktypes.

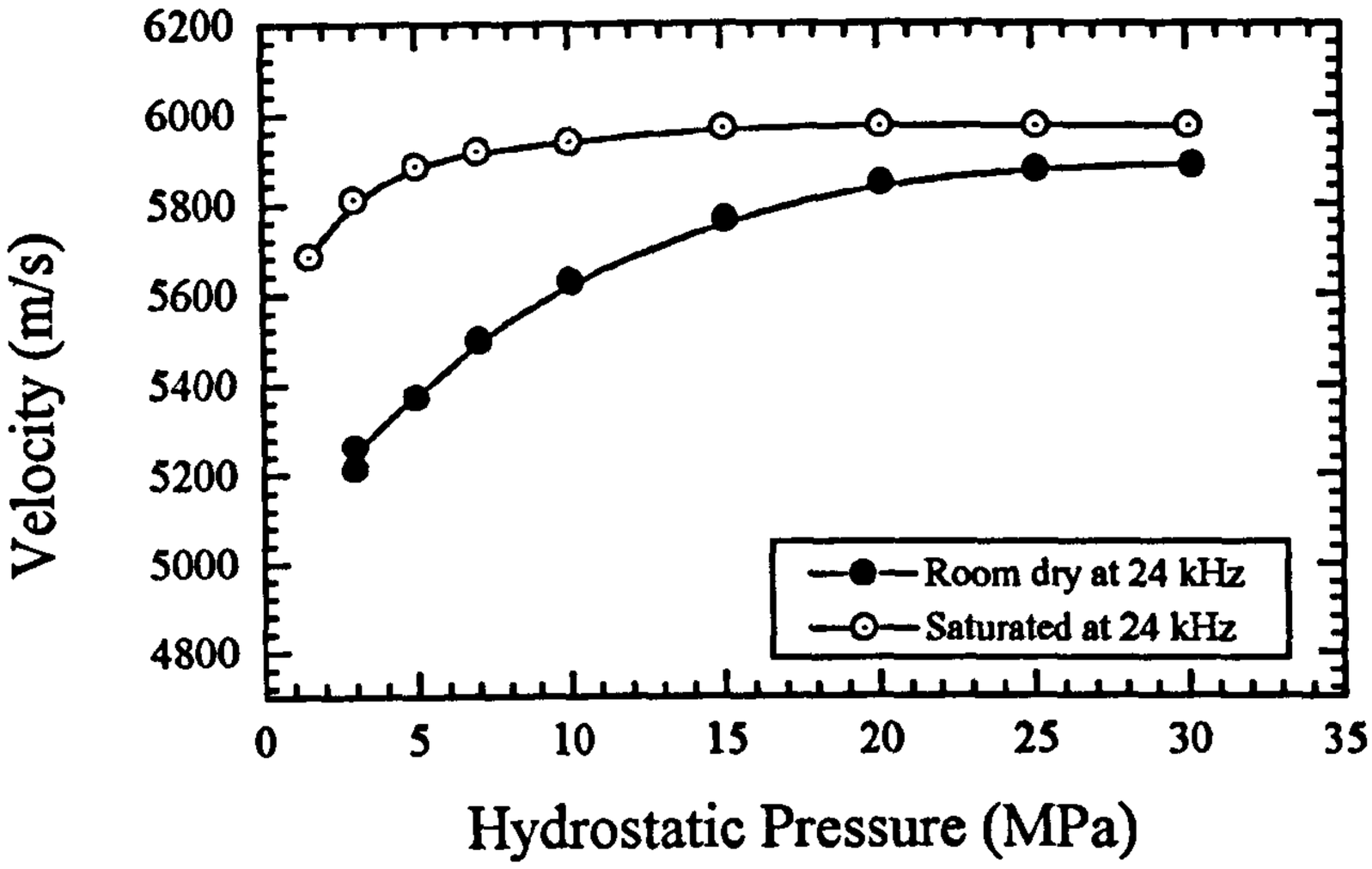

FIGURE 4.5 Velocity versus hydrostatic pressure in dry and saturated limestone.

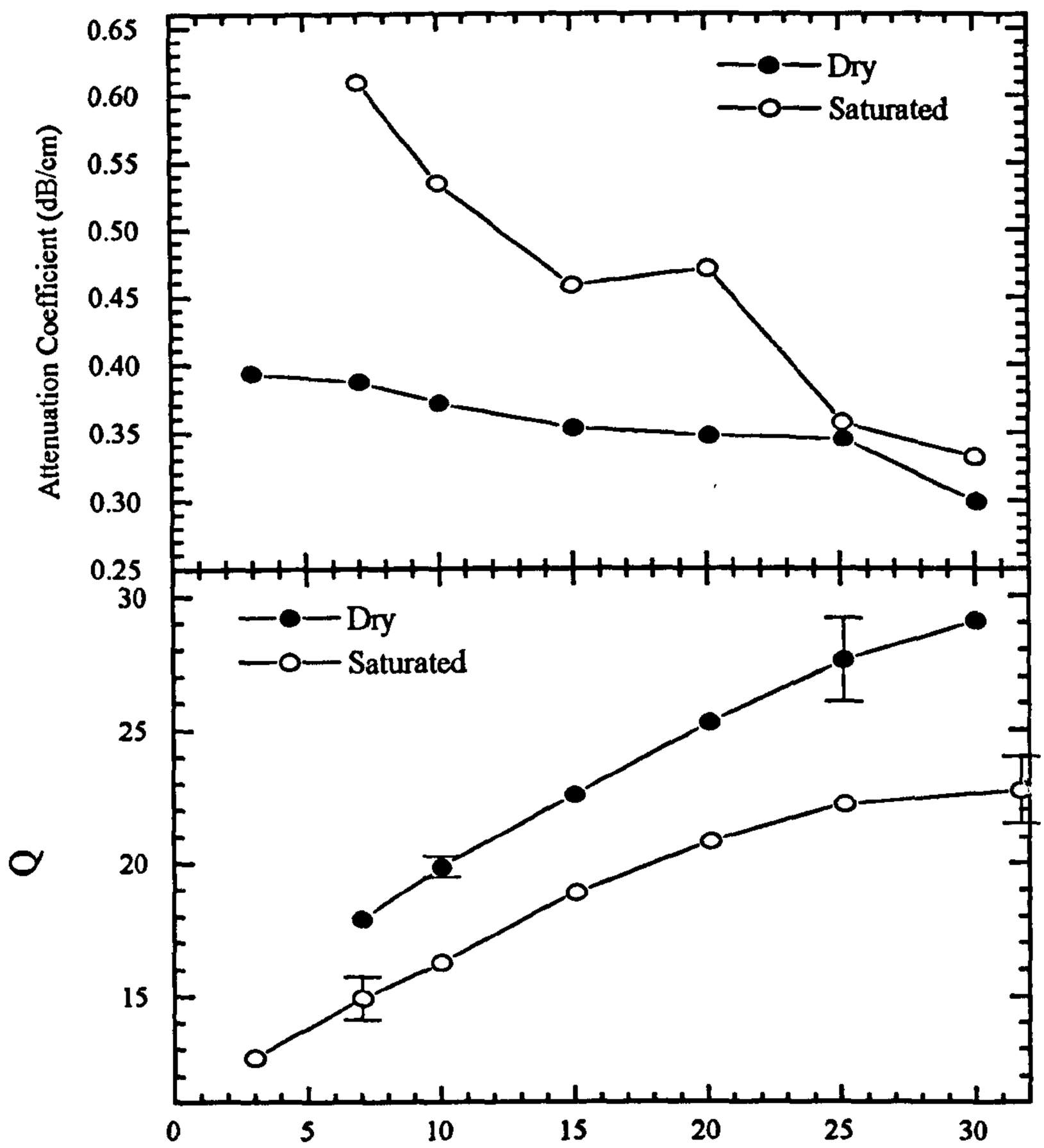

FIGURE 4.6. Attenuation coefficient and Quality factor versus hydrostatic stress for dry and saturated limestone at 29 kHz.

the saturated bulk modulus approaches that of the mineral constituents alone due to the squeezing of water from cracks and pores. This mineral constituent bulk modulus is represented by the dry bulk modulus under high hydrostatic confinement.

4.3.2 Change in Attenuation with Hydrostatic Stress

Figure 4.6 shows the change in Attenuation Coefficient and Quality Factor with increasing hydrostatic stress for dry and saturated limestone at 29 kHz. The same trend is observed as described in section 2.3.1.1. Attenuation is seen to decrease with the onset of stress and reaches a plateau at higher stress levels. Saturation increases P-wave attenuation due to a combination of the intrinsic pore fluid and rock matrix interaction mechanisms described in section 2.4.

4.3.3 Stress-Induced Velocity Anisotropy.

The phenomenon known as stress-induced velocity anisotropy has already been introduced in section 2.2.1.2. The understanding of the factors affecting this phenomenon is crucial to any proposed method for the in-situ monitoring of rock mass conditions relating to changing stress regimes. Since an in-situ rock mass is not an intact, homogenous entity, this laboratory study will not only consider laboratory samples which are intact and contain a series of microcracks but also samples which have been loaded to failure and therefore contain 'macro' fractures.

Figure 4.7 illustrates two complete experimental velocity measurements on samples of fine grained and coarse grained sandstones plotted with the same linear velocity axis. Each line represents constant axial loading on the sample for a varying radial stress regime. The following points can be observed from the plot,

- An increase in axial stress introduces a marked step increase in velocity
- The initial onset of radial stress brings about a rapid increase in velocity up to around 7 MPa, especially in the case of the coarse grained sandstone. Above 7 MPa, in both cases, further increase in radial stress induces little further increase in velocity compared to the corresponding step increase in velocity that occurs for the same increase in axial stress.

Understanding of the processes involved can be visually improved by plotting the results as a constant velocity contour map using a kriging interpolation technique. These types of plot are shown in figure 4.8 for a number of different rock types under room dry conditions. The plots show the absolute influence of the two stress components acting on the sample on the resulting velocity of the wave propagating

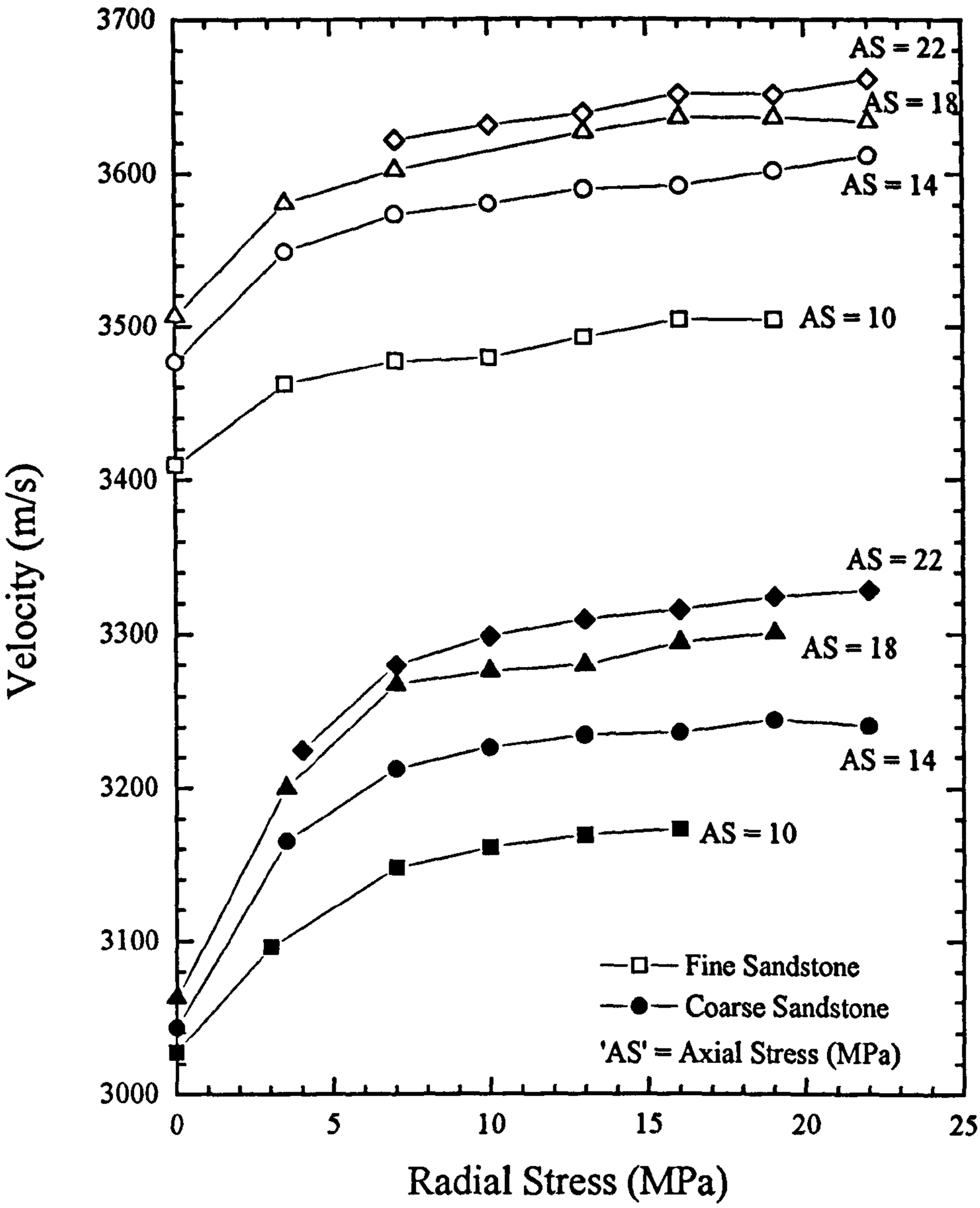

FIGURE 4.7 Velocity versus Radial Stress showing stress-induced velocity anisotropy in coarse grained and fine grained sandstone. Lines represent constant axial stress ('AS' refers to axial stress in MPa)

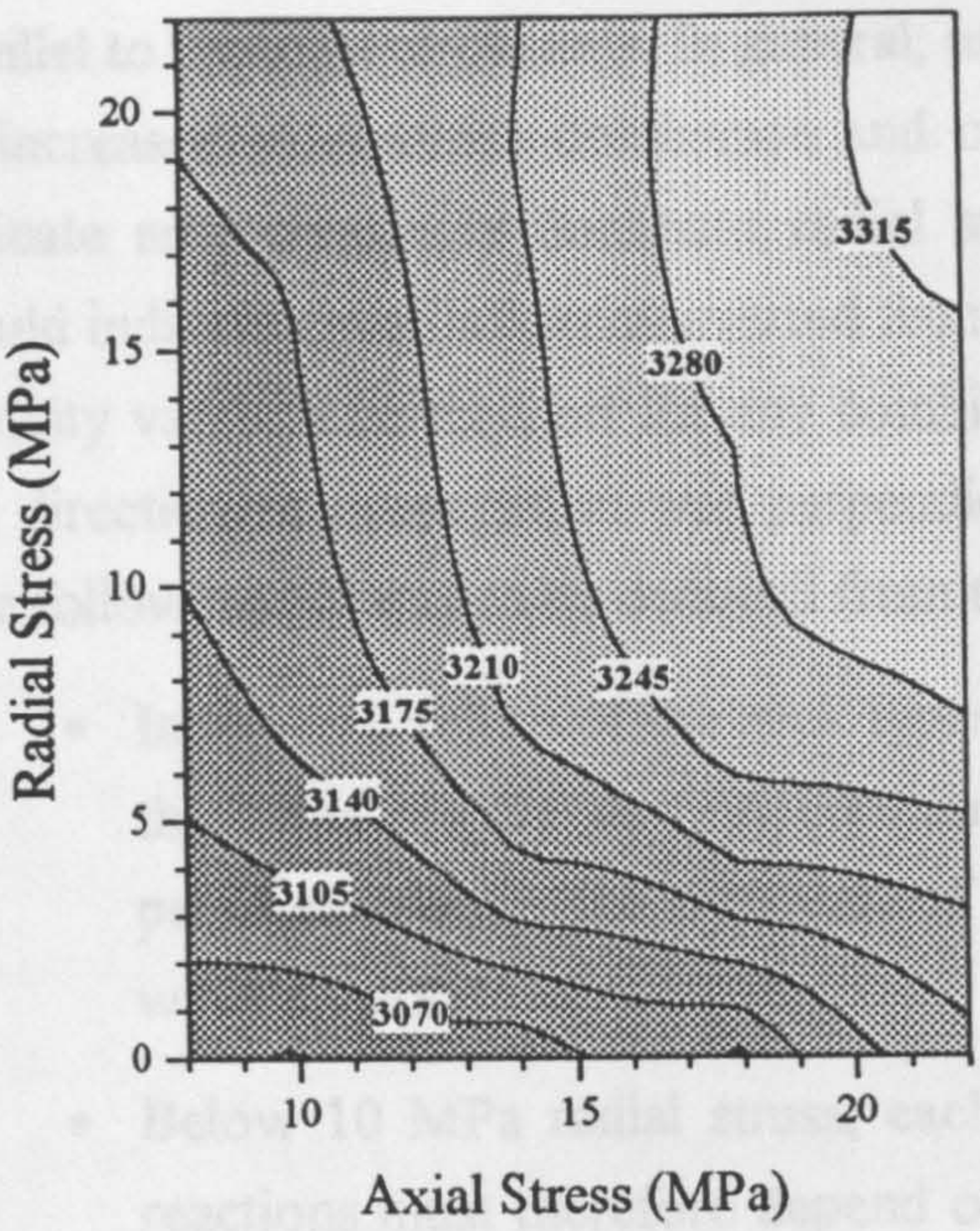

(a)

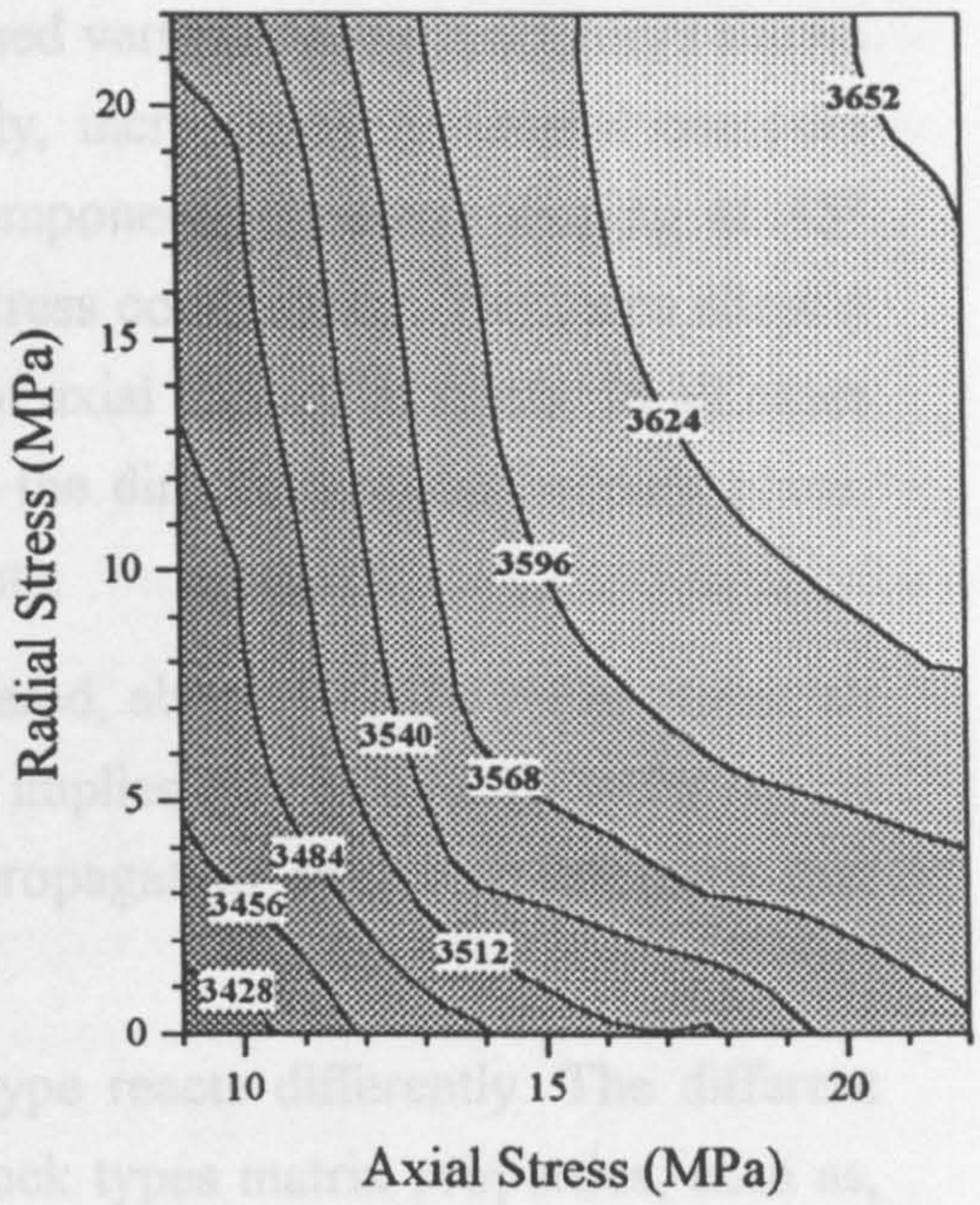

(b)

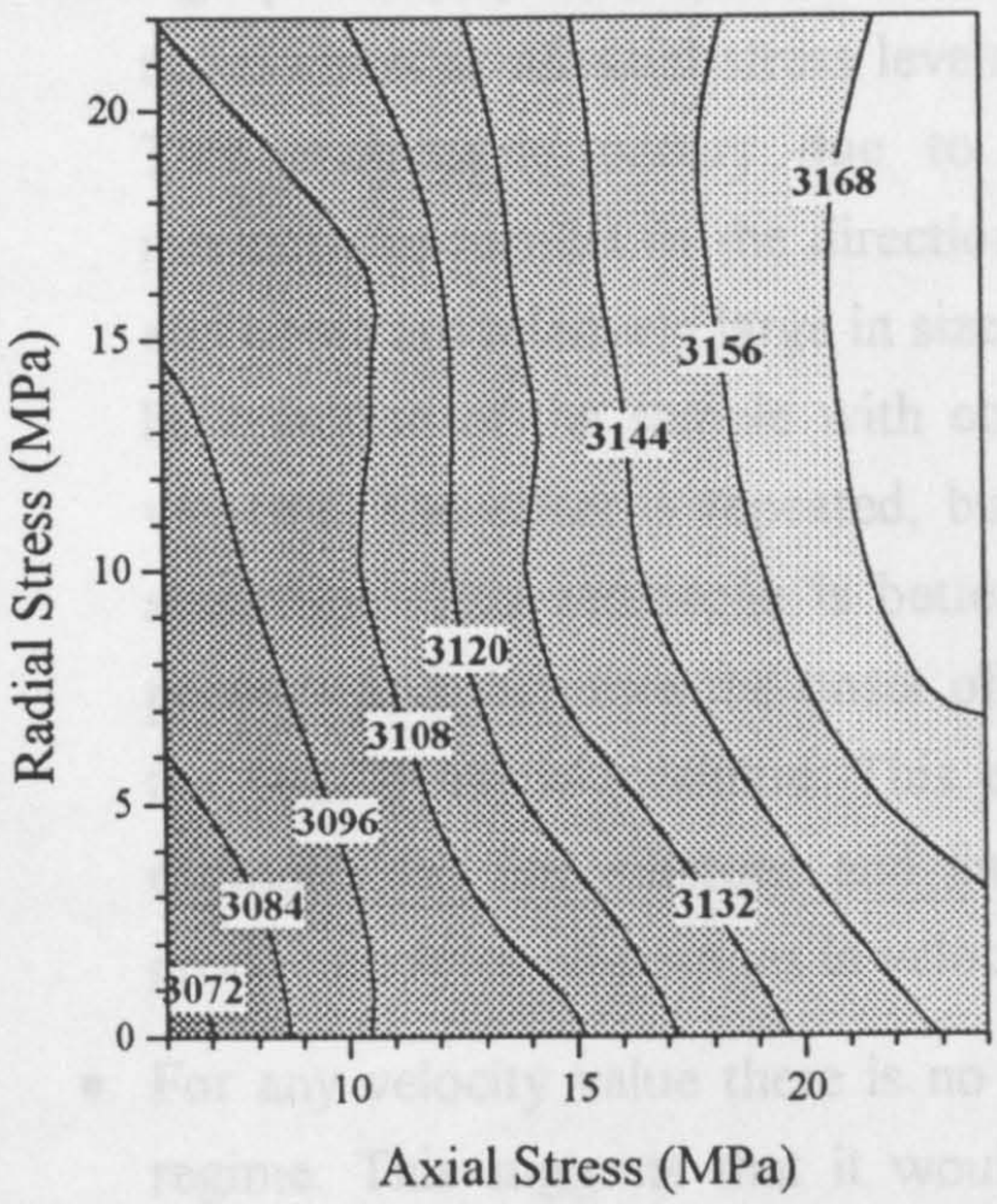

(c)

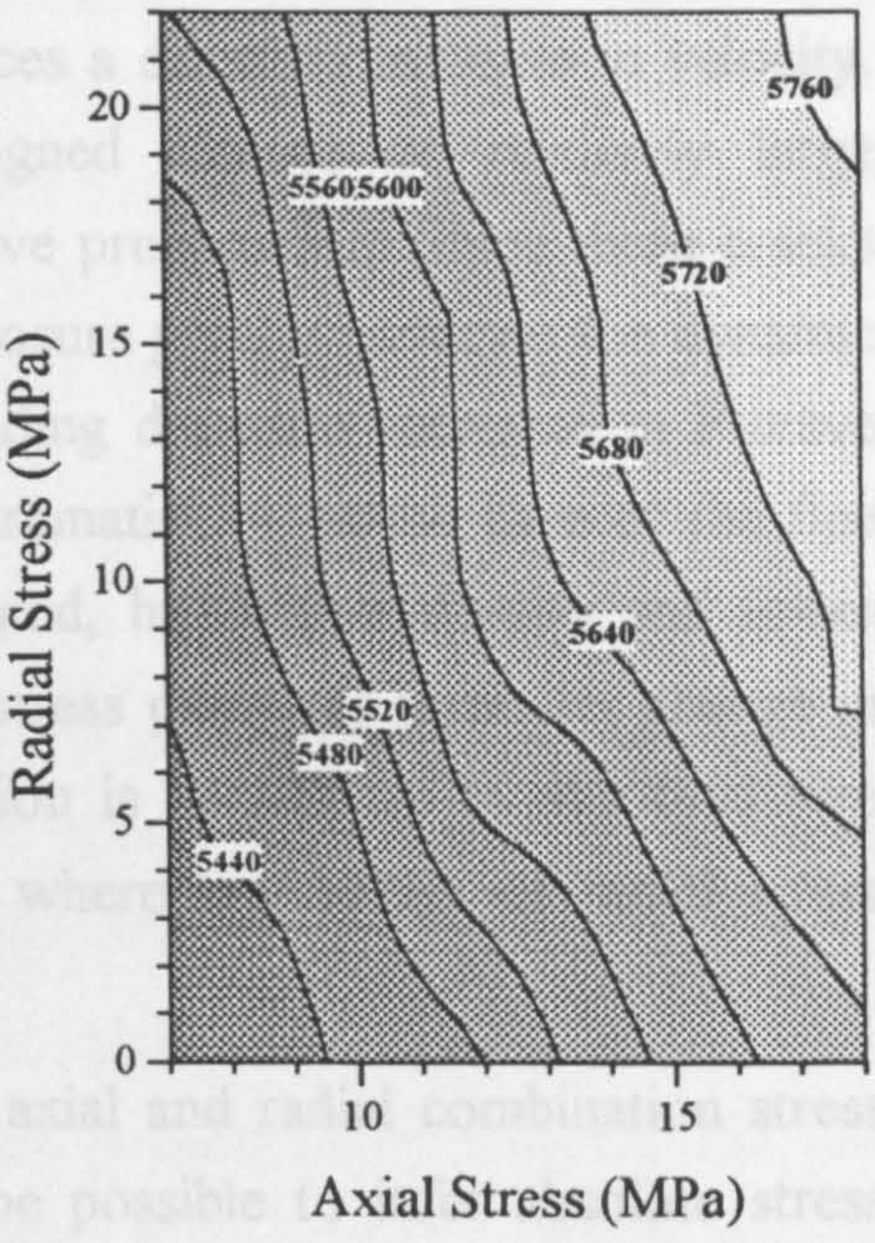

(d)

FIGURE 4.8 Constant velocity contour stress maps plotted using a kriging interpolation method for (a) Coarse grained sandstone (b) Fine grained sandstone (c) Fine grained siltstone and (d) Limestone. Velocities are in m/s.

parallel to the axial stress axis. In general, an increased verticality of the contours shows an increased axial stress dominance and conversely, increasingly horizontal contours indicate an increasingly dominant radial stress component. Contours sloping at 45° would indicate equal influence exerted from both stress components. The maps allow a velocity value to be read off for any combination of axial and radial stress. In all cases the direction of propagation was perpendicular to the direction of the bedding plane. The following points can be deduced from these plots,

- In general, for all of the rock types considered, above 10 MPa radial stress, all the maps display vertical contours. This implies that above 10 MPa, stress perpendicular to the direction of wave propagation ceases to influence that wave's velocity.
- Below 10 MPa radial stress, each rock type reacts differently. The different reactions must therefore depend on that rock types matrix properties, such as, porosity, microcrack distribution and density. In the case of the low density, high porosity, poorly indurated coarse grained sandstone, the initial onset of radial stress at all axial stress levels produces a dramatic increase in velocity. This presumably occurs due to the aligned closure of relatively large microcracks parallel to the direction of wave propagation. Since these cracks and pores are relatively large in size their closure greatly increases the dynamic bulk moduli of the sample with corresponding dramatic increases in P-wave velocity. The effect is repeated, but less dramatically, in the case of the fine sandstone. This sandstone is better indurated, has higher density and lower porosity and therefore the onset of radial stress produces a smaller change in the bulk dynamic modulus. This explanation is backed up by the final two examples for fine siltstone and limestone where low values of radial stress produce only small changes in velocity.
- For any velocity value there is no unique axial and radial combination stress regime. This suggests that it would not be possible to infer absolute stress component values for an in-situ rock mass, but rather a possible combination stress range. However, if one stress component is known (such as the overburden stress) it may be possible to crudely deduce the other likely component from such a plot.

From these investigations it seems sensible to infer that for intact rock, stress perpendicular to the direction of wave propagation exerts a relatively small influence on the velocity of that wave in comparison to the same stress exerted parallel to the propagation axis. The exception to this may be low density, high porosity, poorly

indurated formations, the velocity of which may be significantly influenced by small changes in stress perpendicular to the wave propagation axis at low overall stress levels.

4.3.4 Stress-Induced Attenuation Anisotropy

Velocity anisotropy is relatively simple to measure in the laboratory whereas the measurement of absolute values of attenuation are significantly more difficult. Therefore attenuation anisotropy is more difficult to define since greater inaccuracies and errors may obscure any underlying trend. The other consideration in the measurement of attenuation is the dominant frequency of propagation since different frequency ranges may have different underlying attenuation mechanisms. For example, ultrasonic measurements in the megahertz region may be subject to scattering, 'extrinsic' mechanisms, even within small laboratory samples, since wavelengths of propagation are comparable in size to small scale heterogeneities within the sample. This may be especially true for coarse grained rocks, or rocks displaying small scale density heterogeneity such as limestone (see section 2.3.5). Here rock types with an apparently intact and well indurated appearance show unusually low values of Q. Measurements at the lower frequency range in this study should not suffer from such scattering interference since wavelengths are of the order of cm's rather than mm's. This section will look at measurements of attenuation anisotropy in intact samples at the two different frequency ranges used in this study.

4.3.4.1 Quality factor (600 - 1100 kHz) and attenuation coefficient at 1 MHz.

The graphs shown in figure 4.9 (a) to (d) are all typical of the specified rock types. The plots are of the same format as those in figure 4.6, each line representing conditions of constant axial stress with varying radial stress.

The major distinction between these plots and those in figure 4.6 is the increased sensitivity of Q to changes in radial stress. This is particularly true for the coarse grained sandstone. Here the constant axial stress lines form a series of peaks, each peak occurring at approximately hydrostatic stress conditions along that line. The plot indicates that Q is sensitive to the closure or opening of microcracks in a plane perpendicular to the direction of wave propagation that is controlled by the increase or decrease in radial stress. This apparent sensitivity is drastically reduced in a fine, well indurated sandstone. There is some evidence of the same sensitivity in the fine siltstone and little or no radial stress sensitivity in the isotropic limestone. As with the velocity plots, the anisotropic behaviour of each of the rock types can be better

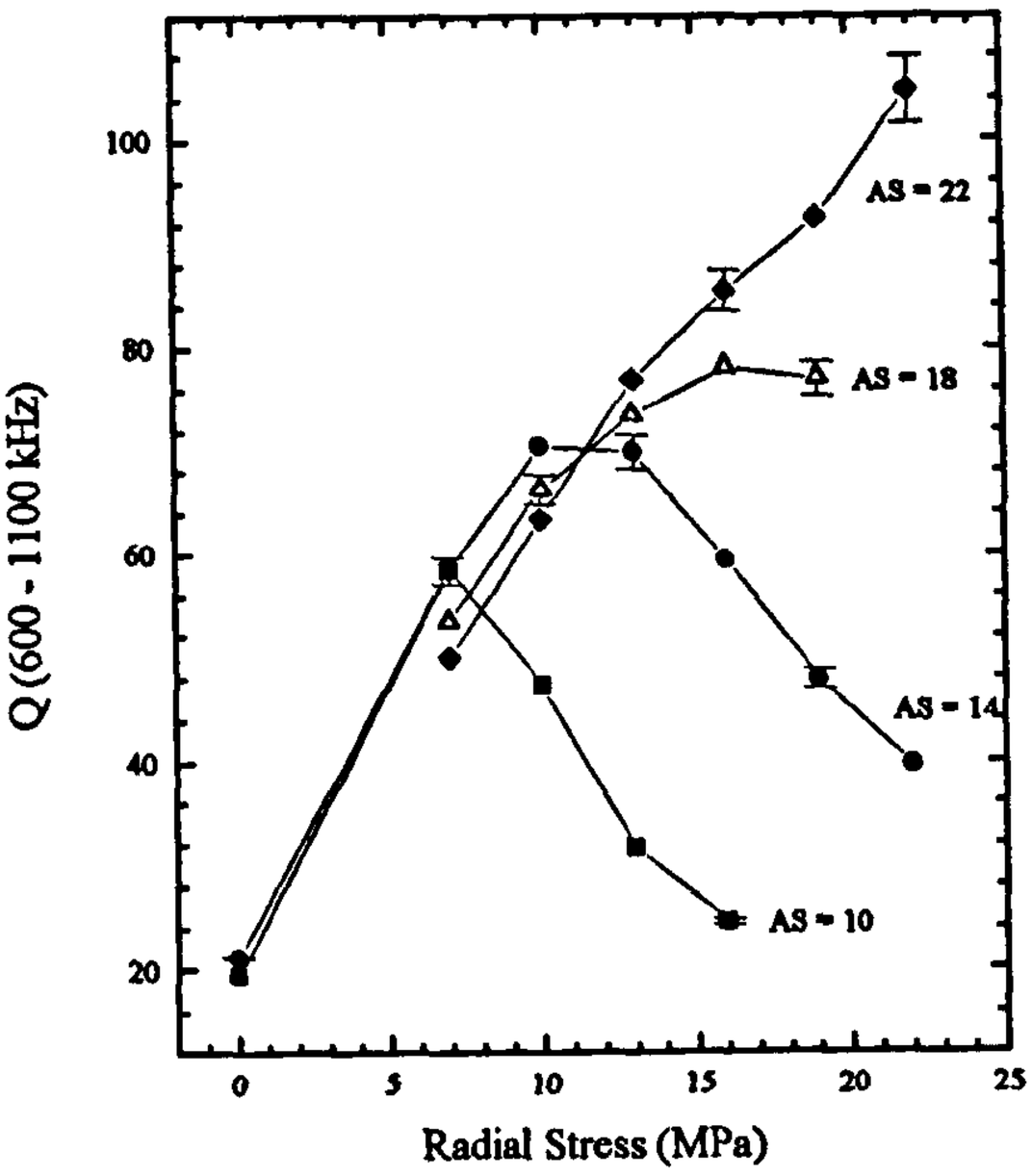

(a)

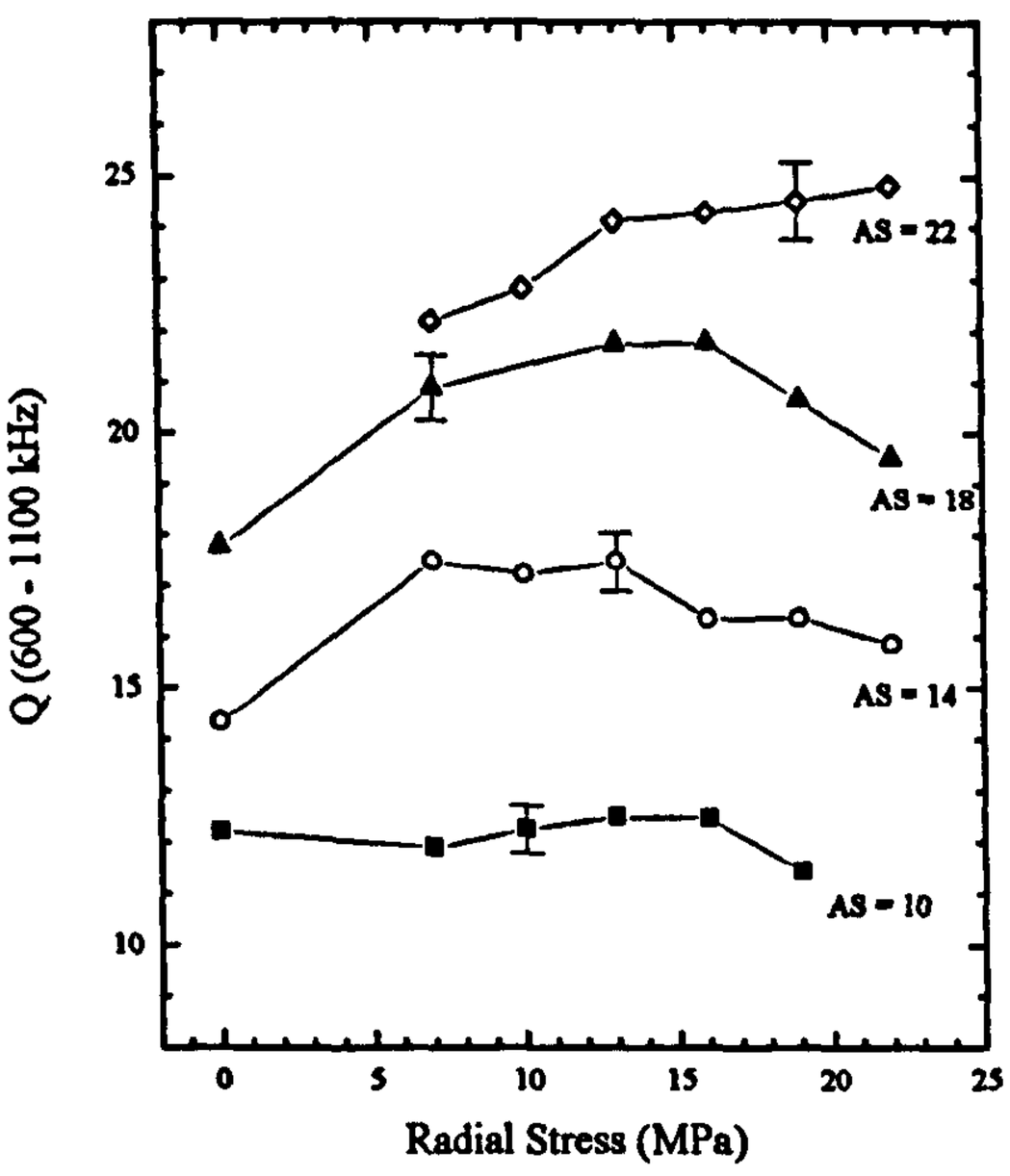

(b)

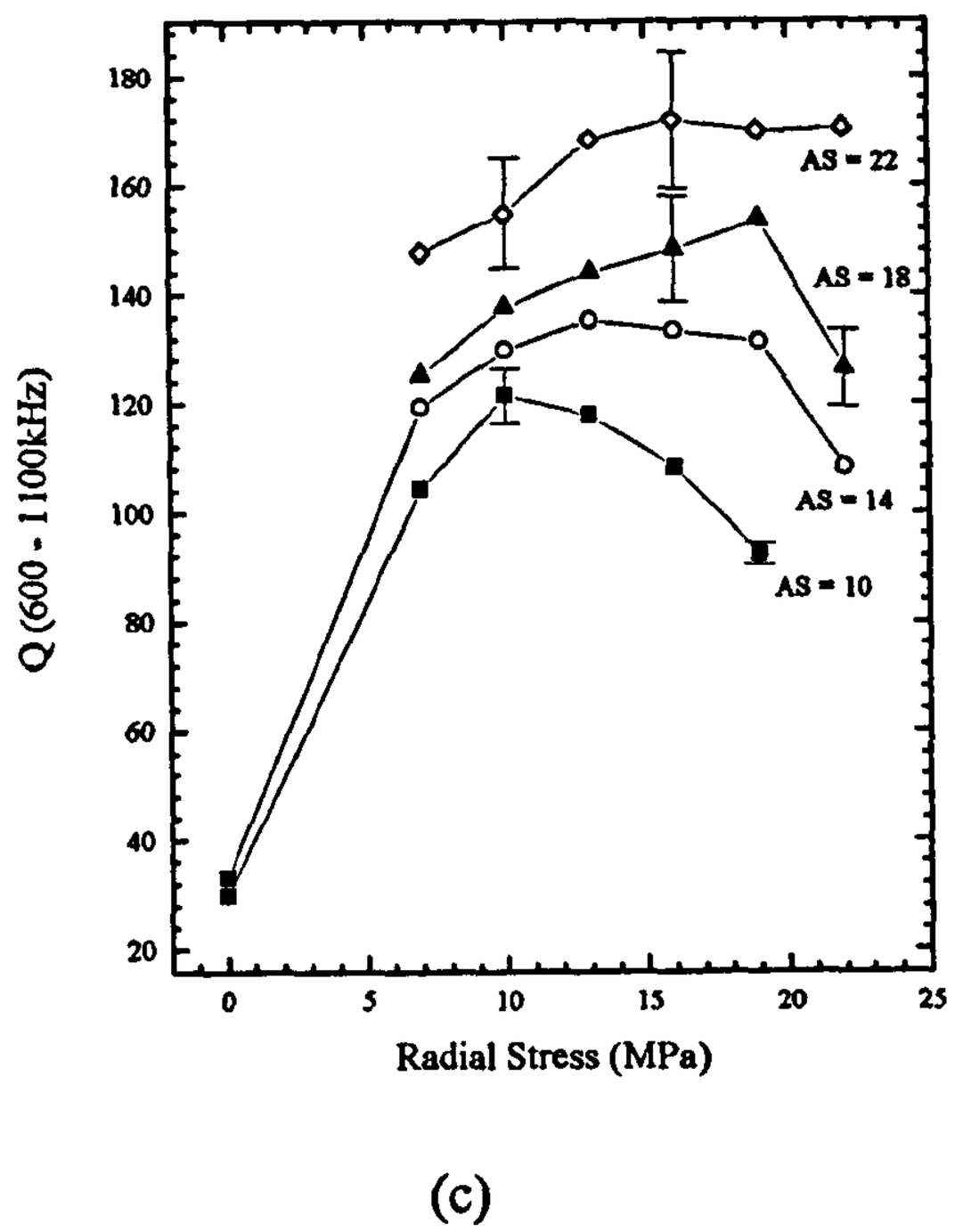

(c)

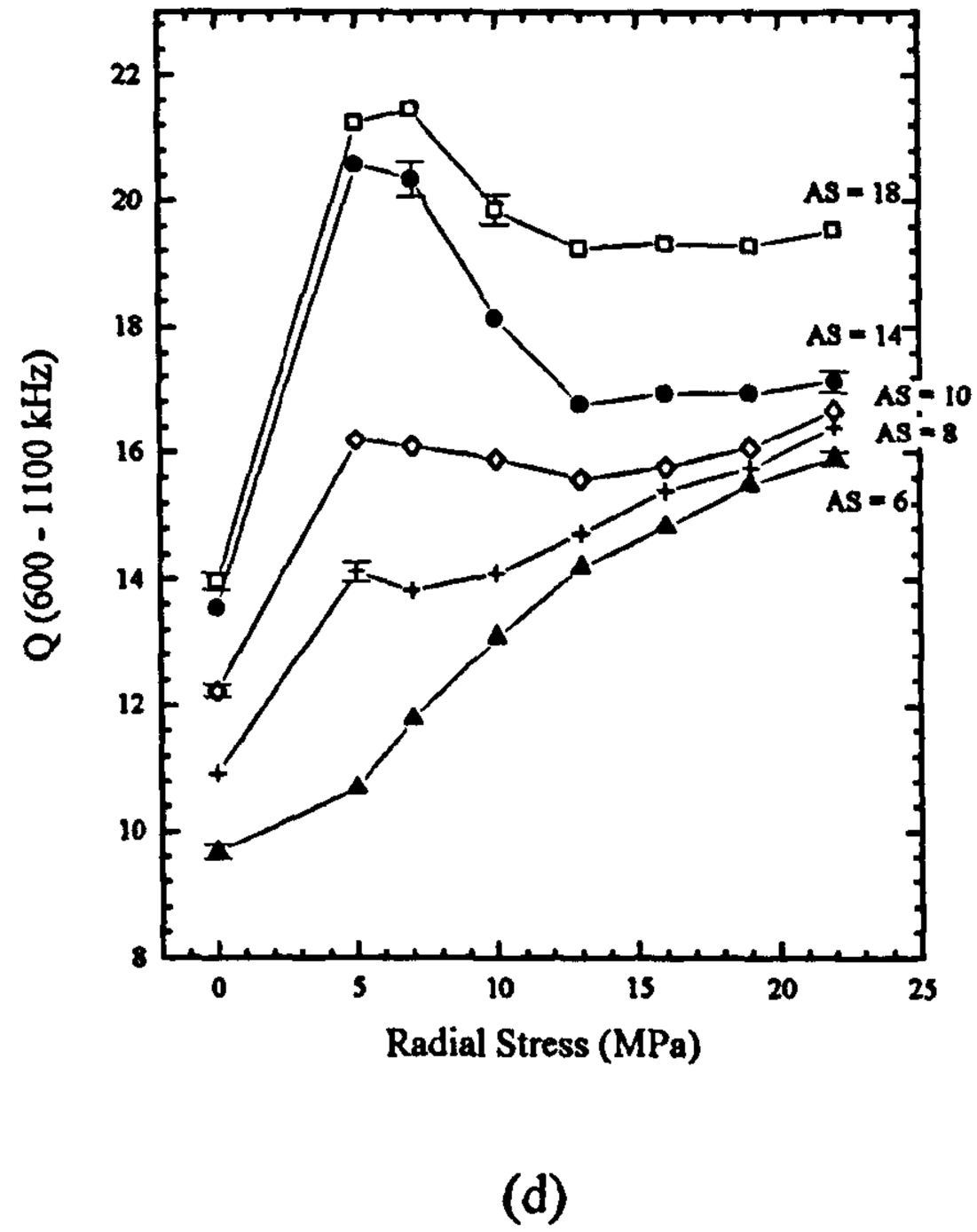

(d)

FIGURE 4.9 Stress-induced attenuation anisotropy for Q measured in the range 600 - 1100 kHz. 'AS' = Axial Stress and each line represents constant axial stress conditions with varying radial stress. The rock types are as follows : (a) Coarse grained sandstone (b) Fine grained sandstone (c) Fine grained siltstone and (d) Limestone. Q is dimensionless and note that the y-axis scales are different.

visualised in a 2-D stress, constant Q contour map format depicted in figure 4.10 (a) to (d). The following points can be identified from these plots,

- The sensitivity of Q to changing radial stress in the case of the coarse sandstone and fine siltstone produces a high Q 'ridge' running along the line of hydrostatic stress. Below conditions of hydrostatic stress (below the ridge) radial stress is the dominant influence over stress-induced Q anisotropy. Above the ridge axial stress becomes the dominant influence.
- The vertical nature of the contours in the fine sandstone case indicate that stress-induced Q anisotropy is only influenced by the axial stress component in this case.
- Below 10 MPa radial stress, the isotropic limestone shows some radial stress-induced Q anisotropy dependence. Above 10 MPa, the vertical nature of the contours suggests that axial stress has become the more dominant influence. The overall low values of Q in this high velocity, well indurated sample would suggest that scatter from density heterogeneities is a dominant attenuation mechanism at these ultrasonic frequencies.

The sensitivity of Q to radial stress in cases (a) and (c) can be explained by the matrix properties of the two rock types. The poorly indurated coarse sandstone has a high microcrack density associated with grain boundaries. The fine siltstone also contains a series of aligned microcracks associated with bedding planes due to the layered formation sequence of this rock type.

Figure 4.11 shows 2-D stress, constant attenuation coefficient calculated at 1 MHz contour plots for the same samples. In all cases the contour lines are vertical, suggesting that the attenuation coefficient is not sensitive to any changes in radial stress, regardless of the rock type. This is a surprising result considering the influence of radial stress over stress-induced Q anisotropy. However, the calculation of Q is carried out over a large frequency range rather than the attenuation coefficient which is measured at a single frequency. Therefore Q monitors changing attenuation across a frequency bandwidth and reflects how this entire bandwidth is being affected by stress induced changes within the sample. For instance at higher stress levels, where a sample has a higher dynamic bulk modulus, higher frequency components would be expected to be less attenuated due to the closure of microcracks. Such components might experience a higher degree of attenuation where microcracks are open at lower stress levels. Therefore Q is, in effect, an expression of the way individual components change across a frequency bandwidth.

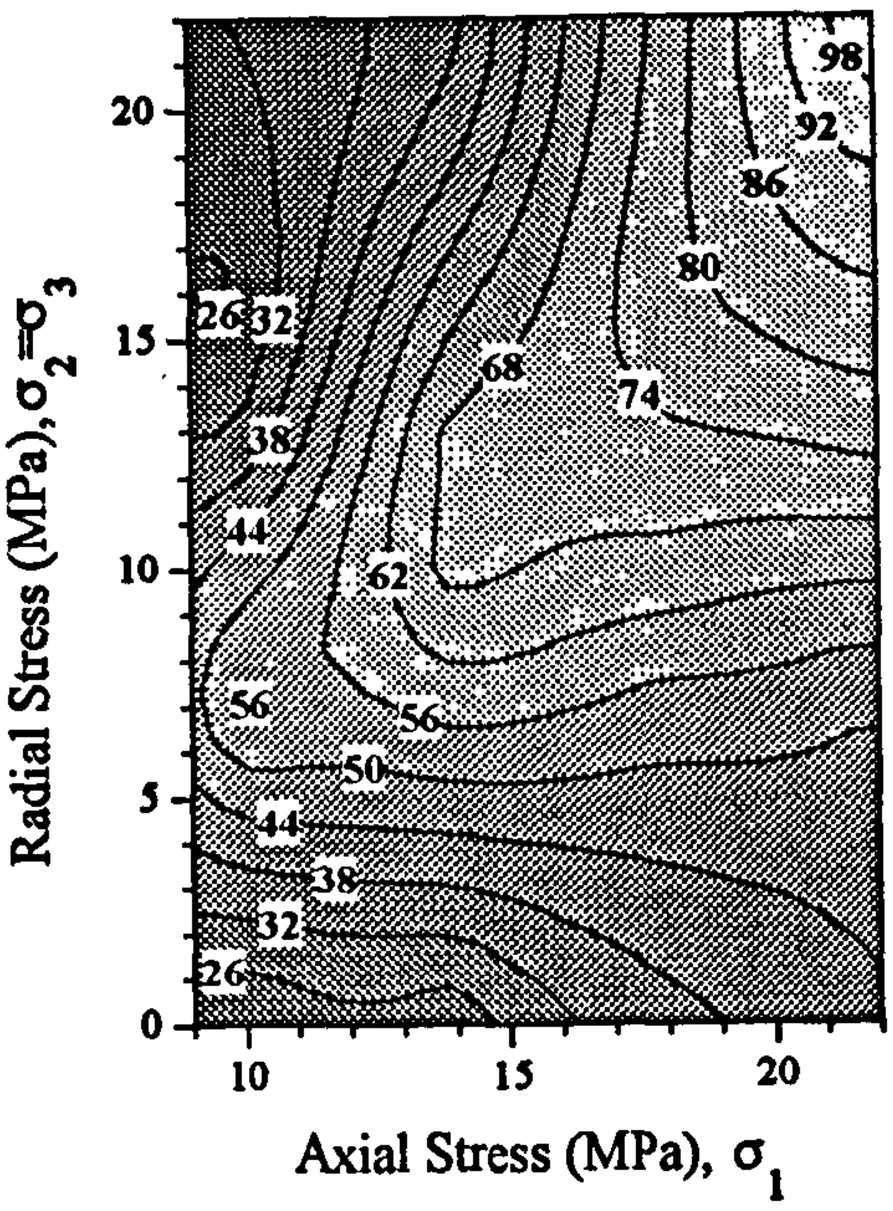

(a)

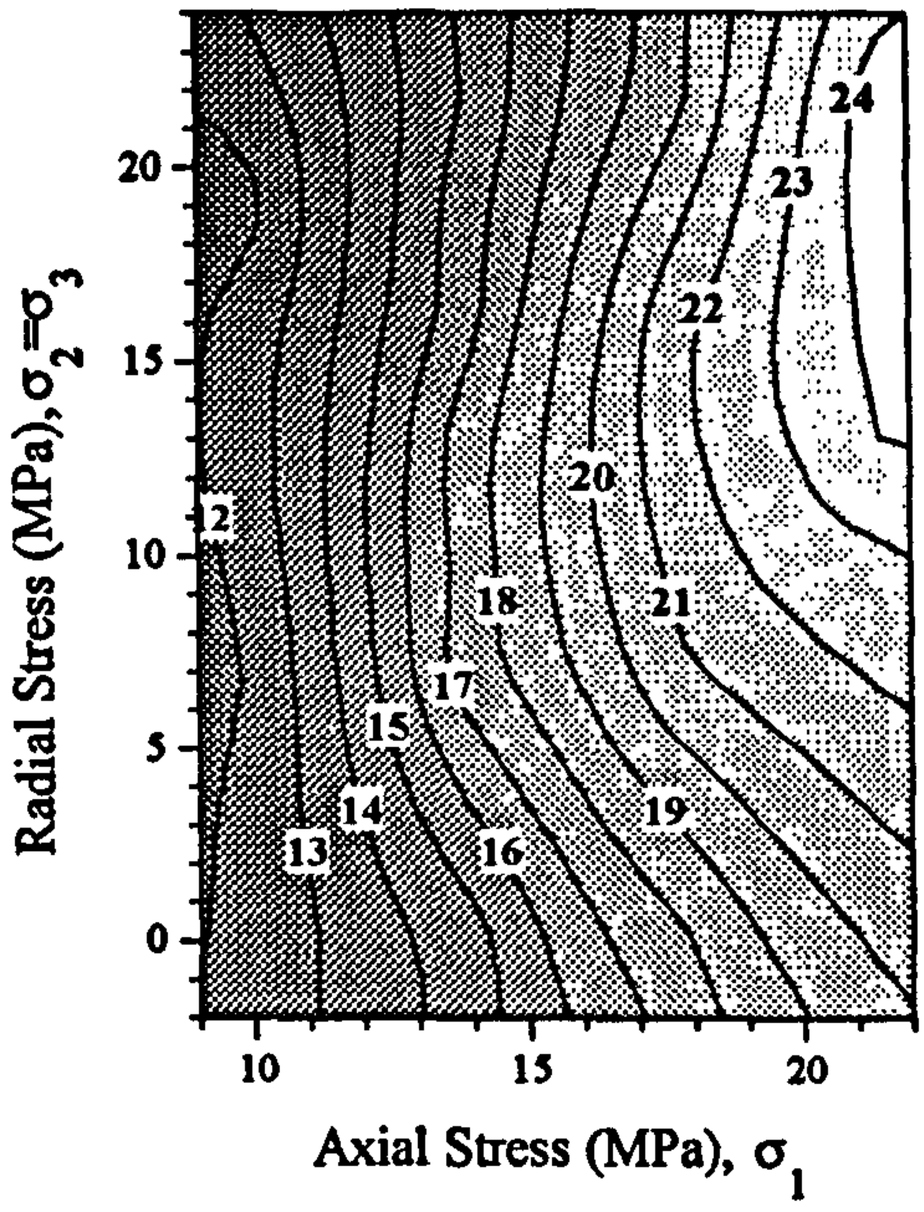

(b)

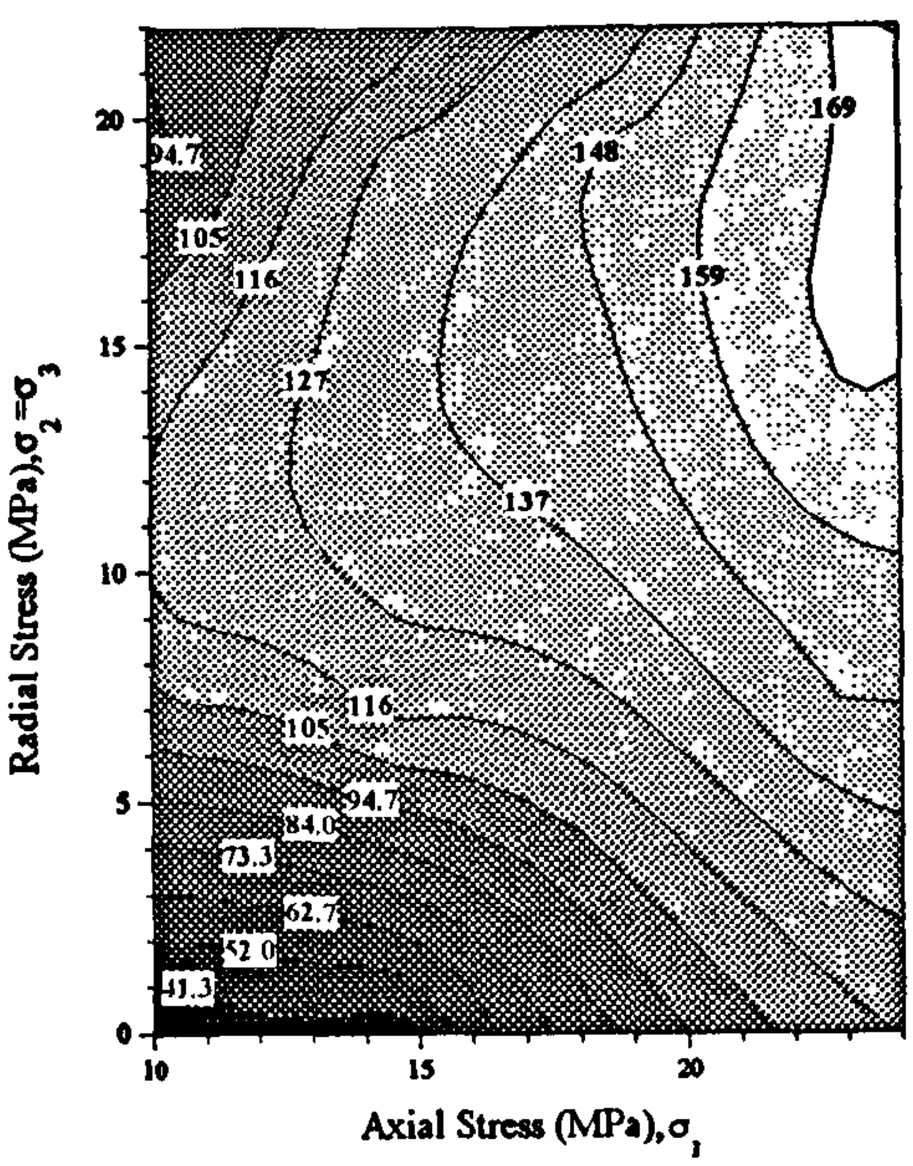

(c)

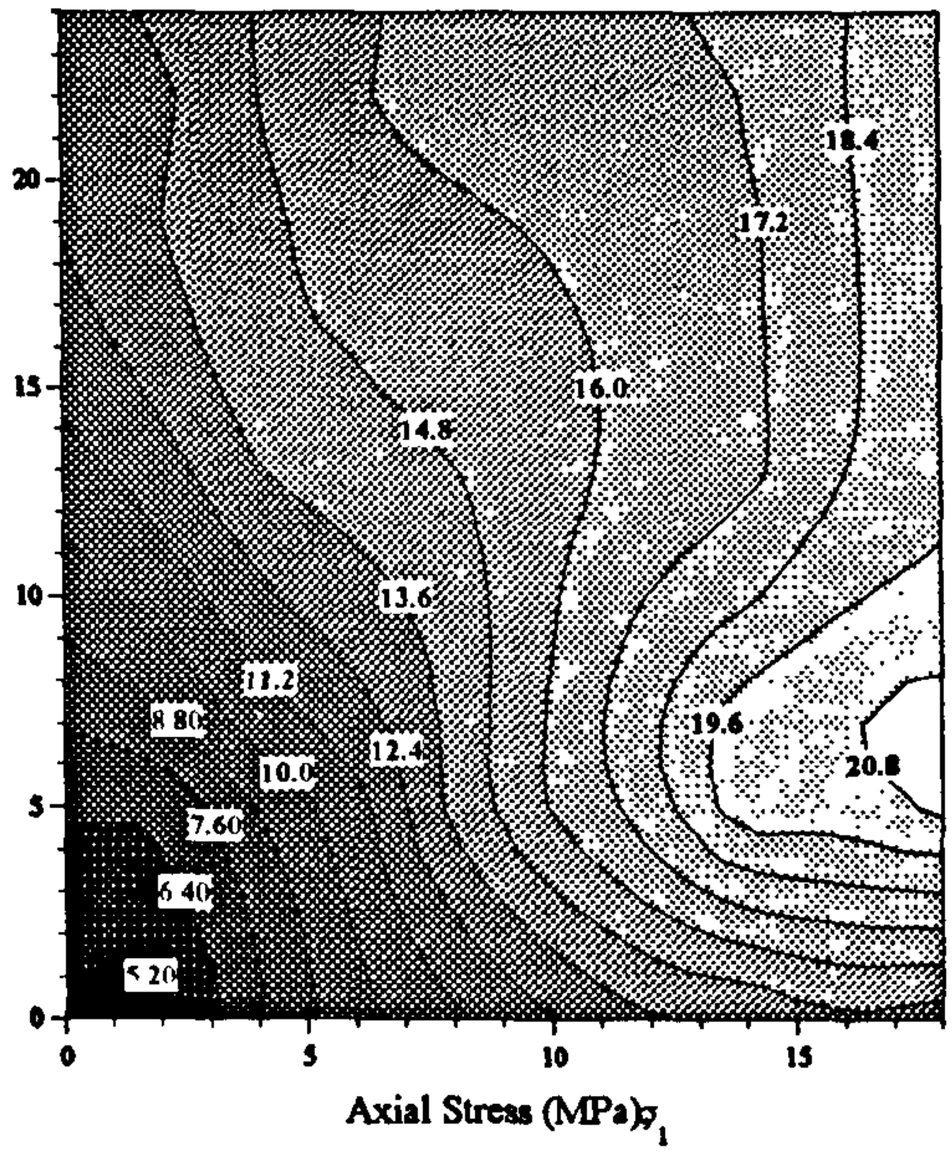

(d)

FIGURE 4.10 Stress-induced attenuation anisotropy contour plots for Q measured in the range 600 - 1100 kHz. The rock types are as follows : (a) Coarse grained sandstone (b) Fine grained sandstone (c) Fine grained siltstone and (d) Limestone. Q is dimensionless

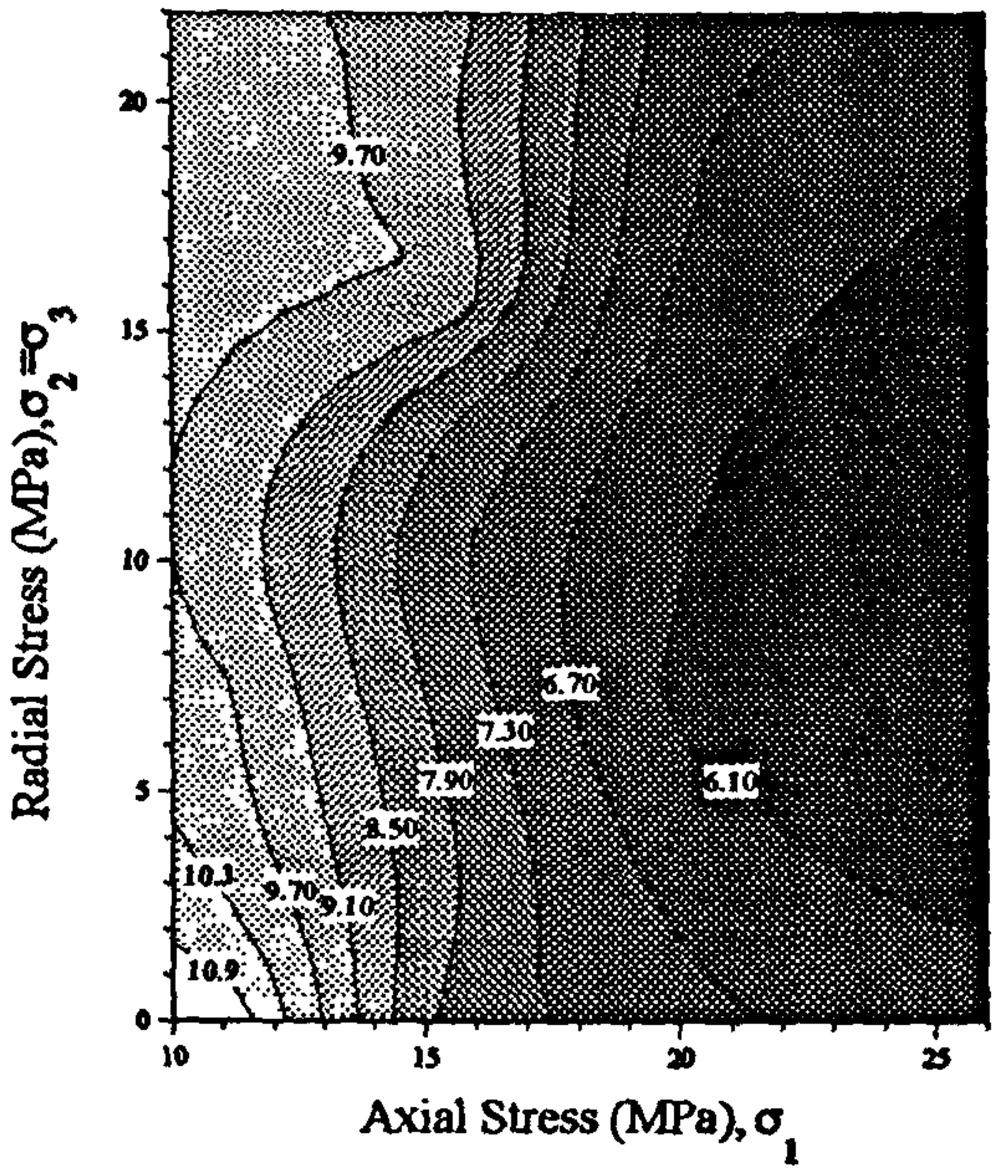

(a)

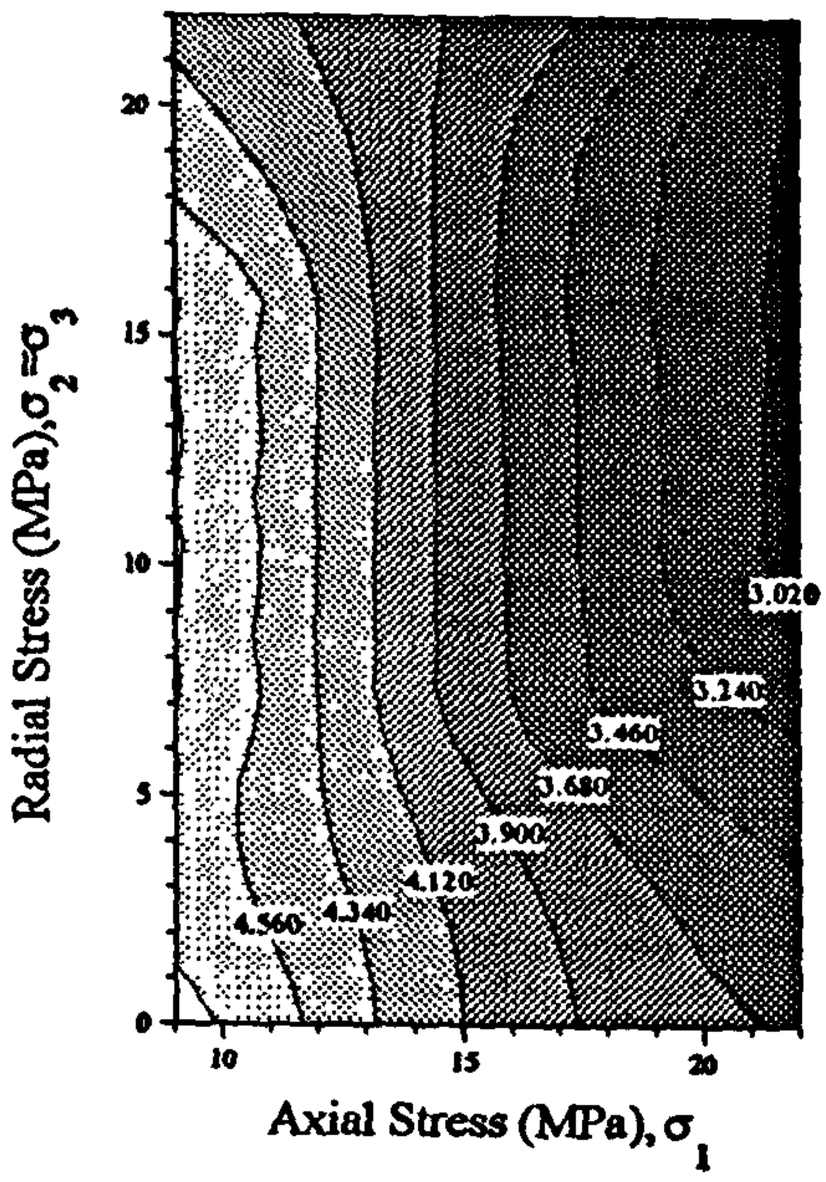

(b)

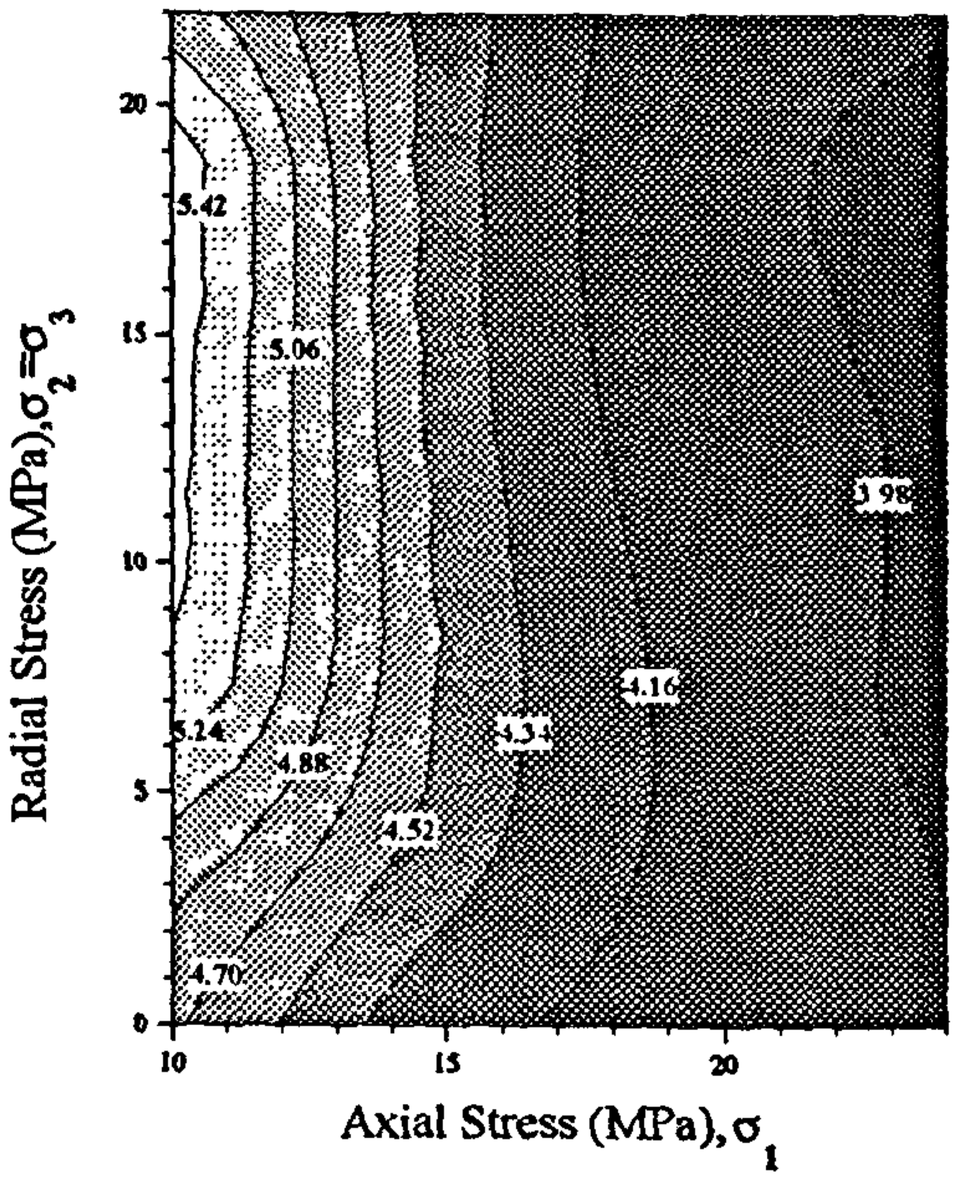

(c)

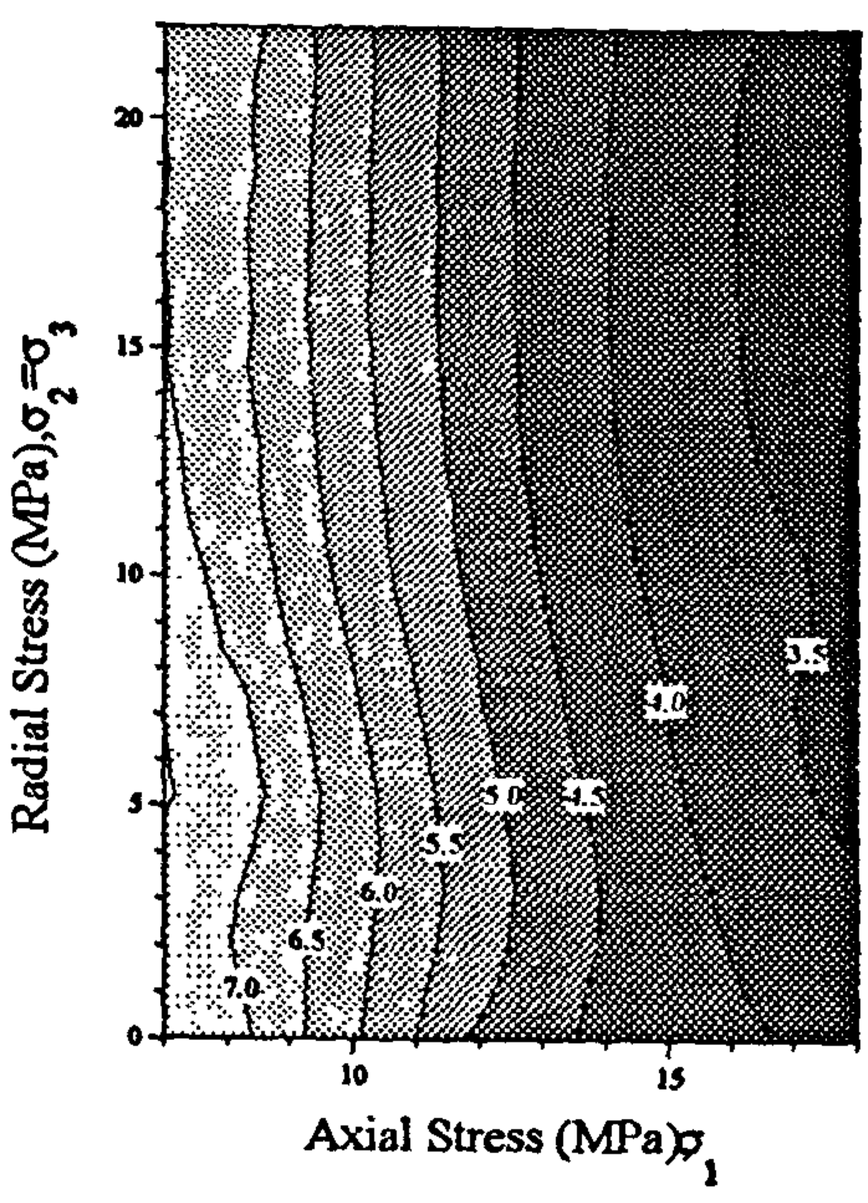

(d)

FIGURE 4.11 Stress-induced attenuation anisotropy contour plots for attenuation coefficient calculated at 1 MHz. The rock types are as follows : (a) Coarse grained sandstone (b) Fine grained sandstone (c) Fine grained siltstone and (d) Limestone. Attenuation Coefficient is expressed in dB/cm.

4.3.4.2 Quality factor (18 - 49 kHz) and attenuation coefficient at 29 kHz.

The lower frequency range tests were conducted on larger NX core size samples, under the same test conditions of the high frequency case. The purpose of these tests was to check if the same patterns of stress-induced anisotropy occurred at the lower frequency range thus discounting that the patterns observed in section 4.3.4.1 resulted from a high frequency attenuation mechanism. Only large samples of the coarse sandstone and limestone were available for this comparison. The anisotropy contour plots for Q calculated between 18 and 49 kHz are reproduced in figure 4.12 for a coarse sandstone and a limestone sample. The corresponding plots of attenuation coefficient stress-induced anisotropy calculated at 29 kHz are reproduced in figure 4.13.

The contour pattern in figure 4.12 (a) for the coarse sandstone is very similar to the same plot for the high frequency case in figure 4.10 (a) with respect to the presence of the high Q ridge which approximately runs along the line of hydrostatic stress. Away from these hydrostatic conditions (above or below the ridge), the larger of the two stress components becomes the dominant influence most probably due to the selective closure or dilation of microcracks caused by the imbalance in the stress field, as with the high frequency case. Q calculated across this frequency range appears to be just as sensitive to microcrack closure as its high frequency counterpart. The same is true for the limestone results in figure 4.12 (b), where Q shows some radial stress dependence at higher values of axial stress.

The attenuation coefficient contour plots, calculated at 29 kHz, for the same samples shown in figure 4.13 (a) and (b) for coarse sandstone and limestone respectively also have identical pattern characteristics to the high frequency examples depicted in figure 4.11. However, attenuation coefficients at 29 kHz are one tenth of the values observed at 1 MHz. Again, the attenuation coefficient measured at a specific frequency shows no sensitivity to change in radial stress and is purely dominated by the axial stress component in both rock types.

4.4 Samples Loaded to Failure

The purpose of this section is to investigate the sensitivity of velocity and attenuation as indicators of sample condition as the confined sample is axially loaded to failure. A similar experiment was conducted by Lockner et al (1977) (section 2.3.1.2) where velocities and amplitude ratios of wave propagation paths were measured normal to the axial load. In this study propagation paths were parallel to the axial load, and

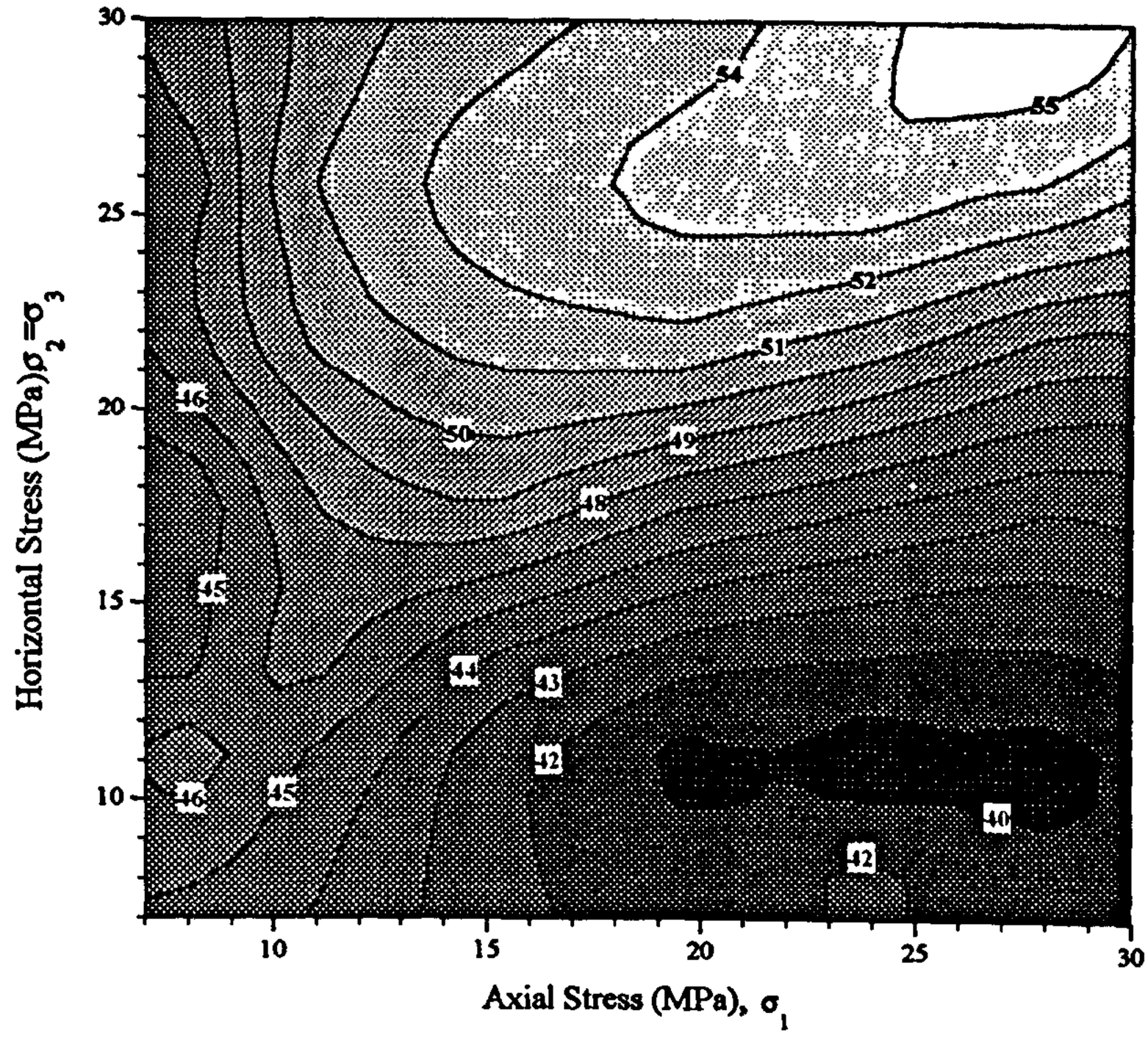

(a)

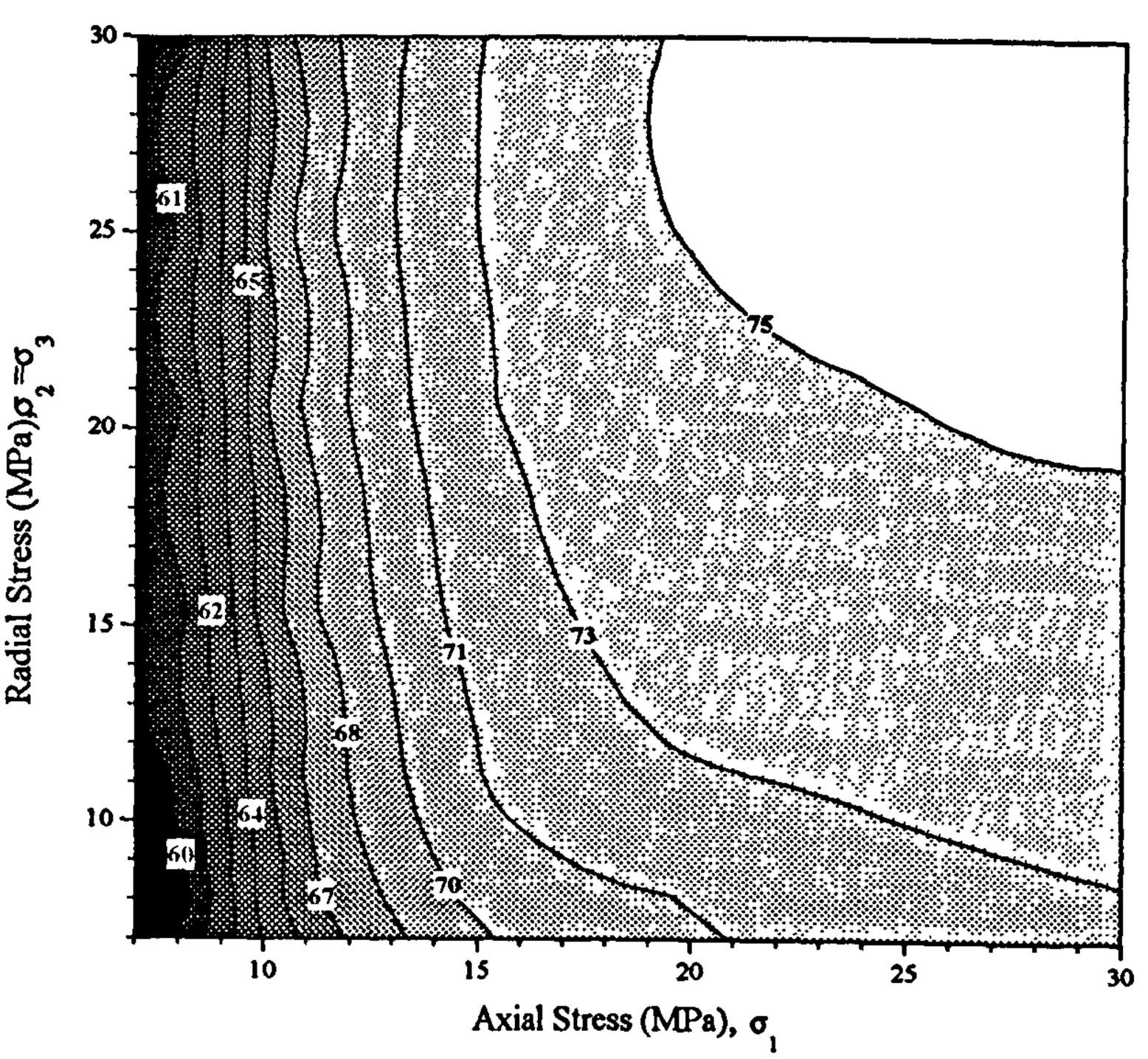

(b)

FIGURE 4.12 Stress induced Q anisotropy plots for Q measured in the range 18 to 49 kHz. The rock types are as follows, (a) Coarse Sandstone (b) Fine grained Limestone.

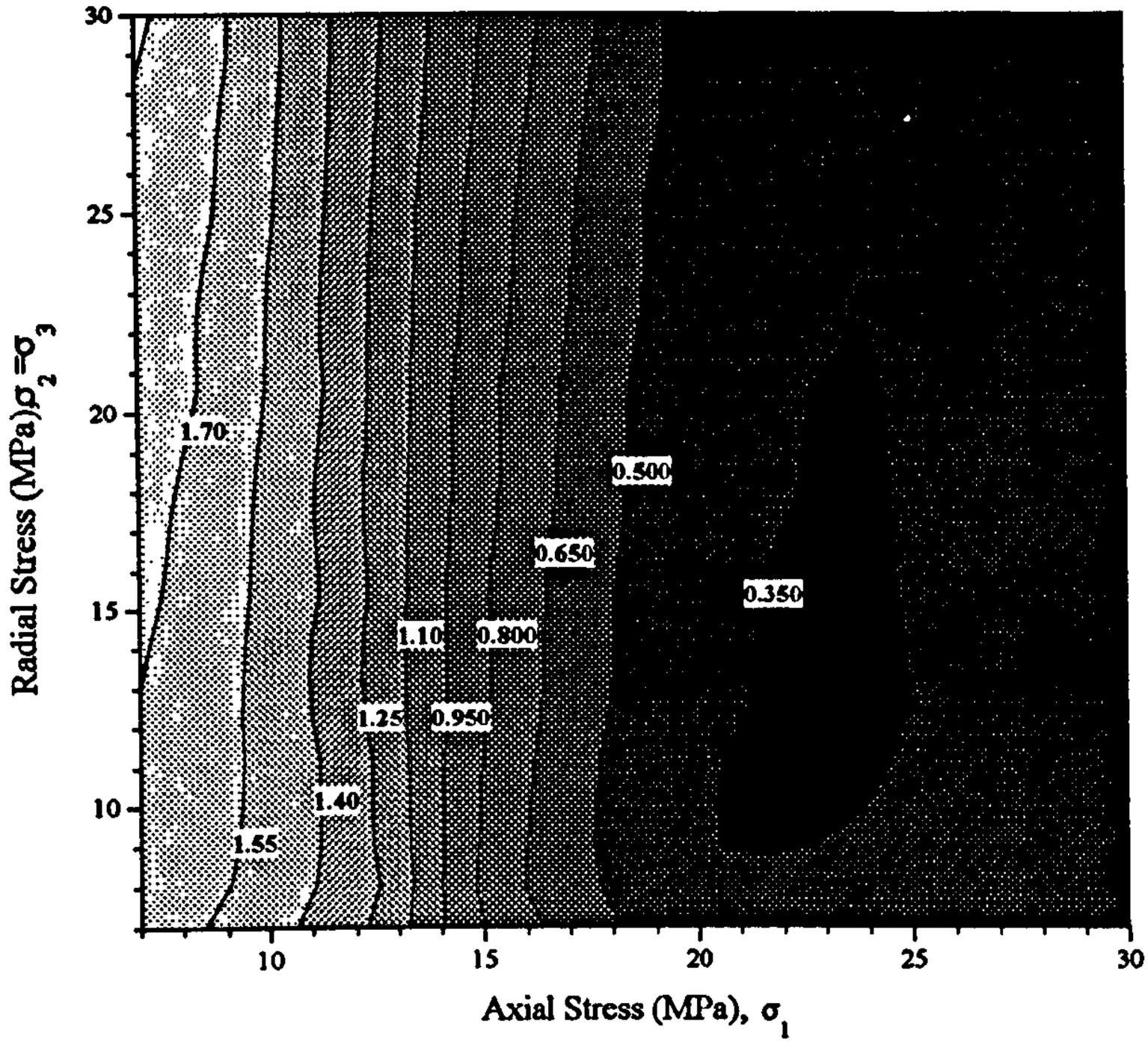

(a)

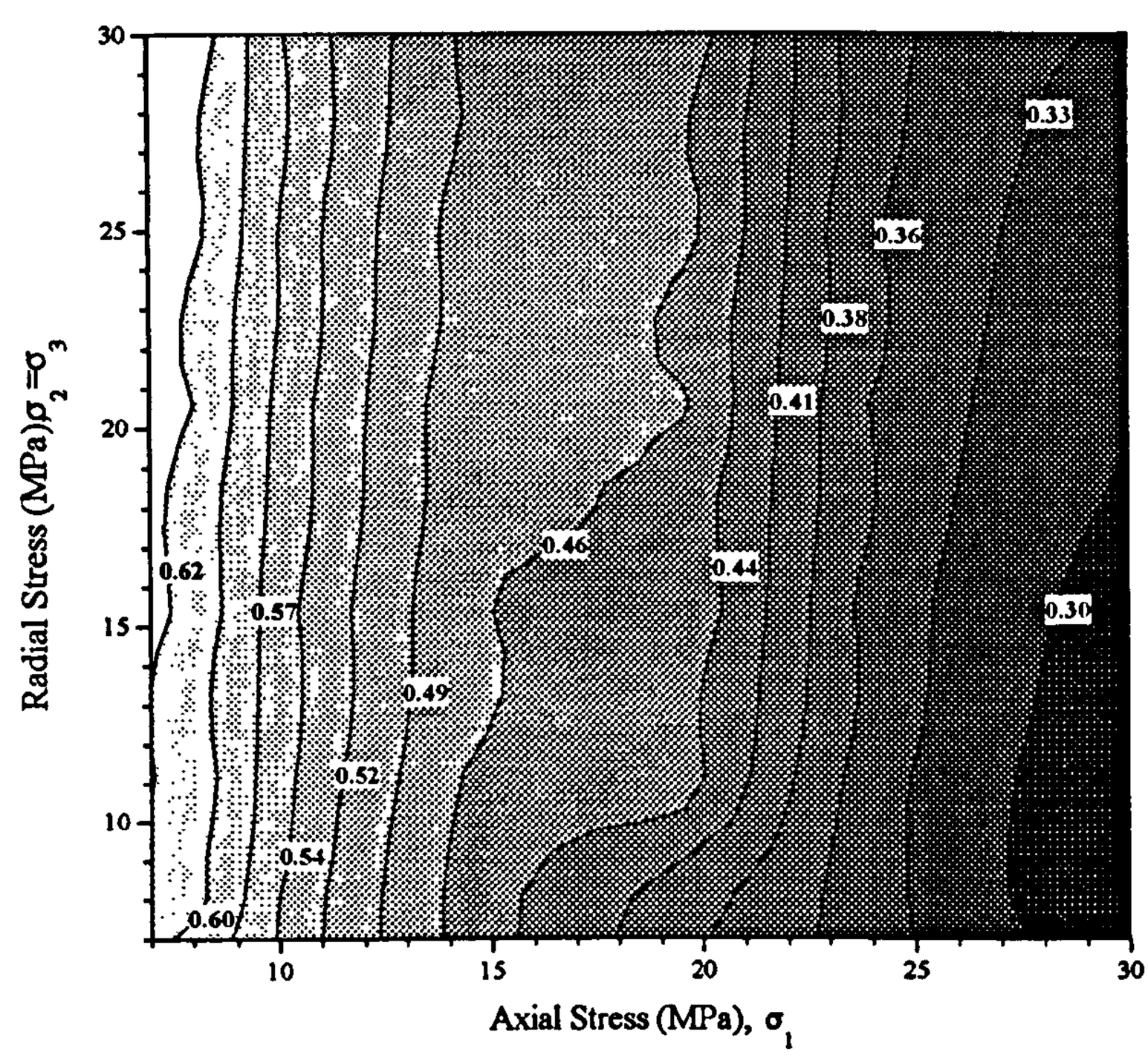

(b)

FIGURE 4.13 Stress induced attenuation anisotropy contour plots for Attenuation Coefficient measured at 29 kHz. The rock types are as follows, (a) Coarse Sandstone (b) Fine grained Limestone. Units are dB/cm.

unlike Lockner's experiment, the samples were triaxialy confined and therefore more realistically simulated in-situ conditions.

Some experimental results for a limestone sample are shown in figure 4.14. Figure 4.14 (a) shows P-wave velocity versus percentage of failure strength. There are three distinct stages to the graph,

- Stage 1 is the increase in velocity with the initial onset of axial load. The reasons for this have been comprehensively discussed in sections 4.3.1 and 2.2.1.1., i.e. microcracks are closing and the acoustic coupling between rock grains is improving.
- Stage 2 is the plateau region reached after the axial load has reached sufficient levels to completely close the vast majority of microcracks within the sample. This occurs at about 60% of the failure strength within this limestone. The plateau region spans from 60 to 90% of the failure strength.
- Stage 3 is a short decline in velocity from the plateau value as new microcracks develop. This occurs from 90% failure strength and culminates in the failure of the sample.

Figure 4.14 (b) shows quality factor versus the percentage of failure strength for the same limestone sample at 7 MPa confining pressure. As in figure 4.14 (a) there are three distinct stages to the graph,

- Stage 1 is the increase in Q with the initial onset of axial load. The reasons for this increase have been comprehensively covered in sections 4.3.2 and 2.3.1.1.
- Stage 2 is the plateau region and spans from 40 to 80% of the percentage of failure strength.
- Stage 3 shows a bigger decline than in case (a) occurring from 80% of the percentage of failure strength, and ending at failure.

To interpret both of these results, the work of Chow et al (1995) gives a good insight into the internal processes involved in the failure of a laboratory sample. Chow's experiment tomographically imaged the change in ultrasonic velocity after each of 28 successive loading cycles where the peak stress within the sample was less than or approximately equal to the onset of volumetric strain reversal. In the test conducted here, the sample was not cyclically loaded to failure. Chow et al (1995) concluded that microfractures began to form after the first load cycle and new cracks were introduced with each subsequent load cycle. Load cycling also caused an overall decrease in the velocity after each cycle. Velocity difference tomograms indicated that

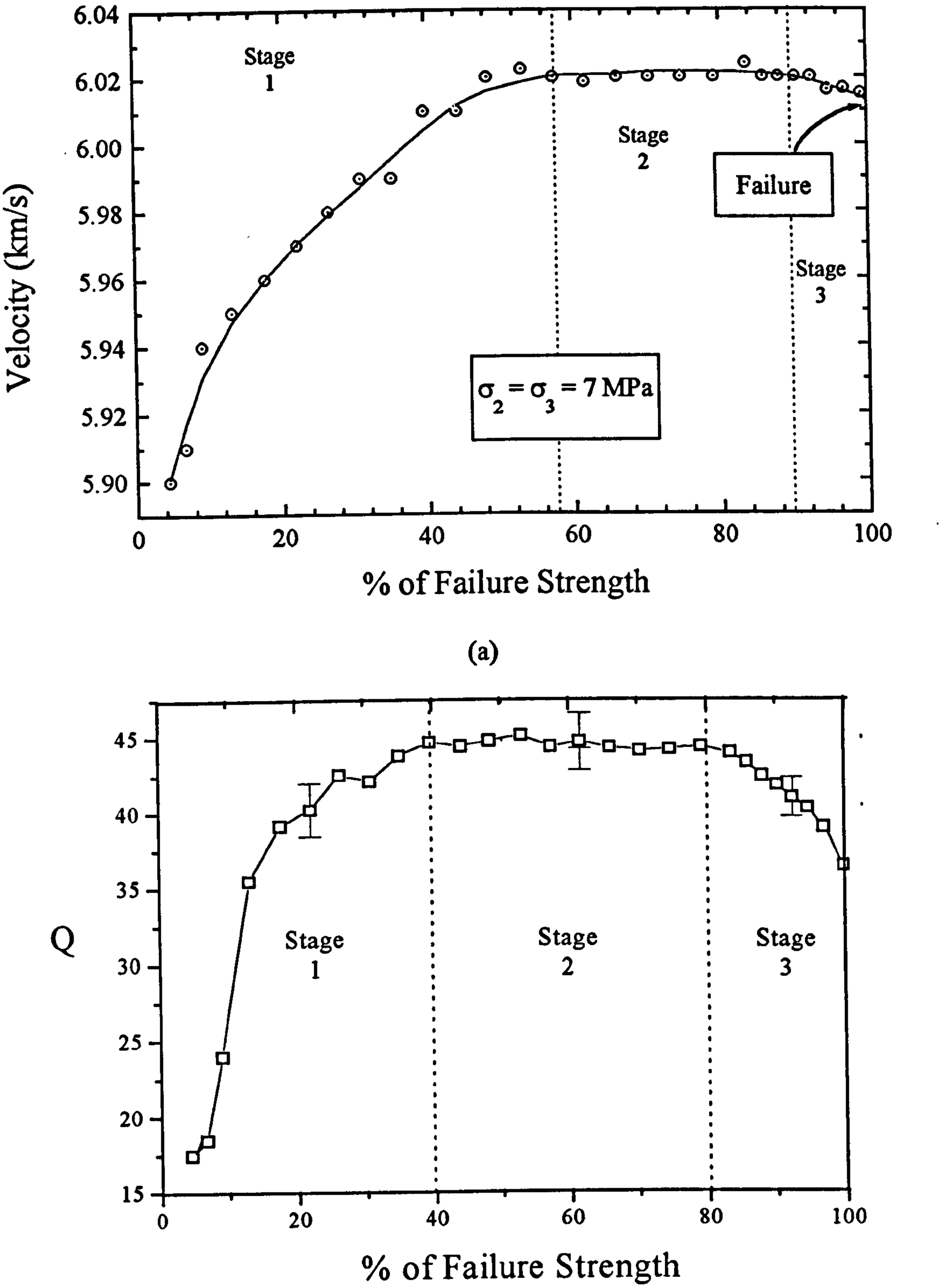

FIGURE 4.14 (a) Velocity versus percentage of failure strength in limestone. (b) Quality factor versus percentage of failure strength for the same sample.

new microcrack planes were primarily orientated sub-parallel to the core axis and formed preferentially in a donut-shaped zone around the middle of the core cylinder.

The plots in figure 4.14 (a) and (b) provide a similar insight into the failure process, but the full process is taking place sequentially rather than after a near failure load cycle is completed as is the case with Chow et al (1995). In figure 4.14 (a) stage 1 and 2 represent preferential microcrack closure within the sample. The velocity reaches a plateau and no further change is observed until 90% of the failure strength of the sample is reached where a small drop occurs before failure. The drop is of the order of 2 to 3% of the plateau value which is small and therefore difficult to detect. In the case of the figure 4.14 (b), the same Q increase and plateau region is observed, but a decrease of 31% occurs between 80% of the failure strength and actual failure. The most likely cause for the decrease in both velocity and attenuation is the development of microcracks between 80% of the failure strength and sample failure. Chow et al (1995) showed that these microcracks were orientated parallel to the loading axis. Therefore new development of pre-existing cracks and initiation of new cracks causes dilation of the sample, decreases velocity and increases attenuation of the wave propagating along the axis of loading. Attenuation is obviously a more sensitive indicator than velocity that microcracks have started to develop within the sample. With Q, this detection occurs earlier and the decline of the sample in stage three is easier to monitor within the bounds of experimental error.

The implications of these results for single seismic measurements through a rock mass are as follows (Pearce & Wade, 1996a),

- Both velocity and attenuation are sensitive to low values of stress change along the axis of propagation, where the stress values are low compared to the strength of the in-situ confined rock mass (between 40 % and 60 % of the failure strength).
- At high stress levels, both velocity and attenuation become insensitive to stress change (between 50 % and 80 % of the failure strength)
- Where a rock mass is becoming dangerously overstressed or concentration of stress is occurring at specific points, causing localised microfracture development and failure, this will be accompanied by a decrease in both velocity and attenuation. A drop in attenuation should occur first, followed by a drop in velocity as the rock mass reaches a critical stage. This applies to conditions where stress concentrations reach 80 % and above of the percentage of the rock mass failure strength.

4.5 Fractured Samples

Once a sample had been tested to failure, it was retested under the same varying triaxial stress regime used for the intact case. The integrity of failed samples was maintained by enclosing them in a thick plastic sheath whilst still intact and keeping the confinement pressure on the sample after failure. The plastic sheath kept the sample together, and prevented internal damage to the triaxial cell. The failed sample test was then conducted straight away without removing the cell, or the transducers, in order to preserve original contact conditions as far as possible. In the majority of the tests, the samples failed diagonally across the core cylinder, with a number of major fractures running parallel to the cylinder axis. Following removal of the transducers after the failed test was completed the sample ends were inspected and in most of the cases were found to be intact or only slightly damaged at the edges. This meant that the transducer contact conditions had remained as close to the original, intact sample experimental conditions as possible. Where the cylinder ends had been badly damaged due to poor sample failure, the results were discarded from any subsequent analysis.

This section will consider three different fractured limestone samples. Two of the samples were taken from Milldam Mine, which is the field site documented in chapter 8 and the other from Gillfield Mine, the field site in chapter 6. The two samples from Milldam Mine were cored from a large sample taken from the B-West Horizon (see chapter 8 section 8.4) from a development blast. The sample from Gillfield mine was cored from a large sample collected from some stowed workings at the survey site described in chapter 6. After failure the three samples had the fracture characteristics pictorially described in figure 4.15 and the properties described in table 4.2.

4.5.1 Velocity

4.5.1.1 Sample 1

Sample 1 contained a single macrofracture across the core cylinder normal to the loading axis. A complete set of experimental velocity results for the sample is shown in figure 4.16. Figure 4.16 (a) shows the stress-induced velocity change for the intact sample before the single failure along a calcified joint set. Figure 4.16 (b) shows the stress-induced velocity change after the fracture. Figures 4.16 (c) and (d) show the two plots subtracted in terms of actual and percentage velocity change respectively. These plots show the increase (or decrease) in stress-induced anisotropy characteristics caused by the fracturing process.

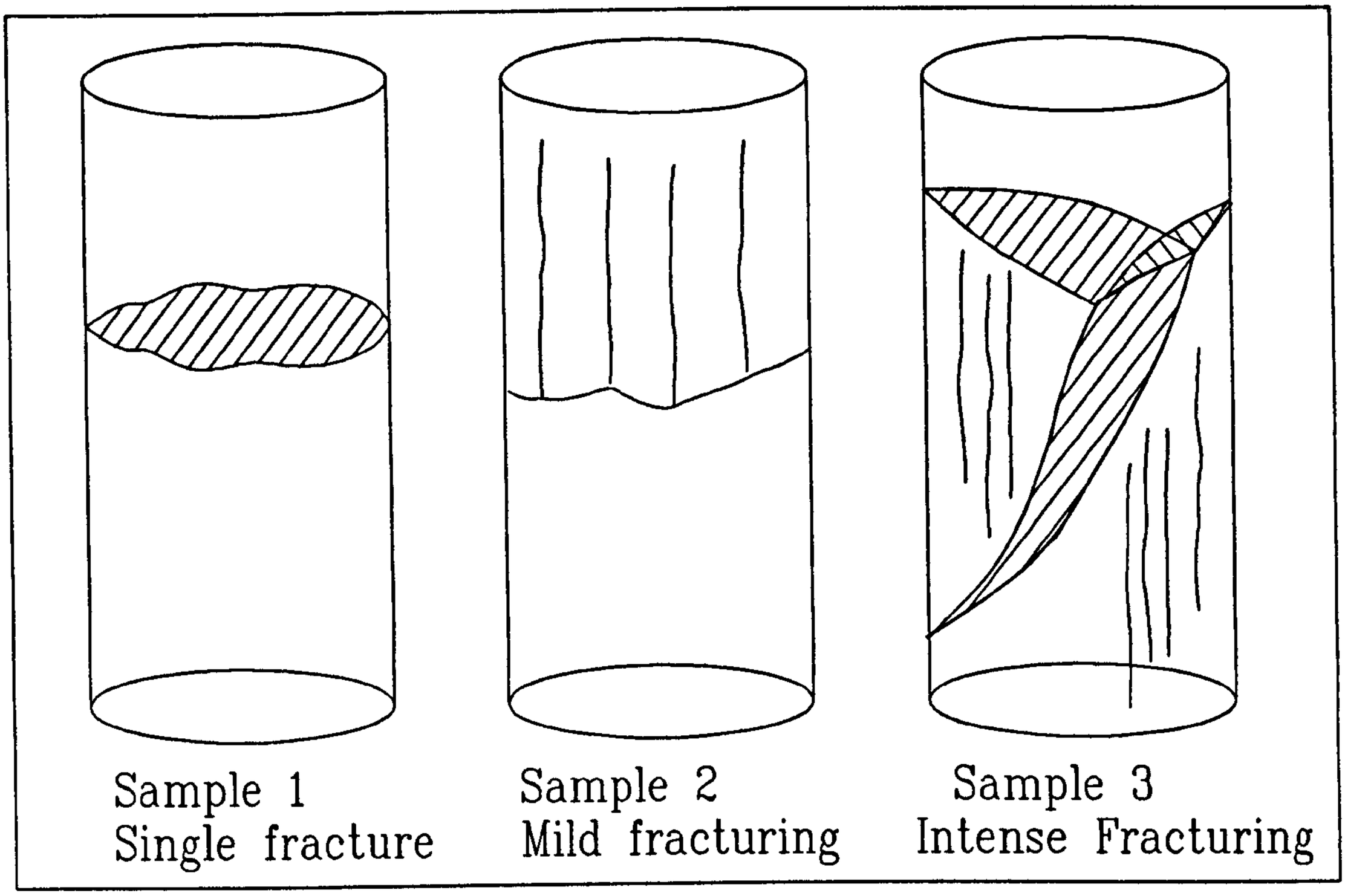

FIGURE 4.15 Pictorial representation of the degree of failure and fracture of samples 1, 2 and 3. Shaded areas represent complete fracture planes. Vertical lines represent macrofractures.

Sample	Description	Intact Density	Comp. Strength	Fracture State
1	Milldam Mine Limestone (B-West Horizon	2610.7	65 MPa	Single fracture
2	Gillfield Mine Limestone	2695.0	70 MPa	Mild fracturing along half of the core cylinder
3	Milldam Mine Limestone (B-West Horizon	2758.9	85 MPa	Large diagonal fracture across core and minor fracturing parallel to axis

TABLE 4.2 Fractured sample description and properties

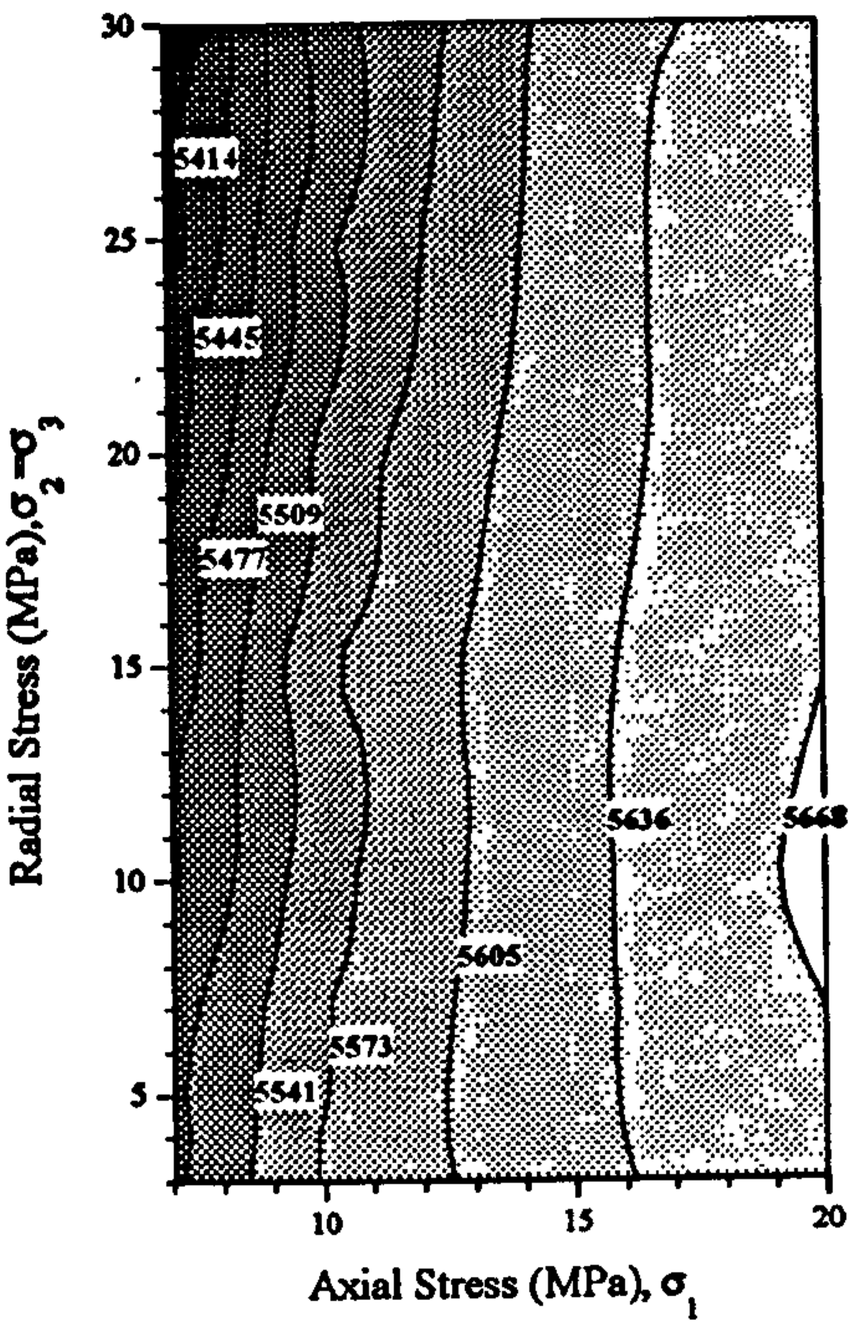

(a)

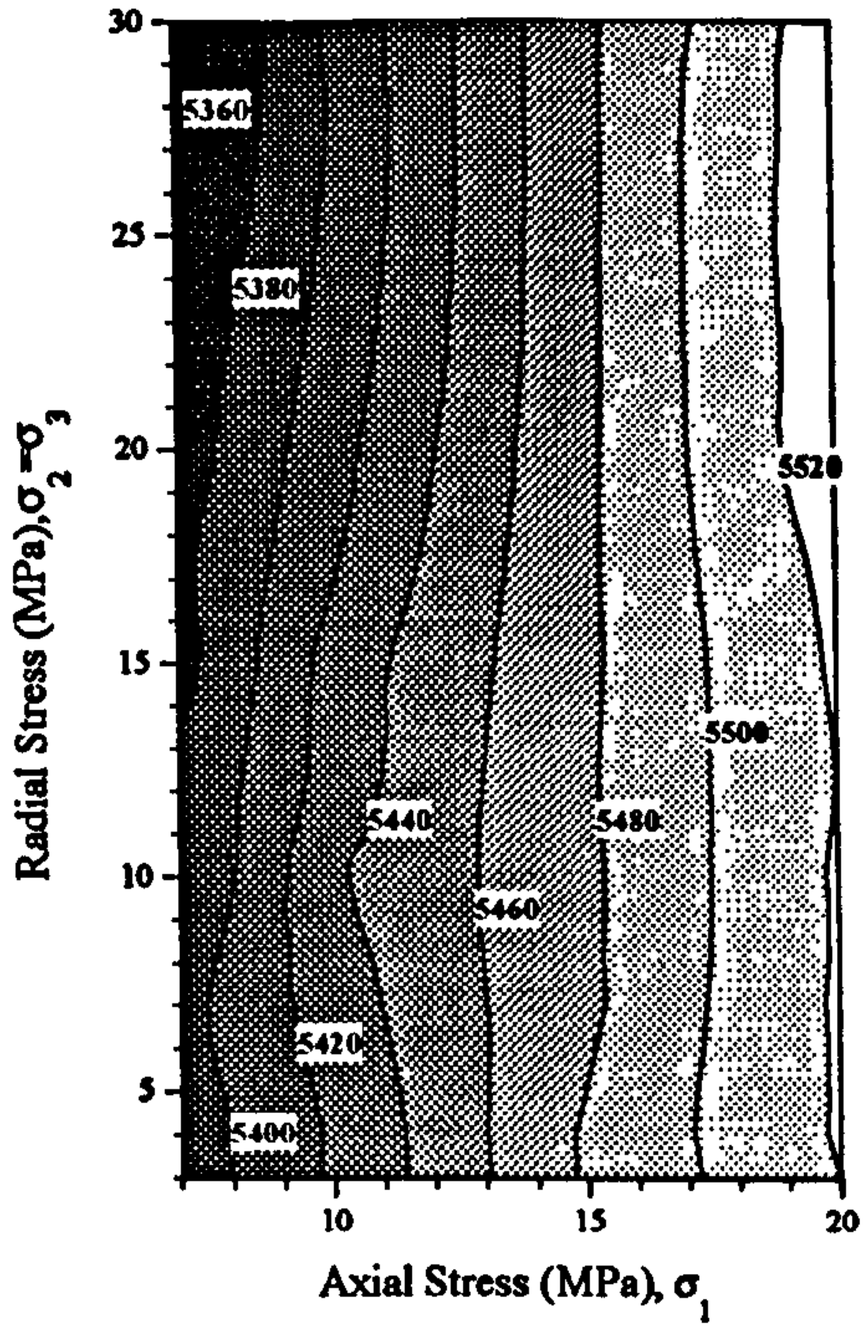

(b)

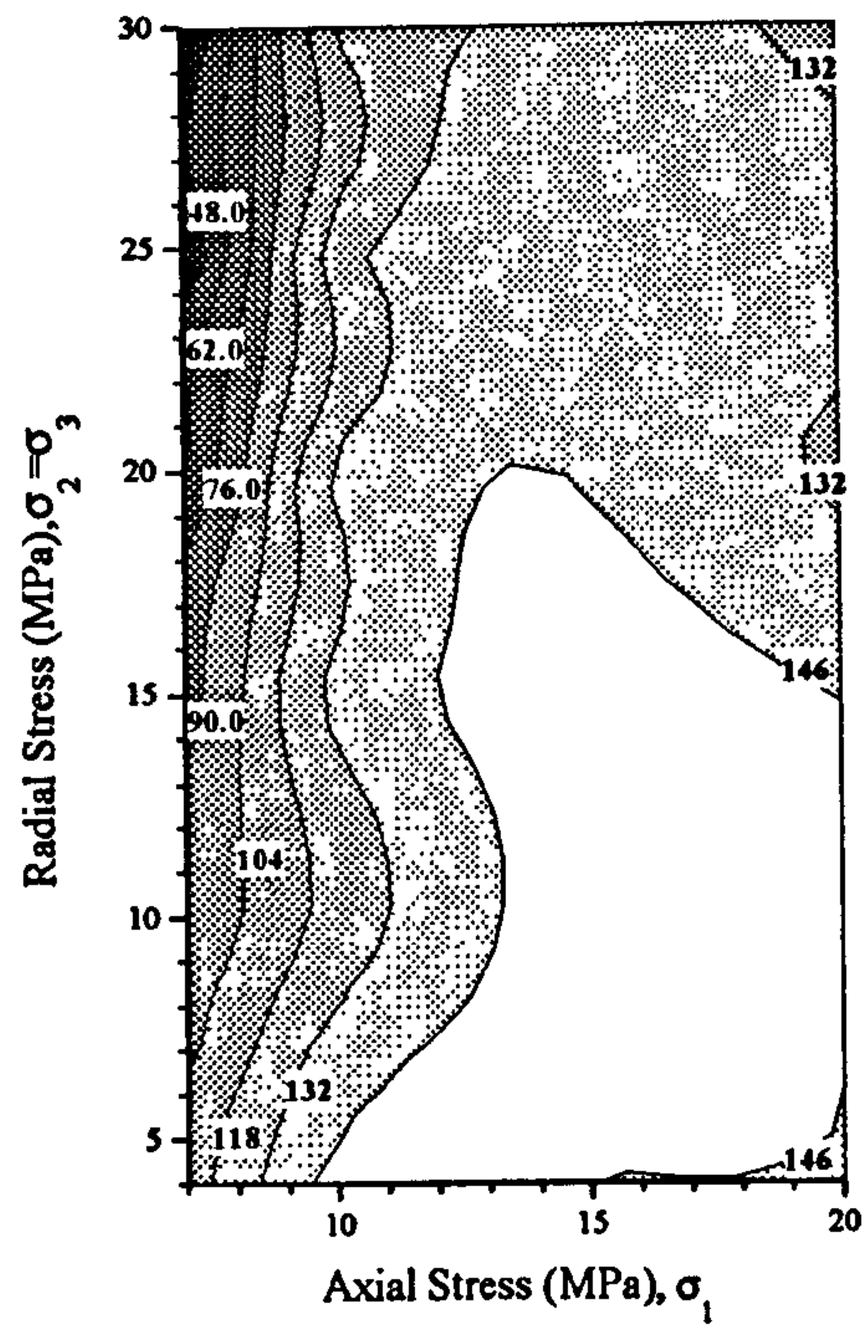

(c)

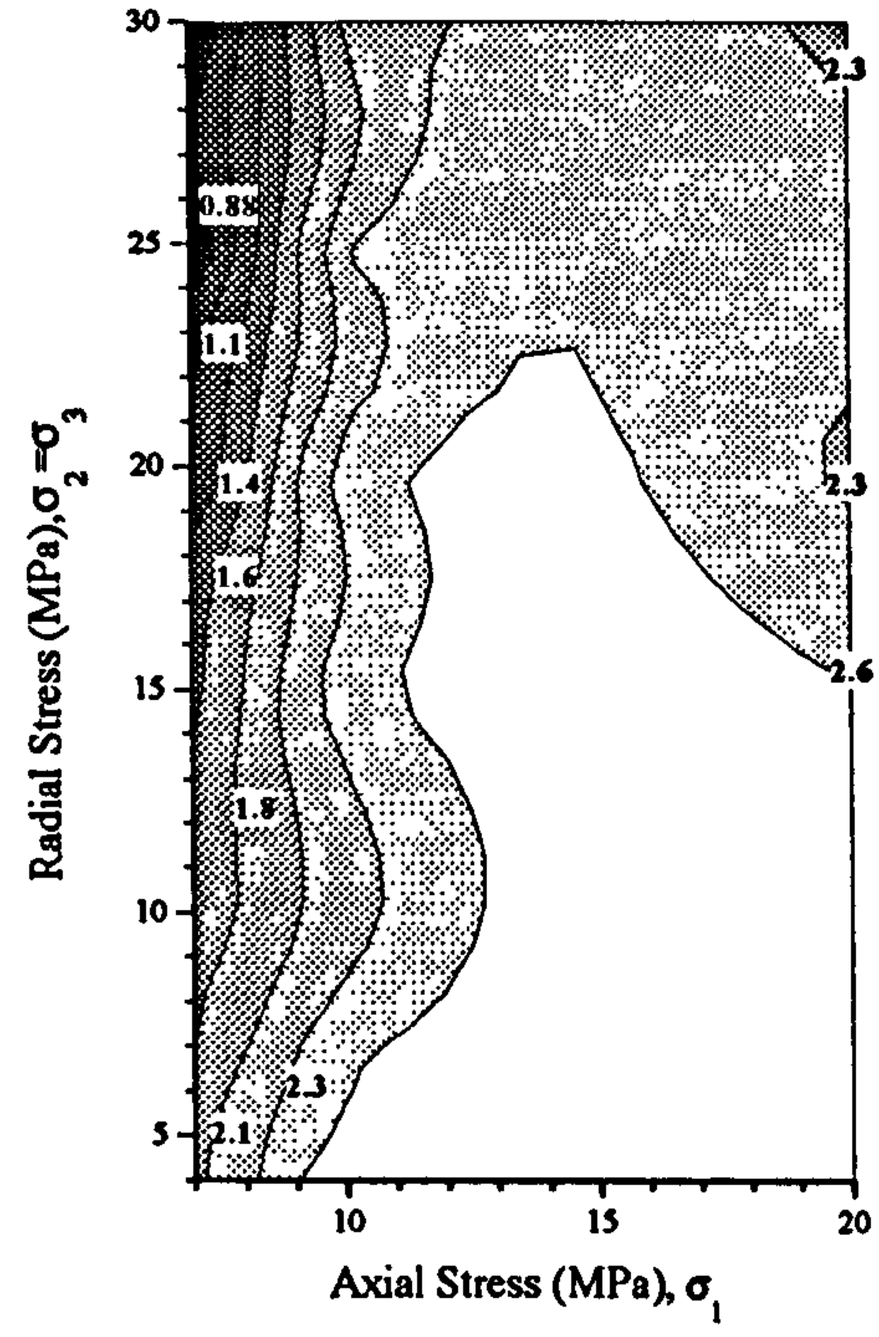

(d)

FIGURE 4.16 Stress-induced velocity anisotropy contour plots for sample 1 with a single macrofracture (a) Intact sample (b) Fractured sample (c) Velocity change between (a) and (b) (d) Percentage velocity change between (a) and (b). Velocities are all expressed in m/s.

The constant velocity contours are vertical for the both the intact and singly fractured case showing that velocity is insensitive to any change in radial stress. The limited range of axial stress within the experiment was necessary to prevent any slip along the fracture plane. During the experiment at an axial stress of 7MPa, a large radial stress caused shear action along the discontinuity.

The velocities range from 5495 to 5669 m/s and 5360 to 5520 m/s in the intact and failed cases respectively over an axial increase of 13 MPa. These figures relate to a percentage increase of 0.24% and 0.22% in velocity per MPa of increase in axial stress for the intact and failed case respectively. Therefore the single fracture has no significant effect on the degree of stress-induced velocity anisotropy within the sample but reduces the overall velocity by 2.62% of the intact values. This is confirmed by the plots in figure 4.16 (c) and (d).which show that velocity change is uniform over the entire stress range (118 - 146 m/s or 2.1 to 2.6 %), except where low values of axial stress (7 to 10 MPa) are accompanied by high values of radial stress (20 to 30 MPa). The most probable cause of this anomalous zone of reduced velocity difference is slippage along the fracture plane. Such slippage would grind the fracture, so improving the contact between the two sides in terms of the surface area touching. Evidence of this grinding shear action was present after the test had been conducted, with some fine powdered debris present within the fracture.

4.5.1.2 Sample 2

On inspection after failure sample 2 was found to be only mildly fractured. A number of vertical macrofractures ran down the core parallel to the core axis, but the sample remained intact after removal of the plastic sheath. A complete set of contour plots describing the stress-induced velocity anisotropy are shown in figure 4.17 (a) to (d). Figure 4.17 (a) and (b) shows the stress-induced velocity change for the sample before and after failure. Figures 4.17 (c) and (d) show the two plots subtracted in terms of actual and percentage velocity change respectively.

The dominantly vertical nature of the contour lines in figures 4.17 (a) and (b) show that any stress induced velocity anisotropy is predominantly controlled by changing axial stress. The velocities range from 5588 to 6145 m/s and 4368 to 5116 m/s for the intact and fractured cases respectively over an axial stress increase of 26 MPa. These figures equate to percentage increases of 0.35% and 0.56% in velocity per MPa of increase in axial stress. The higher percentage value for the intact case, compared to sample 1, suggests that this rock type is intrinsically more anisotropic than sample 1, most probably due to a higher density of microcracks. The difference between

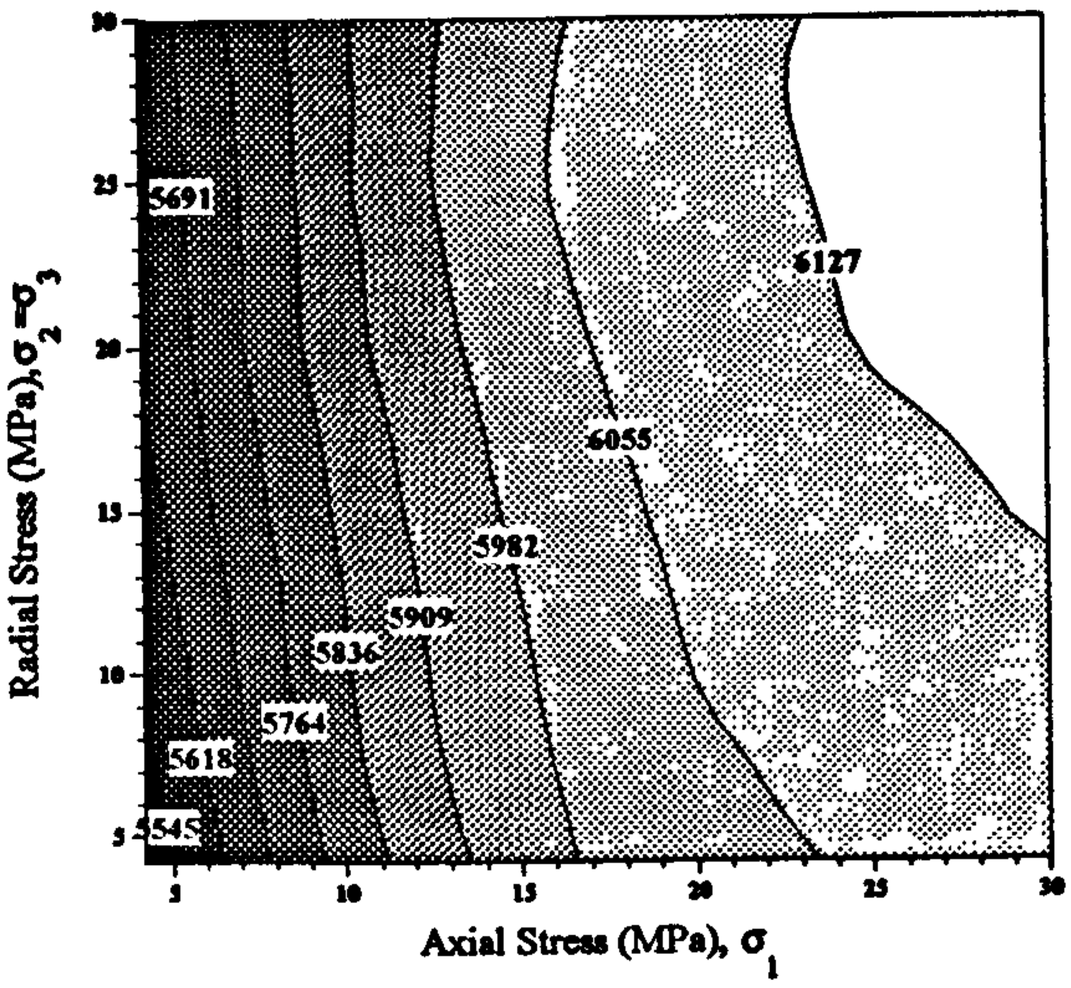

(a)

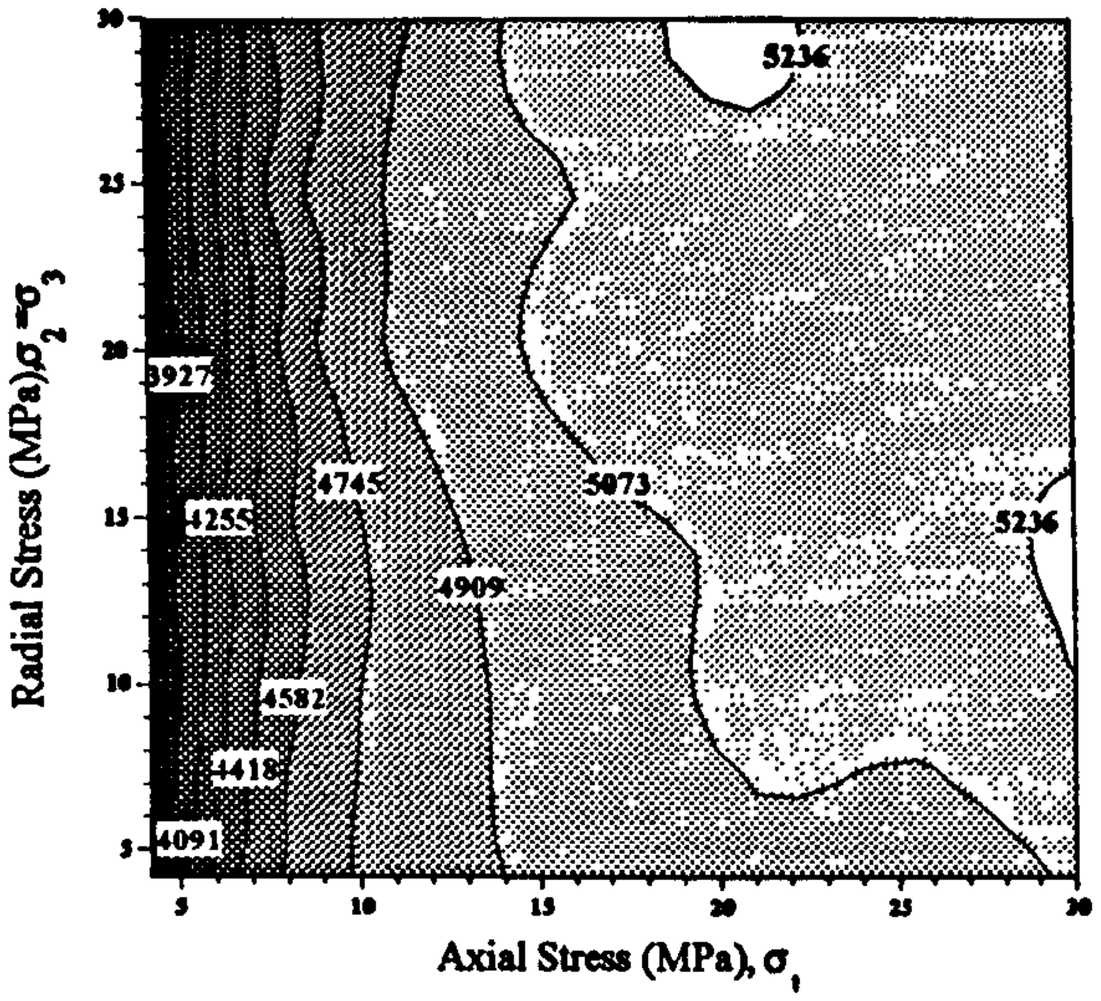

(b)

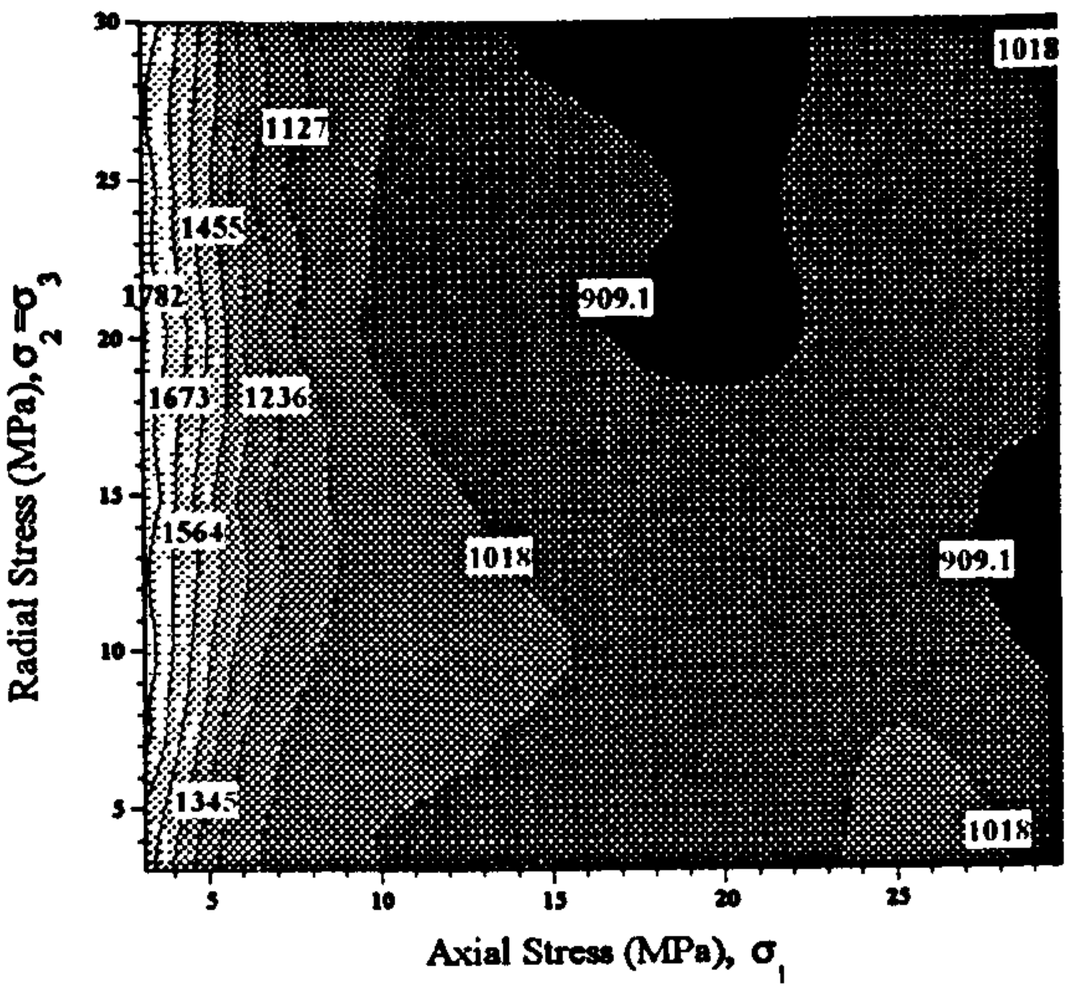

(c)

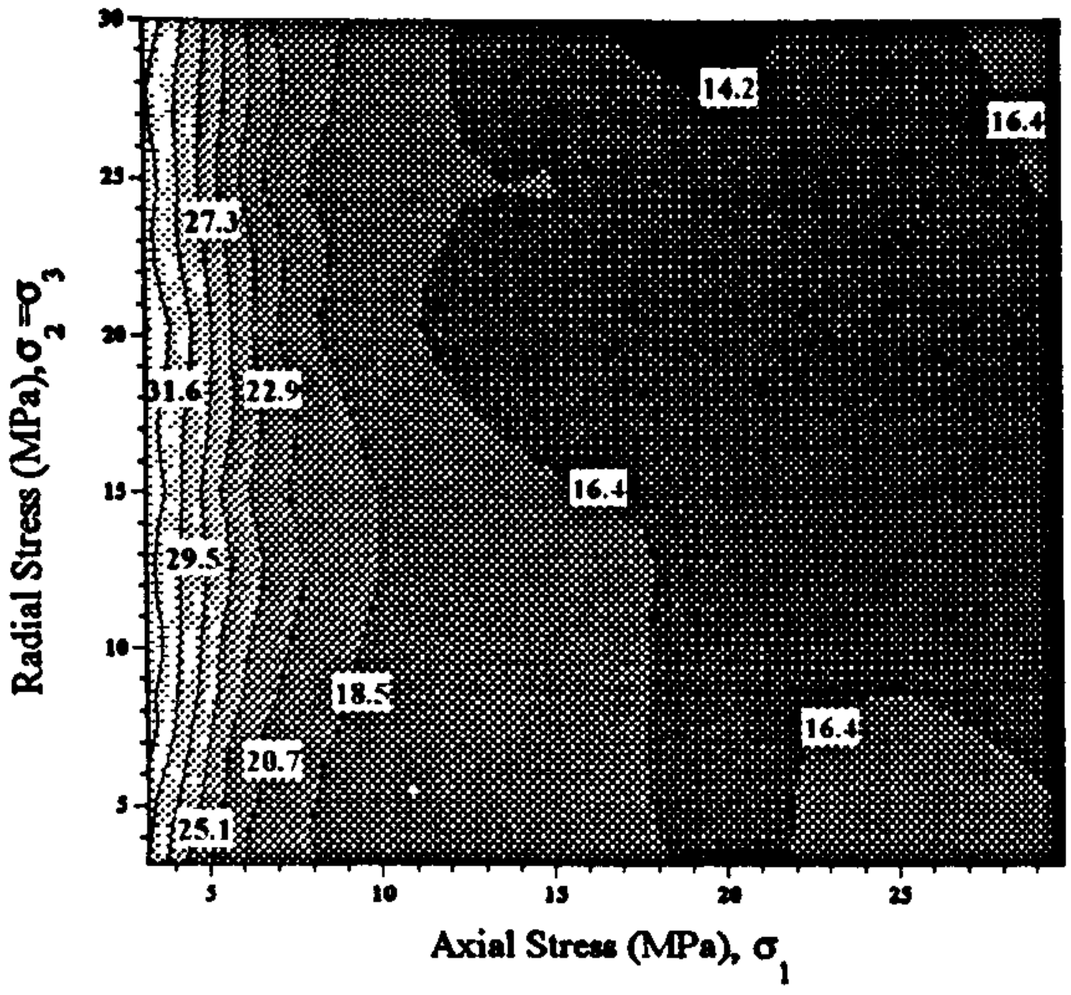

(d)

FIGURE 4.17 Stress-induced velocity anisotropy contour plots for sample 2 with mild fracturing (a) Intact sample (b) Fractured sample (c) Velocity change between (a) and (b) (d) Percentage velocity change between (a) and (b). Velocities are all expressed in m/s.

the two figures for intact and fractured cases for sample 2 shows that a large change has occurred in the anisotropic characteristics of the failed sample. This can be checked by looking at the plots in figure 4.17 (c) and (d). Above an axial stress of 10 MPa, the change in velocity remains constant at 16.4% below the intact state, a change amounting to between 900 and 1000 m/s. However, below 10 MPa the velocity difference changes rapidly from between 18.5% to 31.6% of the original intact values, a change amounting to between 1000 and 1780 m/s. These results are a reflection of the fractured state of the sample. The large reduction in velocity from the intact sample below 10 MPa is most likely due to the macrofractures within the sample. The dilation of these fractures at low stress levels has caused velocity differences of up to 31.6%. However, the onset of higher stress levels rapidly closes these large fractures, improving the transmission characteristics and rapidly reducing velocity differences. The sample has, of course, been irreparably damaged with the growth of existing and the introduction of new microfractures (see section 4.4) and the reduction in velocity at higher stress levels is a reflection of this increased microfracture density.

4.5.1.3 Sample 3

On inspection after failure sample 3 was found to be intensely fractured throughout the core cylinder. The sample had failed with a classic diagonal fracture across the sample and a number of smaller associated fractures running parallel along the core axis. A complete set of contour plots describing the stress-induced velocity anisotropy is shown in figure 4.18 (a) to (d). Figures 4.18 (a) and (b) show the stress-induced velocity change for the sample before and after failure. Figures 4.18 (c) and (d) show the two plots subtracted in terms of actual and percentage velocity change respectively.

As in the other cases the stress-induced velocity anisotropy is predominately influenced by the changing axial stress component. The velocities range from 6258 to 6349 m/s and 4003 to 5265 m/s for the intact and fractured samples respectively over an axial stress increase of 26 MPa. These range values equate to an increase of 0.06% and 0.92% in velocity per MPa increase in axial stress for the intact and fractured case respectively. The low value in the intact case indicates that the sample has very low intrinsic stress-induced anisotropic properties, such as microcrack density or porosity. Of the three samples, this has the largest change between the intact and fractured state. This is due to the complete failure of the sample and is reflected in the velocity real and percentage difference plots in figures 4.18 (c) and (d). Below 10 MPa axial stress, as with sample 2, there is a rapid change in the reduction in velocity between the intact and fractured sample state, with macrofractures causing up to 42% difference in

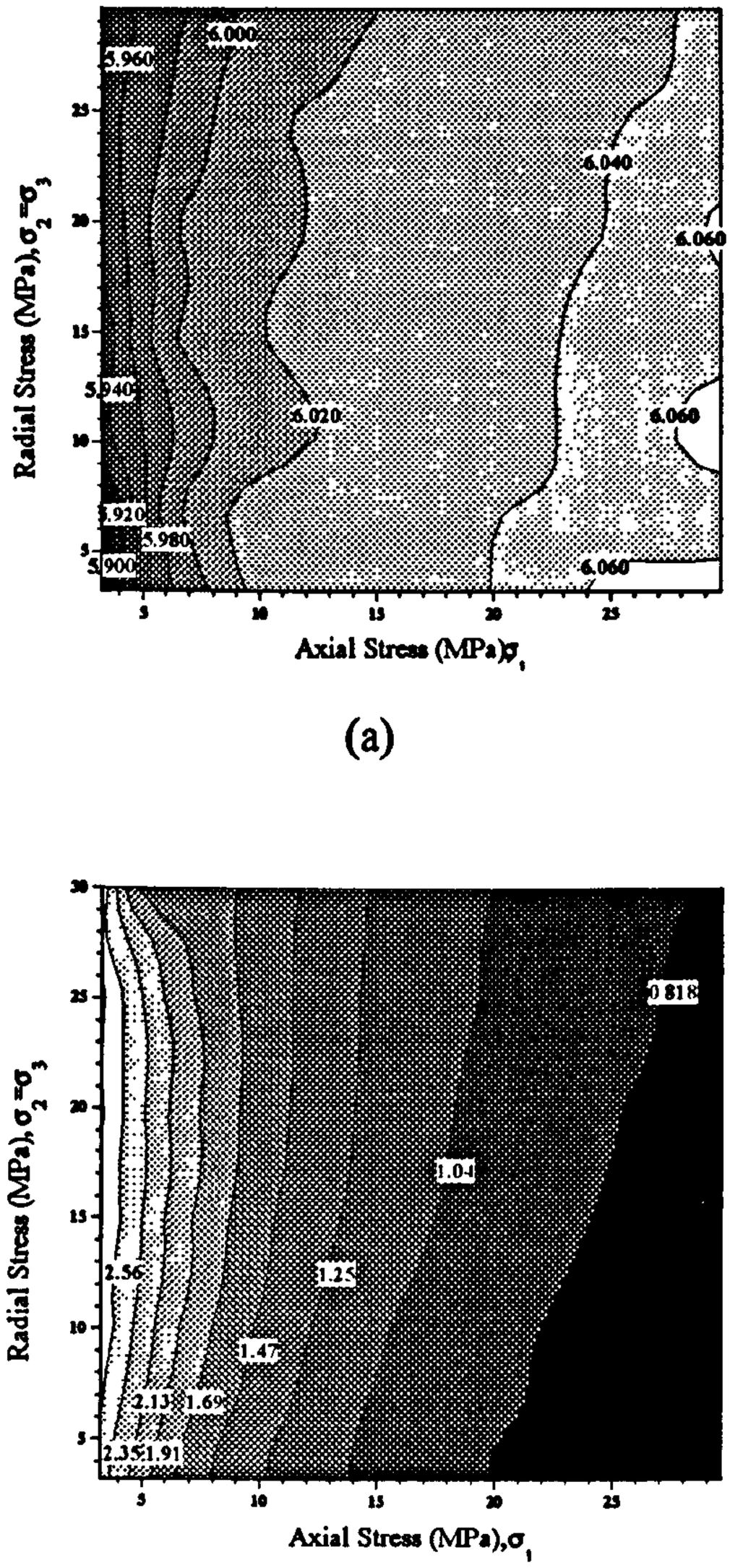

FIGURE 4.18 Stress-induced velocity anisotropy contour plots for sample 3 with intense fracturing (a) Intact sample (b) Fractured sample (c) Velocity change between (a) and (b) (d) Percentage velocity change between (a) and (b). Velocities are all expressed in km/s.

velocities at low stress levels. However, unlike sample 2, these difference changes extend beyond an axial stress of 10 MPa due to the intense fracturing and extensive damage within the sample. The rate of change of velocity difference decreases above the 10 MPa axial stress boundary which implies that most of the larger cracks have already been closed.

4.5.2 Q (18 - 49 kHz)

4.5.2.1 Sample 1

Figure 4.19 (a) and (b) shows stress-induced Q anisotropy contour plots for the intact and fractured sample 1.

The vertical contours in plot (a) show that Q measured in the intact sample is mostly only affected by a change in axial stress. Q values range from 21 to 47 across a 13 MPa increase in axial stress and this corresponds to a percentage Q change of 4.26% per MPa increase. After failure of the sample by a single fracture normal to the direction of wave propagation the contour plot in figure 4.19 (b) is completely changed. Q values now range from 8.2 to 34 across the same axial stress range which equates to a percentage increase 5.84% in Q per MPa increase in axial stress. As with the previous Q plot examples, a high Q ridge appears across the plot, corresponding to conditions of hydrostatic stress. Away from these hydrostatic conditions (above and below the ridge) Q values are lower due to the effect of the unbalanced stress regime on the single fracture. For instance a low Q anomaly occurs at one of the extremes of the experimental dataset for axial stress of 7MPa and radial stress of 30 MPa. The reduction in Q at this point could be due to one of two things, either dilation of the crack by the large radial stress component, or damage to the fracture caused by shear, again due to the large radial stress component.

The Q difference plots in Figure 4.19 (c) and (d) reveal the changes in the attenuation anisotropy characteristics of the sample after the single fracture. A trough runs across both of the plots at conditions parallel to, but above hydrostatic stress where a minimum change in Q occurs between the intact and fractured sample. What is more, this trough has an almost constant value across the entire dataset. This indicates that at these stress conditions, where the ratio of radial to axial stress is around 1.5 : 1, the single fracture has not altered the anisotropic characteristics of the sample, but the constant reduction in Q between the intact and fractured sample is solely due to the loss of seismic energy across the fracture. Below these stress conditions (below the ridge) the Q difference increases with decreasing radial stress. This shows that

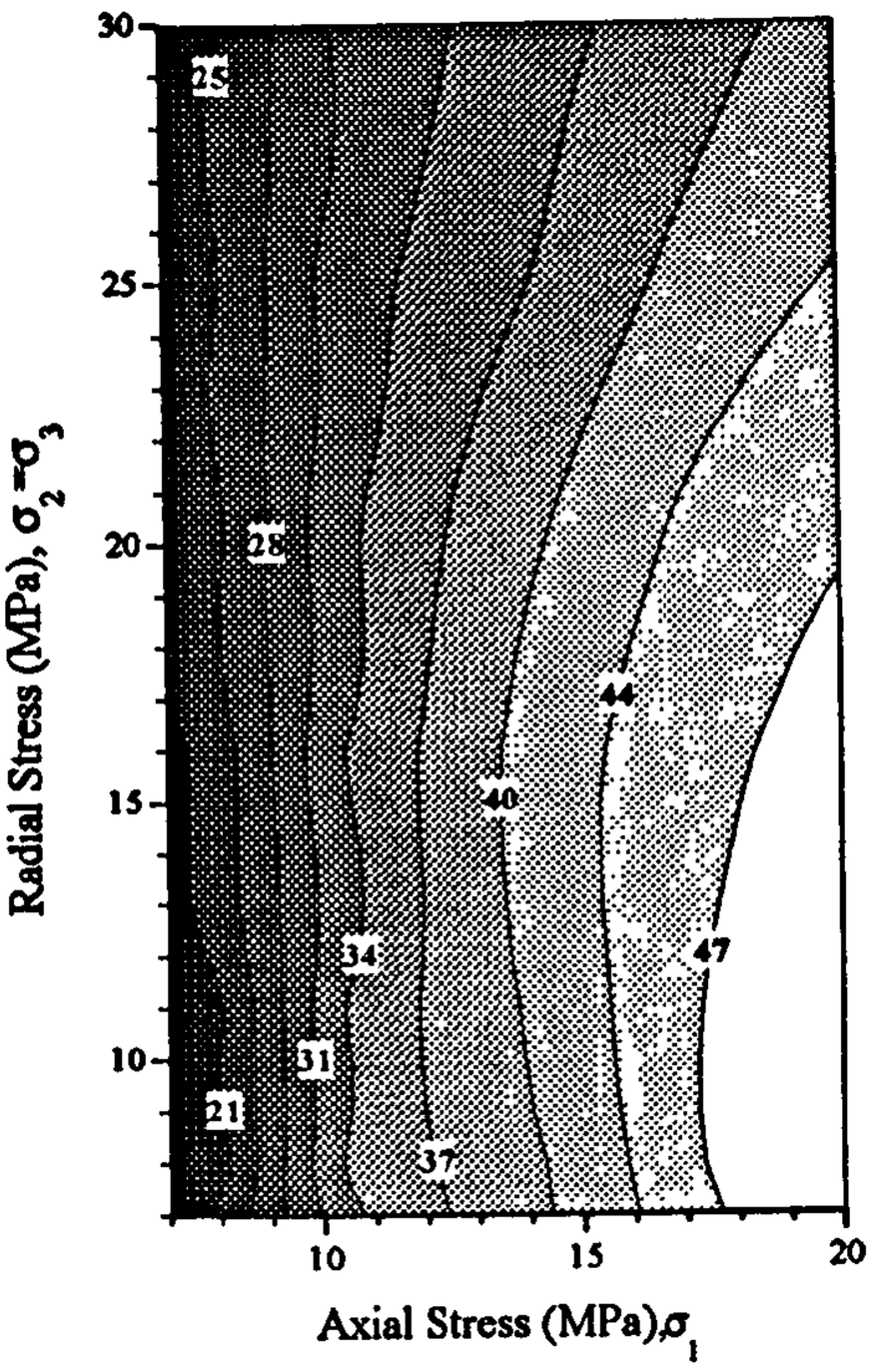

(a)

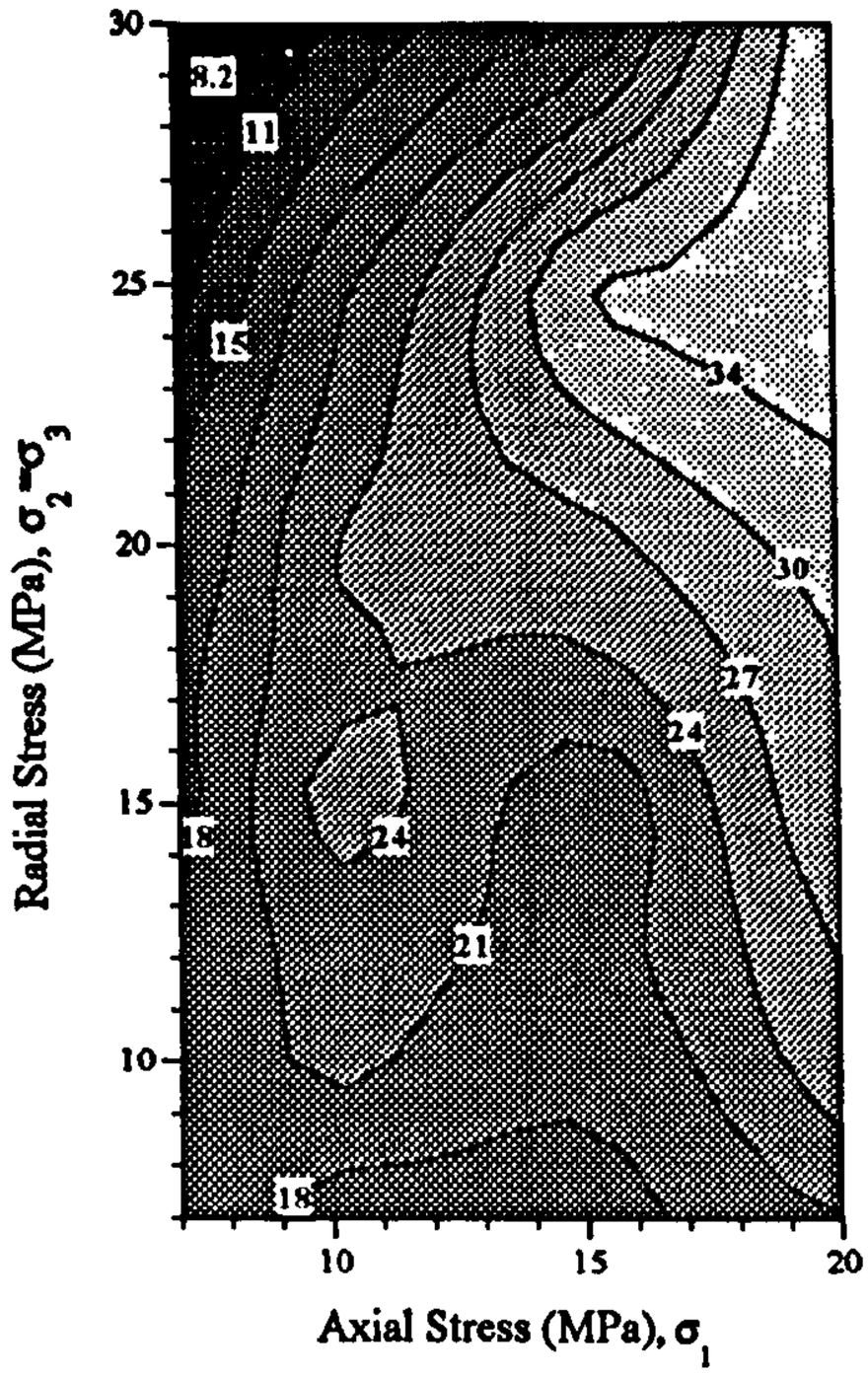

(b)

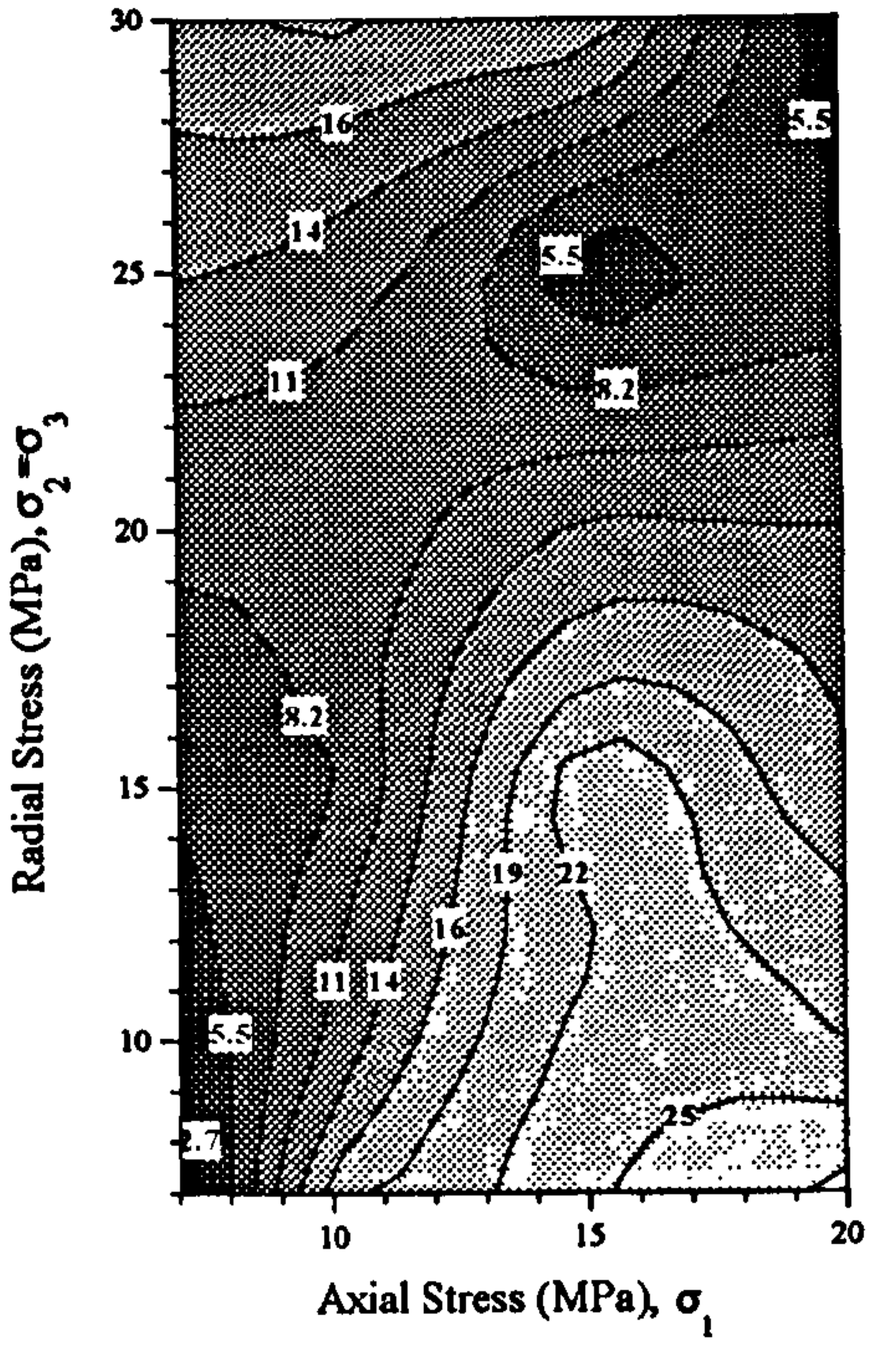

(c)

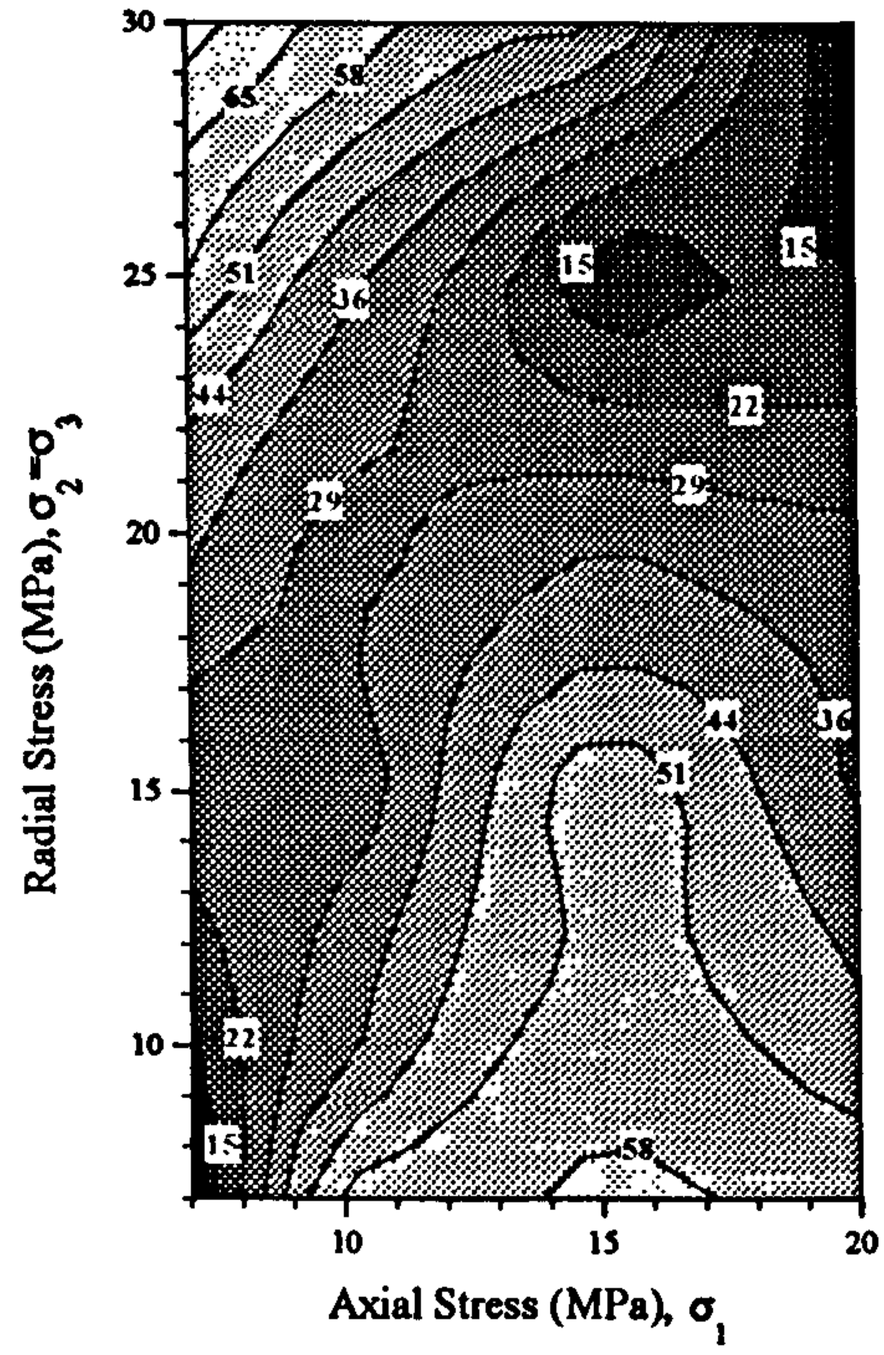

(d)

FIGURE 4.19 Stress-induced attenuation anisotropy contour plots for sample 1 with a single macrofracture (a) Intact sample (b) Fractured sample (c) Q change between (a) and (b) (d) Percentage Q change between (a) and (b). Q is the dimensionless quality factor.

increasing radial stress up to this 1.5 : 1 axial stress ratio condition helps to consolidate the single fracture and improve seismic energy transmission. Above the ridge, the opposite effect occurs and an increase in radial stress reduces the consolidation of the two sides of the fracture (most probably by dilation or shear) so degrading the transmission of seismic energy.

4.5.2.2 Sample 2

Figure 4.20 (a) and (b) shows the stress induced Q anisotropy contour plots for the intact and mildly fractured sample 2. The vertical nature of the contours below 20 MPa axial stress in plot (a) shows a stress-induced Q dependency based purely on the change in axial stress below this level. Above 20 MPa, changing radial stress has the greatest influence over Q. After mild fracturing the plot in (b) has radically changed from its intact counterpart. Q ranges from 35 to 85 and 13 to 23 in the intact and fractured plots respectively over an axial increase of 23 MPa. These ranges equate to a percentage change of 2.56% and 1.89% in Q per MPa increase in axial stress for the intact and fractured case respectively.

The fractured sample plot (b) has the characteristic ridge feature spanning the conditions of hydrostatic stress. However, the amplitude of the ridge is much less pronounced than is the case in sample 1, especially at higher hydrostatic stress levels where it forms a constant Q plateau spanning into areas of non hydrostatic stress. Q rapidly increases from 7 to 10 MPa axial stress, as was observed in the velocity plots for the same sample. The most probable cause for this rapid increase, which does not occur in the intact case, is the closing of macrofractures within the sample.

The aforementioned plateau is revealed in the Q difference plots (c) and (d) above 20 MPa axial stress where the change in Q between the intact and fractured states remains at a constant level of around 70-75%. By this stage, macrocracks will have been mostly closed within the sample and the lower value of Q in the fractured case results from the permanent damage that the sample has suffered during failure.

4.5.2.3 Sample 3

Figure 4.21 (a) and (b) shows the stress-induced Q anisotropy contour plots for the intact and intensely fractured sample 3. In plot (a), below 15 MPa axial stress, the vertical contours show that the sample displays stress-induced Q anisotropy based purely on the change in axial stress. Above 15 MPa, radial stress gains some influence over Q anisotropy. After intense fracturing the situation is somewhat

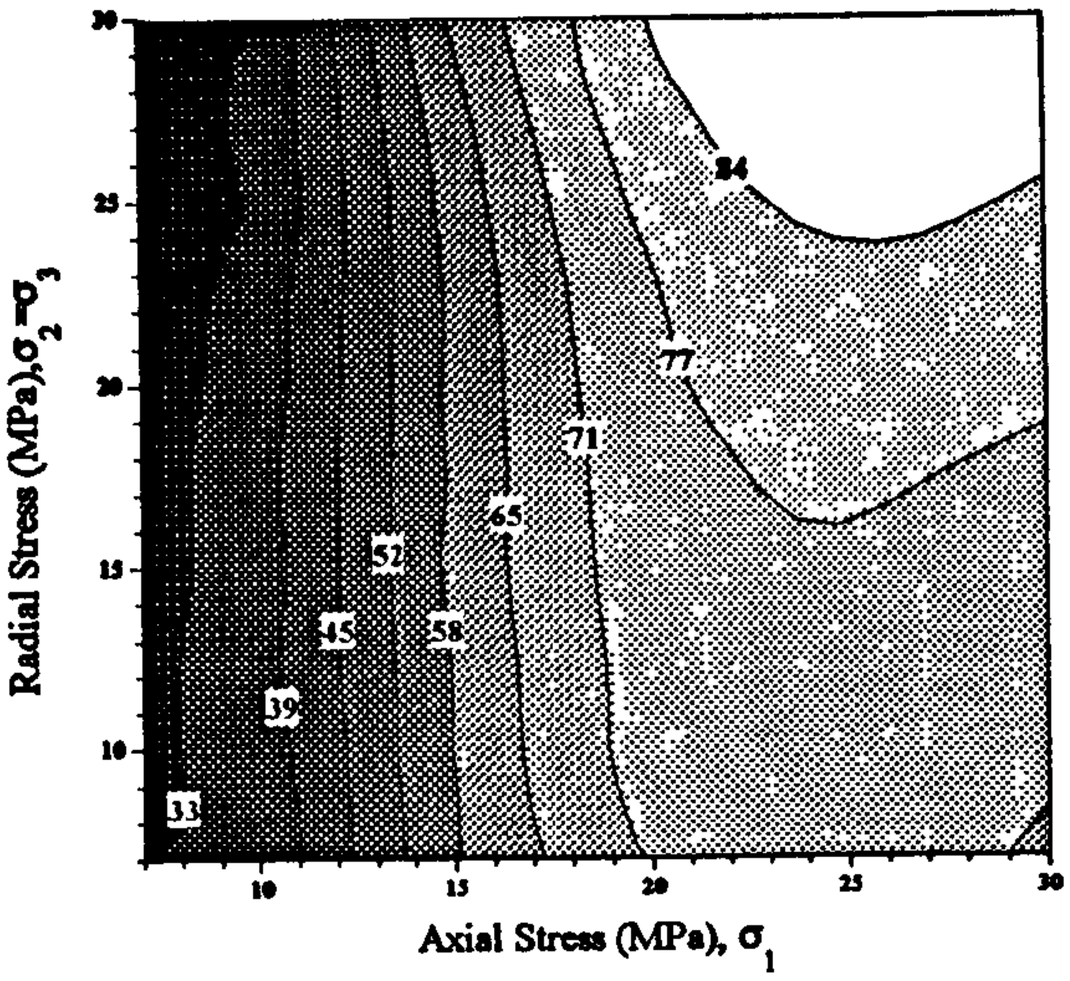

(a)

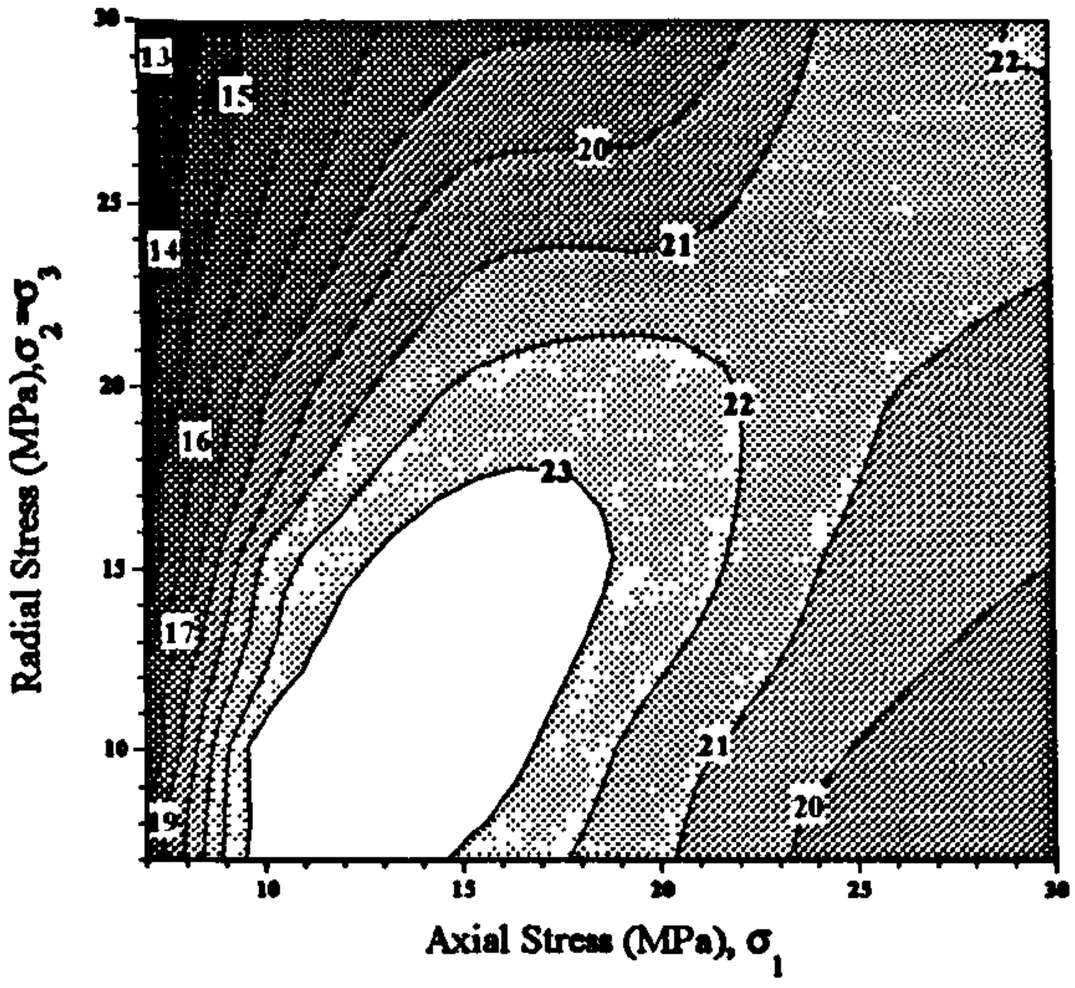

(b)

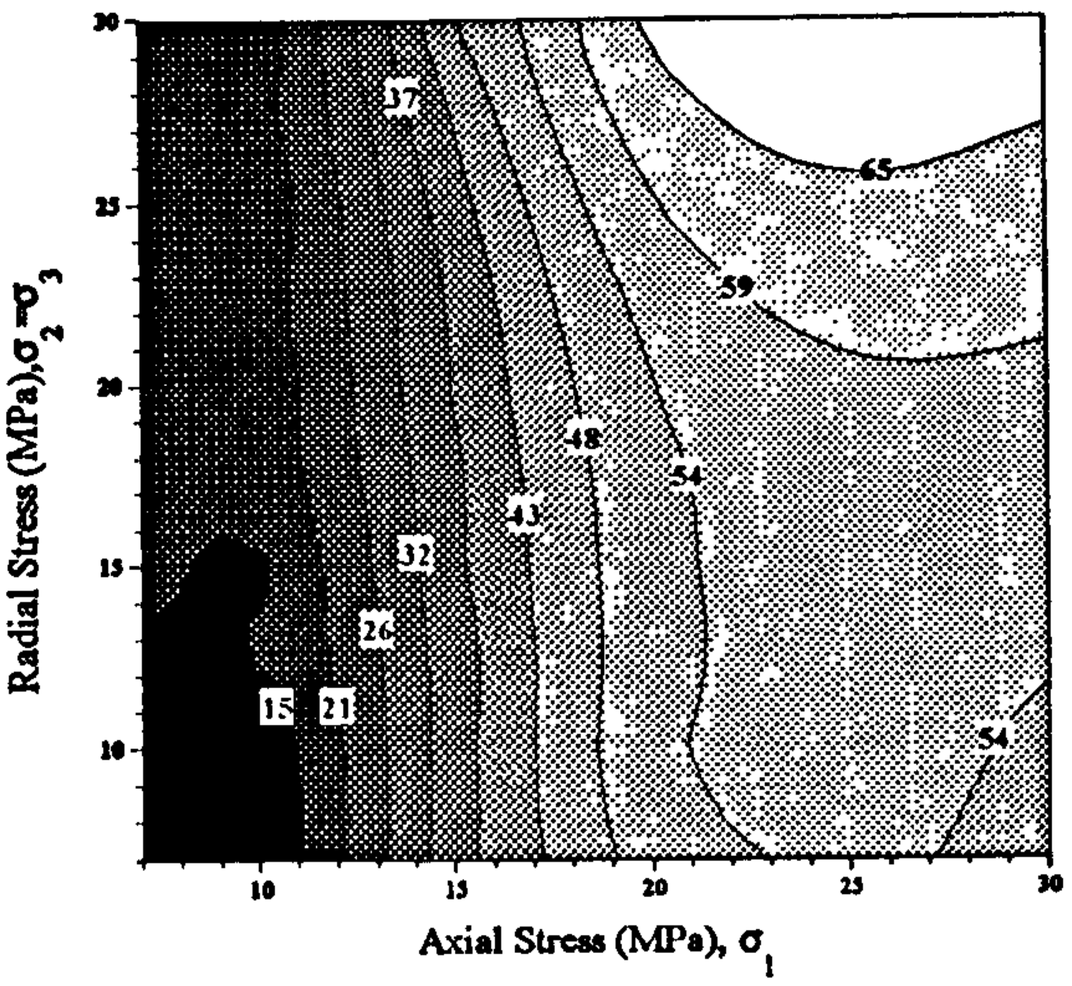

(c)

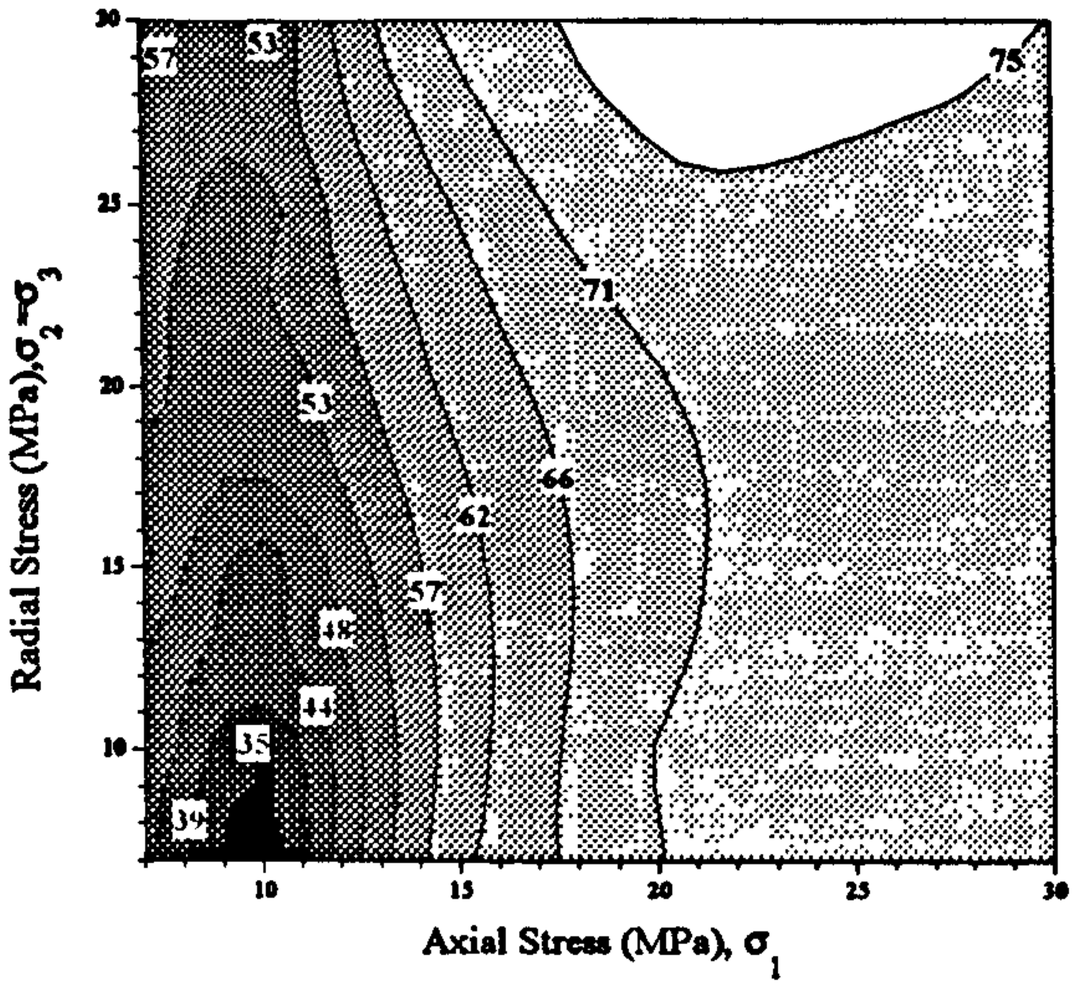

(d)

FIGURE 4.20 Stress-induced attenuation anisotropy contour plots for sample 2 with mild fracturing (a) Intact sample (b) Fractured sample (c) Q change between (a) and (b) (d) Percentage Q change between (a) and (b). Q is the dimensionless quality factor.

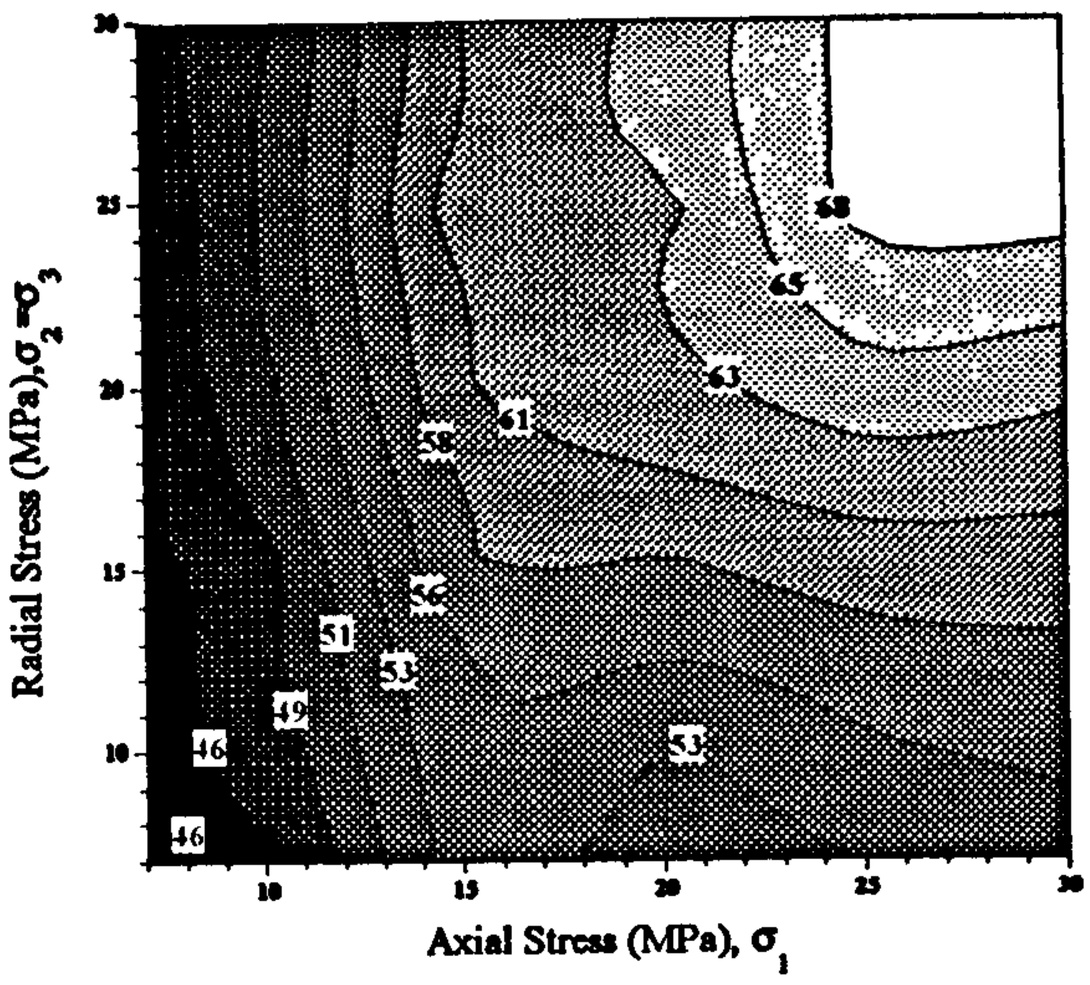

(a)

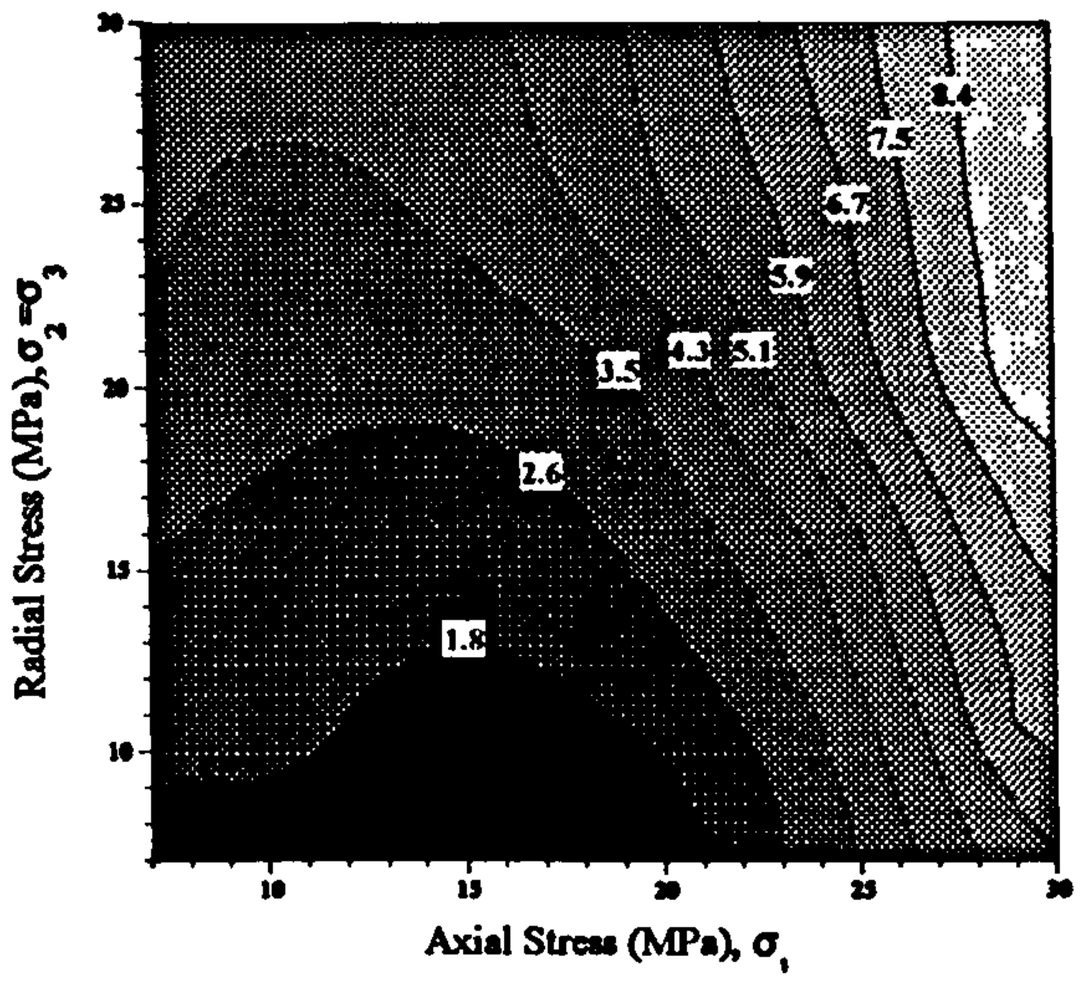

(b)

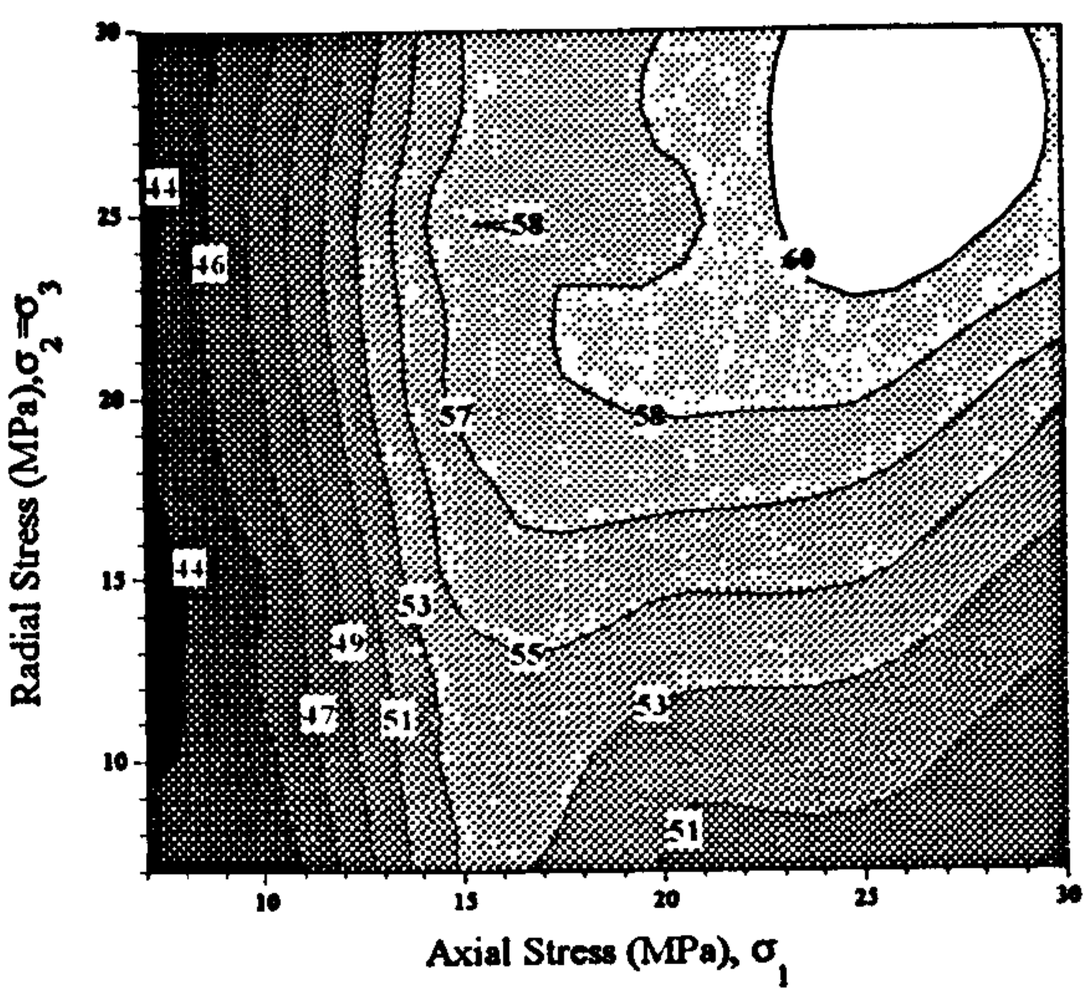

(c)

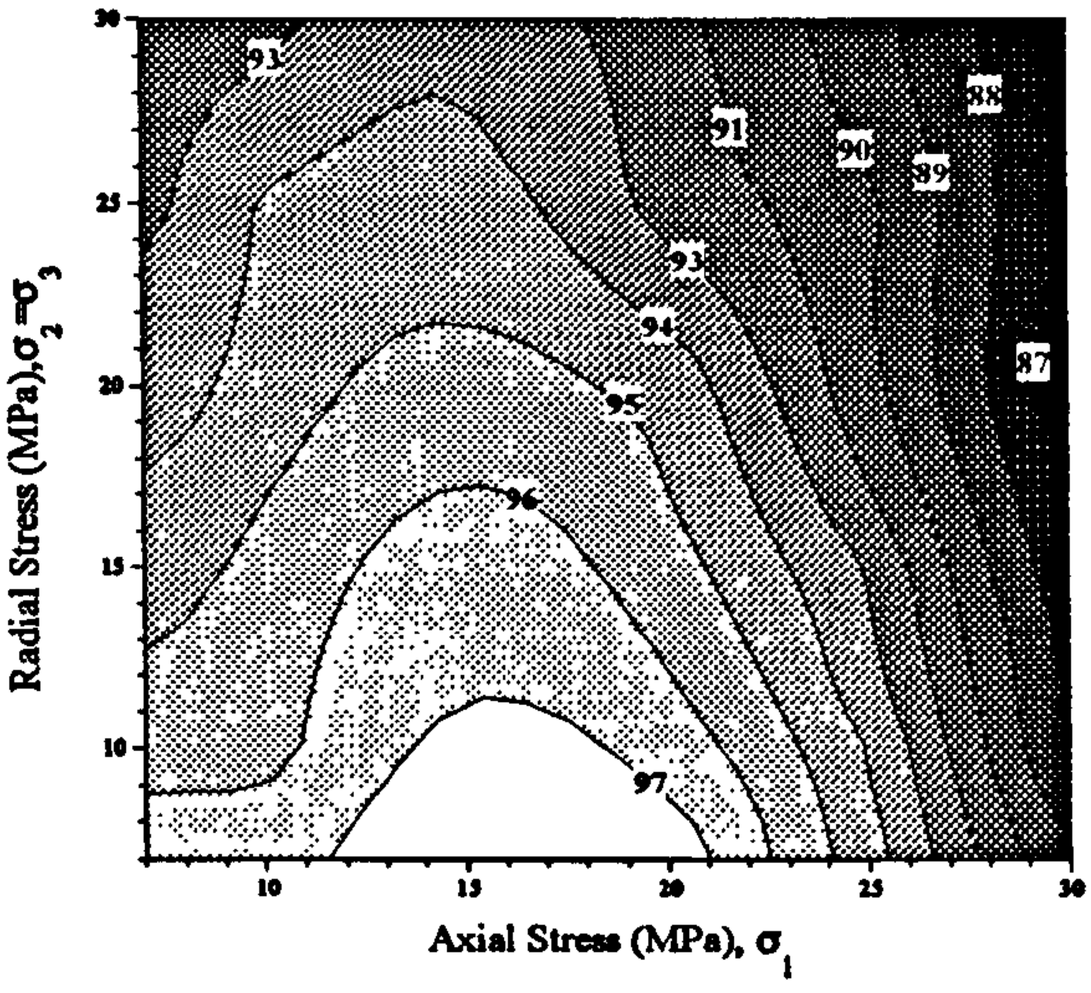

(d)

FIGURE 4.21 Stress-induced attenuation anisotropy contour plots for sample 3 with intense fracturing (a) Intact sample (b) Fractured sample (c) Q change between (a) and (b) (d) Percentage Q change between (a) and (b). Q is the dimensionless quality factor.

reversed. Radial stress is the dominant influence in stress-induced Q anisotropy below axial stress values of 20 MPa. Q values are very low in this region which is a reflection of the complete failure damage. The diagram of sample 3 in figure 4.15 shows a major diagonal fracture plane across the core cylinder. The presence of this fracture provides a good explanation for the influence of radial stress in figure 4.21(b), where the onset of this stress closes the fracture plane and improves seismic energy transmission. Above 20 MPa hydrostatic stress Q starts to increase showing that the major fracture has closed. However, the final Q value of 8.4 at a hydrostatic stress of 30 MPa shows that the sample is permanently, severely damaged.

Q ranges from 46 to 68 and 1.8 to 8.4 in the intact and fractured cases respectively across an axial stress increase of 23 MPa. These ranges equate to percentage increases of 1.41% and 3.42% per MPa increase in axial stress.

The percentage Q difference plot in figure 4.21 (d) shows that the largest percentage difference between the intact and fractured case occur at low axial and radial stress levels (less than 20 MPa in both components) presumably due to the large number of macrofractures within the fractured sample. Above this level, the differences reduce quickly as these macrofractures close and the transmission properties of the sample improve. This sample improvement at higher stress levels is indicated by the plateau region in figure 4.21(c) where Q values remain consistently lower than the intact case by about 58 to 60. This region, as in sample 2, indicates that macrofractures have closed.

4.5.3 Comparison and Discussion

The prime aim of this comparison between measurements of velocity and attenuation is to attempt to discover the suitability of the field measurement of absolute P-wave velocity or attenuation, and the same measurements conducted over a time period, to define the static or changing conditions within a rock mass.

4.5.3.1 Quantitatively defining stress-induced anisotropy

Table 4.3 compares the statistics that have already been quoted in the previous sections. The new parameter used here is the percentage of increase in either velocity or attenuation per MPa of increase in axial stress (or MPa of increase in stress in the direction of wave propagation), referred to from here as %V and %Q for velocity and attenuation respectively. Subscripts i and f denote intact and fractured cases respectively. This parameter can be used to quantitatively define the level of stress-

Sample	Velocity			Q		
	Intact $\%V_i$	Fractured $\%V_f$	Change %	Intact $\%Q_i$	Fractured $\%Q_f$	Change %
1	0.24	0.22	-0.02	4.26	5.84	1.58
2	0.35	0.56	0.21	2.56	1.89	-0.67
3	0.06	0.92	0.86	1.46	3.42	1.96

TABLE 4.3 Comparison between velocity and Q anisotropic characteristics of samples 1, 2 and 3 in the intact and fractured states. %V refers to the percentage increase in velocity per MegaPascal increase in stress in the direction of propagation. %Q is the percentage increase in Q for the same stress increase. Subscripts i and f denote intact and fractured cases respectively.

Sample	Velocity at 15 MPa Hydr Stress				Q at 15 MPa Hydr. Stress			
	Intact km/s	Fract. km/s	Change km/s	% Change	Intact	Fract.	Change	% Change
1	5.605	5.460	-0.146	-2.59	41	20	-21	-51.21
2	5.982	4.991	-0.991	-16.57	58	23	-35	-60.34
3	6.020	4.900	-1.120	-18.60	56	2.2	-53.8	-96.07

TABLE 4.4 Comparison between absolute velocity and attenuation values at 15 MPa hydrostatic stress.

Rock Type	$\%V_i$ (%/MPa)	Figure	$\%Q_i$ (%/MPa)	Figure
Coarse Sandstone	0.52	5.8 (a)	5.65	5.10 (a)
Fine Sandstone	0.47	5.8 (b)	3.84	5.10 (b)
Fine Siltstone	0.15	5.8 (c)	5.04	5.10 (c)

TABLE 4.5 Values of $\%V_i$ and $\%Q_i$ for other rock types in this study and the corresponding plot numbers.

induced anisotropy displayed by a sample and can be calculated for each case, therefore allowing comparison between each of the samples and their intact or fractured states.

In the intact case, the parameter is a measure of the internal properties of each sample. Already, this chapter and chapter 2 have described the intrinsic processes of stress-induced microcrack closure that increase the bulk modulus of the sample and hence increase the velocity and reduce attenuation. Therefore, an intact sample with a high value of $\%V_i$ or $\%Q_i$ must contain a higher density of microcracks compared to an intact sample with displays a low value of $\%V_i$ or $\%Q_i$. Alternatively, the intact sample with a high value of $\%V_i$ or $\%Q_i$ may contain a high density of aligned microcracks (bought about by diagenesis conditions or an ensuing tectonic stress regime) which is particularly sensitive to increasing stress in one direction.

In the fractured state, the parameter is a measure of the combined effect of the intrinsic sample properties, the degree of fracturing within the sample and the change induced by failure. A high value of $\%V_f$ or $\%Q_f$ within the fractured sample, or a large change between the intact and measured values would signify extensive damage within the sample.

4.5.3.2 Comparison of %V and %Q

From table 4.3, the following points are apparent,

- For the three samples, the values of $\%V_i$ show that sample 2 has the greatest intrinsic microcrack density, followed by sample 1 and then sample 3. The same trend is not observed with $\%Q_i$, which reverses the order of sample 1 and 2. The values of $\%Q_i$ are between 7 to 24 times larger than $\%V_i$, showing that Q is, on average, 16 times more sensitive to changes in stress in the direction of wave propagation.
- In sample 1, $\%V_f$ does not significantly change from $\%V_i$ after failure by a single fracture. However, $\%Q_f$ increases by 1.58%/MPa from the intact value, showing the sensitivity of Q to the presence of a single macrofracture.
- As fracturing becomes progressively more intense from sample 1 through to 3, $\%V_f$ becomes larger, and the change between $\%V_i$ and $\%V_f$ also increases.
- The increase in the intensity of fracturing from sample 1 to 3 increases $\%Q_f$ from the intact value with the exception of sample 2, which shows a decrease. The change between $\%Q_i$ and $\%Q_f$ for samples 1 and 3 is at least 2.5 times larger than the corresponding change in %V between the intact and fractured states. The decrease in $\%Q_f$ for sample 2 from the intact state can be explained

from figure 4.20 (b). The pattern of macrofractures within this sample causes the high Q plateau at axial stress levels above 13 MPa. The value of $\%Q_f$ calculated for the Q change below this level is 4.35%/MPa which equates to a positive change between $\%Q_i$ and $\%Q_f$ of 1.79%/MPa.

4.5.3.3 Comparison of Velocity and Q at 15 MPa Hydrostatic Stress

To compare the absolute change in velocity and attenuation between the intact and fractured cases, table 4.4 considers absolute values at 15 MPa hydrostatic stress. The following points can be raised,

- After failure by a single fracture in sample 1 velocity changes by 2.59% whereas Q changes by 51.21%. Therefore Q is 19 times more sensitive to the presence of the single macrofracture.
- After failure by mild vertical macrofracturing in sample 2 the velocity is reduced by 16.57%. Conversely, after failure by intense fracturing in sample 3 the velocity is changed by 18.60%. The relative changes in Q for the samples 2 and 3 after fracturing are 60.34% and 96.07% respectively. Therefore Q is 3 and 5 times more sensitive than velocity in detecting the fracture state in samples 2 and 3 respectively. The velocity changes are large and therefore easy to measure. Q values change even more dramatically and therefore provide conclusive proof of sample damage.

4.5.3.4 Discussion

The laboratory results in the previous section give an insight into the potential of velocity and attenuation field measurements for the characterisation of a rock mass. The results positively show that for all samples, whether intact or fractured, attenuation is the most sensitive indicator of changes in stress in the direction of wave propagation. Measurements of attenuation are also sensitive to changes in stress components away from the direction of wave propagation even in rocks that have small values of $\%Q_i$. Both velocity and attenuation become more sensitive to stress change in the direction of wave propagation after fracturing due to an increased density of microfractures and the creation of macrofractures.

Both velocity and attenuation change when a rock mass is fractured. This fracturing process may be due to,

- a combination of stress concentration and relief, or cyclic loading caused by, for example, repeated advancement of an excavation (Martin & Read, 1992).

- blast induced damage which may extend considerably into the sidewall of the excavation (Pusch & Stanfors, 1992).
- forced fracture by blasting to produce extensive damage which induces an extractable mineral to cave in a production stope.
- extreme stress concentration in deep underground excavations which results in elastic energy release by a microseismic event or 'rockburst' causing localised failure.
- pre-existing infilled faults or fractures that become reactivated by changes in the in-situ stress regime

Therefore these laboratory results and the figures quoted in table 4.4 show that repeated field re-measurement and monitoring of velocity and attenuation over a period of time can indicate where fracture damage has occurred. In particular, the results show that attenuation is more sensitive to mild fracturing (this confirms the findings of section 4.4 which showed that measurements of Q detected microcrack development before velocity in samples loaded to failure) or to the presence of single fractures such as faults or joint sets. Therefore, where a large change in attenuation (around 50% in the case of limestone) is accompanied by no apparent change in velocity this could be an indicator of single fractures or faults as well as a warning precursor of imminent rock mass failure for data which has been collected over a time period (see section 4.4). For more intense fracturing, the velocity changes are much larger (15% to 20% for limestone) and therefore easier to detect, and given the increased difficulty of measuring attenuation in-situ, velocity measurements should provide an adequate indicator of these circumstances. Large velocity changes of this kind would of course be accompanied by even larger relative attenuation changes which would give further proof that intensive fracturing has occurred.

Away from the detection of fractures or rock mass damage, the sample contour plots and the parameters calculated in table 4.3 could provide a new method for the detection of smaller scale stress changes in an in-situ rock mass. Take the case of an intact homogenous rock mass with a low density of natural faults and fractures. Such a rock mass could be considered to be a series of large blocks which interact with each other. Stress acting on this configuration of blocks will change each block's intrinsic microcrack distribution properties. So apart from the contribution to velocity or attenuation change from the effect of stress on these single, largely spaced fractures, a component of this change will be due to intrinsic stress-induced anisotropy within the individual blocks, $\%V_i$ or $\%Q_i$. The process is summarised by equations 4.1 and 4.2,

$$\%V_f = \%V_i + \%V_{frac} \quad (4.1)$$

$$\%Q_f = \%Q_i + \%Q_{frac} \quad (4.2)$$

where,

$\%V_{frac}$ = the percentage velocity change per MPa increase in stress in the direction of wave propagation which is caused by a single or multiple macrofracture(s).

$\%Q_{frac}$ = the percentage attenuation change per MPa increase in stress in the direction of wave propagation which is caused by a single or multiple macrofracture(s).

Table 4.3 shows that the intrinsic component can be large compared to the component due to the fractures. However the relative size difference between the two parameters decreases as the degree or density of fracturing increases. For example, in the case of sample 1 the $\%V_i$ and $\%V_f$ values do not change significantly within experimental error. This shows that the intrinsic microfracture density and therefore the intrinsic stress-induced anisotropy within the solid parts of the sample remains 100% dominant even after failure by a single fracture. In other words, $\%V_{frac}$ in equation 4.1 is equal to zero. For the same sample $\%Q_f$ increases by 1.58%/MPa from a $\%Q_i$ of 4.26%/MPa, so after fracture the intrinsic microcrack distribution is responsible for 73% of the total $\%Q_f$ and $\%Q_{frac}$ is responsible for the remaining 27%. As the density of fracturing increases, so the 'block' size reduces and the number of fractures increases, thereby increasing the overall influence of $\%Q_{frac}$ within $\%Q_f$. For example in the highly fractured sample 3, $\%V_f$ has changed by 0.86%/MPa from the intact value of 0.06%/MPa showing that the $\%V_{frac}$ component contributes 93% to the overall value of $\%V_f$ and the intrinsic component only provides the remaining 7%. Similarly with %Q values in the same sample, $\%Q_f$ changes by 1.96%/MPa from the intact value, indicating that $\%Q_{frac}$ component in equation 4.2 influences 57% of the overall value of $\%Q_f$ with the remaining 43% influence coming from the intrinsic microcrack distribution.

In terms of monitoring stress change in-situ within a rock mass by using repeated seismic measurements of velocity and attenuation along identical raypaths the following can be postulated from the fracture sample experiments and the ensuing discussion,

- For a homogeneous rock mass with widely spaced, isolated fractures compared to the size of the survey area under consideration, stress change in the direction of wave propagation could be measured by the change in velocity and

approximated by using laboratory determined values of $\%V_i$ for the specific rock type from the following equation,

stress change (MPa) = (velocity change / original velocity) / $\%V_i$ (4.3)

If the original tectonic stress regime is known, then the value of $\%V_i$ could be calculated more accurately, close to the this stress range.

For the limestone samples in this study the values of $\%V_i$ are relatively low. For example a change of 5 MPa in axial stress in the case of the intact sample 1 would only produce a percentage change of 1.2% in velocity. Such a change would be very difficult to detect in-situ and would introduce the need for high sampling rates in data acquisition. Other rock types do however have higher values of $\%V_i$ (see table 4.5) therefore making stress change easier to detect. Only stress changes that produce a velocity change of the order of 2% would be detectable using the current highest sampling rates found on typical seismographs. This velocity difference corresponds to a stress increase of between 3.5 and 10 MPa depending on the value of $\%V_i$ in table 4.5. Alternatively velocity differences can be determined more accurately by using waveform matching processing techniques to measure traveltime differences at a scale less than the sampling rate (Mao & Gubbins, 1995).

Since $\%V_i$ is un-influenced by stress change perpendicular to the direction of wave propagation, by measuring velocity change across many different paths of a rock mass, it should be possible to accurately map a changing stress field in 2 or 3 dimensions. Alternatively, tomographic reconstruction techniques of velocity difference tomograms show the velocity change in 2 and 3 dimensions and therefore could show the direction in which velocity change is occurring, thereby allowing interpretation of the stress field.

- Detecting the magnitude of stress change in the direction of wave propagation using the difference in Q values over a time period is more difficult since this section and section 4.3.4 have already shown that Q can also be altered by changes in stress perpendicular to the axis of propagation, and therefore, presumably, by stress changes at other more oblique angles. However, the previous section has also shown that the sensitivity of Q to stress change is much greater and therefore easier to measure.

For the case of the homogenous 'blocky' rock mass, sample 1 has shown that $\%Q_f$ is affected by the presence of a single isolated fracture. Therefore, to use %Q to predict stress change it is necessary to determine likely values of $\%Q_f$.

Measurement of $\%Q_f$ is not too difficult in the laboratory for a sample with a single fracture. For the limestone sample with a single fracture normal to the direction of wave propagation $\%Q_f$ is 5.84%/MPa. Realistically, in-situ values of Q can only be measured with errors of around 5 to 10% (Blair, 1982), but are not dependent upon the sampling rate (depending on the method used to calculate Q). Therefore, for a rock mass with similar properties to sample 1, a 10% change in Q would equate to a stress change of less than 2 MPa, nearly two to five times the sensitivity of velocity depending on the value of $\%V_i$.

- The other two sample cases do not apply to a homogenous intact rock mass, but might apply to a naturally fractured and fissured zone, such as a shatter zone, an area of localised faulting, or an area associated with tectonic activity, such as localised folds or upthrusts, where stress relief and concentration results in fracture. Equally possible, the other two samples could represent the fractured zone that extends into the sidewall of an excavation, blast induced damage, or fracture damage due to the concentration and quick release of elastic energy. The characteristics of such a rock mass, as with the fractured laboratory samples, are closely spaced fractures, faults or fissures with small intact blocks in between. The fractures will have some alignment dependent upon the direction of principal stress before fracture.

For measurements of velocity and attenuation anisotropy in the fractured samples 2 and 3, the contribution that $\%V_i$ and $\%Q_i$ makes to the overall values of $\%V_f$ and $\%Q_f$ reduces with an increase in the degree or density of fracturing. Therefore, predicting stress change by using values of $\%V_i$ of $\%Q_i$ in these cases would be incorrect. Measuring values of $\%V_f$ or $\%Q_f$ would also be very difficult since a detailed knowledge of the fracture pattern and density in relation to the wave propagation direction would need to be known. This fracture pattern would then need to be created in the lab and stress tested.

The results show that in the case of a fractured rock mass, it would be very difficult to use velocity and attenuation change to predict changes in stress.

4.6 Conclusions

This chapter started with the simple consideration of using velocity and two different measures of attenuation as potential in-situ lithology indicators. Only velocity showed any positive relationship due to density, with some distinction between grain

sizes in lower density rocks. Attenuation coefficient and Quality factor showed a large degree of scatter, with no apparent trends.

The effect of hydrostatic stress on velocity and attenuation was documented and the results compared well with those obtained by other workers.

The phenomenon of stress-induced velocity and attenuation anisotropy was experimentally investigated in intact samples and in general it was found that both velocity and attenuation are sensitive to changes in stress in the direction of wave propagation, whilst only attenuation is sensitive to changes in stress along an axis normal to the wave propagation. Stress-induced attenuation anisotropy was investigated at two different frequency ranges and the same patterns occurred in both cases. This showed that the phenomenon is not dependent on specific high frequency or low frequency attenuation mechanisms, but occurs right across the large frequency spectrum used in this study.

Velocity and Q were measured in triaxialy confined intact samples loaded to failure and three distinct stages were identified. In stage one, velocity increases and attenuation rapidly decreases due to the closure of microcracks. In stage 2 no further change is observed in velocity and attenuation where microcracks have mostly been closed. In stage three, velocity is seen to decrease and attenuation increase as further microcrack extension and sample damage occurs close to failure. In particular, stage 3 was detected first by an increase in attenuation at about 80% of the samples failure strength. The relative amplitude of the change in stage 3 is larger for attenuation than for velocity.

The phenomenon of stress-induced velocity and attenuation anisotropy was again investigated, but this time in a sample with a single fracture, a second sample with mild fracturing and a third sample which had been intensely fractured. A new parameter was introduced for quantifying the degree of anisotropy within a sample in terms of the velocity or attenuation percentage change with one MegaPascal increase in stress in the direction of wave propagation.

Absolute values of velocity and attenuation were found to reduce after a single fracture in sample 1. However, the presence of a single macrofracture did not affect the velocity anisotropic characteristics which suggested that it should be possible to calibrate and measure stress change in-situ in a relatively homogenous rock mass consisting of intact blocks with widely spaced isolated fracture patterns. Absolute values of velocity and attenuation changed in samples 2 and 3 after failure and could be used to give an indication of the degree of fracturing. Stress-induced anisotropy

characteristics were also significantly changed, and it was concluded that it would not be possible to use in-situ measurements of velocity or attenuation change to predict stress change in a highly fractured or faulted rock mass.

CHAPTER 5

5. Seismic Tomography

5.1 Introduction

Up to now, the thesis has been focused on the laboratory determination and analysis of velocity and attenuation for the characterisation of rock properties. This next sequence of chapters considers the field measurement of P-wave velocity and attenuation, starting with a full description of the field technique used in most of the documented tests - combined transmission and reflection traveltime tomography.

The concept of seismic tomography has been briefly introduced in Chapter 1. This chapter will review some examples of the application of tomography, taken from the scientific literature, that have been used to characterise rock masses in civil and mining engineering contexts. The rest of the chapter is devoted to a rigorous stepwise mathematical definition of the tomographic inversion technique used throughout the rest of this work. For the purposes of this section, it is assumed that the reader has a working knowledge of matrix mathematics.

5.2 The Principle

The word tomography is derived from the Greek words 'tomo', meaning 'slice and 'graphia' meaning 'writing' (Lee & Pereyra, 1993). The method uses the principle of the central slice theorem (Lee & Pereyra, 1993 after Radon, 1917), which shows that a 2-D section may be constructed from multiple 1-D line integrals measured experimentally across that section. In effect, this means the reconstruction of the internal properties of an object from a complete angular set of line averages. Equally possible is the combination of 2-D slices to reconstruct a 3-D model of the object. A mathematical discussion of model parameterisation, raytracing and tomographic inversion is given later in the chapter.

5.3 Applications.

The first practical application of tomography was in the medical field of radiology where a beam of X-rays is passed through a part of the human body and an image produced in terms of the linear absorption coefficient of the X-rays. One of the first

applications of this method to the study of Earth structure was carried out by Aki and Lee (1976) to image the variations in crustal and upper mantle velocities using P-wave traveltime data obtained from a number of earthquakes. Since this pioneering work, the field has expanded rapidly in its complexity and improved in its ability to characterise Earth structure not just in terms of seismic velocity but using other parameters such as seismic attenuation, density or resisitivity, to name a few.

Rather than chart the development of this field, this section will look at some applications of tomography with particular bias towards mining and engineering scenarios. A good review of this area is provided by Goulty (1993). In engineering geology, seismic tomography is a natural extension of the recognised use of cross-hole seismic measurements where only single raypath measurements are considered. Tomography better resolves these investigations by providing more complete angular coverage of a rock mass to produce 2-D or 3-D images.

In the field of mineral exploration, Gustavsson et al (1986) reported the successful mapping of a magnetite orebody in the Kiruna Research Mine, Sweden. A section 165m by 50m bounded by two underground galleries and two boreholes revealed the relatively low velocity magnetite ore in the surrounding crystalline country rock. Leung et al (1988) employed cross-hole seismic tomography to discern low velocity features in Devonian carbonate rocks in Western Australia. One anomaly was later proved, by drilling, to be a pod of massive lead-zinc sulphide.

Similarly tomography has been employed in coal exploration, particularly in the estimation of coal reserves in seams which have previously been worked underground, (Goulty et al, 1990), but with limited success due to poor raycoverage sampling of low velocity goaf areas.

Of more interest is the small body of research concerned with attempting to quantify rock mass conditions and potential hazards using tomography. The technique is established in engineering site investigations for structures such as dam foundations, permanent underground installations and underground nuclear waste disposal sites. Of importance in such investigations is the detection of cavities, faults, fractures and other weak zones which could affect the integrity of civil structures. Work by Cottin et al (1986) and Carabelli (1988) proved the usefulness of tomography in the initial investigation and longer term monitoring of Dam sites. Cottin et al (1986) used tomography to estimate the degree of weathering of basalt foundation rock to identify areas where extra work would be required. Carabelli (1988) used tomography as a long term monitoring tool to identify areas of potential structural weakness.

Of key interest to this study is the recent application of tomography to the longer term monitoring and prediction of stress related mining hazards such as mining induced seismicity, rock bursts and stress concentration. One of the first applications of this kind was carried out by Kormendi et al (1986) in an Hungarian coal mine. Tomography was used to monitor velocity change across a 50m longwall section in front of the face, to see if the technique could predict the likelihood of outbursts. The mine was historically prone to seam outbursts due to the presence of a 20m thick rigid limestone layer above the 5 to 7m thick seam. To further compound stress problems the seam contained a number of geological disturbances which impeded natural movement and caused seam 'jamming' resulting in stress concentration. Mining experience had shown that the seam was especially prone to bursting at the start of a new longwall face before settling of the rigid roof, or when the face was restarted after a long standstill. Problems were also experienced when the face approached a fault, gallery or other excavation. Time-lapse tomograms were produced for the area in front of the face for the above cases and clearly show zones of increased velocity moving 15 to 25m ahead of the advancing face caused by the increased stress zone in this area. In one example, sequential plots are shown where the face approaches a throwdown fault and an increased velocity zones appears in the forefield of the face, with a high velocity maximum at the top road behind some small faults throwing down the seam. On the other side of these faults a low velocity zone appears where the seam is thrown upwards. The faults are effectively jamming the seam and a large amount of elastic energy concentrated in a limited volume caused the increased velocity. In another example, a high velocity zone is observed around an existing gallery as the face approaches it. At the velocity maximum, tunnel supports were deformed the day after the measurement and the roadway suffered heavy damage. Kormendi et al (1986) concluded that tomography could effectively monitor the stress conditions of a large area in a quantitative way and aid mine design to minimise the risk of rockbursts.

Maxwell and Young (1994) cite two case studies, the first monitoring velocity change around a circular tunnel 3.5m diameter, at a depth of 420m, the second monitoring a remnant pillar in a seismically active mine. In the first example notches were seen to form in the roof and floor of the tunnel orthogonal to the maximum principal stress. The velocity structure was tomographically imaged using active explosive sources and then some 25,000 seismic events were recorded over a 6 month period and located using the velocity model. These events, regarded as passive seismic sources, were simultaneously inverted for velocity and location and were predominantly clustered around the notch regions. A plot of maximum compressive stress was computed for a cross section plane around the tunnel using a boundary element

program based on information obtained from a suite of extensometers and strain gauges. The final velocity model corresponded well with this stress model in that the high velocity regions present around the notch areas corresponded to the predicted region of high compressive stress. Similarly, the low velocity regions correlated with the aseismic destressed tunnel sides.

In the second case study, Maxwell and Young (1994) tomographically imaged a remnant pillar again using passive source arrival time inversion. The tomogram shows mining induced microseismic events clustered in high velocity regions and low velocity regions remained virtually aseismic. A later magnitude 2.6 microseismic event, which resulted in significant rockburst damage and the ultimate closure of the stope, was found to be located in the region of highest velocity.

Maxwell and Young (1994) point out the implications of these findings for earthquake monitoring and prediction. Traditionally, only microseismic events are monitored, but this research shows that the temporal change in velocity may be just as important. In an area of interest, if the velocities start to increase but the region remains aseismic, this may indicate an increase in stored elastic energy and the increased risk of a larger seismic event. Another application could be the imaging of hydrocarbon reservoirs for temporal change in velocity to monitor and manage the in-situ stress field to optimise oil recovery. Microseismic events are also associated with the recovery processes, for instance at the sites of local fluid injection where drops in pressure induce fractures and tremors. Depression of a reservoir due to fluid extraction and mass unloading of the upper crust causes larger seismic events due to large slips on faults longer distances away from the reservoir.

Friedel et al (1995) applied 3-D tomography to study another remnant ore pillar in Lucky Friday silver mine, Canada. This ore pillar contained two silver bearing ore veins at a depth of 1700m below surface which had been previously extracted and sand backfilled above and below the pillar. A finite element stress model was created for this pillar region and a 3-D tomographic survey carried out between two levels approximately 60m apart, from crosscuts and haulage drifts surrounding the pillar on three sides at the top and the bottom. The model predicted a region of high stress above the backfilled stopes. The interpretation of this was that the backfill could not support any substantial stress, and subsequently it was shed to the adjacent more competent vein. The main feature of the tomograms were low velocity regions around the drifts, indicating stress relief, and high velocities above mined out and backfilled parts of the vein showing stress concentration. This pattern showed good agreement with the stress model. Three anomalously low velocity regions were apparent from the plots

corresponding to an area of fracturing at the intersection of the crosscut with a haulage drift, and at two sites of prior rockburst activity. Friedel et al (1995) discussed the limitation of tomography in that it was not possible to resolve mine structures such as the ore vein or the backfilled stopes. Low velocity structures like these were not well resolved due to the preferential sampling of high velocity features by seismic raypaths. They use an interesting method to attempt to quantify the risk of seismic events or rockbursts by assigning velocity threshold values for high stress regions and fractured regions. The probability that each tomogram cell would exceed one of these thresholds was then computed and the result displayed as a 3-D surface map of constant probability. This computation was based on data extracted from a number of tomograms which were themselves computed from different starting models, assuming a normal distribution. The technique goes some way to reducing the subjectivity of tomogram interpretation and produces more robust results. The probability plots show the high risk areas corresponding to those identified from the stress model.

Friedel et al (1996) applied 2-D seismic refraction tomography to image the sandstone refractor beneath two different coal pillars subjected to varying mining induced stress regimes. Both surveys were simple in nature and temporal velocity change was attributed the stress change occurring within the pillars transmitted to the floor region. The velocity change pattern occurred parallel to the primary coal cleat direction and normal to the advancing face. Regions of velocity change were coincident with localised deterioration of the pillar such as the appearance of cracks and surface spalling of the coal. Friedel et al (1996) concluded that the technique provided a simple qualitative approach for monitoring coal pillar stress conditions on a daily basis. The authors also indicated that with further refinement, it may be possible to obtain quantitative stress estimates. This might be achieved by developing techniques to deal with the uncertainty in the reconstructed tomographic image, i.e. the non-unique solution, and secondly by using a combination of laboratory stress testing on local site rocks and in-situ stress measurements to investigate the kinds of velocity change to be expected with a varying stress regime.

Research into the uses of time-lapse tomography is still in its infancy. The limited amount of work completed so far indicates that there is great potential for a quantitative technique for the non-destructive in-situ assessment of rock mass condition based on seismic velocity or attenuation tomograms. This previous work has highlighted a number of areas which deserve further investigation and some which have not yet been tried. The first of these areas is laboratory work. The velocity change in rock samples in controlled laboratory conditions can greatly increase the understanding of the effects of

a stress regime on a rockmass. Samples need not be intact, but may be subjected to loads to induce fracturing, or failed completely. Both fractured and intact samples may then be subjected to varying triaxial stress regimes and their seismic properties investigated. Tests of this kind will provide detailed information on the percentage velocity change which may be expected to accompany phenomena such as rockmass fracturing, stress concentration or destressing. Equally possible is the monitoring of velocity change across joints or discontinuities which are subjected to a triaxial stress regime. The purpose of this type of experiment would be to provide clues to the likely velocity change that might accompany the dilation, closure or major movement of geological discontinuities.

The second of these areas is the major omission of seismic attenuation measurements from all the cited studies. In the laboratory, attenuation can be measured in all the aforementioned scenarios. By its very nature it is a measurement of the inelastic properties of a rockmass and should therefore be of key interest in monitoring the effects of a varying stress regime on a rockmass. The measurement of attenuation in-situ, although difficult, provides another seismic parameter to improve the interpretation of the more traditional velocity tomogram.

This chapter will now continue with a complete description of the tomographic reconstruction technique used for all field measurements in the rest of this study.

5.4 Tomographic Inversion - a mathematical discussion.

This section will mathematically illustrate the actual procedure used for each of the steps required to define the tomographic iterative process.

The concept of traveltime tomography relies on the traveltime of a given ray, t_{ray}, from source to receiver being the integral of the slowness along that ray. For 2-D model space this integral is as follows:

$$t_{ray} = \int_{ray} s(x,z)dl \qquad (5.1)$$

where,

x and z are the Cartesian co-ordinates,

dl is the differential distance along the ray,

$s(x,z)$ is the slowness (or the reciprocal of the velocity) at point (x,z).

The fundamental difficulty with equation 5.1 is the fact that the raypath to be found depends on the unknown slowness and hence this problem is defined as non-linear in slowness. Tomography is the process of linearisation of equation 5.1 about some initial slowness model. Instead of solving equation 5.1 for s, it is easier to solve an approximation to equation 5.1 for the perturbations of s from the initial slowness model. A set of linearised equations can be produced by individually tracing each raypath or source-receiver combination through our initial slowness model of the form,

$$\delta T = A.\delta v \tag{5.2}$$

δT is a vector of length n, the number of raypaths, representing the differences between observed traveltimes and the theoretical times obtained by ray tracing the slowness model. The perturbations to the slowness, δv are related to the traveltime differences through a matrix A which contains the source-receiver and raypath geometry information. The elements of A are $A_{ij} = \delta T_i / \delta v_j$.

A is a tomographic matrix whose elements A_{ij} represent lengths of propagating rays in the slowness model, i.e. the i th row of matrix A describes the path of the i th ray from source to receiver. For a subsurface model which is discretised in to simple cells, the number of rows is equal to the number of rays, whereas the number of columns is equal to the number of cells. Usually A_{ij} is an overdetermined matrix, i.e. the number of rows is greater than the number of columns. This is simply because a model should be traced with as many rays as possible and ensures that cells within the model are not smaller than the resolving power of the data.

Equation 5.2 can be solved using an iterative least squares method in order to minimise δT. These methods are known as generalised inversion procedures when applied to geophysical inverse problems.

In combined transmission and reflection traveltime tomography we are faced with the problem of finding a model of velocity and depth to interface which minimises G, a function of the difference between theoretical traveltimes raytraced through our model and observed traveltimes recorded for real earth

$$G = \left| t_0 - t_T(p) \right|^2 \tag{5.3}$$

where,

$t_T(p)$ is a non-linear function of the interface and slowness parameters.

t_0 is a vector of N source-receiver real traveltime observations

For a particular choice of the model parameter vector p, comprising of m_s slowness and m_i interface parameters, rays can be traced between source and receiver

co-ordinates to create a vector of theoretical traveltimes that correspond to the real traveltime vector. This theoretical traveltime vector is represented in equation 5.3 by t_T of length N.

After Mao and Stuart (1995) the particular non-linear optimisation technique used here to minimise G is the Gauss Newton method (Gill et al, 1981), (Fletcher, 1987). By expanding G using Taylor Expansion about an initial point p_0 we get the following normal equations,

$$A^T A\delta p = A^T r \tag{5.4}$$

where,

δp = correction vector of model parameters.

$A = N.(m_i + m_s)$ matrix of elements of $\delta t_T(p)/\delta p$

$r = \left|t_0 - t_T(p)\right|$ is the traveltime residual for the initial model.

The solution is found iteratively by linearly approximating the non-linear problem.

Given the definition of the problem, Combined Transmission and Reflection Traveltime Tomography attempts to provide a solution using a multistage iterative calculation procedure through the following series of steps,

- STEP 1. The definition of a subsurface earth model called an 'initial velocity model' which provides the starting point for the tomographic inversion procedure.
- STEP 2. The raytracing of this initial model from source to receiver points identical to those measured in the field experiment to produce a corresponding set of theoretical traveltimes and determine the difference or perturbation between these theoretical traveltimes and the real data.
- STEP 3. Inversion of the traveltime differences to improve the fit of the initial model to the real data.
- STEP 4. Steps 2 and 3 are repeated until the observed deviation of the 'current' velocity model drops below a preset value. The model is then deemed to be a suitable approximation of the real earth velocity structure.

5.4.1 STEP 1. Mathematically defining the slowness model, p

The inversion method depends to a large extent on the type of medium parameterisation employed. Models must be discretised in some way to allow their input into computer programs. In the case of simple transmission traveltime

tomography earth models are usually discretised into a finite number of rectangular or square cells and a simple raytracing algorithm employed such that the source-receiver pairs are joined by straight lines. The distances can then be simply computed using trigonometry. To include reflection traveltimes in our inversion calculation rays must of course reflect at specified interfaces which are defined in our model. This requirement makes rectangular block models such as those employed by Aki & Lee (1976) undesirable, simply because of their inability to represent heterogeneous structure, slight gradients in velocity or oblique strata discontinuities. Some greater degree of detail may be achievable by decreasing the cell size, but a cut off will be reached where a large number of small blocks will result in a problem in which the size of the cells is smaller than the resolving power of the available data. The result is a matrix which is underdetermined and which will suffer from computational difficulties.

An alternative method to block discretising is to use layers in which the velocity is constant in the vertical direction but is given by interpolation between vertical lines or nodes in the horizontal direction (Hawley et al, 1981). The particular parameterisation scheme adopted here, after Mao & Stuart (1996), is to represent each reflective interface and the slowness between successive pairs of interfaces in the horizontal direction in terms of a cubic 2-D B-spline function.

The B-spline function allows irregular interfaces and smoothly varying material properties between interfaces to be represented analytically and allows accurate model parameterisation and raytracing. B-splines also allow discretised cells between adjacent nodes to take complex shapes with the advantage that hundreds rather than thousands of parameters (as would be the case in squares or rectangular block models) are dealt with in the inversion procedure and yet it is still possible to produce detailed tomographic images.

The velocity model is divided in to a number of layers by a series of interfaces which can vary with depth. The depth of each interface $D_i(x,y)$ is expressed by a 2-D B-spline function of the form,

$$D_i(x,y) = D_{i0} + \sum_{m=j-3}^{j} \sum_{n=k-3}^{k} a_{mn}^{i} B_{m,4}(x) B_{n,4}(y) \qquad (5.5)$$

where,

D_{i0} is the background depth of the i th interface.

a_{mn}^{i} is a perturbation coefficient of depth in the range $x_j < x < x_{j+1}$ and $y_k < y < y_{k+1}$ for $j=0,1,\ldots,J$ and $k=0,1,\ldots,K$.

$B_{m,4}(x)$ and $B_{n,4}(y)$ are 4th order B-spline basis functions, (De-Boor, 1978).

The laterally varying slowness between each successive pair of interfaces is also assumed to be a 2-D cubic B-spline function in the horizontal direction,

$$s_i(x,y) = s_{i0} + \sum_{m=j-3}^{j} \sum_{n=k-3}^{k} b_{mn}^{i} B_{m,4}(x) B_{n,4}(y) \qquad (5.6)$$

where,

s_{i0} is the background slowness of the i th layer.

b_{mn}^{i} is the perturbation coefficient of slowness in the range $x_j < x < x_{j+1}$ and $y_k < y < y_{k+1}$.

$B_{m,4}(x)$ and $B_{n,4}(y)$ are 4th order B-spline basis functions.

Velocities of adjacent layers are independent across an interface and may therefore be continuous or discontinuous across the interface. This allows modelling of velocity discontinuities in both vertical and horizontal directions and also various complex geological structures with abrupt velocity changes, such as faults. However, B-splines attempt to approximate to smooth continuous functions, so to produce abrupt change in structure it is necessary to adopt non-uniform node spacing (vertical line spacing) for the spline function. The various aspects of the model parameterisation are pictorially explained in figure 5.1.

5.4.2 STEP 2. Producing the theoretical traveltime vector, t_T, by raytracing p.

The purpose of raytracing is to produce a vector, t_T in equation 5.3, of theoretical traveltimes between source and receiver points which matches the vector of paths for which traveltimes have been picked from the field data. Raytracing relies on the approximation that seismic energy travelling from source to receiver does so along rays normal to the wavefront. This approximation allows the reduction of the wave equation to two ordinary differential equations for raypath and amplitude, the so called Eikonal and transport equations, (Aki & Richards, 1980). We can solve the ray equations for a given velocity model for source/receiver pairs. In the case of transmission simply the source and receiver configuration is required, but reflection raytracing requires the definition of the chosen reflector interface. The problem that must be solved by raytracing is firstly finding the path taken by the seismic wave between each source/receiver pair (either via or not via a reflector interface) and secondly calculate the time taken to traverse this path.

Just as there are many ways to parameterise an earth model, so there are as many ways to calculate raypaths, but usually the latter is dependant on the method of the

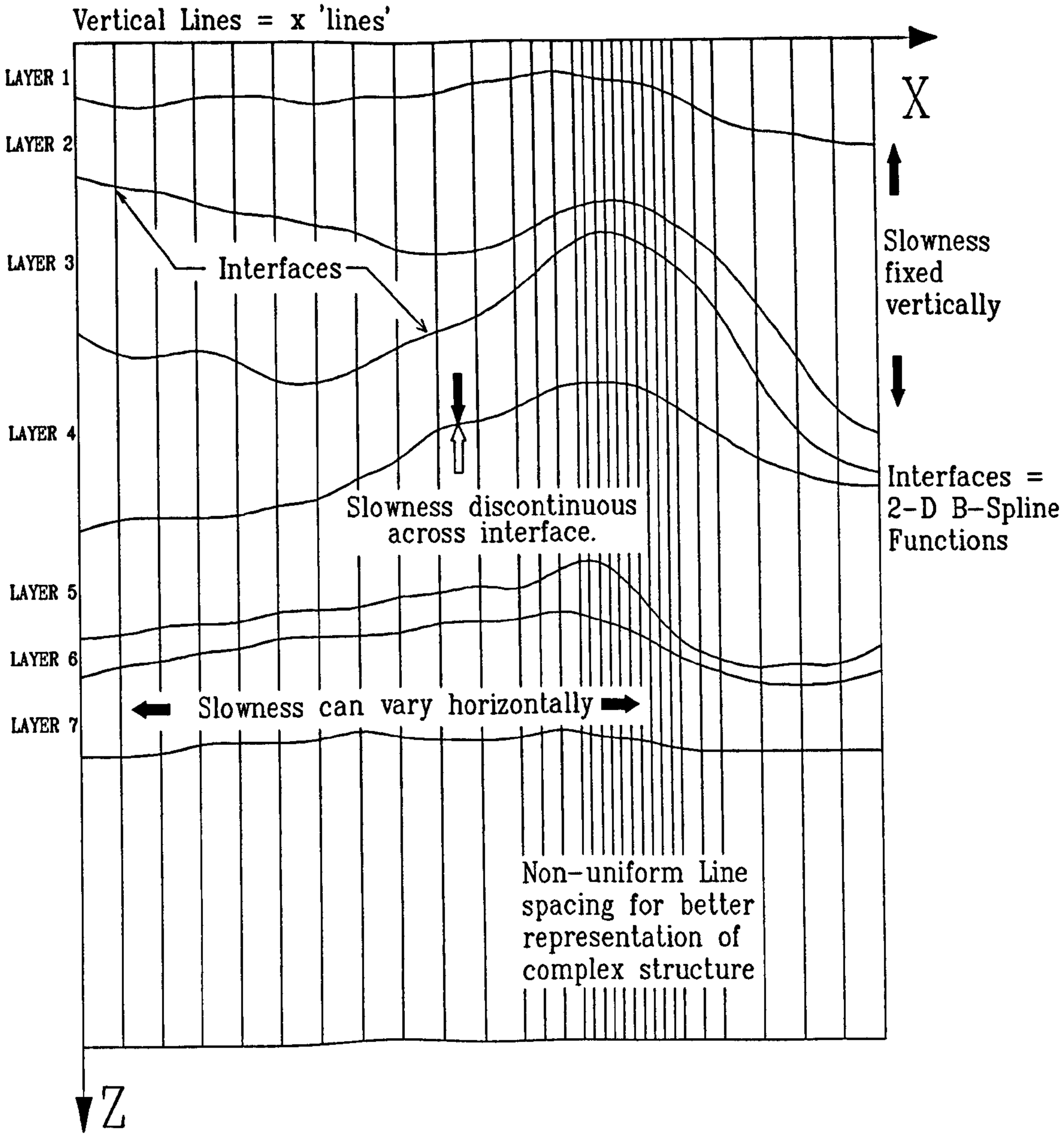

FIGURE 5.1 Pictorial representation of the aspects of the model parameterisation scheme adopted for the combined transmission and reflection traveltime method.

former. The procedure adopted here after Mao and Stuart (1996) is applicable to 2-D or 3-D velocity structure raytracing. The technique must be computationally efficient since raytracing of the current velocity model is carried out as part of each inversion step and a reduction in the raytracing time helps to reduce the overall tomography procedure computation time. The procedure used here can calculate the theoretical raypath traveltimes, ray trajectories and partial derivatives for the inversion process for waves of various phases, including transmitted, reflected, refracted and mode converted waves through the parameterised model. Consider a ray travelling from a source point A to a receiver point B through a 3-D medium with slowness $s(x,y,z)$. From the Eikonal equation, the traveltime t_A^B is given by,

$$t_A^B = \int_A^B s(x,y,z).dl \tag{5.7}$$

where,

$dl = \left[dx^2 + dy^2 + dz^2\right]^{1/2}$ is the differential length of the ray.

This assumes that the ray crosses $N-1$ interfaces between A and B and the layer thickness between any two successive interfaces is sufficiently small that l_i the length of the i th path segment between the i th and the $(i-1)$th interfaces can be approximated as,

$$l_i = \left[(x_i - x_{i-1})^2 + (y_i - y_{i-1})^2 + (D_i - D_{i-1})^2\right]^{1/2} \tag{5.8}$$

where x_i, y_i, D_i are co-ordinates of the ray at the i th interface. The traveltime integral in equation 5.7 can be approximated by the sum,

$$t = \sum_{i=1}^{N} s_i(\tilde{x}_i, \tilde{y}_i) l_i(x_{i-1}, x_i, y_{i-1}, y_i) \tag{5.9}$$

where,

$s_i(\tilde{x}_i, \tilde{y}_i)$ = slowness at the midpoint of the i th path segment.

Fermat's principle states that any event observed as a first arrival has a raypath of minimum traveltime in propagating from A to B and may necessarily have followed the shortest distance route. To obtain the minimum traveltime we therefore set the partial derivatives of t with respect to x_i and y_i to zero. We obtain a system of $2N-2$ non-linear equations of the form,

$$t_{xi} = \frac{\delta s_i}{\delta x_i} l_i + \frac{\delta l_i}{\delta x_i} s_i + \frac{\delta s_{i+1}}{\delta x_i} l_{i+1} + \frac{\delta l_{i+1}}{\delta x_i} s_{i+1} = 0$$
$$t_{yi} = \frac{\delta s_i}{\delta y_i} l_i + \frac{\delta l_i}{\delta y_i} s_i + \frac{\delta s_{i+1}}{\delta y_i} l_{i+1} + \frac{\delta l_{i+1}}{\delta y_i} s_{i+1} = 0 \qquad (5.10)$$

where,

$$t_{xi} = \frac{\delta t}{\delta x_i} \text{ and } t_{yi} = \frac{\delta t}{\delta y_i}$$

and $i = 1$ to $(N-1)$

We can reduce this system of non-linear equations to one of linearised perturbation ray equations using Taylor expansion of t_{xi} and t_{yi} around an initial solution x_0 and y_0.

$$\sum_{j=i-1}^{i+1}\left(\frac{\delta t_{xi}}{\delta x_j} dx_j + \frac{\delta t_{xi}}{\delta y_j} dy_j\right) = -t_{xi} \qquad (5.11)$$

$$\sum_{j=i-1}^{i+1}\left(\frac{\delta t_{yi}}{\delta x_j} dx_j + \frac{\delta t_{yi}}{\delta y_j} dy_j\right) = -t_{yi} \qquad (5.12)$$

where $i = 1$ to $(N-1)$.

Alternatively we could write equations 5.11 and 5.12 in a matrix format as follows,

$$\begin{pmatrix} A_{xx} & A_{xy} \\ A_{yx} & A_{yy} \end{pmatrix} \begin{pmatrix} \delta x \\ \delta y \end{pmatrix} = \begin{pmatrix} -T_x \\ -T_y \end{pmatrix} \qquad (5.13)$$

where $A_{xx}, A_{xy}, A_{yx}, A_{yy}$ are $(N-1)$x$(N-1)$ tri-diagonal matrices whose elements represent the first and second partial derivatives of slowness and interface depth with respect to x and y. Equation 5.13 is solved by an iterative last-squares method, starting with an initial guessed raypath from the source point (x_0, y_o, D_o). A shooting ray scheme shown in figure 5.2 is used to calculate this initial guessed raypath and is crucial to the reliability and the convergence rate of the iterative technique. The initial raypath must be of the correct specified wave type, i.e. transmitted or reflected or refracted wave modes. The initial guessed raypath is calculated by applying Snell's law to a local region around the raypath. Two co-ordinate systems are shown in figure 5.2, a global co-ordinate system (X, Z) represented by solid lines, and a local co-ordinate system by dashed lines. The local system is derived by rotating the global system by an angle φ_i about the point $(x_,, D_i)$ at which the ray crosses the i th interface. For an angle θ_i between the ray and the Z-axis at (x_i, D_i) and an angle φ_i, the tangential direction of the i th interface at (x_i, D_i) to the X-axis of the global co-ordinate system, the point

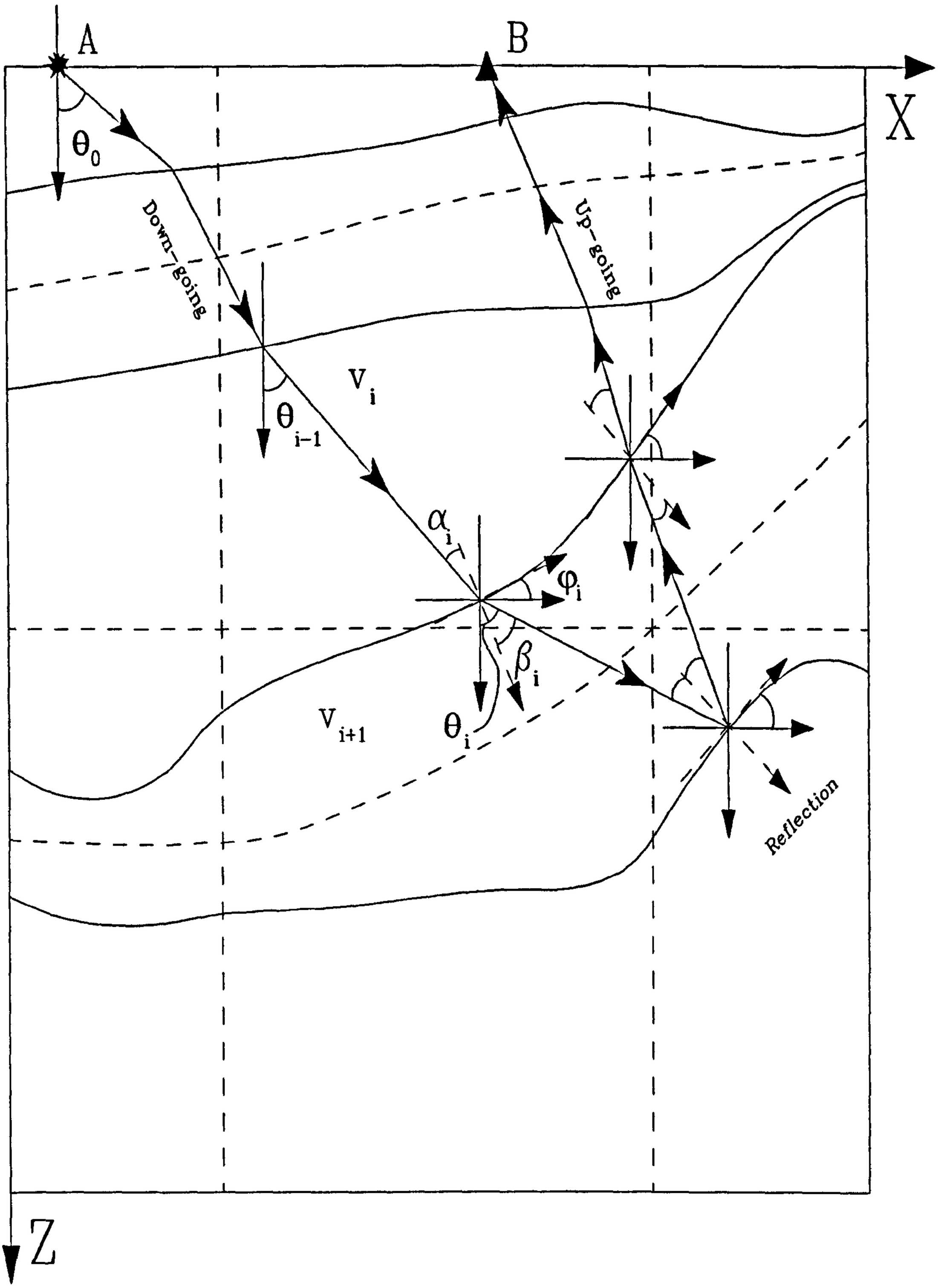

FIGURE 5.2 Shooting scheme used to find the initial guessed raypath, close to the global minimum-time path. Snell's law is applied to a local region around the raypath for a simple 2-D case.

(x_{i+1}, D_{i+1}) at which the ray crosses the $(i+1)$ th interface can be calculated using the following expression,

$$\tan\theta_i = \frac{x_{i+1} - x_i}{D_{i+1} - D_i} \tag{5.14}$$

θ_i is given by,

$\theta_i = \phi_i - \beta_i$ for $\theta_{i-1} < \phi_i$

$\theta_i = \phi_i + \beta_i$ for $\theta_{i-1} \geq \phi_i$

where,

$$\phi_i = \frac{\delta D_i}{dx_i}$$

and B_i is the angle of refraction which may be obtained from Snell's Law,

$$\sin\beta_i = \frac{v_{i+1}}{v_i}\sin\alpha_i$$

where,

$\alpha = |\theta_{i+1} - \varphi_i|$ is the angle of incidence at the i th interface and v_i and v_{i+1} are local velocities above and below x_i. Given a take-off angle θ_0 at the source point A and a reflective interface the emergence point of the ray back at the 'surface' can be calculated. This may however be far from B depending on θ_0. By making repeated adjustments to θ_0, a raypath can be found that propagates from exactly A to B. In complex media with multiple layers, the raypath becomes extremely sensitive to θ_0 to the point where raytracing becomes very time consuming and in some cases may be unsuccessful. However, since the guessed ray only provides an input to the least-squares iterative procedure it is only required to be 'close' to the true raypath. When the distance between the emergence point and the receiver is smaller than a given value ε, the process is stopped and that ray is taken as the initial guess. The value of ε should be less that half the geophone spacing.

Once the initial guessed ray has been calculated, the ray perturbation solution δx and δy can be found from equation 5.13 and an updated ray is calculated from,

$$x_k = x_{k-1} + \delta x_{k-1}$$

$$y_k = y_{k-1} + \delta y_{k-1}$$

Iteration is stopped when the root mean square of the partial velocities t_{xi} and t_{yi} is less than 10^{-5}s km^{-1} or the variation in traveltime with each iteration is very small (around 10^{-3} ms).

5.4.3 STEP 3. Inversion

Linearised inversion is carried out using a process called 'parameter separation'. This is necessary because the model vector p in equation 5.4 has been defined in terms of slowness and interface parameters. The parameter separation technique is synonymous with that used for the simultaneous determination of hypocentre locations of earthquakes and velocity structure. The advantage of separating the parameters is that the potentially large matrix containing the model parameters may be divided into two smaller ones. Linearised inversion is performed by decoupling the velocity field from the interface locations using multiple damping factors, and finding the generalised inverse using singular value decomposition (SVD) (Wiggins, 1972).

The earth model is parameterised using 2-D B-spline functions and is a vector of the perturbation coefficients of those functions defined in equations 5.5 and 5.6,

$$p = (a,b) \tag{5.16}$$

The G matrix (equation 5.3) consists of m_i columns of interface derivatives and the rest of slowness derivatives. It is possible to decompose G into two smaller sub-matrices A and B. Substituting p, A and B in to equation 5.4 we obtain,

$$\begin{pmatrix} A^T A & A^T B \\ B^T A & B^T B \end{pmatrix} \begin{pmatrix} \delta a \\ \delta b \end{pmatrix} = \begin{pmatrix} A^T r \\ B^T r \end{pmatrix} \tag{5.17}$$

or alternatively,

$$A^T A \delta a + A^T B \delta b = A^T r \tag{5.18}$$

$$B^T A \delta a + B^T B \delta b = B^T r \tag{5.19}$$

by rearrangement we get the following linearised equations,

$$\begin{aligned} OA\,\delta a &= Or \\ B^T B \delta b &= B^T \left(r - A\delta a \right) \end{aligned} \tag{5.20}$$

where,

$$O = A^T - A^T B \left(B^T B \right)^{-1} B^T$$

The correction vectors, δa and δb must be damped because OA and $B^T B$ are usually poorly conditioned. This is done by adding a diagonal matrix into OA and $B^T B$. The damped version of equation 5.20 becomes,

$$\begin{aligned} \left(O^* A + \alpha I \right) \delta a &= O^* r \\ \left(B^T B + \beta I \right) \delta b &= B^T \left(r - A\delta a \right) \end{aligned} \tag{5.21}$$

where,

$$O^* = A^T - A^T B\left(B^T B + \beta I\right)^{-1} B^T$$

I is the diagonal identity matrix

α and β are the factors for the velocity and interface respectively.

Equation 5.21 is solved using SVD to find the generalised inverse, from which the correction vectors to the model p, δa and δb can be determined from,

$$\begin{aligned} \delta a &= \left(o^* A\right)^+ O^* r \\ \delta b &= B^+\left(r - A\delta a\right) \end{aligned} \qquad (5.22)$$

where '+' denotes the generalised inverse.

5.5 Conclusion

To summarise, this chapter has reviewed a number of case histories in the literature where seismic tomography has been used to characterise rock masses. Certain key areas were identified as deserving further investigation,

- Laboratory investigations of velocity and attenuation in intact and fractured samples
- Seismic attenuation measurements

The CTRT inversion method has been fully mathematically defined. The method has the following advantages over the standard P-wave transmission traveltime inversion method as follows,

- Complex geological models can be more easily defined using the layer parameterisation technique described in section 5.4.1 which uses less cells or blocks than in a standard discretised model. Therefore the resulting model is smaller and more efficient in terms of computation time as well as more closely resembling the true geological structure.
- The definition of interfaces within the model allows for reflection, refraction and wave converted mode traveltimes to be included in the inversion process. The following field examples in chapters 6 to 8 will show that this can double the number of raypaths compared to the standard transmission traveltime tomographic technique, increase the angular coverage and area of the survey area and therefore improve the quality of the resulting tomogram (or reduce the non-uniqueness of the tomographic solution (see section 1.3)).

CHAPTER 6

6. Combined Transmission and Reflection Tomography in Rock Mass Characterisation.

6.1 Introduction.

Chapter 5 looked at some of the applications of seismic tomography in mining scenarios. It is clear that numbers of examples are small and seismic tomography is still relatively rarely used. Chapter 5 shows that there is great potential in the technique for identification of poor rock mass conditions or the identification of unknown old workings ahead of a current mining operation. All the examples so far cited have used transmission traveltime tomography. For many of these potential uses, transmission traveltime tomography often falls down due to the need for reasonable ray coverage of the block of interest to produce accurate and meaningful tomograms. Where coverage is not adequate, this may lead to a limited survey area, or poor resolution. Many production mining layouts do not provide ideal geometries for tomography surveys of the area of interest and this can either mean that tomography is not possible, or a programme of longhole drilling may be necessary to site receiver or source points in more favourable locations. This added expense may make tomography an unattractive proposition. If tomography is to become a viable tool for regular use, it must become easier to implement with respect to performing well in apparently poor geometry situations. A seismic wave does of course contain a vast amount of potential information apart from the simple direct wave arrival. What is more, this information is available for improved interpretation at no extra cost in terms of the seismic data acquisition. One solution for realising a workable tomographic imaging method is to include seismic reflection traveltimes in our inversion algorithm as well as the already included transmission traveltimes. Reflection seismics is well established in the standard 2-D and 3-D sections used by the oil industry and relies on the fact that geological structure and discontinuities can be imaged from great distances using limited source and receiver points. This chapter will show that it is possible to tomographically image, in detail, a rock mass, using combined inversion of P-wave transmission and reflection traveltimes (CTRT) that would otherwise be inaccessible from just transmission tomography alone. The experiment and result have already been comprehensively described by Pearce and Wade (1995) and Pearce and Wade (1996b).

6.2 The Gillfield Mine Site

6.2.1 Location.

Gillfield Mine is a disused lead mine located in the North Yorkshire Dales, close to Pateley Bridge. The mine consists of a small adit which intersects two veins some 400 m into the hillside. It is currently managed by the Department of Mining and Mineral Engineering at Leeds University and is used for undergraduate training purposes and environmental research.

6.2.2 Geology.

The area around Gillfield mine contains a complex east-north-east trending anticline that reveals carboniferous limestone in a series of domal inliers, surrounded by Millstone Grit. The anticline is faulted on its south flank by the North Craven Fault. Gillfield Adit has been driven into the main anticline through its northern flank and intercepts the near vertical Barite-Fluorspar-Lead Waterhole Vein, where it turns and follows with a reef drive. Figure 6.1 shows the simplified local geology of the area.

A plan of the accessible workings is shown in figure 6.2. At the intercept with the vein, the geometry is such that access can effectively be gained to a solid rock mass on two adjoining sides of a square. This is shown as a hatched region in figure 6.2. The geology in this section provides an interesting location for a 2-D tomographic survey, consisting of a series of steeply dipping limestone and shale layers, a thin chert band and some suspected stowed old stope workings. The apparent inaccessibility provides an ideal location to test the CTRT method to increase the survey area beyond that which would be possible to image with transmission traveltime inversion alone. The survey area is shown in figure 6.3. and the presumed geological structure of the survey site is shown in figure 6.4. This geological interpretation is based on the testimony of Dunham & Stubblesfield (1944) and this author's detailed mapping of the site in the adit and reef drive. The angles and dips of apparent strata boundaries were measured across these roadways and it was assumed that these boundaries extend on a straight course into the survey area at these angles away from the adit.

Veins in this area are associated with the North Craven Fault system, and effectively cut across the general stratigraphy. This can be observed from the lie of the reef drive in comparison to the general angle of stratigraphy across the survey area. Closer inspection of this reef drive revealed a number of small stowed cross cuts entering into the top portion of the survey area. Further inspection to the east of survey point G12 indicated that a smaller reef drive runs parallel, north of the existing drive at a distance of around 5 to 10 m and is connected by the small afore mentioned crosscuts

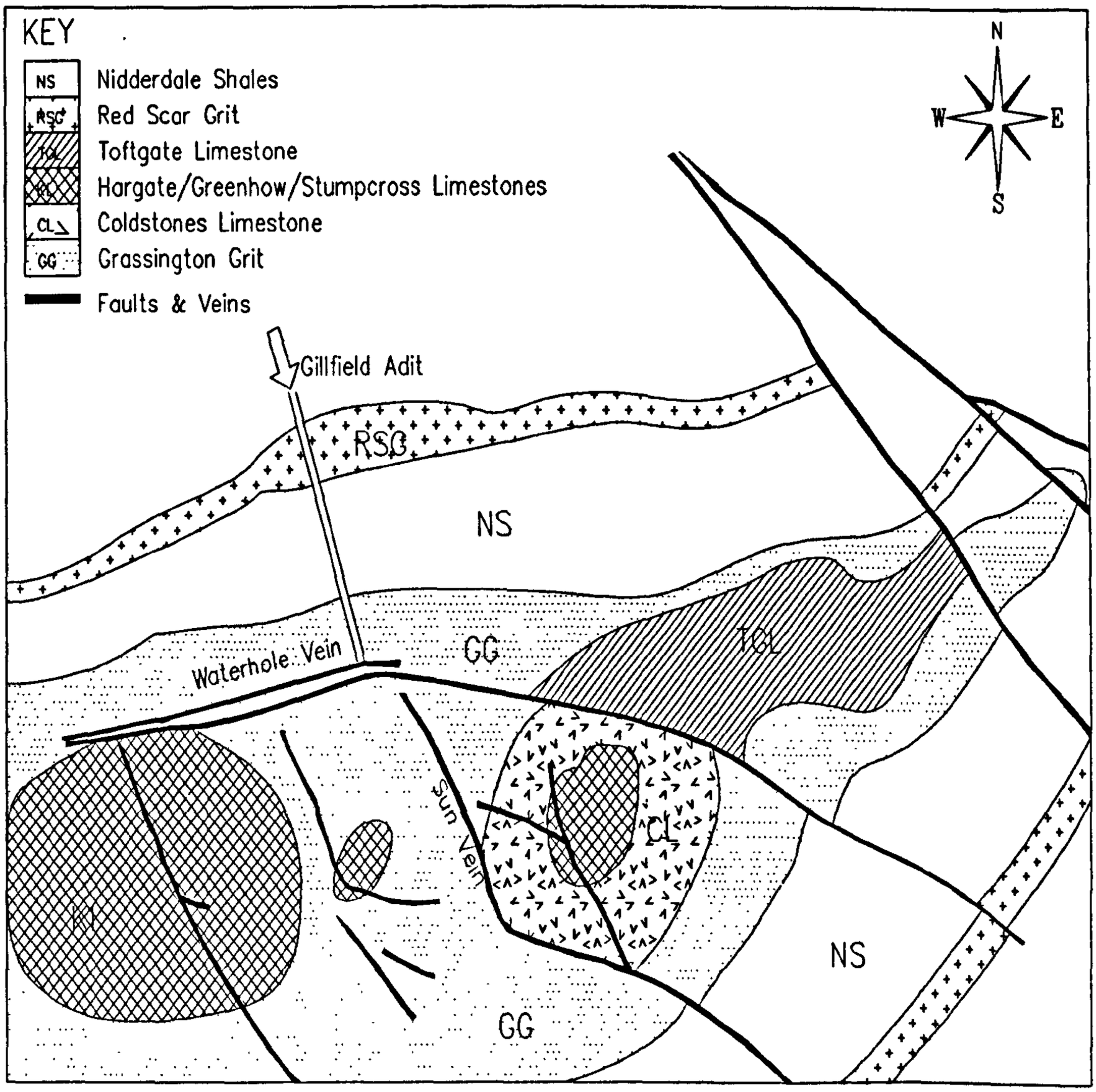

FIGURE 6.1 Local geology at Gillfield, showing adit entrance to Waterhole Vein on the north flank of the anticline.

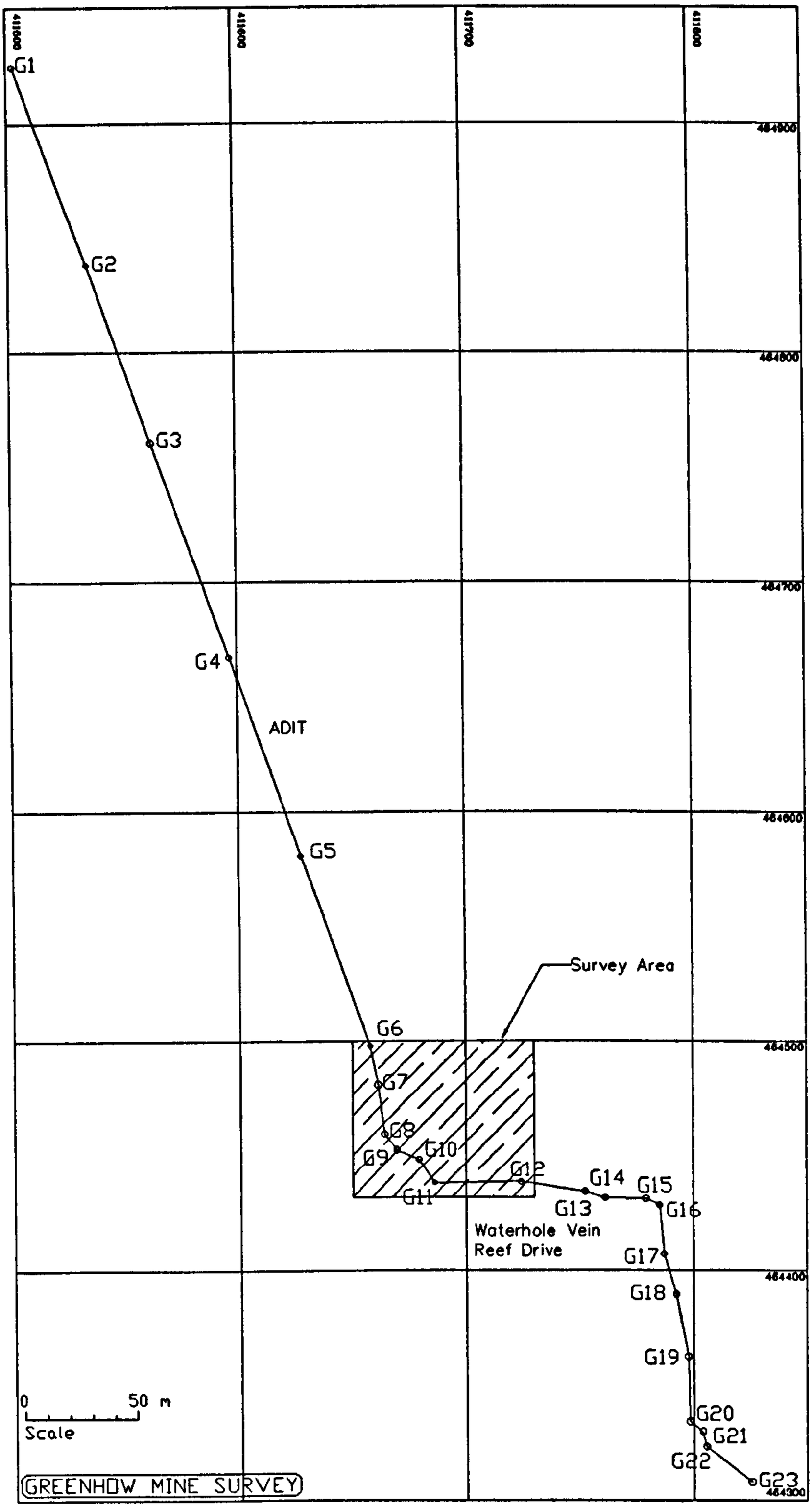

FIGURE 6.2 Gillfield Mine Plan. The survey site is indicated by the hatched region. Positions G1 to G23 are survey pegs.

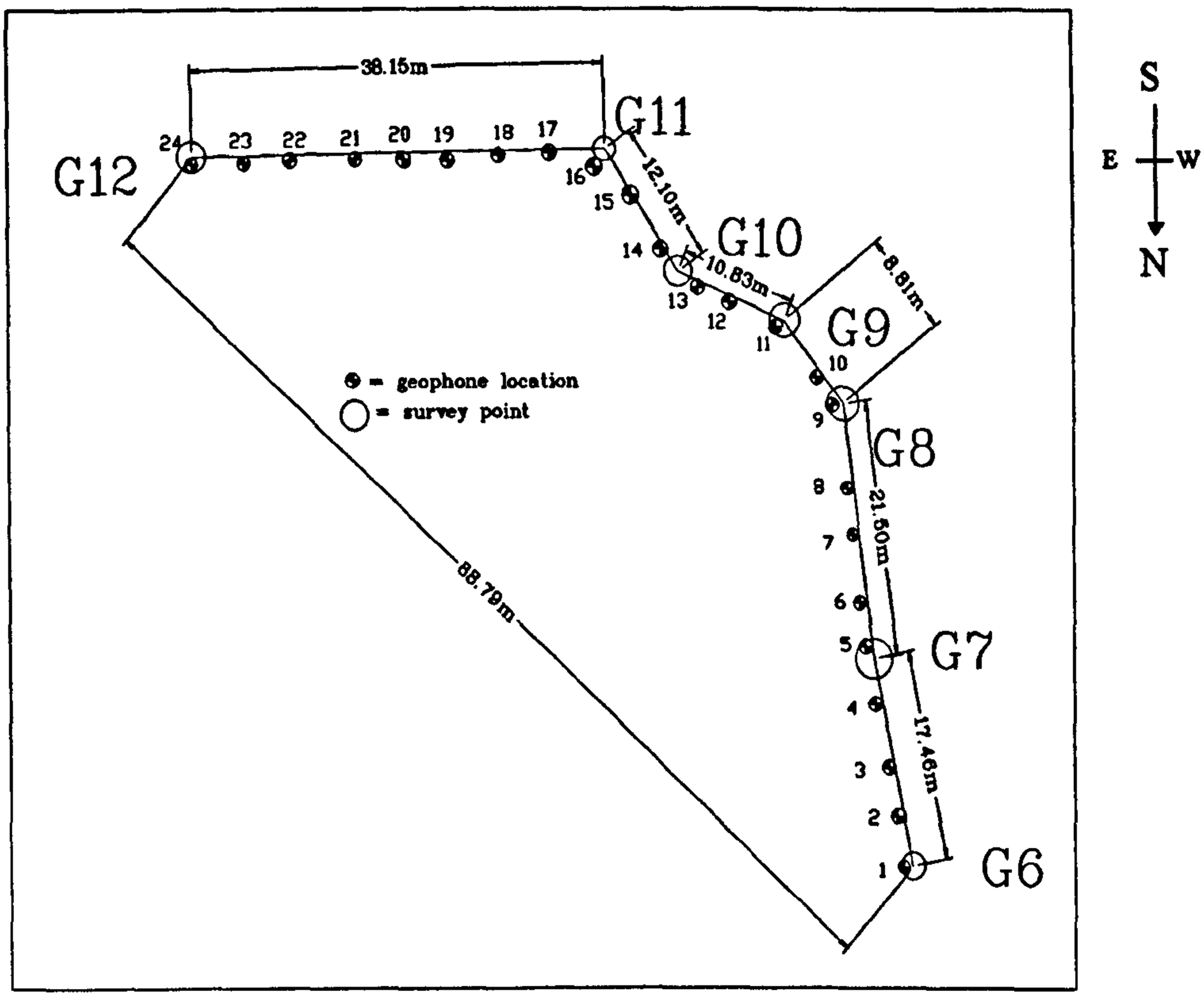

FIGURE 6.3 Zoomed plan view of the survey location shown in the hatched area of Figure 6.2.

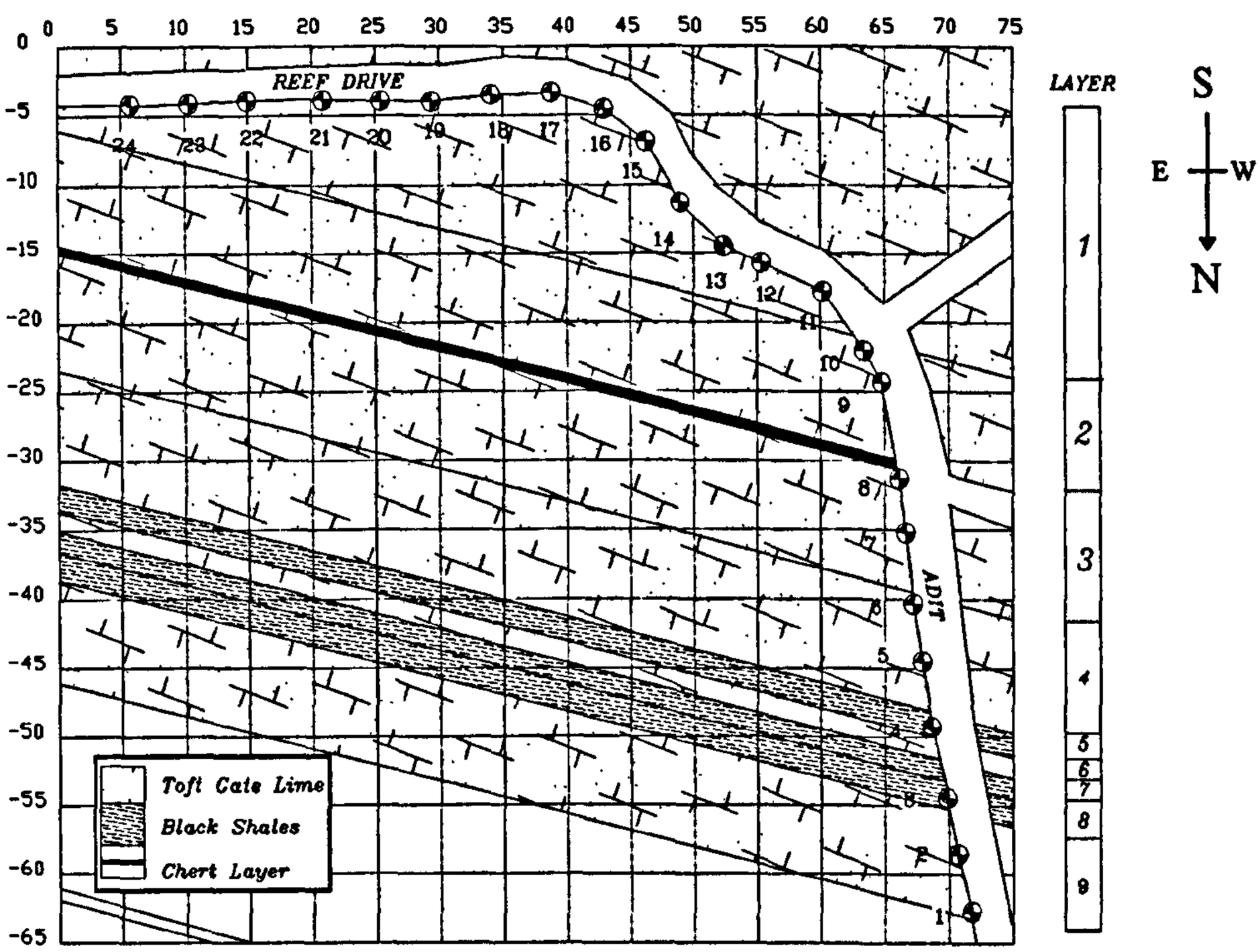

FIGURE 6.4 Presumed geological structure at the survey site.

to the existing reef drive. This second reef drive is apparently stow packed with limestone waste rock across the survey area and should show up as a low velocity anomaly compared to the surrounding country limestone. Because of the inaccessibility of this second drive it is impossible to predict its precise location, and this provides a good opportunity to test if seismic tomography can help resolve the issue.

6.2.3 Field Technique

It was decided to keep the field technique as simple as possible with the purpose of showing that a survey of this kind could be carried out with a minimal amount of equipment in a short space of time. An array of 24 horizontally orientated geophones was established at the site at approximate 5 m intervals along the adit and reef drive walls (see figure 6.3). Geophones were SM-6 type and were fixed to the rock by bolting into brass spikes securely resined in place in small drill holes. A 24 channel, 16-bit seismograph was located at a convenient point between geophones 9 and 10 and connected to the array of geophones. A seismic source was provided by a sledge hammer perpendicular to the wall at each of the geophone locations in turn and was received across the entire array. Each source location was stacked at least 10 times to improve the signal to noise ratio and to improve direct and reflection arrival identification over longer raypaths. The smallest sampling rate of 31 kHz was selected on the seismograph with a record length of 50 ms, in order to improve the accuracy with which transmission and reflection times could be identified (one sample per 0.03125 ms). A total of 576 transmission paths were acquired across the survey area. The total time for the survey amounted to 2 half-days, one half-day to fix the geophone mountings and another half-day to conduct the survey. More source points could have been used in between the geophone locations but this would have increased the survey time and was deemed unnecessary.

6.2.4 Data Processing

CTRT required the following steps to produce the final tomogram:

- Transmission traveltime identification.
- Initial velocity model creation.
- Transmission traveltime inversion.
- Forward modelling of the transmission model.
- Reflection traveltime identification.
- Combined transmission and reflection traveltime inversion.

These steps were designed to maximise the information available from the field seismic data, increase the survey area and improve the final resolution of the tomogram. The steps are discussed in detail in the following sections.

6.2.4.1 Transmission traveltime identification.

All data was initially filtered using a 2 pole Butterworth bandpass between 200 and 750 Hz. These values were selected after carefully considering the main seismic energy density in the frequency domain, especially over long raypaths where attenuation of higher frequencies was considerable. The upper cut-off removed electrical noise that was present in some of the datasets, this being attributed to poor connections in the very wet environment. The first arrival of the transmission wave was located more accurately by zooming in on the trace and with the aid of an automatic first-break identification algorithm. In some cases the transmission wave first arrival was difficult to identify due to the differing orientation of the geophone relative to the source initiation direction. However, since from the survey geometry, each raypath is recorded twice, the two traces were compared to find the most probable first arrival. Each common source gather showed a sharp increase in transmission arrival time between geophones 3 and 4, and this represented the transition across the shale partitions in the adit (see figure 6.4).

6.2.4.2 Initial Velocity Model Creation

The initial velocity model is necessary for all tomographic inversion procedures to define a starting point for the iterative process. The parameterisation of the initial velocity model has been mathematically discussed in chapter 5, section 5.3.1. The model should be based upon prior geological knowledge, the lowest likely velocities encountered in the survey area and the natural interface locations, dips and angles. In this case it was decided to split the survey area into a number of layers, 9 in all, based on the geological information obtained in Gillfield adit. Layer interfaces corresponded to obvious natural interfaces in the survey area such as the intersection of shale bands against limestone, a thin chert layer and a reasonably distinct change in limestone type.

Figure 6.5 shows the initial velocity model adopted at this stage of interpretation for the survey. A local grid system was superimposed over the ordinance survey co-ordinates and geophone locations calculated for this new grid. Table 6.1 shows the layer, corresponding lithology and the velocity value assigned. The velocities chosen were influenced by laboratory determined values from intact core samples of limestone and black shale, subjected to hydrostatic stress. Typically, saturated limestone NX size core gave P-wave velocity values at 29 kHz of between 5.2 and 6.2 km/s.

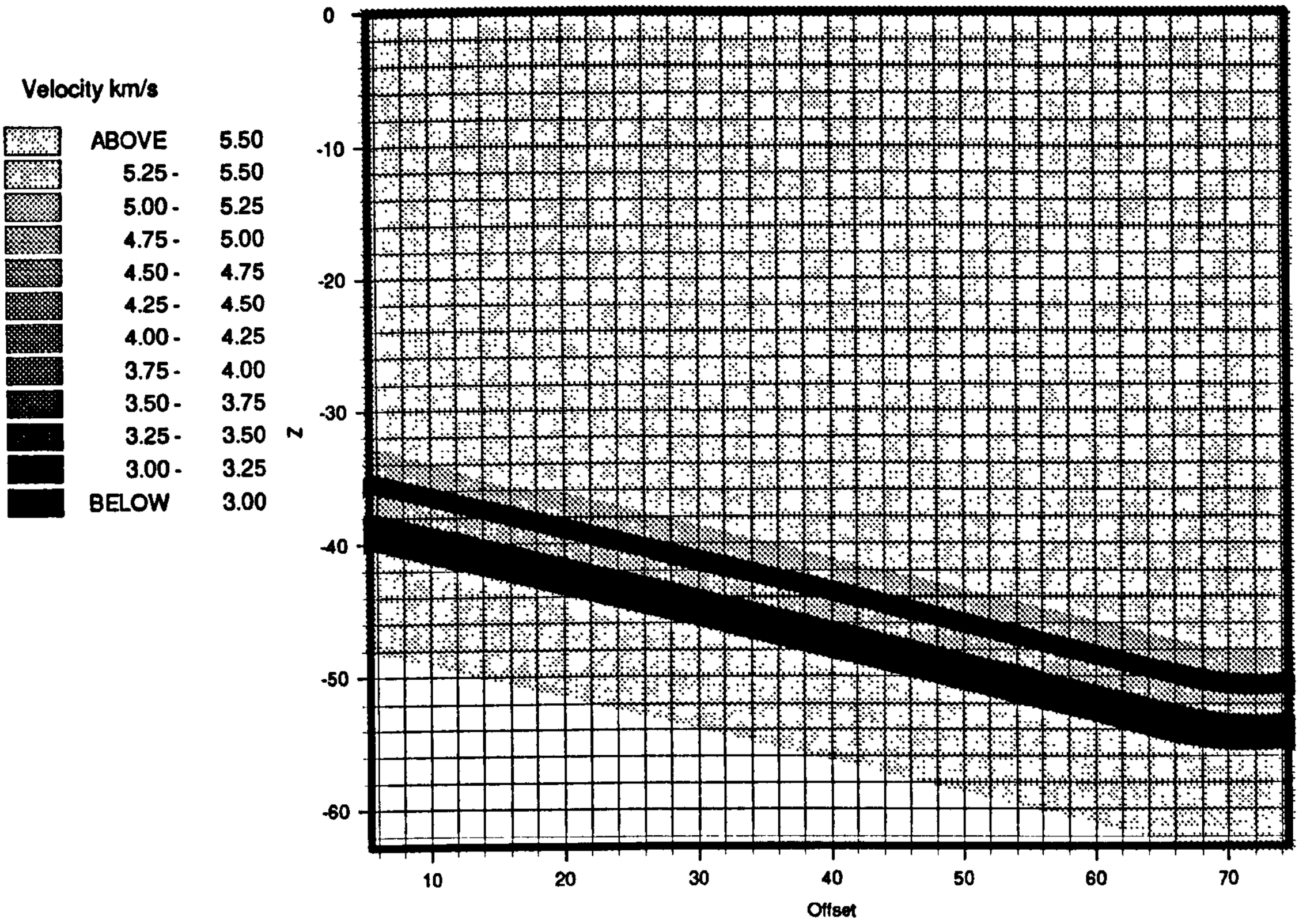

FIGURE 6.5 Initial velocity model for transmission traveltime inversion.

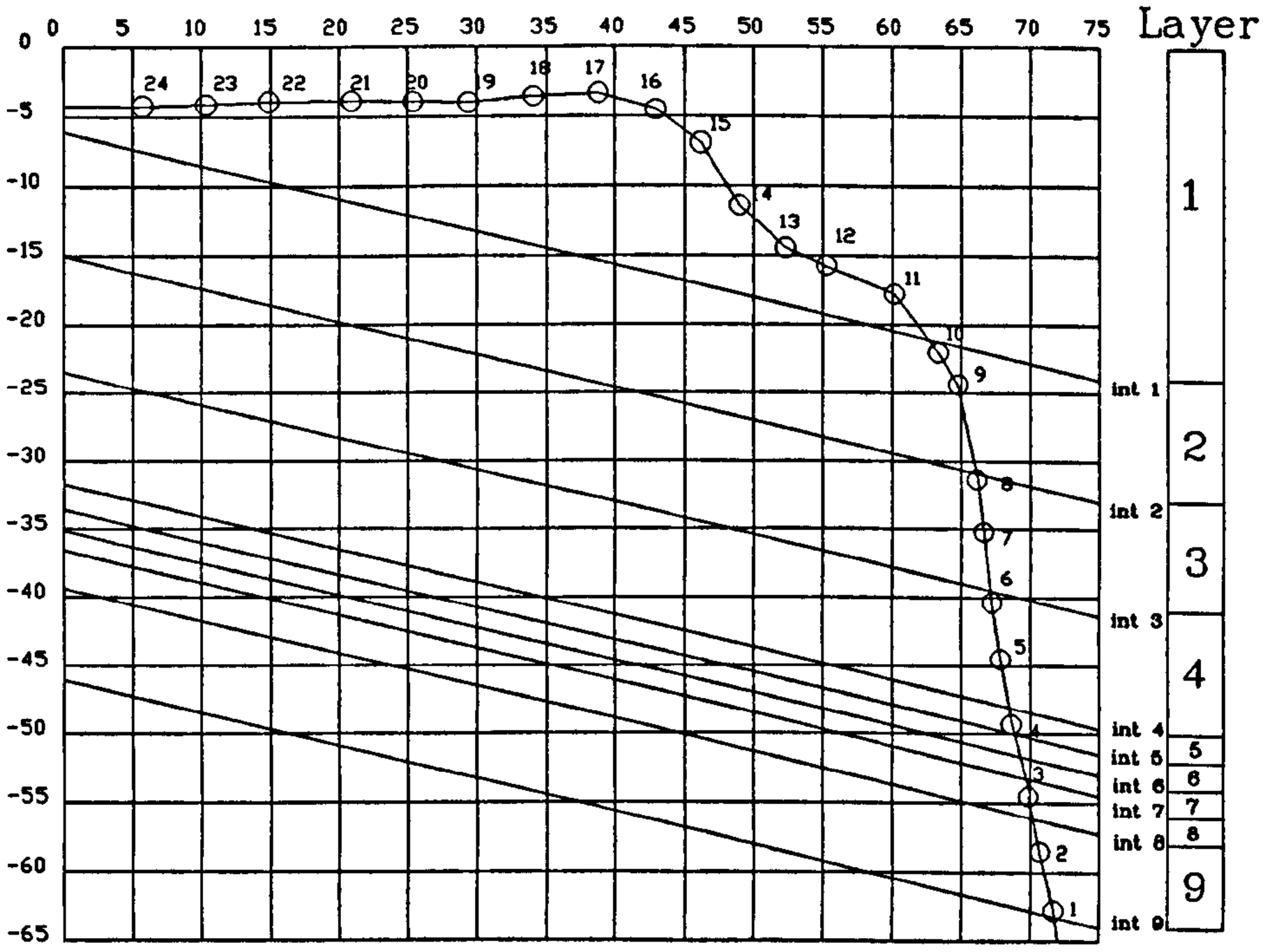

FIGURE 6.6 Grid view of the initial velocity model.

LAYER	DESCRIPTION	VELOCITY
1	Toft Gate Limestone (Fine Grained, grey)	5.50 km/s
2	Toft Gate Limestone and thin chert interface	5.50 km/s
3	Toft Gate Limestone (Course Grained, white)	5.00 km/s
4	Toft Gate Limestone (Course Grained, white)	5.00 km/s
5	Black Shale and Toft Gate Limestone.	4.00 km/s
6	Black Shale	3.40 km/s
7	Toft Gate Limestone with thin Black Shale partings	4.00 km/s
8	More Consolidated Black Shale	3.40 km/s
9	Toft Gate Limestone	5.5. km/s

TABLE 6.1 Initial velocity model layer descriptions and velocities.

The black shale was particularly friable and difficult to core making laboratory determination of velocity difficult. However, it was possible to extract some smaller cores (25mm diameter) and measure dry velocities of between 2.1 and 3.0 km/s at 1 MHz. In-situ velocities for the shale should therefore be greater than these values due to full saturation.

Figure 6.6 shows the same initial velocity model as a grid. The grid represents the system by which the initial model is read by the inversion software. The x lines cut each of the layers into a series of blocks each of which is assigned a velocity. The layer interfaces are defined by identifying the y-value where each interface intercepts each one of the x-axis lines. The initial velocity structure file supplies the following information.

- The number of layers and interfaces
- An initial velocity value for each layer
- The number of x-axis lines and identification of which lines intercept each layer.
- The y-value co-ordinate locations of the cross point of each interface at each x line.
- For each layer, any velocity perturbations above or below the background velocity, for each point where the layer crosses an x line.

This format allows a complete definition of the 2-D model space as a series of layers made up from blocks and also allows the definition of each layer velocity and any horizontal difference in velocity between individual nodes of the same layer.

6.2.4.3 Transmission Time Inversion.

With the initial velocity model defined, inversion of the transmission traveltime data was carried out to iteratively improve the estimate of the velocity structure. The procedure has already been outlined in chapter 5. The amount of change or perturbation allowed for either slowness or interface location could be individually damped to help the iterations converge on a reasonable model with the available transmission data (see chapter 5, section 5.3.3). For example, the position of the interfaces were known with reasonable accuracy compared to slowness values and hence a greater degree of damping was applied to the interface perturbations to prevent significant alteration of the interface locations, whilst the velocity values were less restricted to change. For successful inversion, the initial velocity model needs to be reasonably closely match the true velocity structure.

Where the initial velocity model is incorrect, the iterative inversion process usually fails to converge successfully. However, some improvement in the model will be obtained from the first one or two iteration steps. This improvement can then be used to re-adjust the first incorrect velocity model and the iteration procedure can be restarted. After a number of these steps, the initial velocity model becomes closer to the real model and the inversion process starts to converge successfully. As an alternative to this technique, a process called layer stripping can be employed. Here, a single layer is isolated and the inversion process run with only traveltimes from raypaths between source and receivers located in that one layer. With the smaller number of raypaths the iterative procedure is quick to converge on the true layer velocity. This value and any horizontal perturbation from this value can then be updated in the total initial velocity model. The process can be repeated for other single layers in the model to define accurate layer velocities in the total model. After this process, the initial velocity model closely resembles the true velocity structure and the inversion process will converge successfully. To obtain reasonable control of the inversion accuracy, the iterative procedure was continued until the 2-D velocity model fitted the transmission arrival time data to within a predefined observational error. This observational error was measured and monitored after each complete iterative cycle using the reduced χ^2 misfit,

$$\frac{\chi^2}{L} = \sum_{i=1}^{L}\left(\frac{r_i}{\sigma_i}\right)^2 \qquad (6.1)$$

where,

L = the number of traveltimes used in the inversion.

r_i = the ith traveltime residual

σ_i = the predefined observational error.

An acceptable model was obtained when χ^2/L was less than or equal to 1.000. The resulting tomogram from the successful convergence of the first inversion stage is shown in figure 6.7 with the corresponding raytracing for this model in figure 6.8. For the transmission traveltime inversion, the required observational error was set at 0.38 ms, or approximately 12 times the sampling rate of the data. This value was based on the accuracy to which direct arrival times were identified. The average velocity across the survey area was 3.94 km/s and hence an observational error of 0.38 ms corresponded to an interface location error of 1.5 m. Acceptable closure was achieved after 5 iterations involving 536 transmission traveltimes. The iterations quickly approached the desired observational error cut-off (see figure 6.9 and 6.10) showing that the initial velocity model provided a reasonable starting point for the iterative procedure. Figure 6.11 shows the frequency distribution of the raypath traveltime residuals after zero and five iterations, showing that spread of the residual traveltimes has been greatly reduced.

It is evident that the area of ray coverage shown in figure 6.8 is severely limited by the survey geometry and the velocity structure. Little or no detail is discernible in figure 6.7 with regards to the possible existence of stowed workings in the top portion of the survey area. Equally unsatisfactory is the area of shale banding which does not receive adequate ray coverage to achieve good resolution. This model represents what is achievable from transmission traveltime inversion alone and in the case of poor survey geometry offers little extra detail or clues to the lithological structure of the survey area above and beyond the original geological interpretation. The only way to improve this tomogram is to increase and extend the ray coverage across the area. This may be achieved by considering seismic reflections in our dataset from some or all of those interfaces defined in the initial velocity model. The transmission model provides an ideal starting point for the next stage of CTRT.

6.2.4.4 Forward Modelling

The process of forward modelling was used to help identify reflection peaking arrivals in the field data. Given the transmission model in figure 6.7, it was possible to raytrace this velocity structure for specified source, receiver and interface combinations to calculate the anticipated reflection arrival peaking times. These times were then used

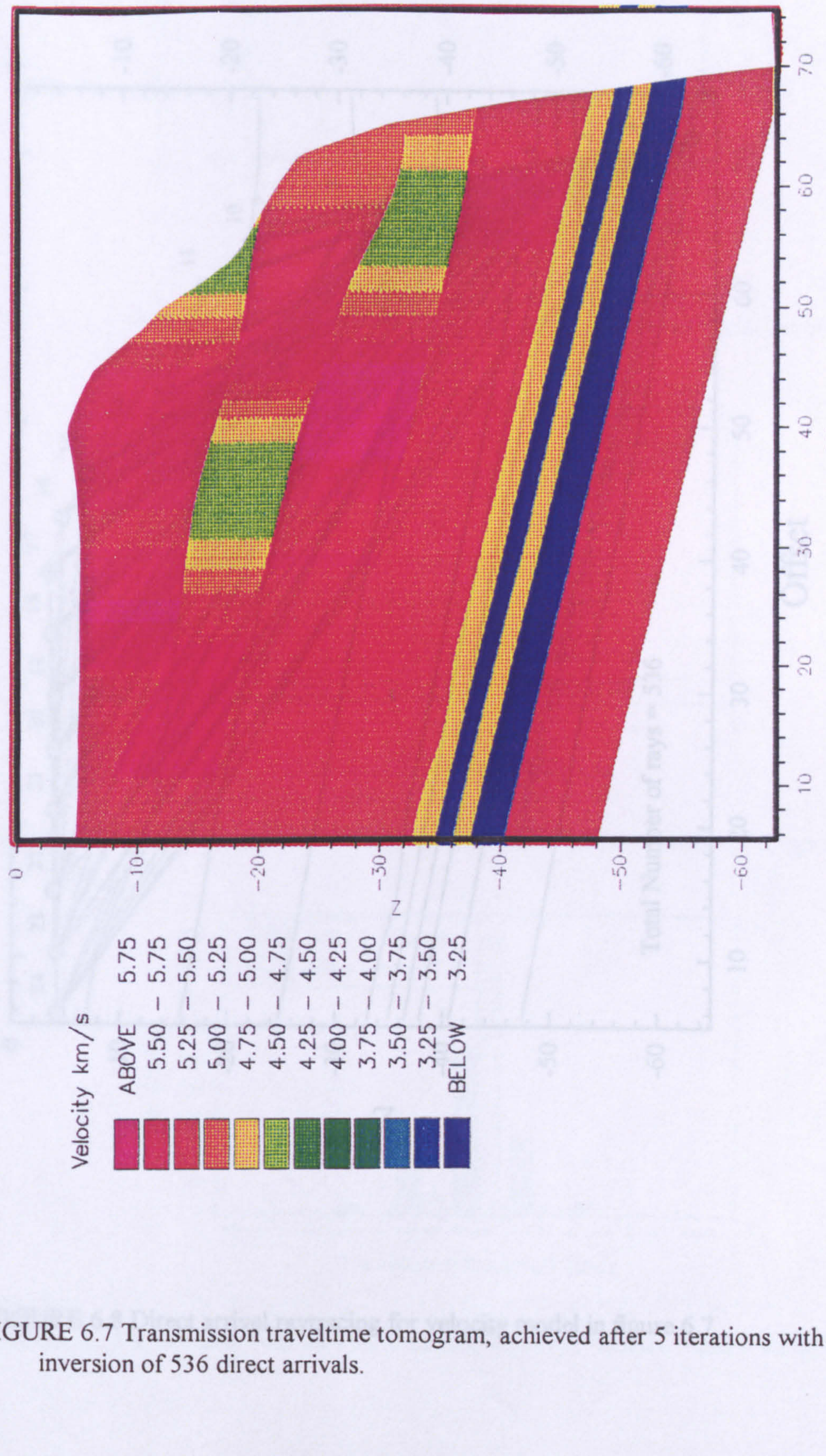

FIGURE 6.7 Transmission traveltime tomogram, achieved after 5 iterations with the inversion of 536 direct arrivals.

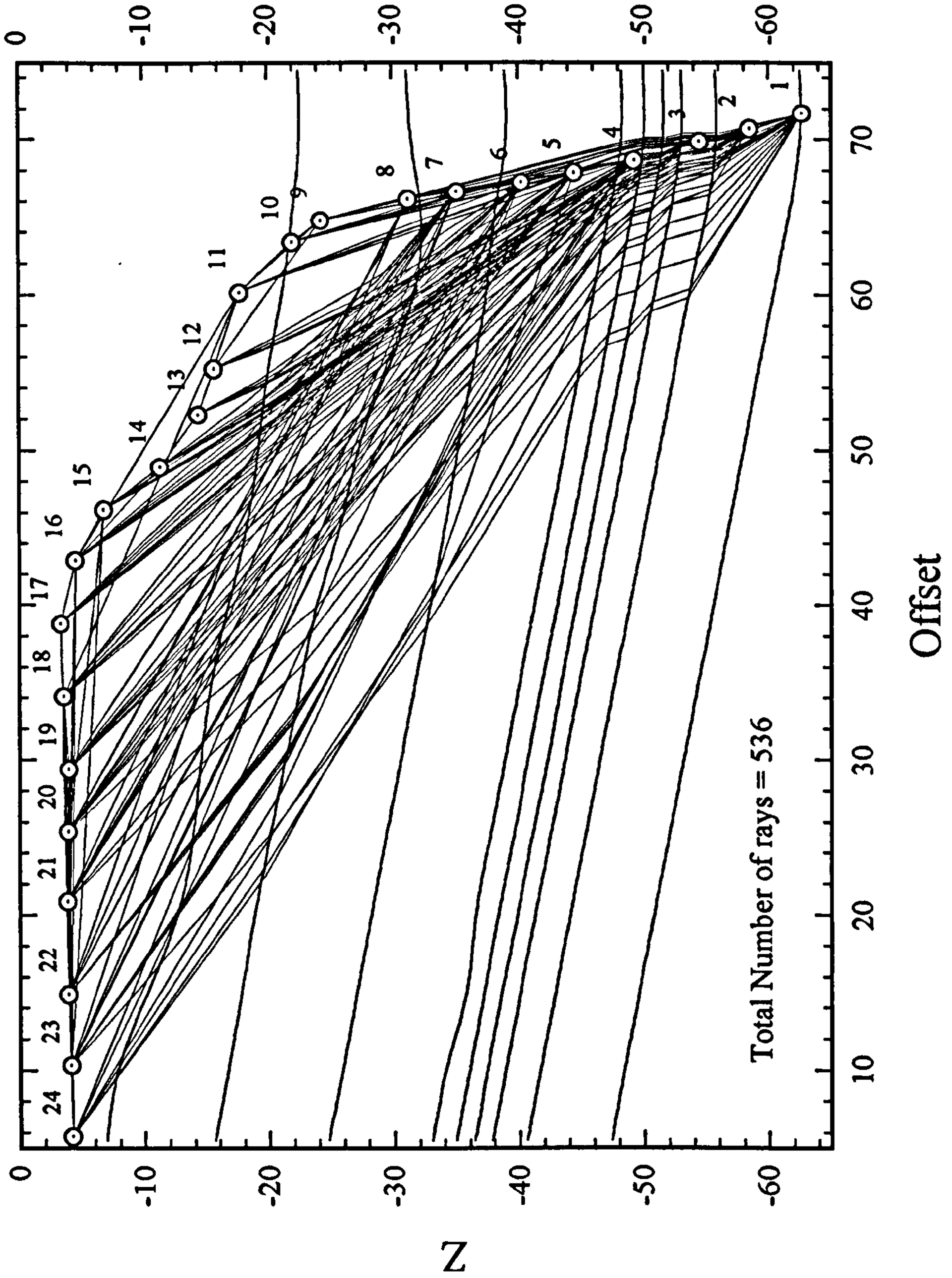

FIGURE 6.8 Direct arrival raytracing for velocity model in figure 6.7

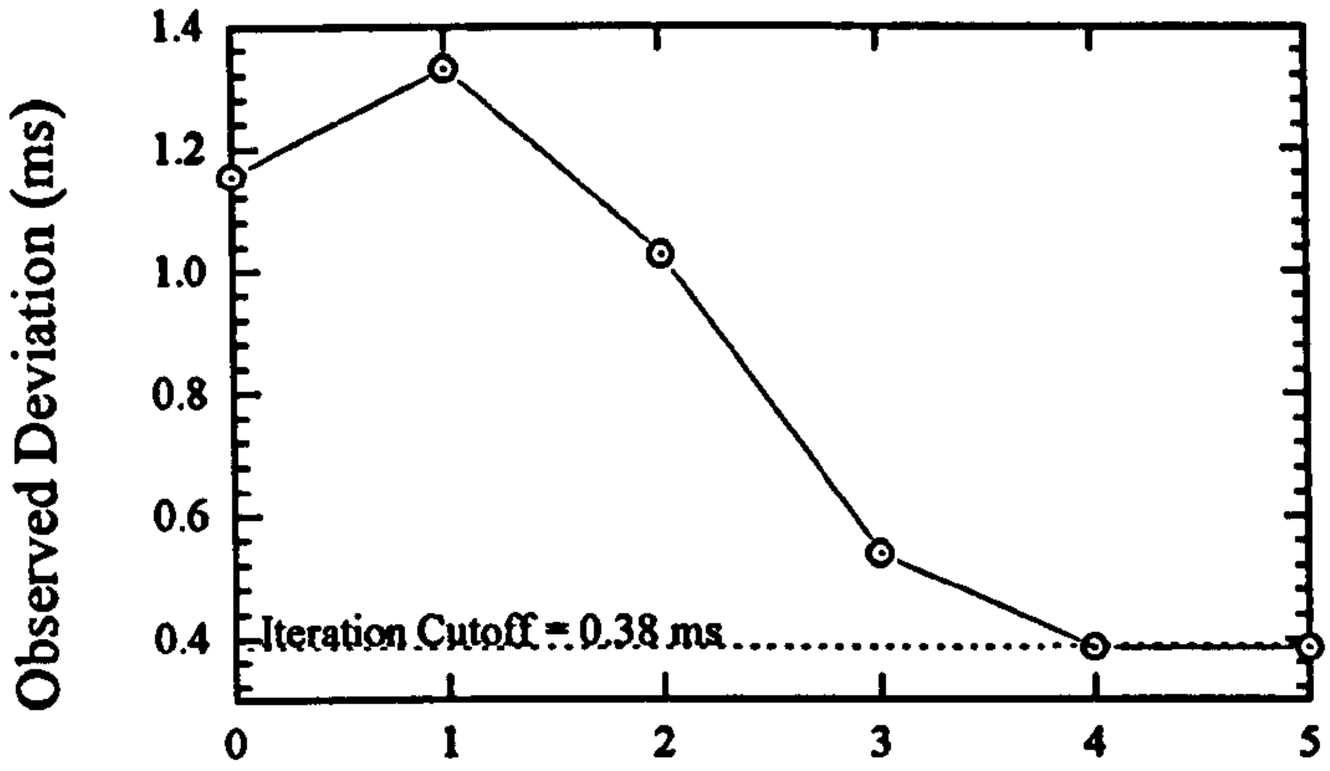

FIGURE 6.9 Observed deviation versus iteration number for the transmission inversion procedure.

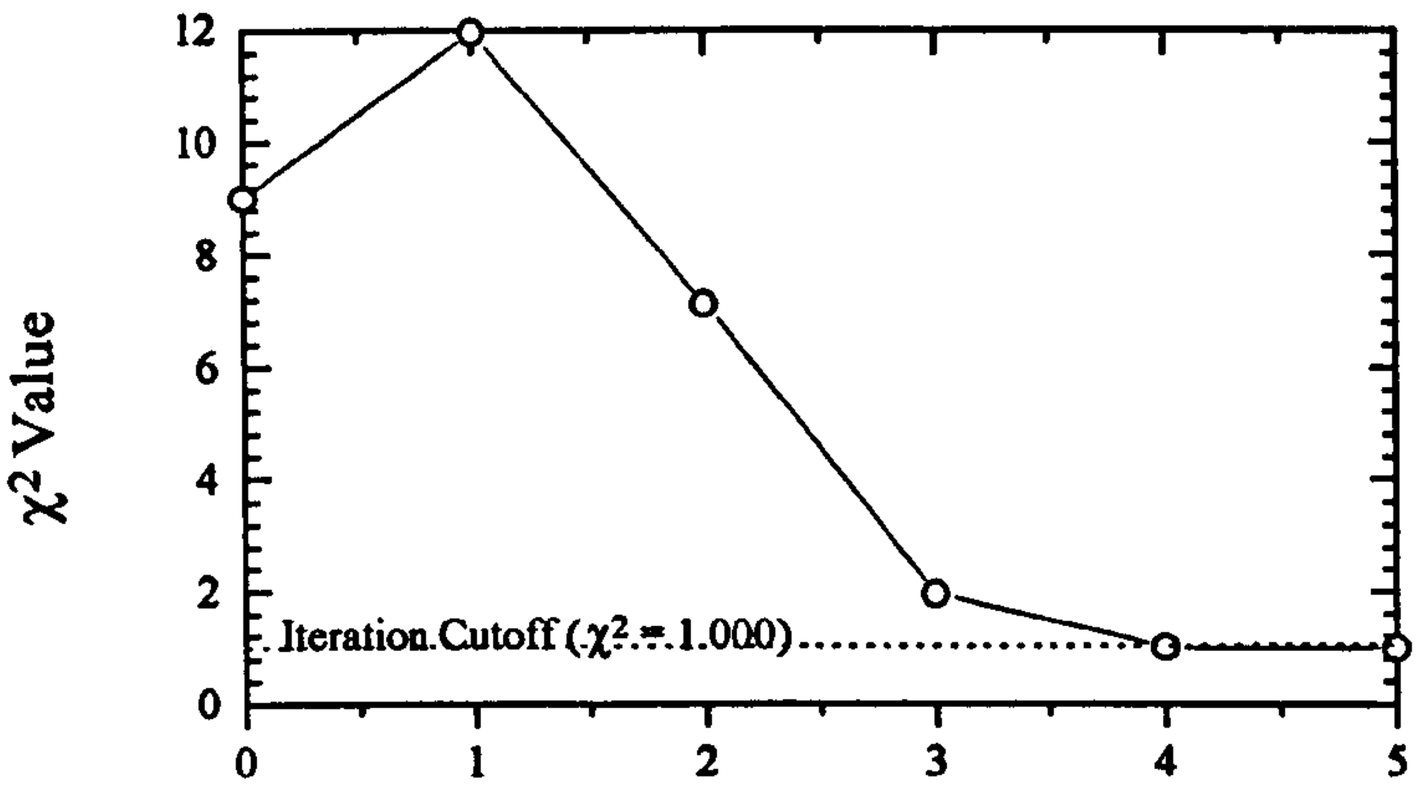

FIGURE 6.10 χ^2 value versus iteration number. Iteration stops when χ^2 drops below 1.000.

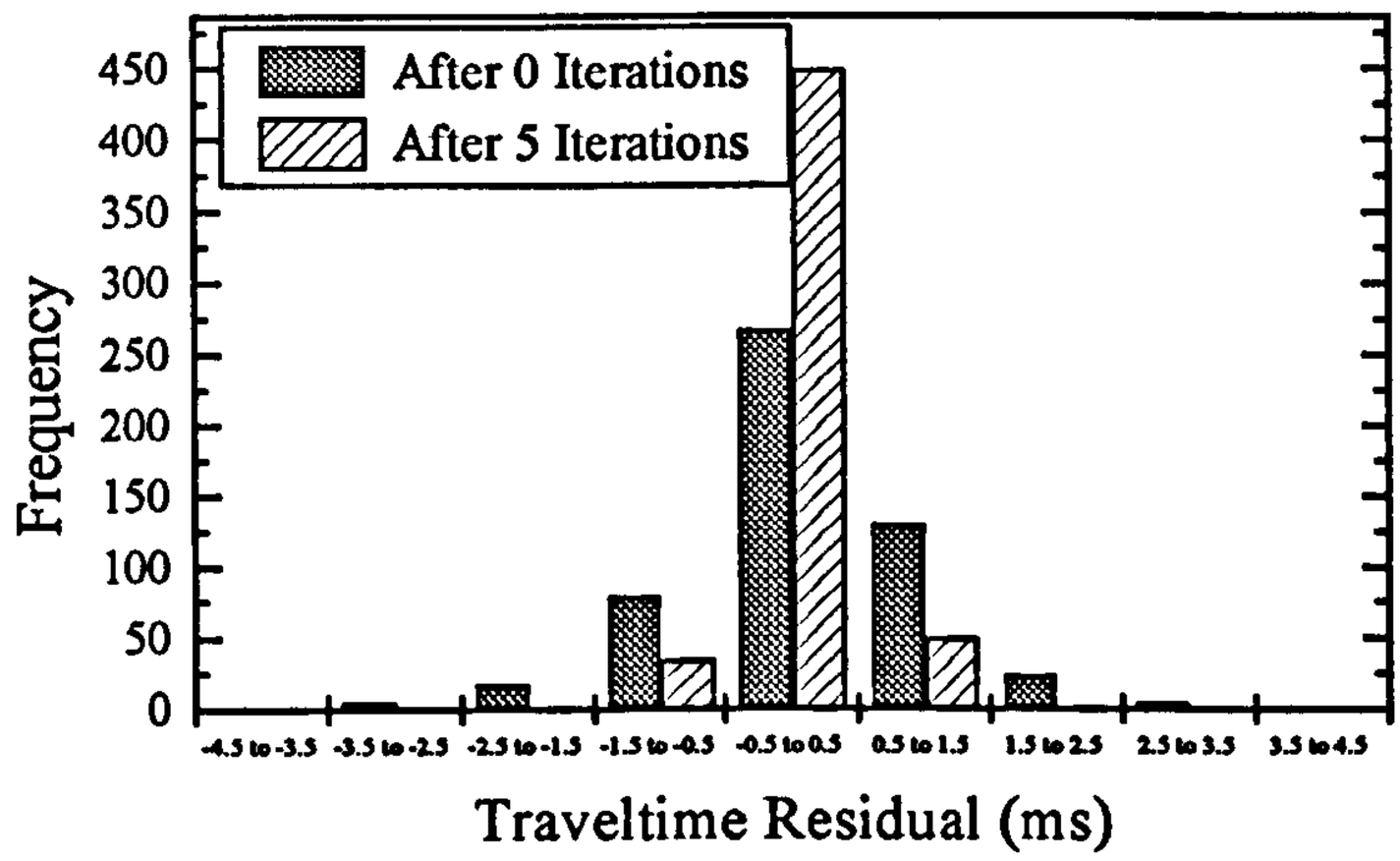

FIGURE 6.11 Traveltime residuals for transmission raypaths after 0 and 5 iterations.

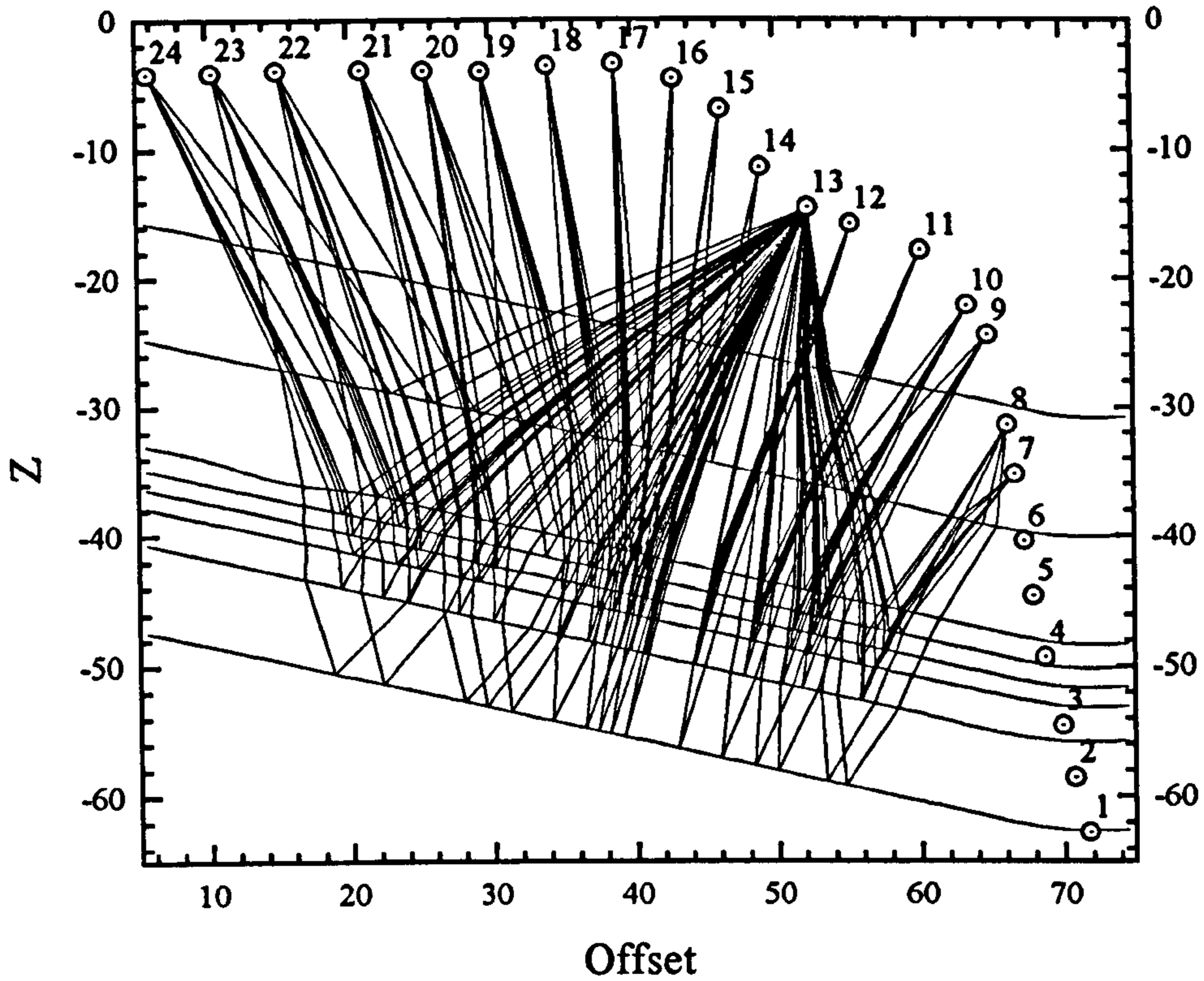

FIGURE 6.12 Raytracing (Forward Modelling) for a seismic source at geophone 13 from interfaces 2 to 9 in the transmission traveltime model.

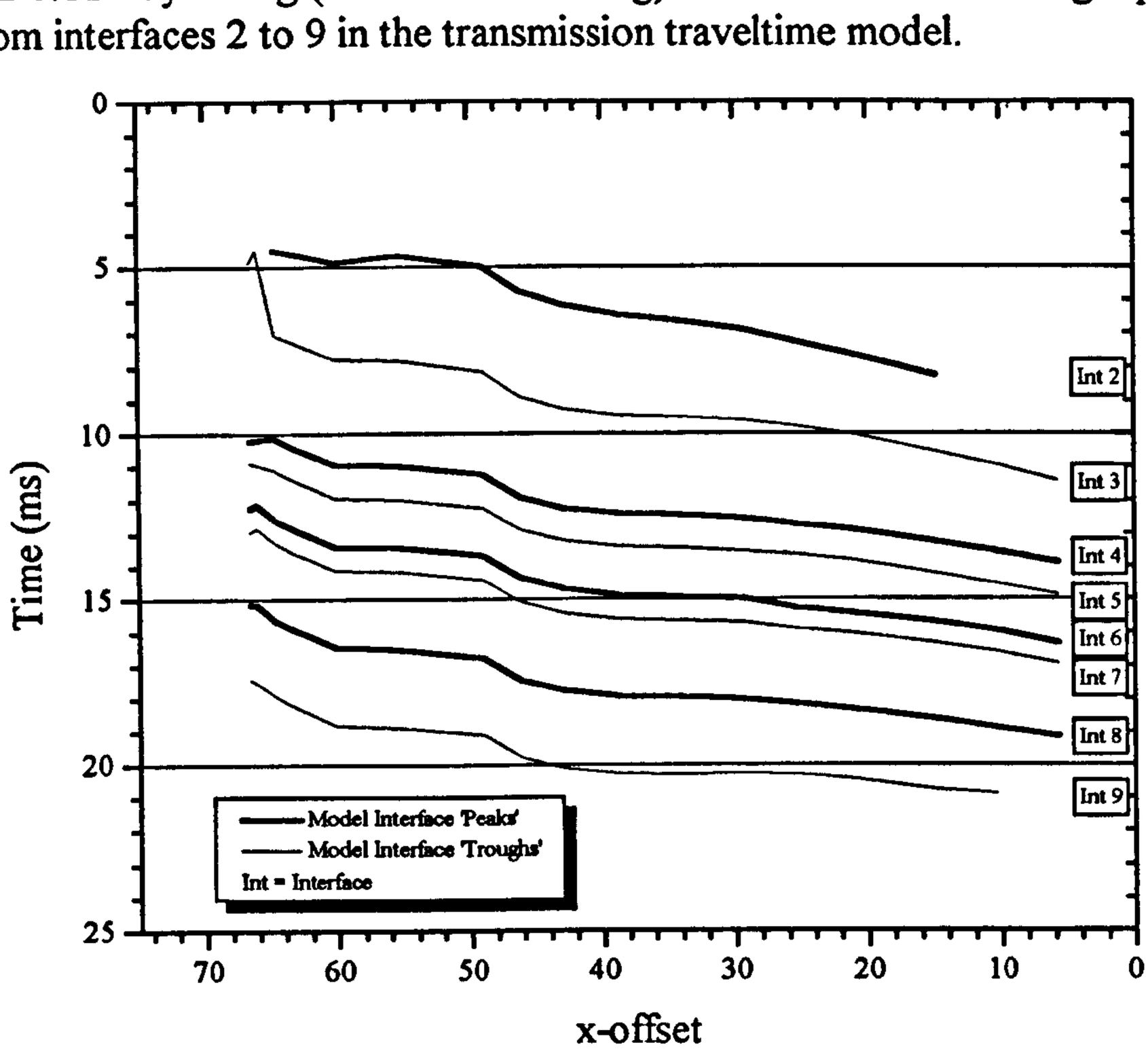

FIGURE 6.13 Reflection peaking arrival times versus x-offset for raytracing in figure 6.12, thick lines represent model 'peaks' and thin lines represent model 'troughs'

to search for the same arrivals in the field data. The process is illustrated in figures 6.12 and 6.13. Figure 6.12 shows the reflection raypaths for a source at geophone 13 reflected from interfaces 2 to 9. The raytracing method used is discussed in chapter 5, section 5.3.2. The ray perturbation equations are solved for the raypath direction and the amplitude. Figure 6.13 shows the peaking arrival times plotted against x offset and figure 6.14 shows a simple synthetic seismogram, showing the phase and relative amplitude of the arriving reflection peaks or troughs. A reflection peak indicates an arrival from an interface where the velocity increases across the two layers. Conversely, a trough indicates a reflection arrival from an interface where the velocity decreases across the two layers. The amplitude of the arriving reflection peak or trough is dependent on the magnitude of the difference in velocity across the reflecting interface. The larger this velocity difference, the greater the amplitude of the returned reflection. A combination of plots 6.13 and 6.14 for each source location and interface reflector was used as an aid to identify reflections in the field data and determine from which geological interface they were likely to have originated in the transmission model.

The real dataset for the source at geophone 13 is shown in figure 6.15. A comparison of reflection peaking identified in this field data and the theoretical reflection arrivals is shown in figure 6.16. Note that it was possible to identify the likely original reflectors based on this comparison. The plot shows that there was good agreement between theoretical and real data in the region of x-axis offset from 65 m to 35 m, corresponding to source-receiver paths from geophone 13 to geophones 7 to 18, reflected from interfaces 2 to 9. The apparent agreement deteriorates at x-offsets of 35 m and below, corresponding to source-receiver paths from geophone 13 to geophones 19 to 24. This apparent divergence of the real data away from the theoretical data would indicate that the transmission model was incorrect in this region of the survey area directly below geophones 17 to 24 for layers 2 to 9. This agreed with direct observations at the site, and the suspected location of the old stowed workings. If these workings did indeed cross the survey area in this region, they would create a low velocity anomaly and therefore explain the extended reflection peaking arrival times. Such a region was not revealed by the transmission tomogram because ray coverage was not sufficient in this area. The extended reflection arrival times in this area may also have been due to velocity variation in the limestone layers 2 and 3 and variation in the thickness or velocity of the shale partitions in layers 4 to 7, since these were now sampled by the reflection raypaths. The transmission model in these areas is simply the value assigned in the initial velocity model and was not raytraced or altered in the transmission traveltime inversion.

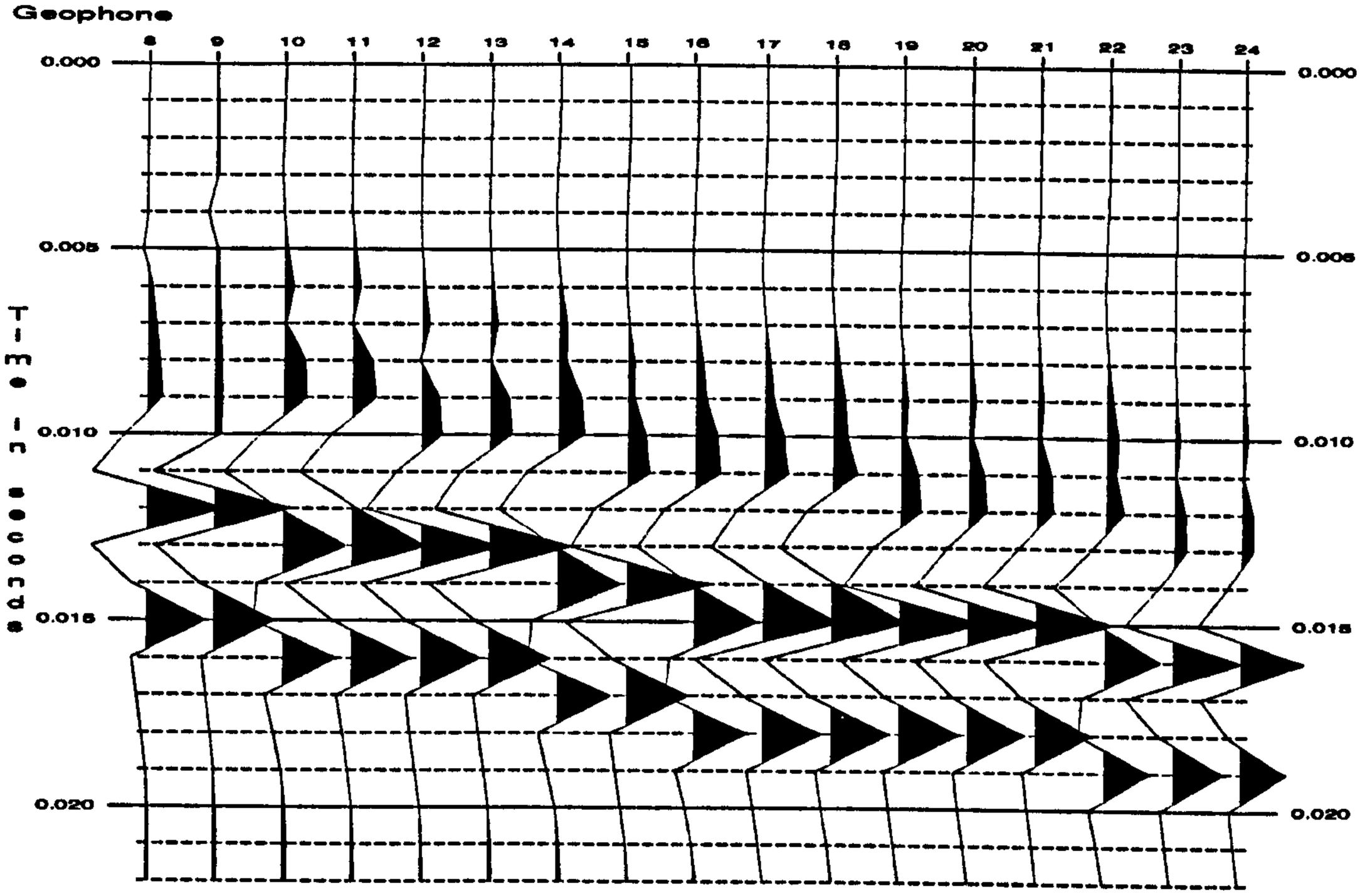

FIGURE 6.14 Synthetic Seismogram created by convolving a source wavelet with the solution to the ray equations for the raytracing shown in figure 6.12. Seismogram shows the phase and relative amplitude of the arriving reflection peaks when a source was initiated at geophone 13.

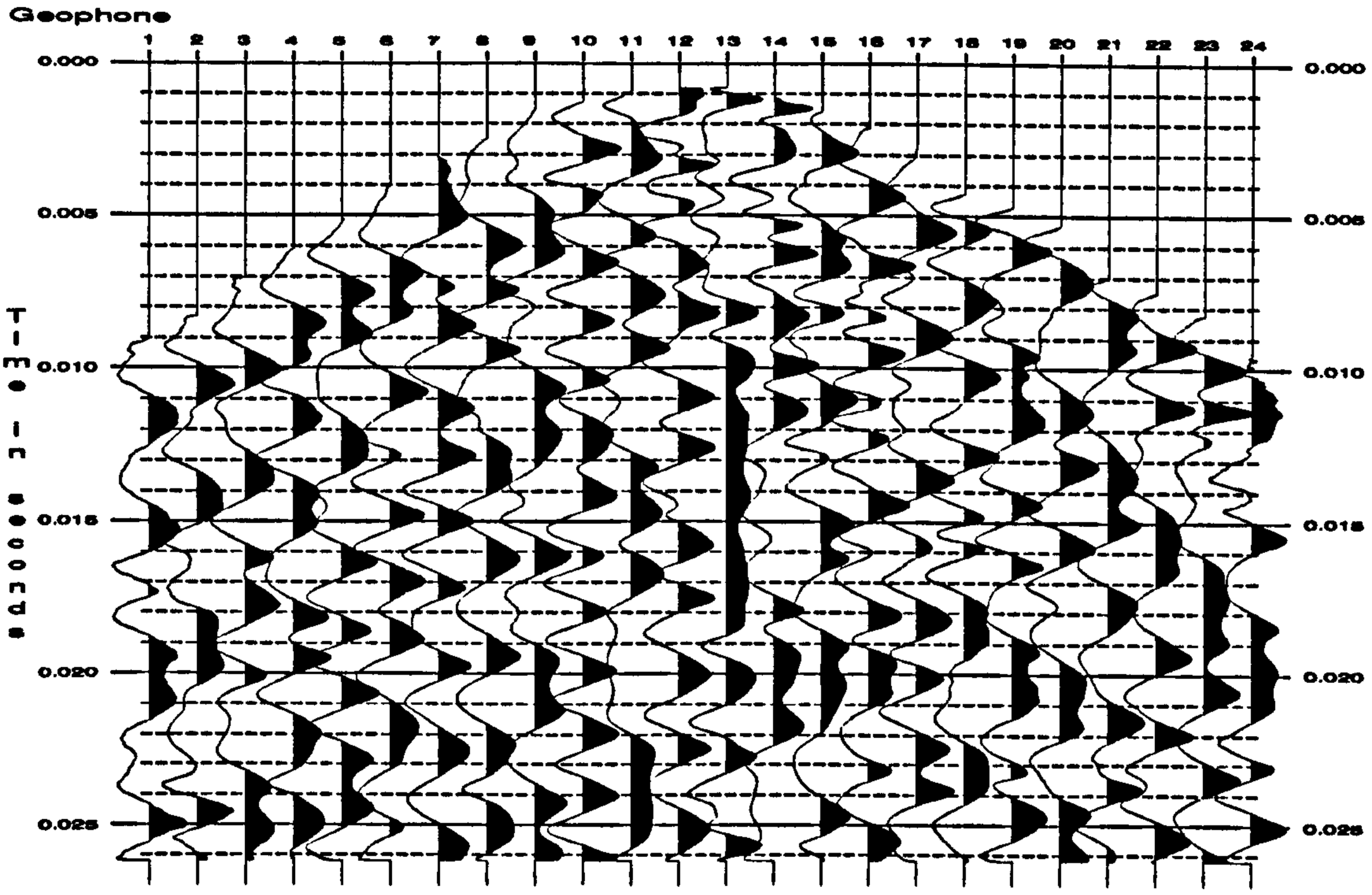

FIGURE 6.15 The real dataset received across the geophone array when a source was initiated at geophone 13.

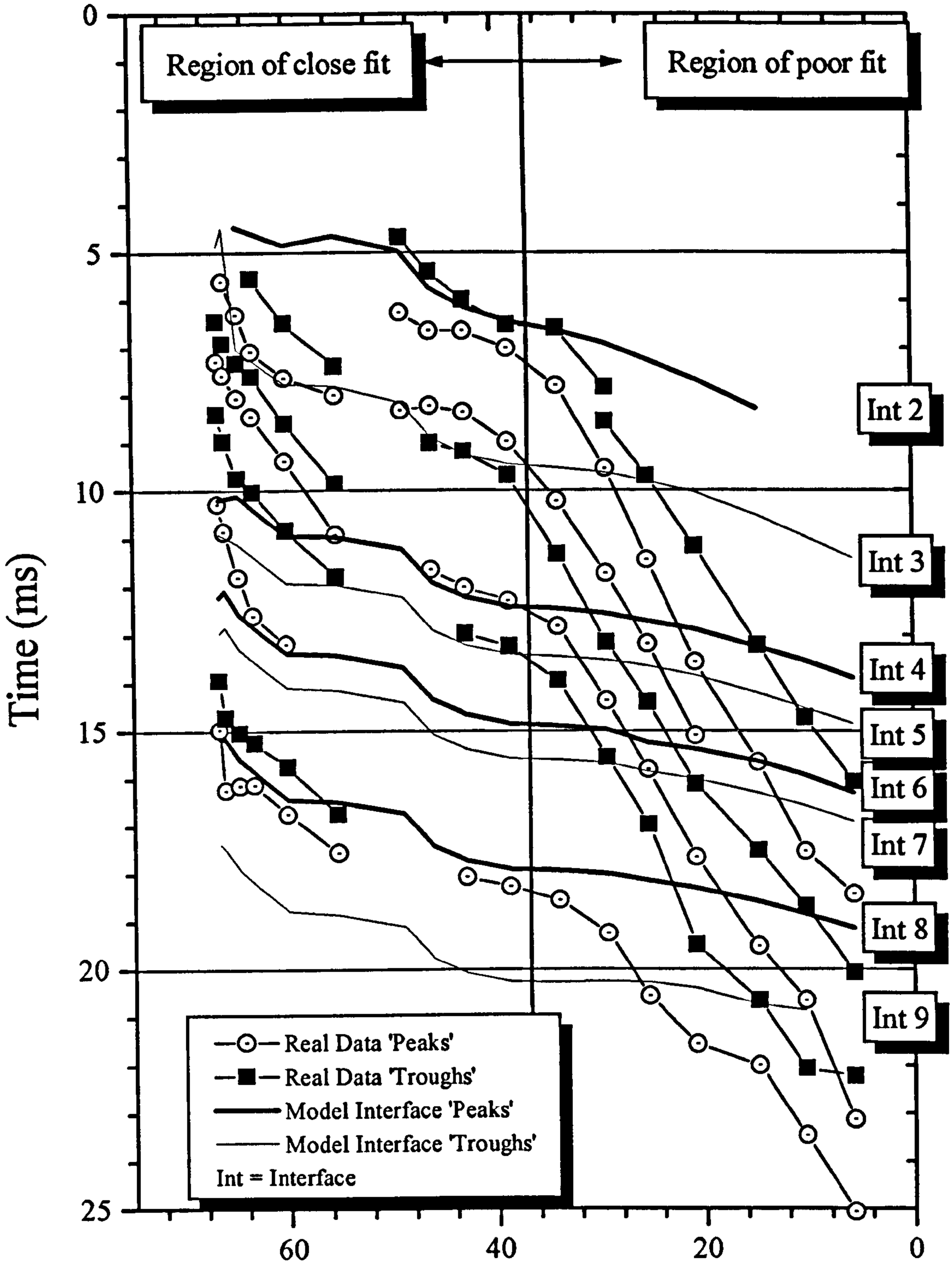

FIGURE 6.16 Comparison of reflection arrival times from figure 6.15 and theoretical arrival times calculated from forward modelling in figure 6.12, showing area of best fit.

6.2.4.5 Combined Reflection and Transmission Traveltime Inversion

Forward modelling helped to reveal, on average, around 32 reflection traveltimes for each source point, giving 561 extra raypaths for the combined raypath inversion process. These traveltimes were then inverted as in the transmission model but with the added control of a raypath 'filter' based on the residual traveltime differences. This 'filter' removed reflection arrivals which were obviously incorrectly identified from the forward modelling procedure. The filter had a user defined cut-off where, if a raypath traveltime residual exceeded this value, it was automatically removed from the inversion procedure. The cut-off was set at 4 ms which ensured that true picking errors were removed and raypaths which had apparently extended traveltimes (from the forward modelling) were still included in the inversion step. The resulting tomogram is shown in figure 6.17 with the associated raypaths shown in figure 6.18. This result was achieved after 10 iterations involving 1049 traveltimes, some 48 traveltimes being 'filtered' out by the above process. The cut-off for the iterative process was again set at 0.38 ms and the change in observed deviation and χ^2 misfit versus the iteration number is shown in figures 6.19 and 6.20 respectively. The change in traveltime residual distribution between 0 and 10 iterations is shown in figure 6.21.

The transmission model was used as the initial velocity model for the combined traveltime inversion, but with a few alterations to improve the resolution. These alterations were possible because of the increased raypath numbers and consisted of,

- decreasing the x line spacing from 5 to 3 m
- adding an extra layer for the suspected location of the old workings.

It is obvious that the CTRT model is much more detailed and covers a greater area than the transmission model. Referring to figure 6.18 shows that the ray coverage of the survey area is more intense and therefore the resolving power of the data is greater. It should also be noted that successful tomography relies on good 'angular' coverage of an object. The reflection raypaths have greatly improved this angular coverage. The size of the survey area has increased by around 50% due to this reflection raypath coverage.

The major outcome of these improvements to the tomogram is that some low velocity anomalies have been revealed such as,

- the likely location of the suspected old workings across the top of the survey area, coming in at x = 5, y = -10 m and extending horizontally into the survey area up to around x = 35 m.

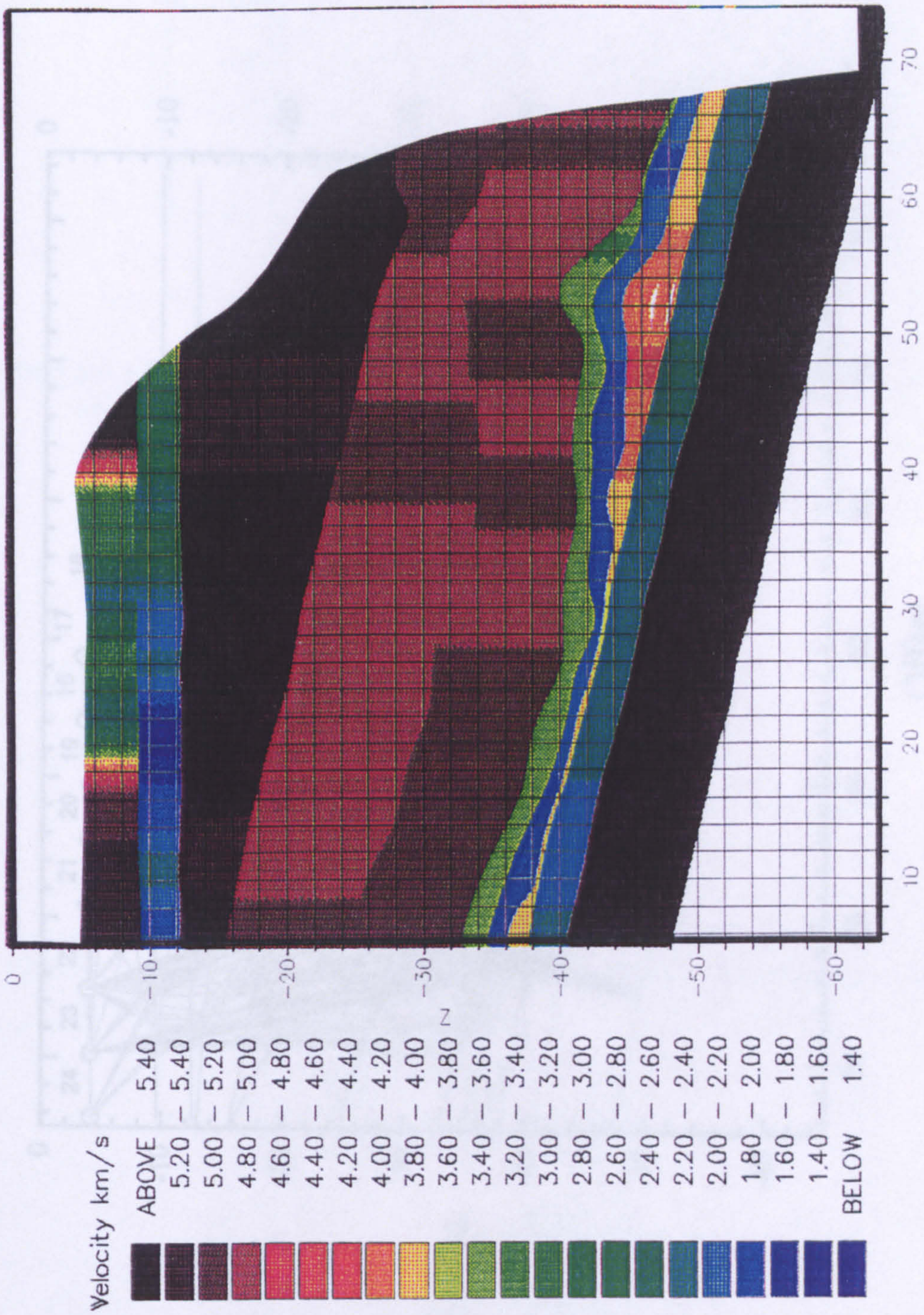

FIGURE 6.17 Combined transmission and reflection traveltime tomogram, achieved after 10 iterations with the inversion of 1049 arrivals.

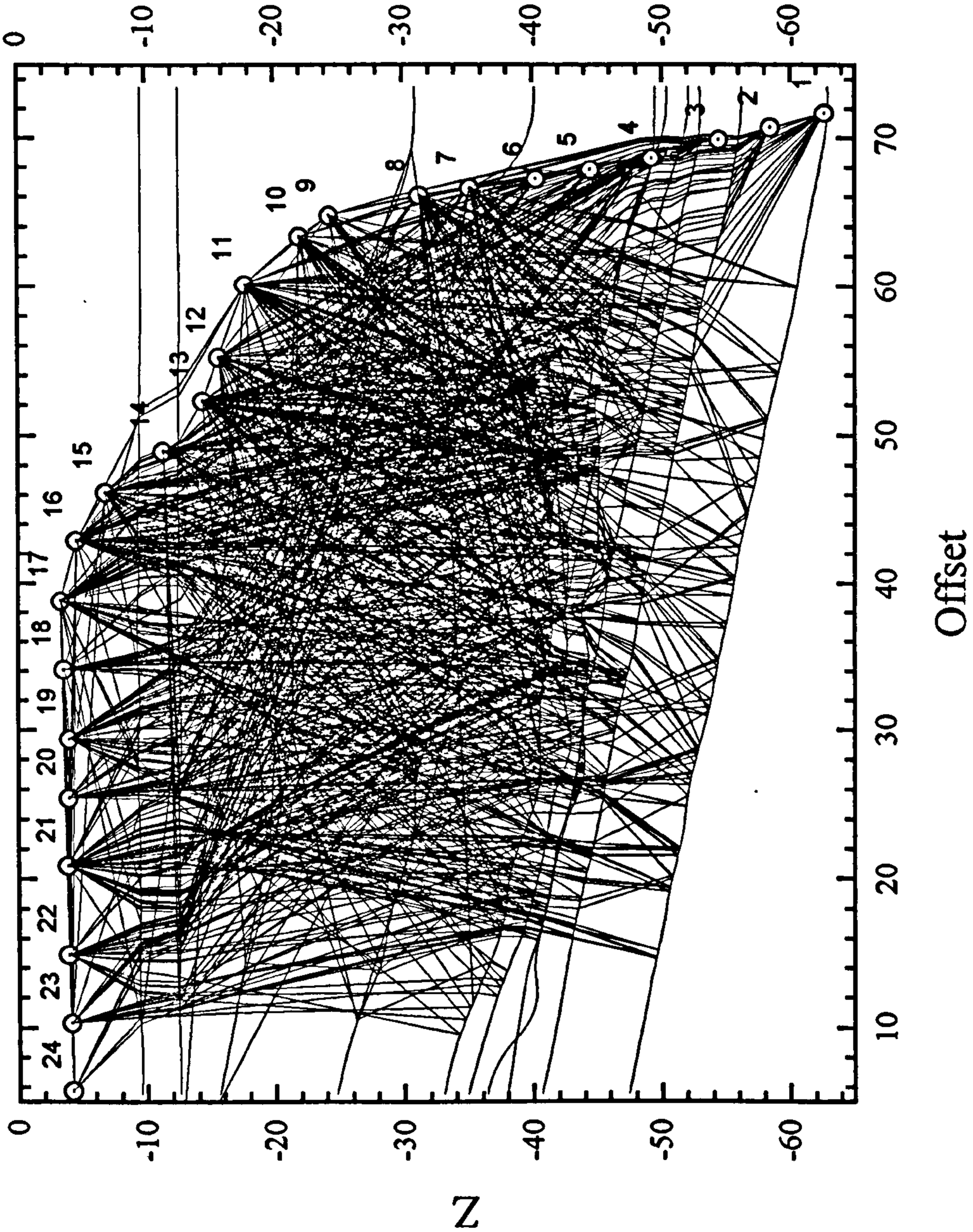

FIGURE 6.18 Raytracing for the combined transmission and reflection traveltime velocity model in figure 6.17

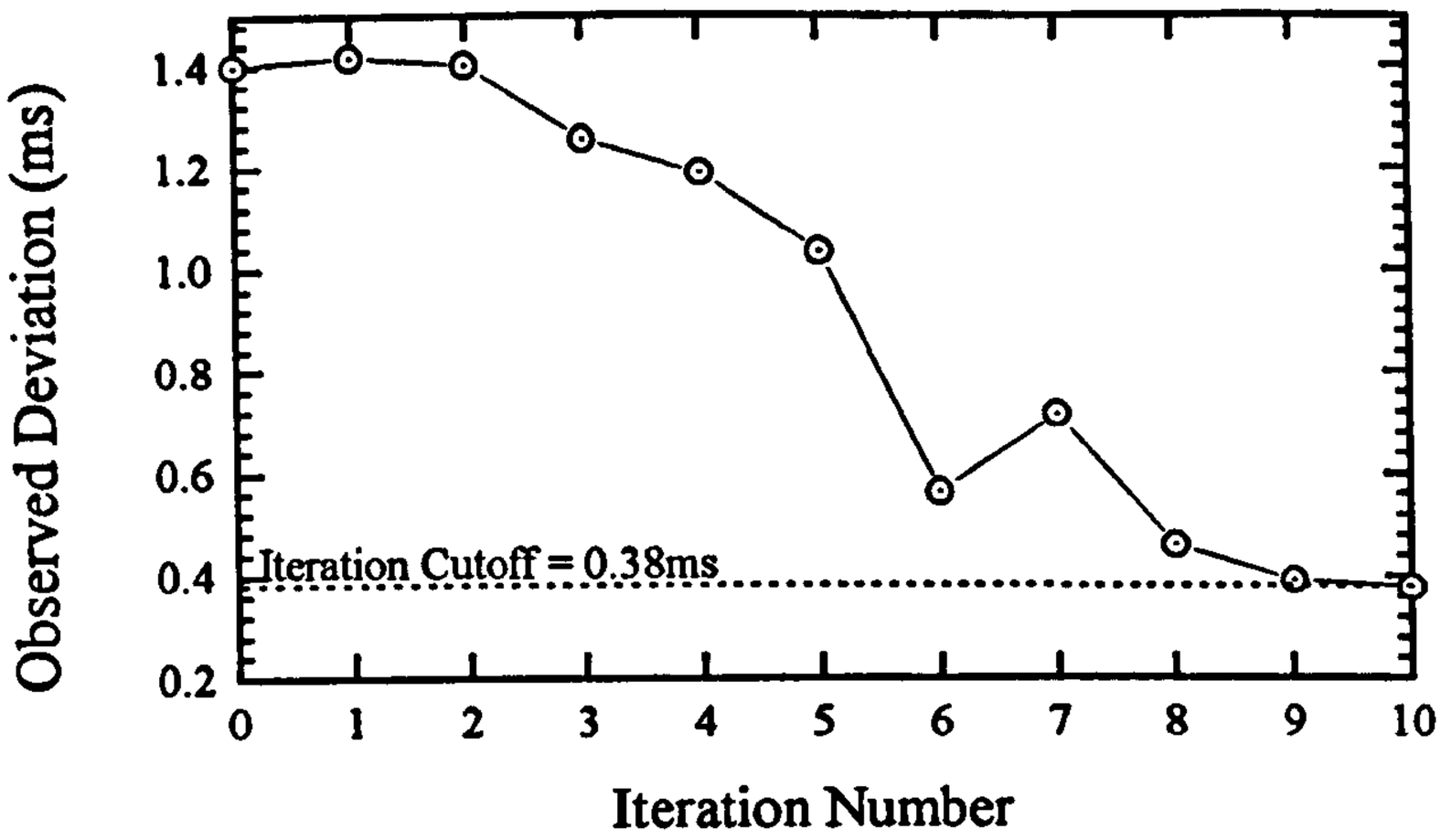

FIGURE 6.19 Model observed deviation versus iteration number for the combined inversion process.

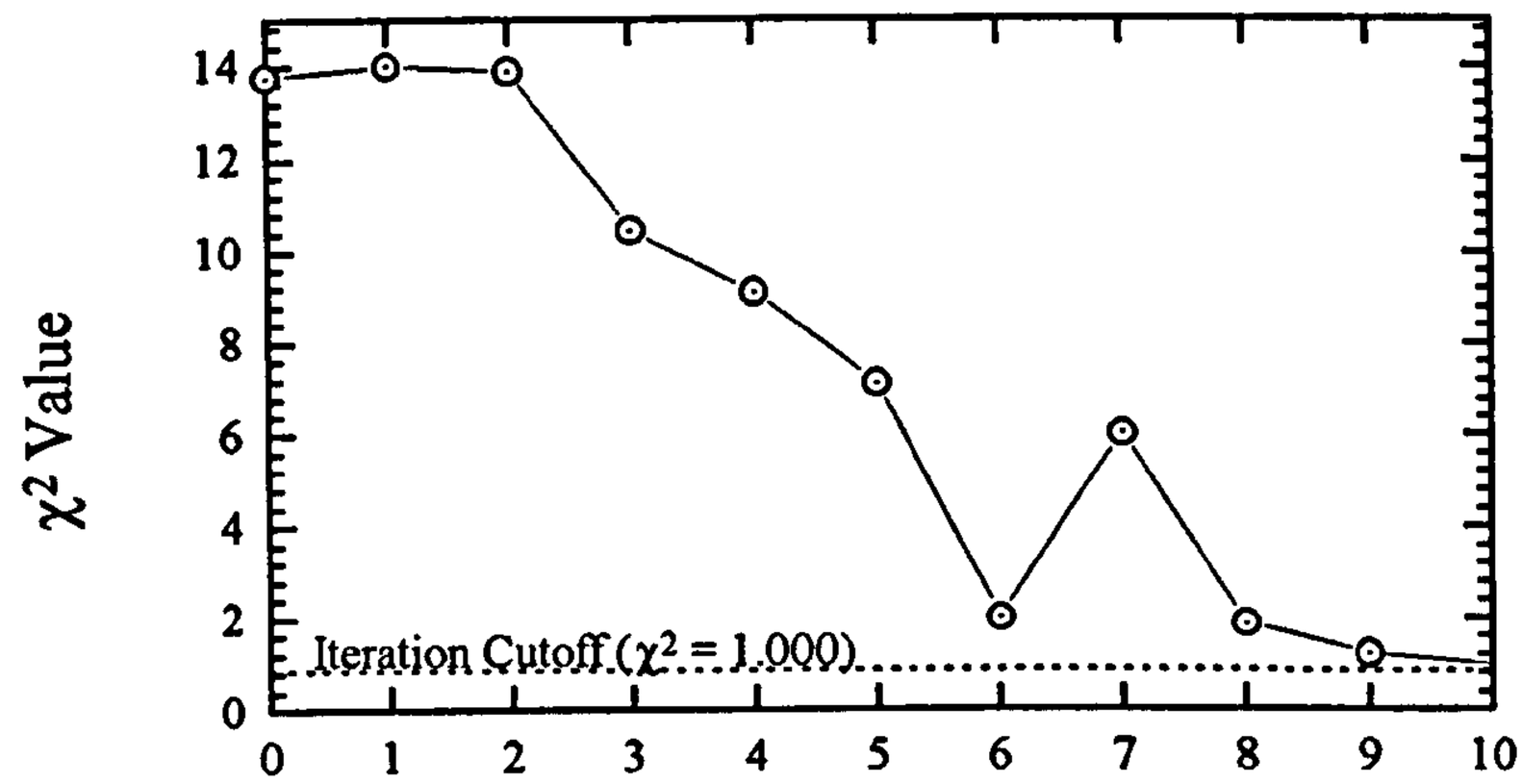

FIGURE 6.20 χ^2 misfit versus iteration number. Iteration process stops when χ^2 drops below 1.000.

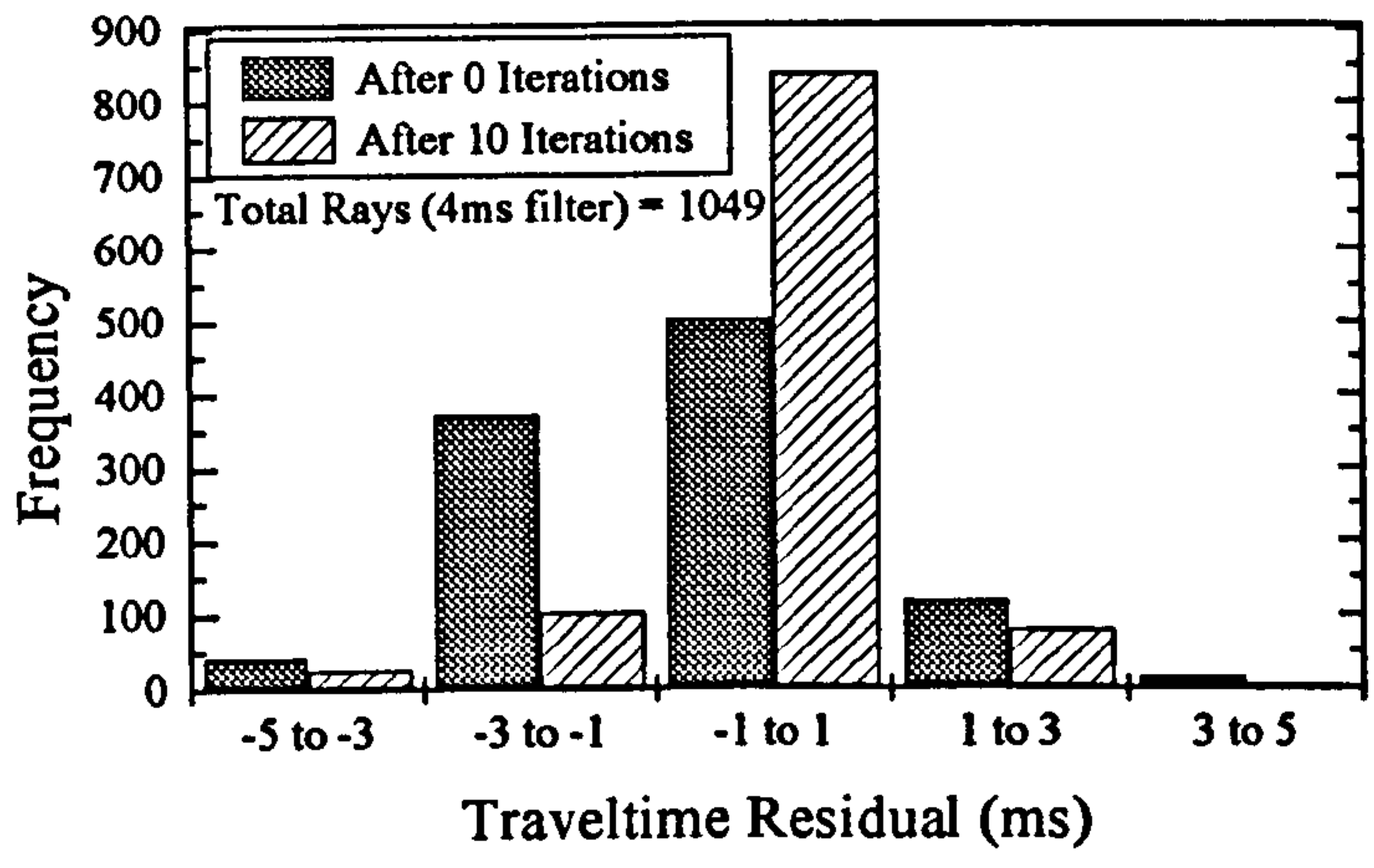

FIGURE 6.21 Raypath traveltime residual distribution plot after 0 and 10 iterations.

- the location of a crosscut between the existing reef drive and these old workings at x = 25 m, y = -4 to -10 m. This crosscut has been stow packed with waste limestone and is visible in the existing reef drive. However the velocity variation appears to be spread out from x = 20 m to x = 40 m. The probable explanation for this low velocity zone is the fractured rock mass in this area between the two reef drives. During further inspection of the reef drive this poor ground was identified.

- The shale banding across the region has now been imaged in greater detail. However the interface locations may not be strictly correct due to errors in the reflection picking but they do take on a more 'geological' appearance in comparison to the straight interface initial velocity model definition.

- The country limestone rock between the old workings and the shale partings shows little velocity variation apart from at the apparent change in limestone type at interface 3 from a finer, darker limestone to a coarser, more chrinoidal, whiter type.

6.2.5 Conclusions.

In conclusion, this chapter has successfully demonstrated that in spite of poor geometry at a potential tomographic survey site, by use of the CTRT method, a high resolution survey was still possible. The more often used, standard transmission time method was not able to resolve geological structure and old workings in the area, due to the limited spatial and angular ray coverage imposed by poor geometry access problems. By including reflection traveltimes in the inversion process, the survey area was effectively doubled in size. The number of raypaths was doubled from the transmission time raypaths and the angular ray coverage across the area greatly improved. As a result, old stowed workings were successfully identified and geological structure in the survey area was resolved with a good degree of accuracy.

This method has many potential applications in both the mining and civil engineering industries for imaging geological structure which is inaccessible to a normal transmission tomographic survey. In effect, the technique makes tomography a more attractive and affordable tool for rock mass characterisation since it negates the need for expensive boreholes or galleries to site source and receiver positions in more favourable locations. The flexibility of the method means that it could be employed in rock mass surveys from existing galleries or roadways which were designed purely for production or excavation purposes. The pre-requisite for use of the method is a small knowledge of the likely geological structure in the survey area, in terms of the changes in rock types and the approximate location of major faults or other discontinuities. This

kind of detail would normally be pre-established by some other form of site investigation or from local geological knowledge in the vicinity. The technique can then be used to more accurately define this geological structure whilst identifying any unsuspected zones of poor rock mass condition, signified by low velocity anomalies.

CHAPTER 7

7. Cross-hole Tomography at Morley Quarry

7.1 Introduction

The previous chapter considered an underground field case where the CTRT method was successfully employed to survey the velocity structure of an inaccessible area. This chapter will consider a more common type of survey known as crosshole transmission tomography, carried out between two boreholes at a surface quarry site. It will show that the CTRT variant can be used to produce a velocity model based solely on transmission traveltimes which is comparable to the more popular seismic tomography reconstruction techniques.

7.1.1 Field Site

The two boreholes are located in the disused Morley Quarry in the Charnwood Forest area of Leicestershire, England. The quarry worked the Charnian system of rocks which are Precambrian in age. The outcrop of this rock type is unique to only three locations in the East Midlands area and is due to an eroded anticline structure that plunges to the south-east. Further to the north, the Charnian succession disappears beneath younger carboniferous limestone, (Evans et al, 1968). The two unlined, 8 inch diameter boreholes at the site are located in the quarry floor and are 820m and 60 m deep and therefore ideal for crosshole 2-D tomography. A plan of the quarry site is shown in figure 7.1. The water table occurred at a depth of 11 m and the boreholes were water filled below this level. Mapping of the quarry walls revealed several general geological features,

- The rock mass consists of large bedded lithological units which dip to the north at an angle of between 15 and 20 degrees.
- A general pattern of vertical joint sets was observed cutting across the beds at an angle of 60 degrees.
- A shatter zone was exposed in the west wall in line with the midpoint between the two boreholes where there was evidence of intense folding which could be associated with an antithetic fault zone. The corresponding east side of the quarry showed a similar structure suggesting that the zone passed directly between the boreholes.

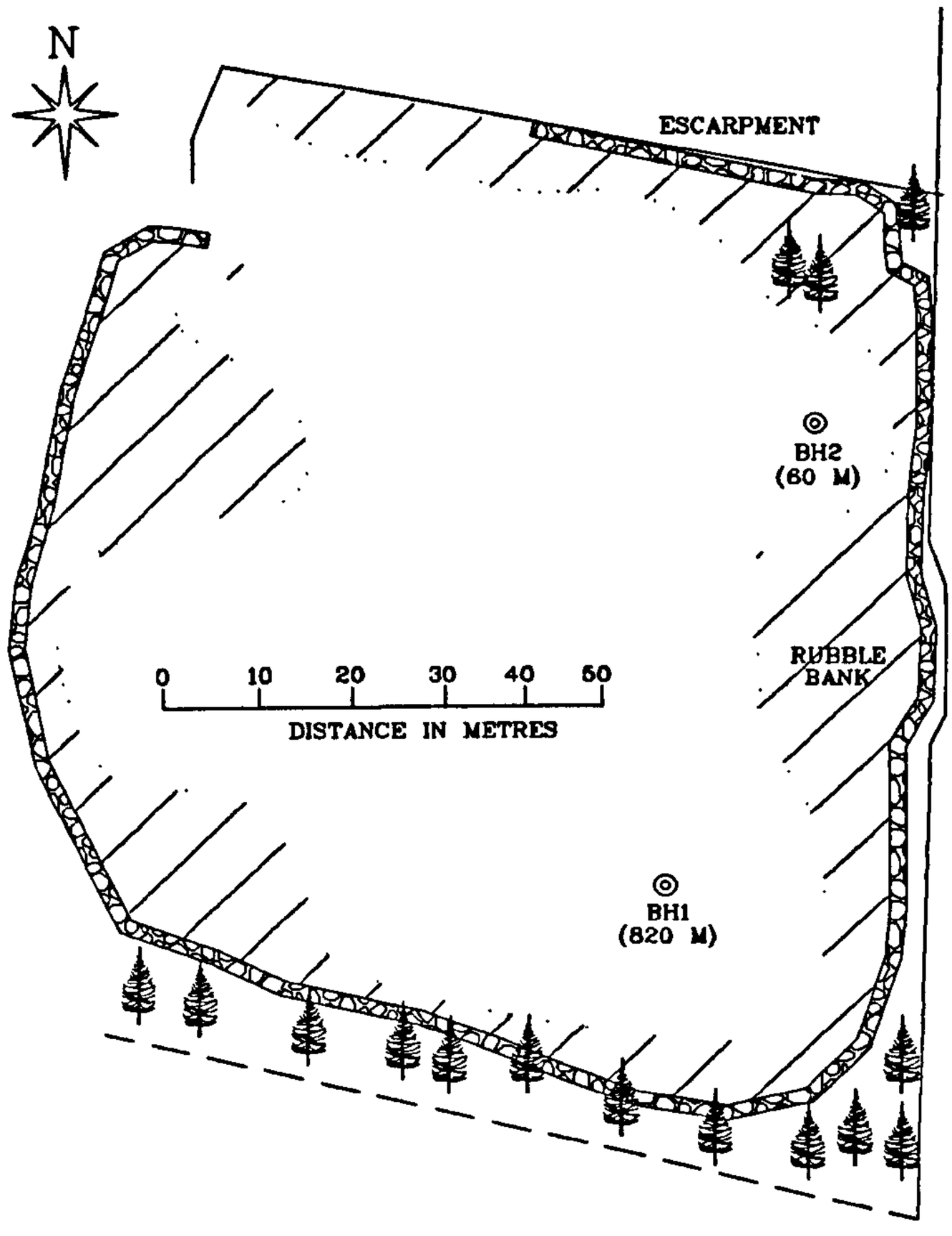

FIGURE 7.1 Plan of Morley Quarry showing the location of the two boreholes, BH1 (820m depth) and BH2 (60m depth).

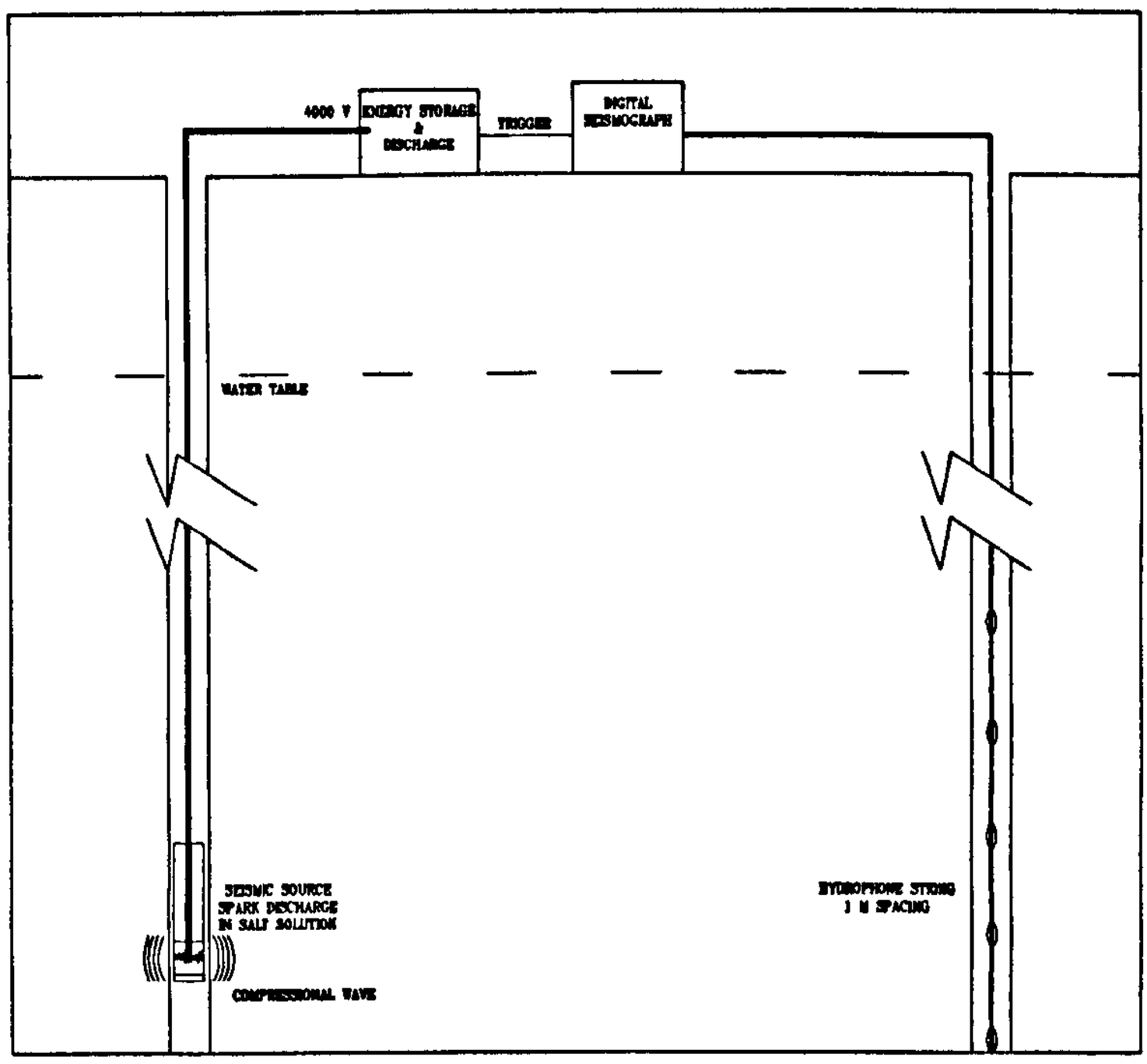

FIGURE 7.2 Experimental set-up at the Morley Quarry site.

7.1.1.1 Field Work Aims

The survey was being carried out to prove the suitability of the sparker as a tomographic field survey source. Borehole number 1 had already been logged with a variety of instruments and this information was available to give localised knowledge of the site within the vicinity of the hole. From this information it had already been identified that a near surface fracture zone existed as a result of quarry blasting activities. Mapping of the east and west quarry walls also indicated that a possible antithetic fault zone passed directly through the middle of the cross section defined by the two boreholes. A tomographic survey should therefore be able to identify the extent and depth of the man-induced fracture zone and also locate the suspected fault.

7.2 Experimental Set-up

The equipment used for the survey is shown in figure 7.2 and consisted of a string of 10 hydrophones in borehole 2 and a sparker source in borehole 1. Data was acquired using an ABEM Terraloc seismograph, triggered by the sparker source power unit. The sparker source consisted of a borehole sonde which comprised of two electrodes housed in a removable container which was filled with a saturated salt solution. An electric charge was built up in a surface power unit from a 24V battery source and discharged across the two electrodes at a voltage of 4000V. The resulting spark produced an expanding gas bubble within the electrolyte solution which produced a short compressional seismic pulse in the frequency range of 250 Hz to 3.5 kHz with peak power at 570 Hz. The source is comprehensively described by Baria et al (1989) and is ideal for tomographic imaging surveys because of its repetitive nature, high frequency content and reliability.

7.3 Seismic Data

7.3.1 Acquisition and processing

Seismic energy was introduced in to the rock mass between the two boreholes using the sparker source. The signal character was optimised by stacking data for a total of 10 shots at each source point. To process the data, traces were muted below 5 ms to remove a recurrent electromagnetic spike induced by the sparker trigger, and then filtered using a 2, 4 pole Butterworth filter across 700 to 1000 Hz. The 4-pole filter at 1000 Hz eliminated high frequency noise that was present throughout the entire dataset. A typical common source gather is shown in figure 7.3 for a source initiated at

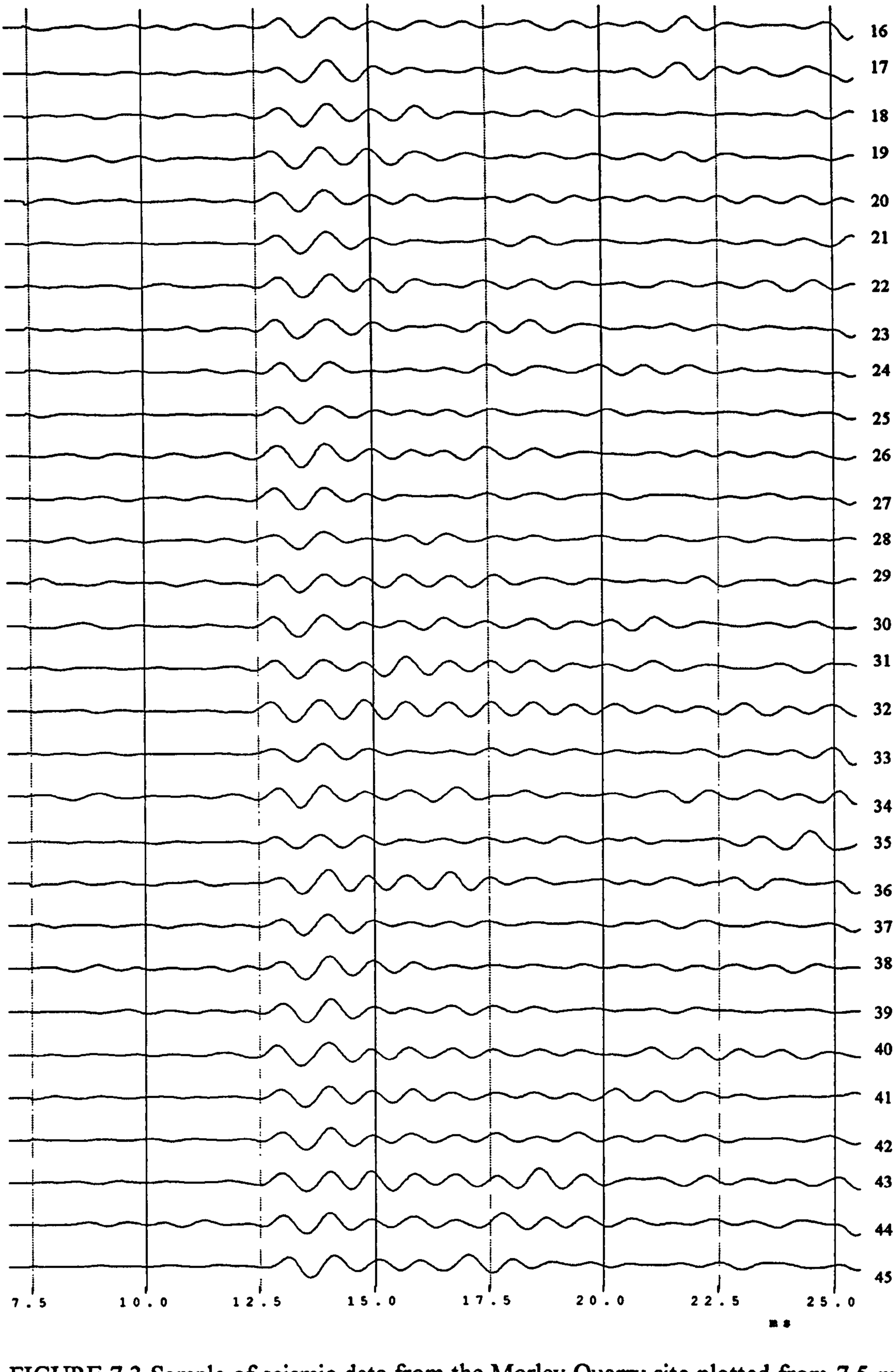

FIGURE 7.3 Sample of seismic data from the Morley Quarry site plotted from 7.5 ms, filtered between 700 and 1000 Hz. Each trace number corresponds to a hydrophone depth in borehole 2. Shot point at depth of 34 m in borehole 1.

34 m depth in borehole 1 and received across the entire hydrophone array. First breaks are well defined and arrive at around 12.5 ms.

7.3.2 Transmission Traveltimes

Of the total 840 raypaths measured, 790 transmission traveltimes were identified successfully. The remainder of the traveltimes could not be identified due to poor signal to noise ratios. A 3-D display of P-wave traveltime picks is shown in figure 7.4 and such a plot was used to check the traveltime pick quality. For a homogenous constant velocity medium, the surface would be saddle shaped, where arrival times would be solely dependent on the source-receiver offset. In heterogenous multi-velocity media, high velocity zones appear as depressions, whereas low velocity zones are elevated relative to the surrounding area. Bad picks show up as isolated spikes or holes in the surface. Figure 7.4 is marginally saddle shaped with obvious undulations suggesting the presence of a significant amount of velocity heterogeneity. Traveltimes decrease and therefore velocities increase with depth in the borehole. The lack of spikes and holes in figure 7.4 suggests that the pick quality is good.

The traveltime dataset was further checked using the techniques depicted in figure 7.5 (a) and (b). A time-distance scatter plot was generated (figure 7.5 (a)) where distances for each raypath were calculated with a straight ray assumption. A second plot of the distribution of apparent velocities was also generated (figure 7.5 (b)) based on the same assumption. In figure 7.5 (a) in a manner analogous to 1-D surface refraction studies, any linear trends may be associated with structural elements or refractors between the two boreholes. The scatter within the plot is considerable, suggesting the same finding in figure 7.4 of considerable velocity heterogeneity. Similarly plot 7.5 (b) shows apparent velocity variation of between 4.2 and 5.2 km/s and assuming a normal distribution, the data averages at 4.72 km/s with a standard deviation of 0.19 km/s. Deviations from this mean (greater than two standard deviations) can be considered to be caused by velocity heterogeneity between the boreholes due to fracturing from quarry workings, or change in geological structure.

Given the mean velocity it is then possible to estimate the seismic resolution that might be expected from the tomographic inversion in terms of the minimum resolvable feature size. Current theory suggests that the resolution of transmission traveltime tomography is one wavelength (Williamson, 1991) and therefore for transmission traveltimes picked from data high-pass filtered at 700 Hz with a mean velocity of 4.72 km/s, the expected seismic wavelength is 6.74 m.

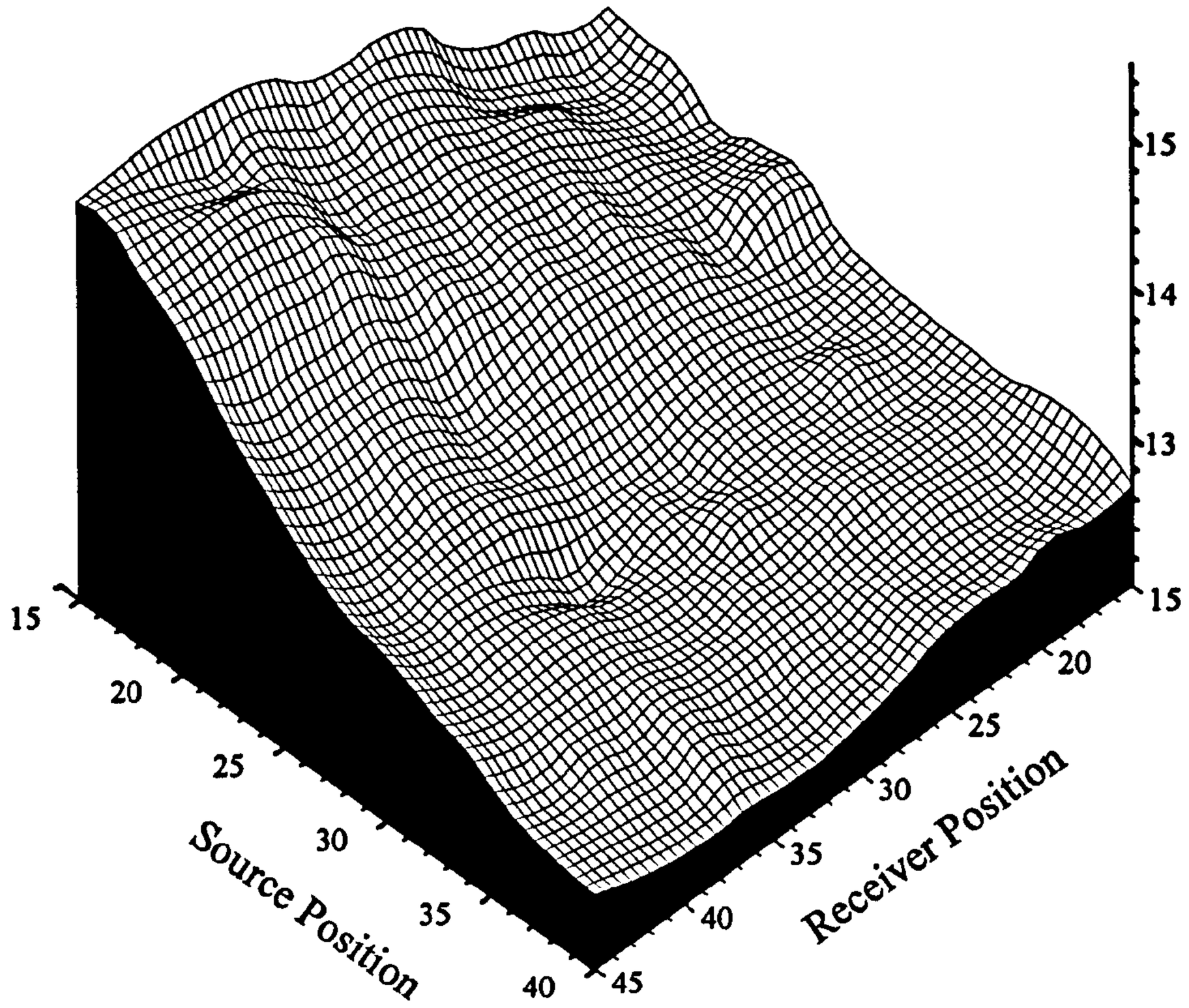

FIGURE 7.4 3-D display of P-wave traveltime picks. Good quality picks are indicated by the lack of holes or spikes. Minor undulations are caused by velocity heterogeneity.

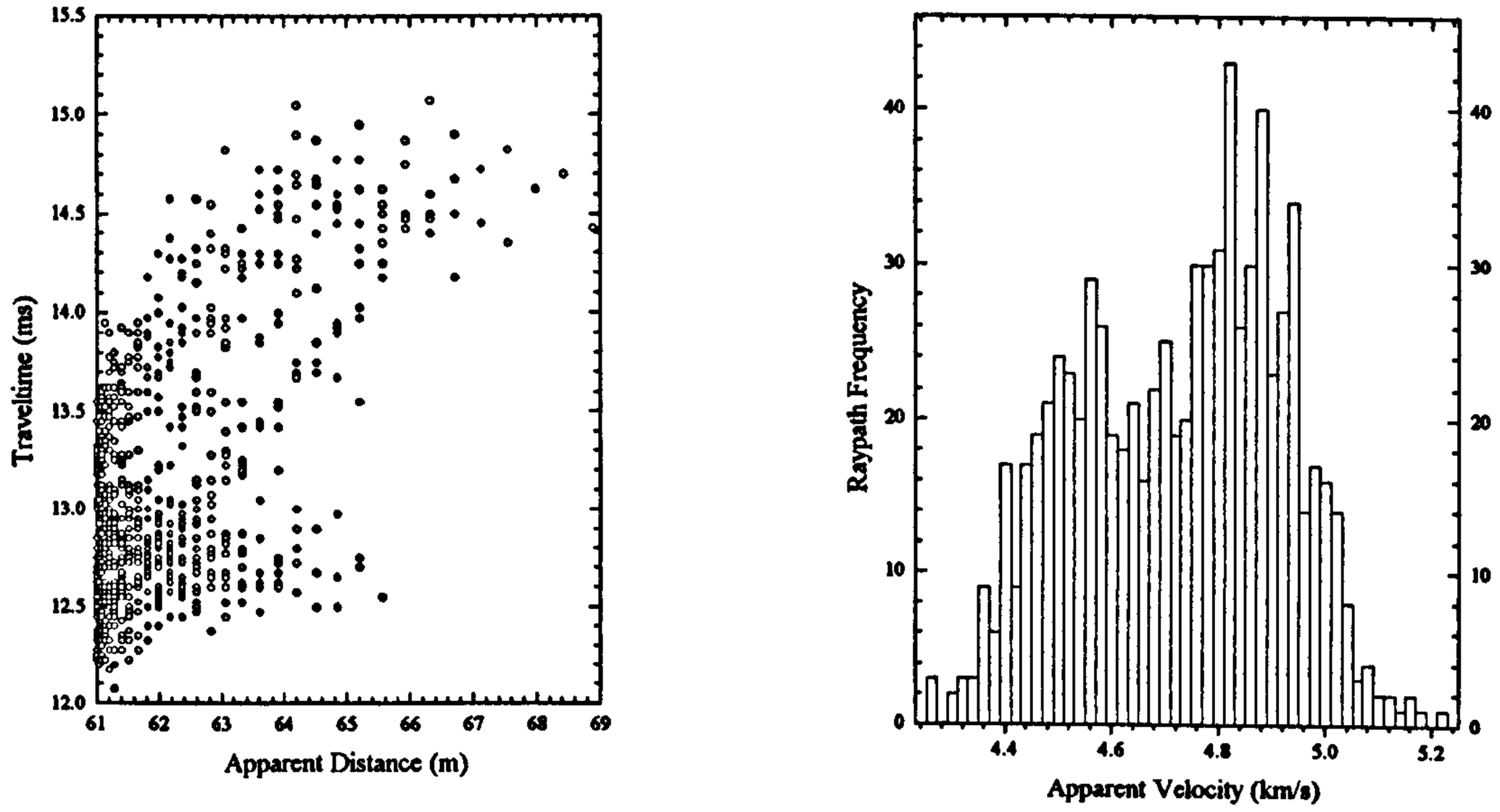

(a) (b)

FIGURE 7.5 (a) Apparent distance (straight raypath assumption) versus traveltime. (b) Distribution of calculated apparent velocities.

7.4 Borehole Information

Information was available for borehole 1 from 10 metres below surface down to a depth of 820 m for the following logs,

- Gamma
- Neutron
- Borehole Televiewer
- Sonic Velocity and full sonic waveform
- Dip meter
- Resistivity

The logging was carried out by three different contractors (Schlumberger, BPB and Atlas Wireline) and could therefore be checked for consistency.

7.5 Tomographic Transmission Traveltime Inversion

7.5.1 CTRT Method

Because of only limited knowledge of any geological interface locations between the two boreholes it was decided to use a block or cell initial velocity model for inversion of the transmission traveltimes similar to those used by more popular tomographic reconstruction algorithms. By defining an x-line spacing of 3 metres and layer thickness of 3 metres, the area between the two boreholes was effectively covered by a grid of three metre square blocks. The entire area was assigned an initial velocity value of 4.72 km/s determined from figure 7.5(b) and the inversion process run to achieve an observed deviation of less than 0.38 ms in line with the other field examples in this thesis. In fact, due to the good quality of the data, it was possible to achieve an observed deviation of less than 0.2 ms after 10 iterations (see figure 7.6). The distribution of the transmission traveltime residuals for the initial velocity model and the model after 10 iterations is shown in figure 7.7. The distribution shows that the initial velocity model is slow with a greater percentage of residuals being negative. After 10 iterations the shape of the distribution is normal, centered around zero.

The resulting transmission tomogram is shown in figure 7.8 with the corresponding raytracing for this model shown in figure 7.9. The major features of the tomogram are a low velocity anomaly at the top region near borehole 1 and two high

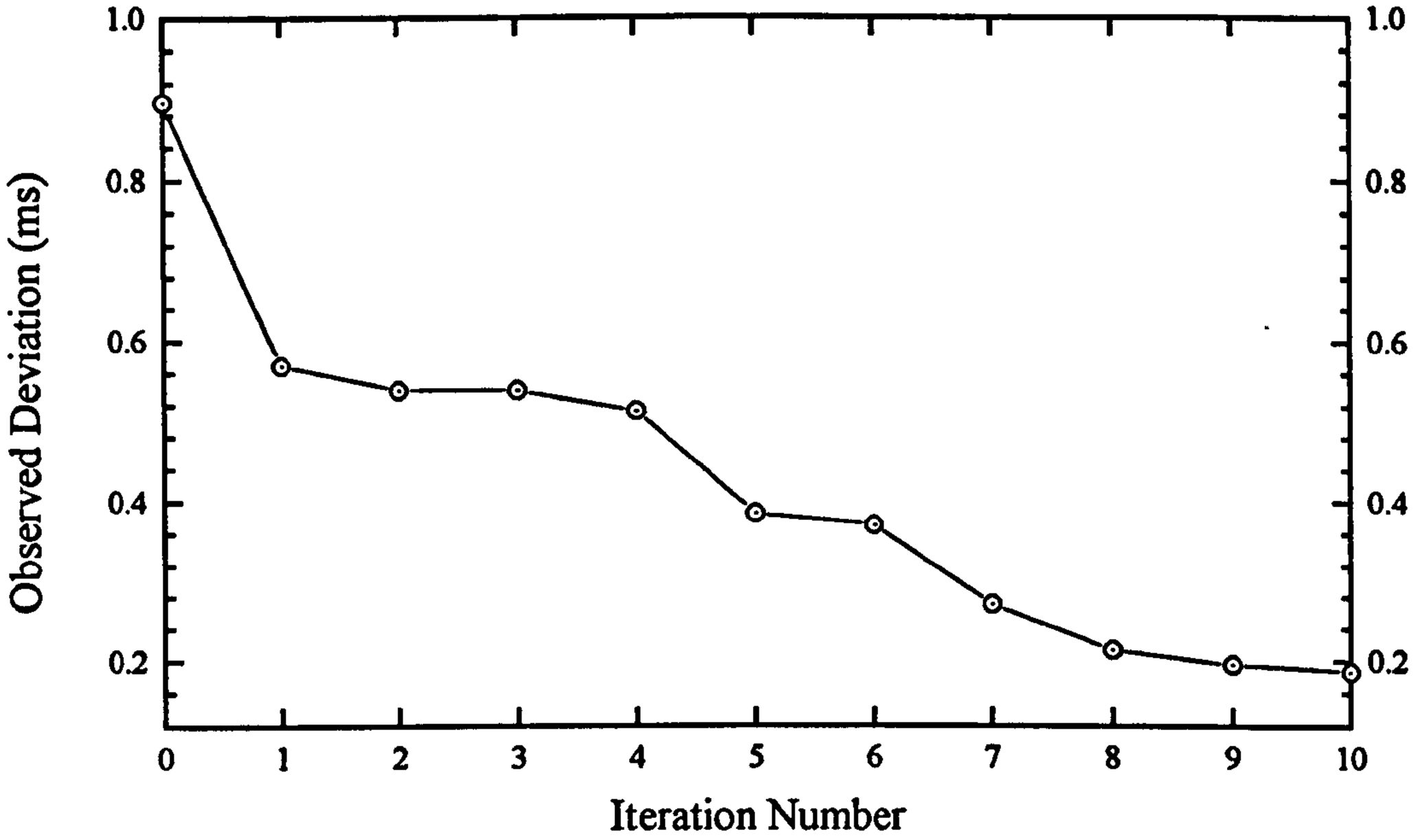

FIGURE 7.6 Observed deviation versus iteration number for the CTRT inversion method.

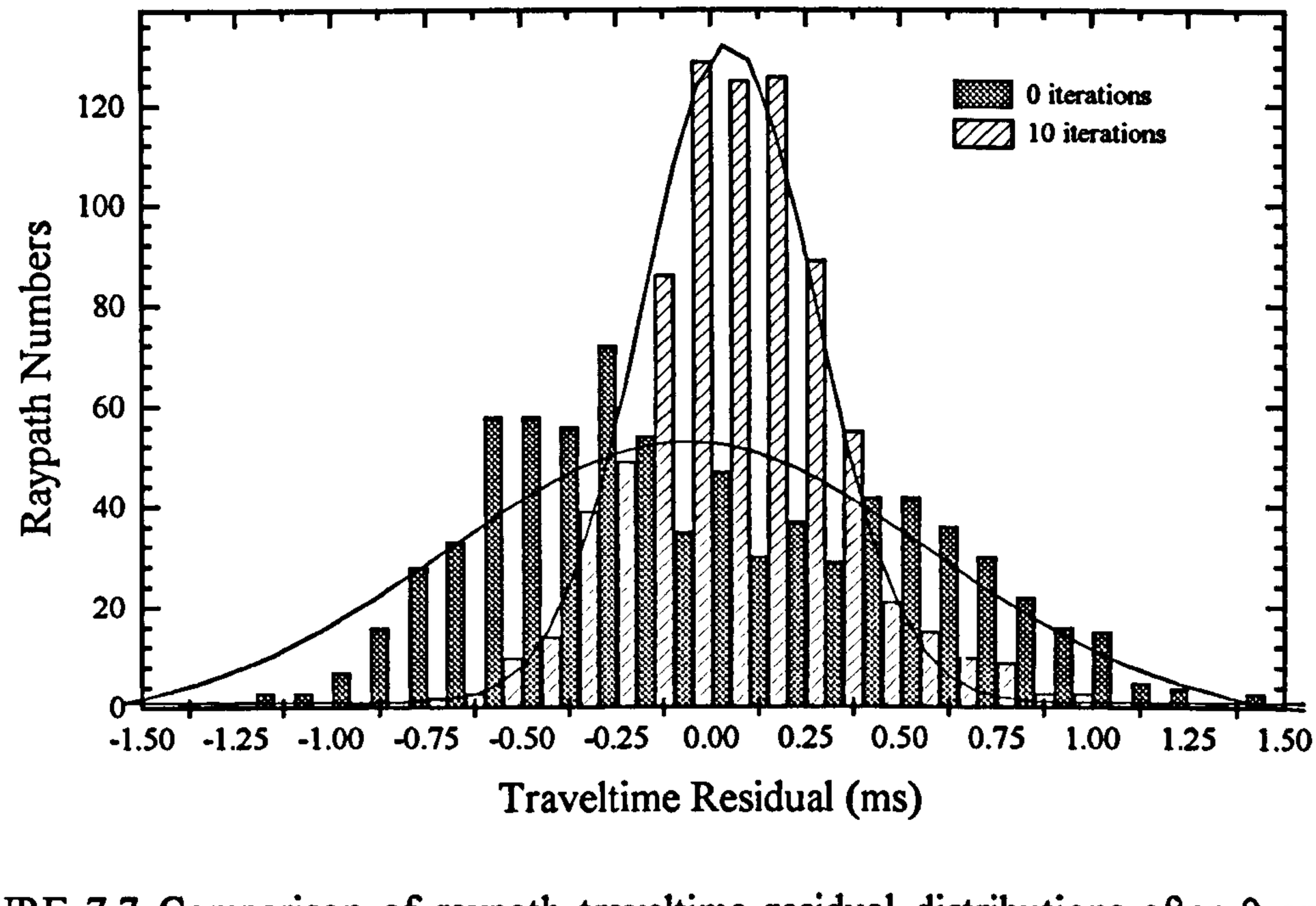

FIGURE 7.7 Comparison of raypath traveltime residual distributions after 0 and 10 iterations.

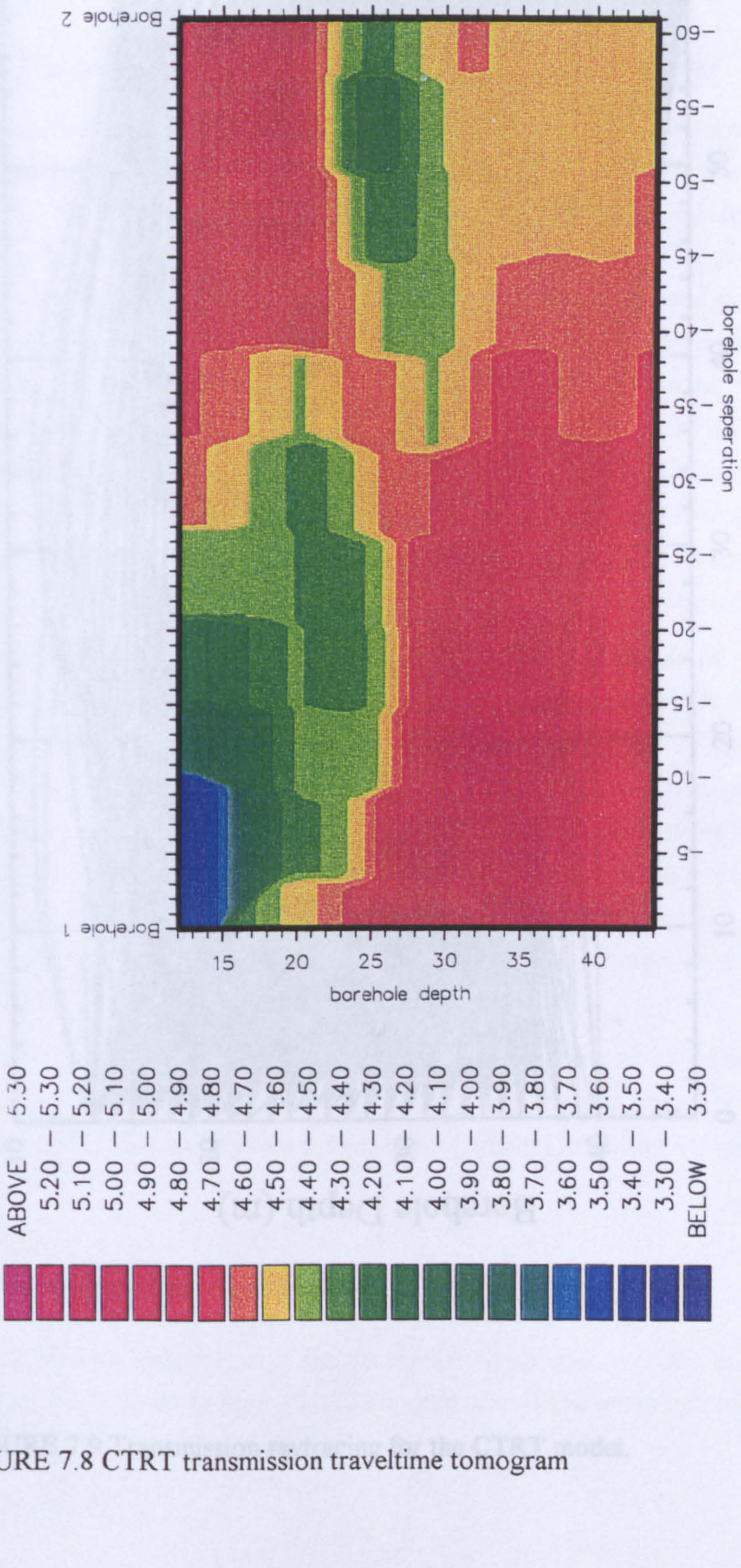

FIGURE 7.8 CTRT transmission traveltime tomogram

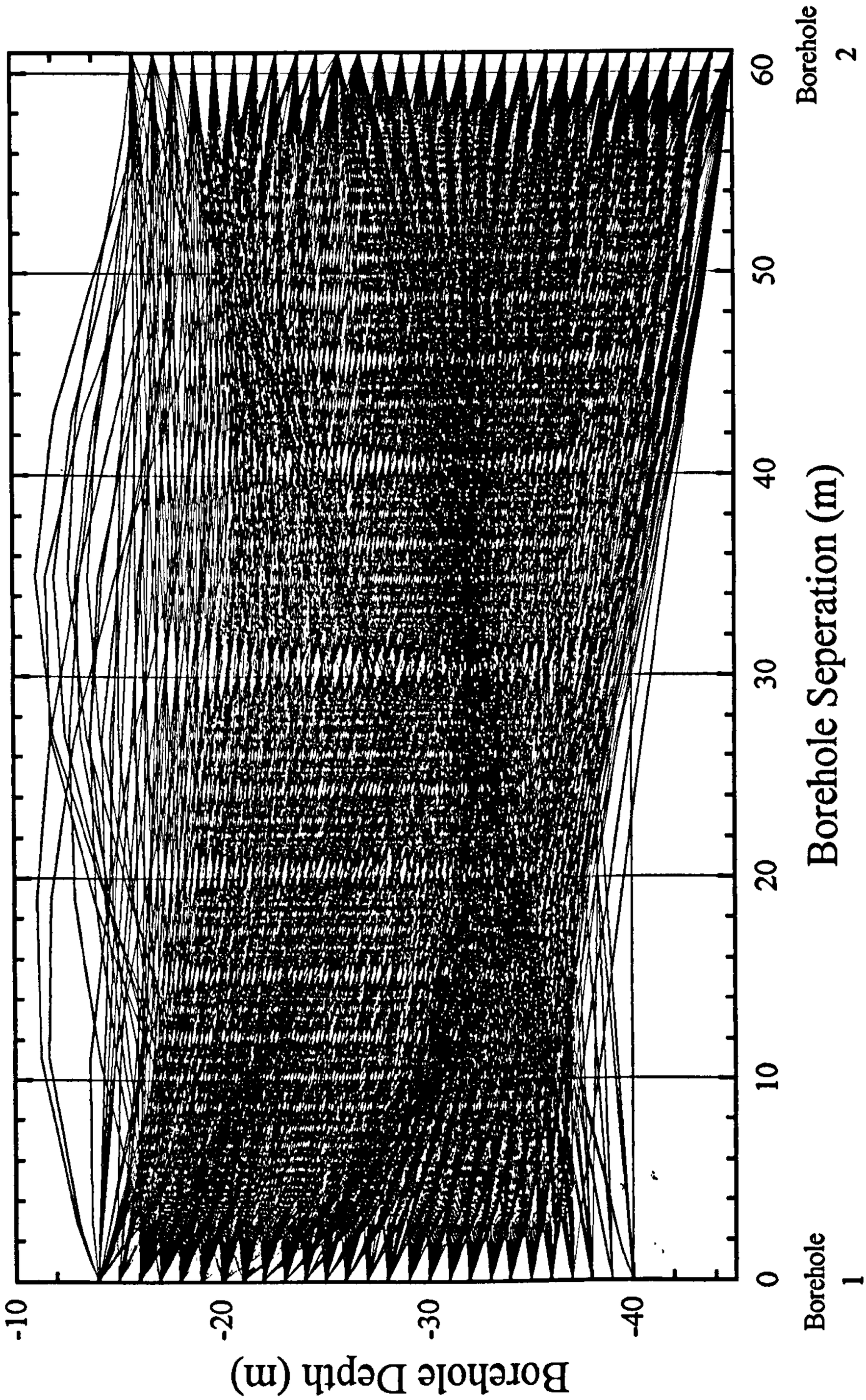

FIGURE 7.9 Transmission raytracing for the CTRT model.

velocity zones which resemble lithological bedded units which have been offset in the middle, presumably by a fault structure. Ray coverage is very intensive across the entire survey area suggesting that all regions of the velocity model have been adequately sampled.

7.5.2 Comparison of Inversion Results with Borehole Logs

To check the consistency of the model and accuracy of velocities, figure 7.10 compares velocities down borehole 1 determined seismically from the tomogram in figure 7.8 with those taken from the sonic log. Sonic velocity values should be greater than the seismic due to the higher frequency of propagation. The two curves in figure 7.10 show good agreement, with reduced velocity in the upper portion of the hole rising to around 5.0 km/s at 25 m depth onwards. At depths greater than 25 m the sonic log shows some variation between 4.8 and 5.4 km/s. The same variations are not present in the CTRT seismic trace. This is most probably due to the frequency of propagation, where the sonic wavelength is of the order of decimetres whilst the seismic is around 6.5 m (see section 7.3.2). Therefore the sonic log has a higher resolution and the variations are most probably due to localised fracturing within the borehole wall. The scale of these local fractures is too small to be resolved seismically.

Other differences may have been introduced as a result of assuming that the raypaths only travel in the 2-D plane between the two boreholes. In fact rays will travel out of the plane and may be curved due to the influence of anisotropic velocity structure. This would mean that raypath lengths and the corresponding calculated velocities were underestimated. Raypath length errors may also have been introduced by the assumption that the boreholes were vertically straight. In fact the holes are likely to deviate considerably and accurate surveying of the upper portion of both holes and adjustment of the receiver and source positions should improve the match in figure 7.10.

The overall good match of the two curves in the vicinity of borehole 1 and the low value of observed deviation at the inversion stage confidently indicates that the velocity tomogram closely represents the real velocity structure across the whole survey area.

7.6 Geological Interpretation

A pictorial description of the geological interpretation of the tomogram presented in figure 7.8 is given in figure 7.11. The plot shows the cross-section between the two

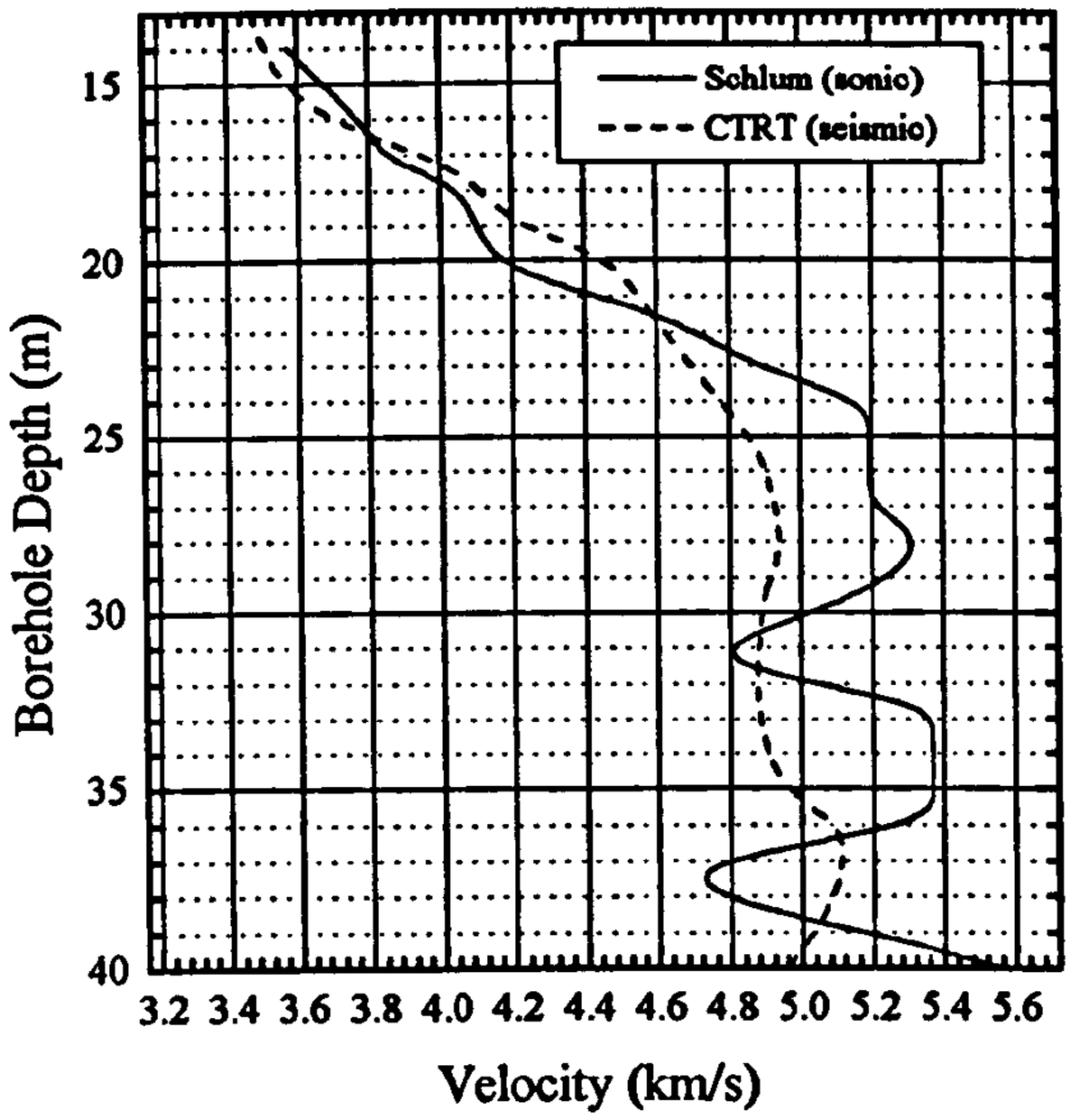

FIGURE 7.10 Comparison of velocities extracted from the CTRT tomogram (CTRT seismic) and those taken from the borehole 1 sonic log (SCHLUM sonic). Readings are taken at 1 m spacing.

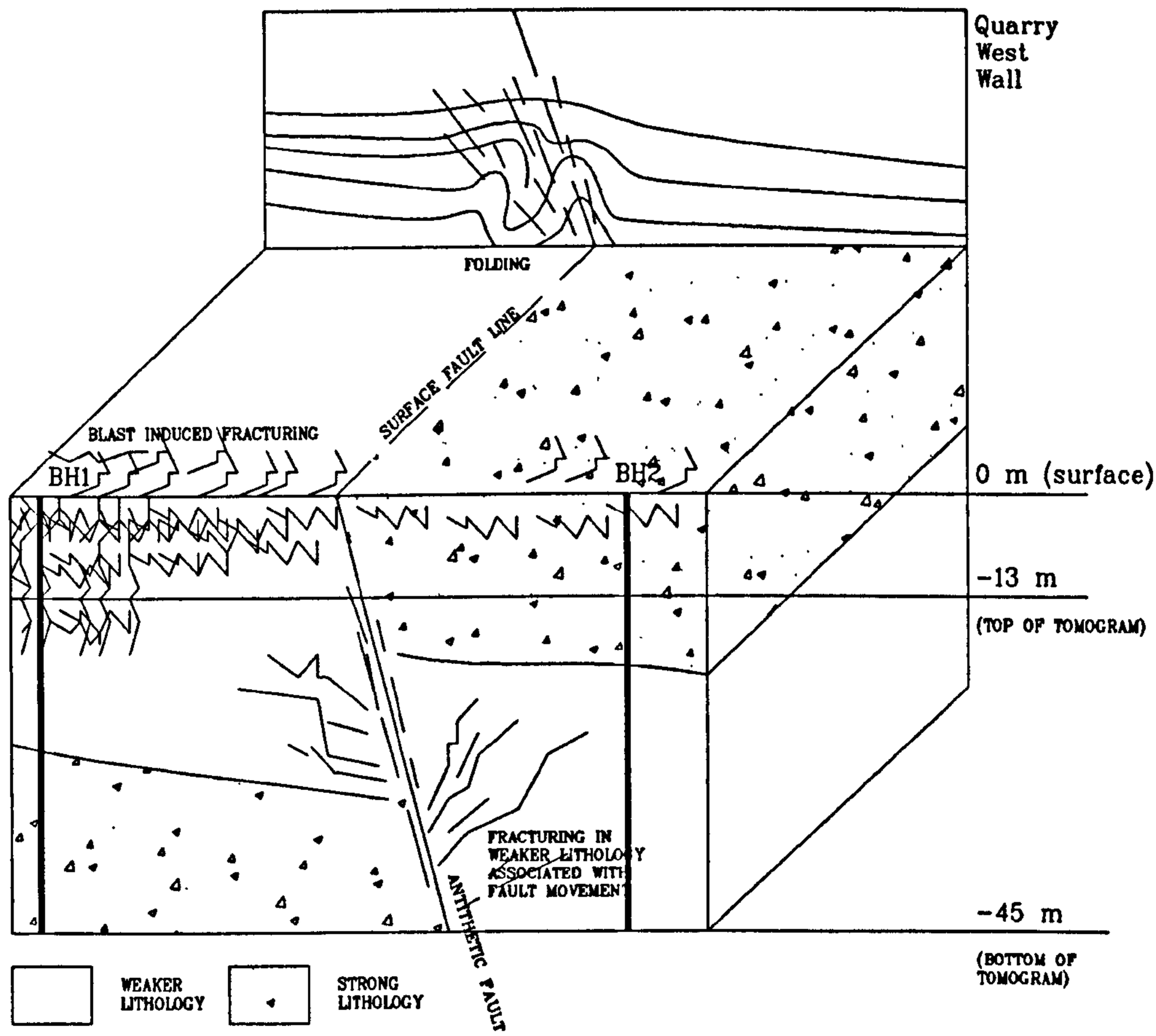

FIGURE 7.11 Pictorial geological interpretation of the CTRT tomogram.

boreholes viewed looking towards the west wall of the quarry. The features of this would have been more difficult to blast due to the reduced area of the free face and interpretation are a blast-induced fracture zone, different strength lithology units and an antithetic fault zone.

The blast-induced fracture zone exists at the top of borehole 1. This produces a low velocity zone in figure 7.8 which extends away from the borehole for at least 10 m. The fracturing was most probably caused by quarry blasting activities. This explanation gains further credibility if the location of the borehole is considered with respect to the geometry of the existing quarry walls. The hole is positioned directly in line with a corner section. Inspection of the walls in this area revealed extremely fractured and friable ground due to blasting activity where two quarry faces meet. This corner area therefore would have required more explosive per square metre. The reduced size of the free face would have resulted in increased fracturing by the expansion of explosive gases, some of which will have extended vertically downwards. Further evidence of this fracturing is the fact that the borehole needed to be lined for the first 12 m to prevent collapse.

The antithetic fault zone is clearly identifiable in the tomogram in figure 7.8 and cuts across the survey area between the two holes in the position shown in figure 7.11. The fault reveals some detail about the lithological units between the two boreholes. The most probable explanation for the high velocity blocks in figure 7.8 on either side is the presence of a stronger lithological unit which has been broken by movement along the fault zone. The lithological units surrounding this strong block are slightly weaker, less well indurated or have an overall lower bulk modulus and therefore have a nominally lower intrinsic velocity of between 0.6 and 0.9 km/s less than the stronger unit. With movement of the fault, stored elastic energy would have been dissipated by breaking the beds and then preferentially fracturing the weaker unit. Evidence of such fracturing is the lower velocity area in figure 7.8 in the weaker unit directly below the strong unit on the borehole 2 side of the fault. The fault reveals itself in the west wall of the quarry in the form of a shatter zone and a region of intense folding. This type of feature is common above or at the top of an antithetic fault zone where fault displacement is smaller than at the centre of the fault plane. Thus instead of the straight forward cutting shear action of the centre of the fault, lithological beds are deformed more slowly and tend to fold and crack.

7.7 Conclusion

With reference to the original aims of this field work, the CTRT transmission inversion model successfully identified the suspected geological features at the site. With no prior knowledge of the geological structure between the two boreholes, it was decided to use a block initial velocity model to resolve the structure. The tomogram identified a region of blast induced fracture damage, a change in lithology strength or modulus and the location of a fault zone passing through the cross-section. This model is comparable to the types of model that can be produced using more popular transmission traveltime inversion algorithms such as SIRT, ART or CG. However, the advantage of the CTRT method is that the model can now be forward modelled to identify reflections in the dataset. However, the strong lithological units should prove to be moderate reflectors and use of the final step of combined transmission and reflection traveltime inversion will more accurately locate the interfaces between the units, any velocity variation within the beds and the location of the fault. An improvement in the resolution of the model would be expected, similar to that obtained in chapter 6.

CHAPTER 8

8. Seismic Velocity and Attenuation Field Measurements in Rock Mass Behaviour Prediction

8.1 Introduction

So far, the field examples in this thesis have only considered static cases. That is they have only been concerned with the imaging of static rock masses which have not undergone any change for considerable time periods. The field examples considered in this chapter are in an active mining environment and therefore the rock mass surrounding the mine workings is continuously experiencing a changing stress field. The excavation and removal of a mineral product or waste material intrinsically unsettles the original stress regime and causes instability. Stresses must therefore be redirected and re-concentrated to other areas. This process reveals itself by requiring the rock mass to move, fail or collapse, or redistribute elastic energy to re-establish a condition of stability. Chapter 2 has considered how a changing stress field influences the seismic properties of velocity and attenuation. This was followed up in chapter 4 by an intensive laboratory study of these factors. That study revealed the sensitivity of both velocity and attenuation to a changing stress regime in both intact and fractured samples. Therefore this chapter is a natural climax to the preceding work, by attempting to use velocity and attenuation in an active environment as a predictive tool for rock mass behaviour monitoring.

8.2 The Milldam Mine Site.

Milldam Mine is owned and run by Laporte Minerals. The sole purpose of the workings is the production of fluorspar for the steel and chemical industries. The underground mine is situated in the Peak District National Park in Derbyshire, England. The geology is very similar to the conditions at Gillfield Mine, consisting of a shale limestone sequence. The constituents of the vein include galena, barytes, calcite and up to 90% fluorspar and in some areas it has already been extensively worked for its galena content. As at Gillfield, the vein is almost vertical and is associated with a large fault system. Current workings are based on a single decline entrance located in the limestone hangingwall, 2 kilometres in length, which intercepts the vein, passes through it, and then connects to production roadways which are all sited in the footwall.

8.2.1 Geology

Figure 8.1 depicts a cross section through the vein. The sequence consists of limestone country rock overlying a volcanic tuff basement at a depth of 150 m. The vein is associated with a large fault, where the basement is upthrown 4 to 5 m. The hangingwall consists of limestone, and the footwall comprises of a disseminated high grade fluorspar limestone, referred to as the mineralised limestone or replacement zone, which changes to the more competent limestone. The vein itself is a weak fluorspar, barytes, galena deposit, which is highly variable and contains many air pockets. In areas the vein has been extensively worked for its galena content right down to the volcanic basement. The exact locations of these workings, known as 'old man workings', are rarely known. The replacement zone normally contains high grade fluorspar material and is removed and processed along with the vein. It is more competent than the vein but may contain small pockets of clay, known as washout zones, or can be extensively faulted parallel to the vein, these faults containing clay gouge infill. Vein widths vary from 1 to 5 m and replacement zone widths vary from 5 to 10 m. Near to the vein, the limestone hangingwall may also be extensively faulted and contain clay pockets which can cause stability and dilution problems during vein extraction.

8.2.2 Mining Method

All production access to the vein is sited in the footwall. The mining method is a variant of sublevel caving shown in figure 8.2. Two parallel footwall drives are driven along the strike of the vein within the competent limestone. The vertical distance between these two levels may vary from 25 to 40 m depending on ground conditions. At 10 m intervals along strike cross-cuts are driven on both levels from the footwall drives to intercept the vein. Long holes are driven up from the lower cross-cut into the mineralised zone and are angled to intercept the vein beneath the upper cross-cut (see figure 8.2). The holes are part charged, starting with the lower portion of the stope and blasted. This process induces caving of the weak vein material, which is drawn off by LHD loaders at the bottom cross-cut. Repeated progressive blasting of the longholes induces caving within the mineralised zone. Once all the vein material and the disseminated zone has been removed, or ore dilution due to hangingwall or footwall collapse becomes unacceptable, the stope is backfilled from the upper level using waste stone from development drives to stabilise the area. Each stope has a short life span of 4 to 6 weeks, with two stopes in production at any one time. Consequently, the mine must continually develop the parallel footwall drives and cross-cuts to prepare new stopes. Ideally at any one time the mine will have a working production sequence as in figure 8.3. An old stope will provide a dumping point for development waste rock as

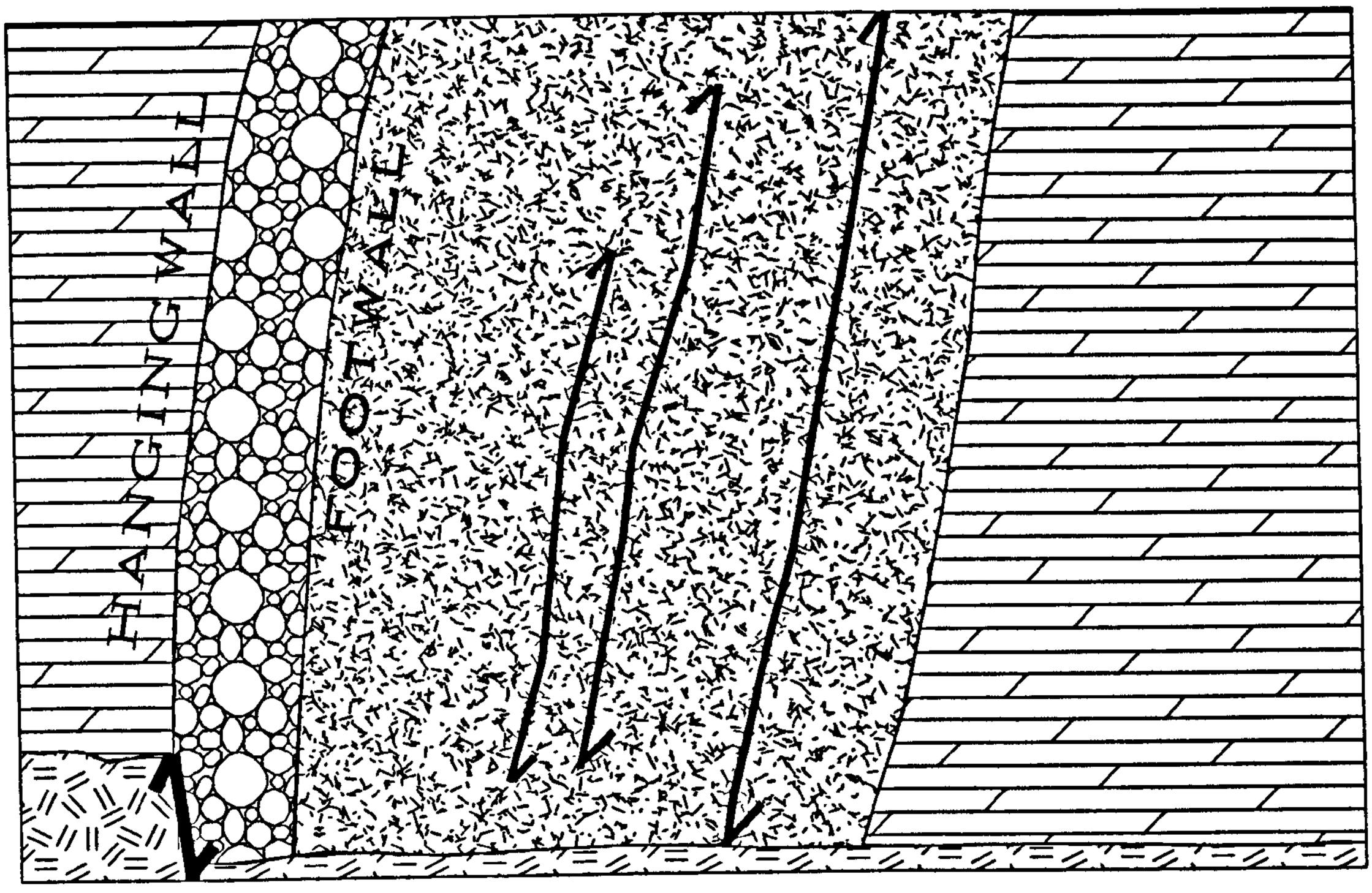

FIGURE 8.1 Cross section through the vein at Milldam Mine.

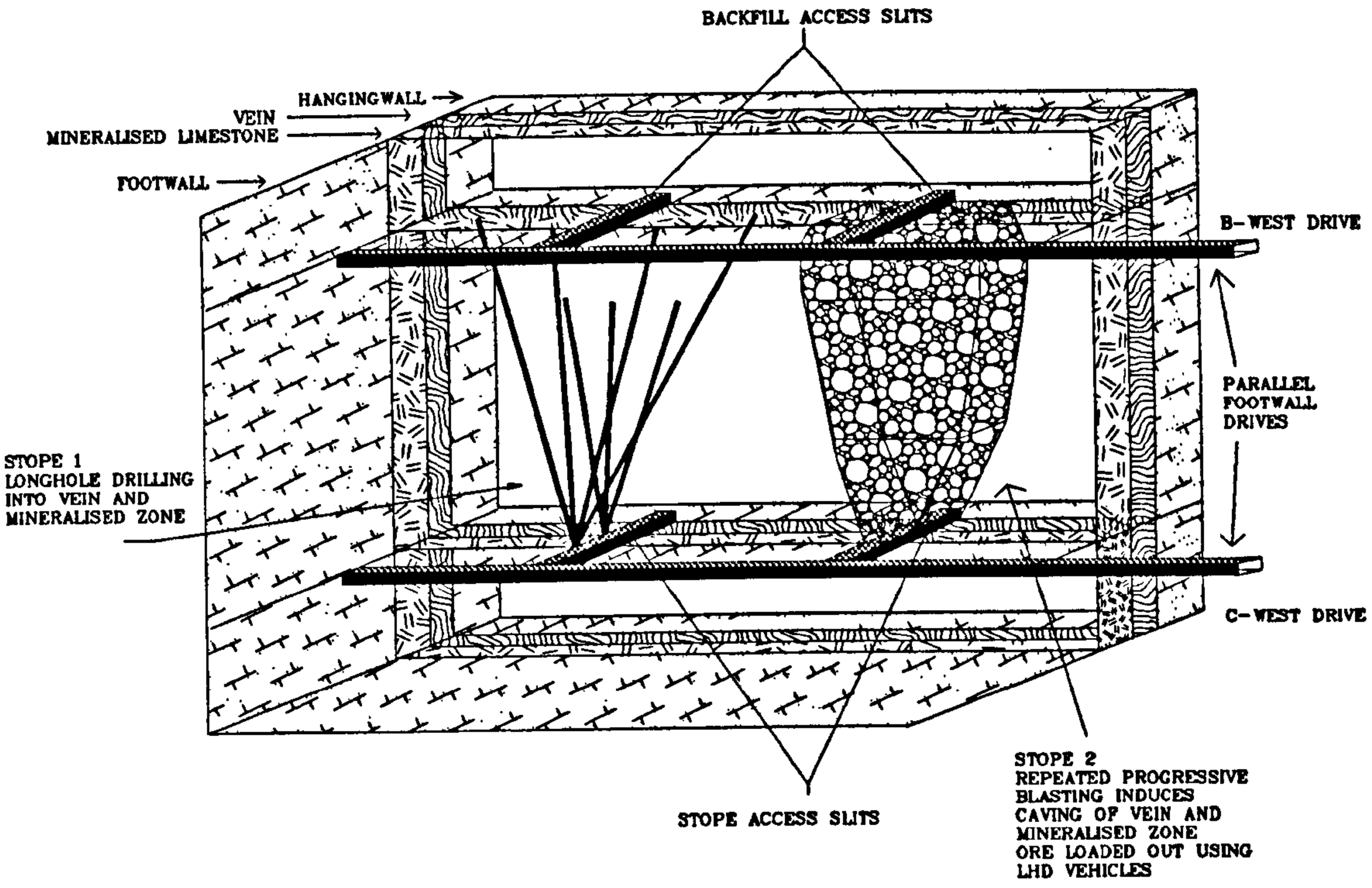

FIGURE 8.2 Mining method employed at Milldam Mine.

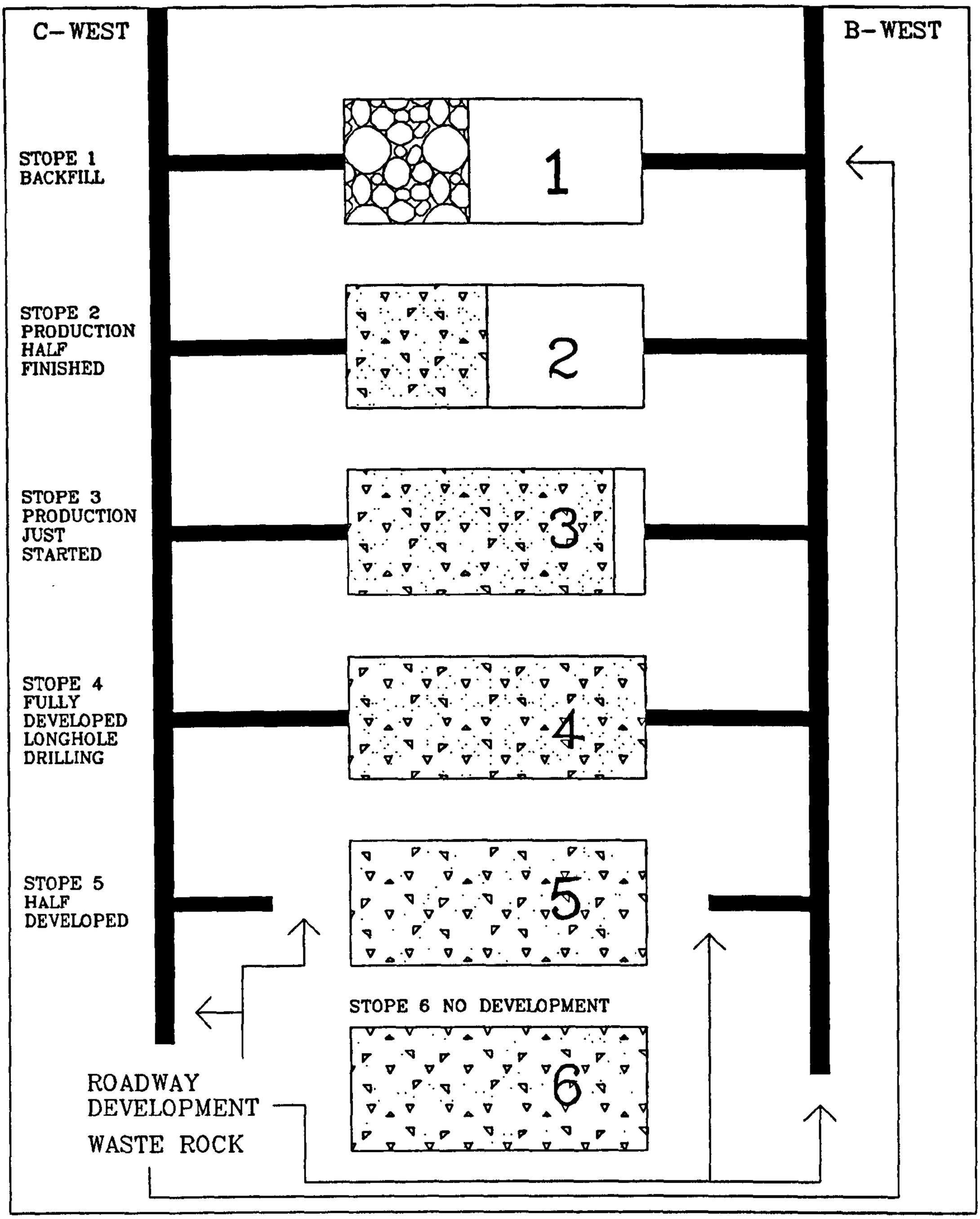

FIGURE 8.3 Milldam Mine production schedule.

backfill. Two stopes will be in production and a further two to three stopes will be being developed. Three major problems can cause catastrophic stope failure and interrupt this working cycle. They are,

- Hangingwall collapse, causing blockage and dilution of the stope.
- Crown pillar collapse above the stope. In the event of this happening, the mine has little control over the movement of the weak vein material and, in extreme cases, the vein has been known to chimney to surface.
- Fault movement in the footwall. In an extreme case an entire footwall block, bounded by the access cross-cuts, may slip causing loss of the bottom and top cross-cuts and a large amount of damage to the upper parallel footwall drive.

8.2.3 Field Work Aims

Given the problems outlined in the previous section it was decided to conduct a number of field experiments to tomographically image a production stope throughout its working life. The aim of this field work was to discover the suitability of seismic velocity and attenuation measurements as a tool for the prediction of stope stability. Due to the geometry of the production access layout in the footwall, it was impossible to conduct measurements in the hangingwall and therefore to address the problems of hangingwall collapse and crown pillar collapse. These are however, the rarer of the three occurrences. The production layout did however, provide excellent access for seismic measurements to be conducted within the footwall. This problem of footwall stability is potentially the mine's greatest hazard, since it threatens the two parallel footwall drives, an integral part of the production layout. By seismically imaging the footwall right up to the vein, the following objectives seemed feasible,

- Identification of the boundary of the mineralised and competent limestone between the two levels. By locating this boundary, the mineable volume of the stope could be accurately determined.
- Identification of highly fractured or faulted ground between the two levels, especially where this could lead to collapse of the footwall block. Problem areas could be a particularly weak mineralised zone or a large concentration of vertical faults within this area. Alternatively, the faulted zone may extend into the competent limestone area, causing stability problems for the footwall block and the parallel drives. This may be a problem where the parallel drives have inadvertently been driven too close to the mineralised zone.

- Monitoring of the stope throughout its production life to observe the degree of caving and of destressing of the footwall with the extraction of the vein. In particular, to observe if velocity and attenuation measurements could identify the precursors to dangerous movement of faults within the footwall.

8.3 Calibration Trials at Milldam Mine

As discussed in chapters 6 and 7, the design of a good tomographic survey which achieves the required level of resolution within acceptable error estimates depends on prior knowledge of some of key parameters unique to each site. Seismic resolution is related to the wavelength of the propagating energy. While seismic energy with shorter wavelengths (higher frequency) can provide greater resolution, it is more strongly attenuated in rock and limits the overall range of propagation. Current theory suggests that the resolution of transmission traveltime tomography is about one wavelength, (Williamson, 1991). However other workers claimed to have achieved resolution closer to one half wavelength, (Freidel et al, 1996).

Because of the small dimensions of the proposed survey site, it was necessary to obtain estimates of the likely seismic velocities to be encountered and to try a number of seismic sources to observe typical propagating seismic energy frequency ranges. An extra limitation was that the source system needed to be easy to implement and inexpensive to operate. The need for relatively high propagating frequencies also introduced considerations of the type of receiver required. Standard P-wave geophones have a limited working bandwidth and are more suited to lower seismic frequencies. For good reproduction of higher frequencies it was foreseen that it may be necessary to employ active (signal amplifying) receivers such as active geophones or hydrophones. Of equal importance was the consideration of the method of receiver mounting on or within a solid rock mass to achieve good coupling and reproduction of the propagating seismic wave.

8.3.1 Source and receiver types.

With the above factors in mind a series of trials was conducted to try the following source and receiver types,

Sources,

- Dry borehole, high frequency sparker source.
- Explosive source

- Hammer source

Receivers,

- Passive hydrophone
- Passive geophone
- Active hydrophone (developed by the BGS Geophysics and Engineering Geology Group)
- Commercially available active geophones.

The dry-hole sparker was the same configuration as the super sparker used in the investigation documented in chapter 7 but downgraded by around 30% and operated in a three inch diameter horizontal dry hole using a borehole packing system (Jackson & McCann, 1990). Explosives were provided by the mine and consisted of single high explosive, electric detonators with the option to use additional small charges of gelignite. The hammer source consisted of a large sledgehammer, using an EG&G piezo-electric trigger switch taped to the hammer shaft.

8.3.2 Sparker source trials.

A calibration test was carried out in an intact unmined area of Milldam Mine between two roadways to investigate the frequency output of the BGS dry-hole sparker source. Five different receivers were employed for this test, two different passive hydrophones, an active hydrophone and a passive and active geophones. A plan view of the survey area in figure 8.4 shows the location of the borehole used for the different hydrophones and the location of a spike mounting for the two geophones. Raw seismic traces from the test are shown in figure 8.5. The increase in noise for the geophone data is due to a local pump being switched on at the time of acquisition. The frequency response of this raw data is shown in figure 8.6. For all cases the peak amplitude occurs at around 350 to 400 Hz. Hydrophones 1 and 2 have significant energy up to 650 Hz. The geophone peak frequencies are slightly shifted to the left due to the extra distance of the raypath and therefore greater overall attenuation of the higher frequencies. Due to the relatively low frequencies measured it is clear that there was no conceivable advantage in using active receivers since the frequencies under consideration were well within the workable range of the passive receivers. Figure 8.7 shows the same data filtered using a second order Butterworth bandpass between 250 and 750 Hz. First arrivals are well defined and can be read accurately to within 2 or 3 sample points (0.05 ms). The first arrivals are documented in table 8.1 for the various receiver types along

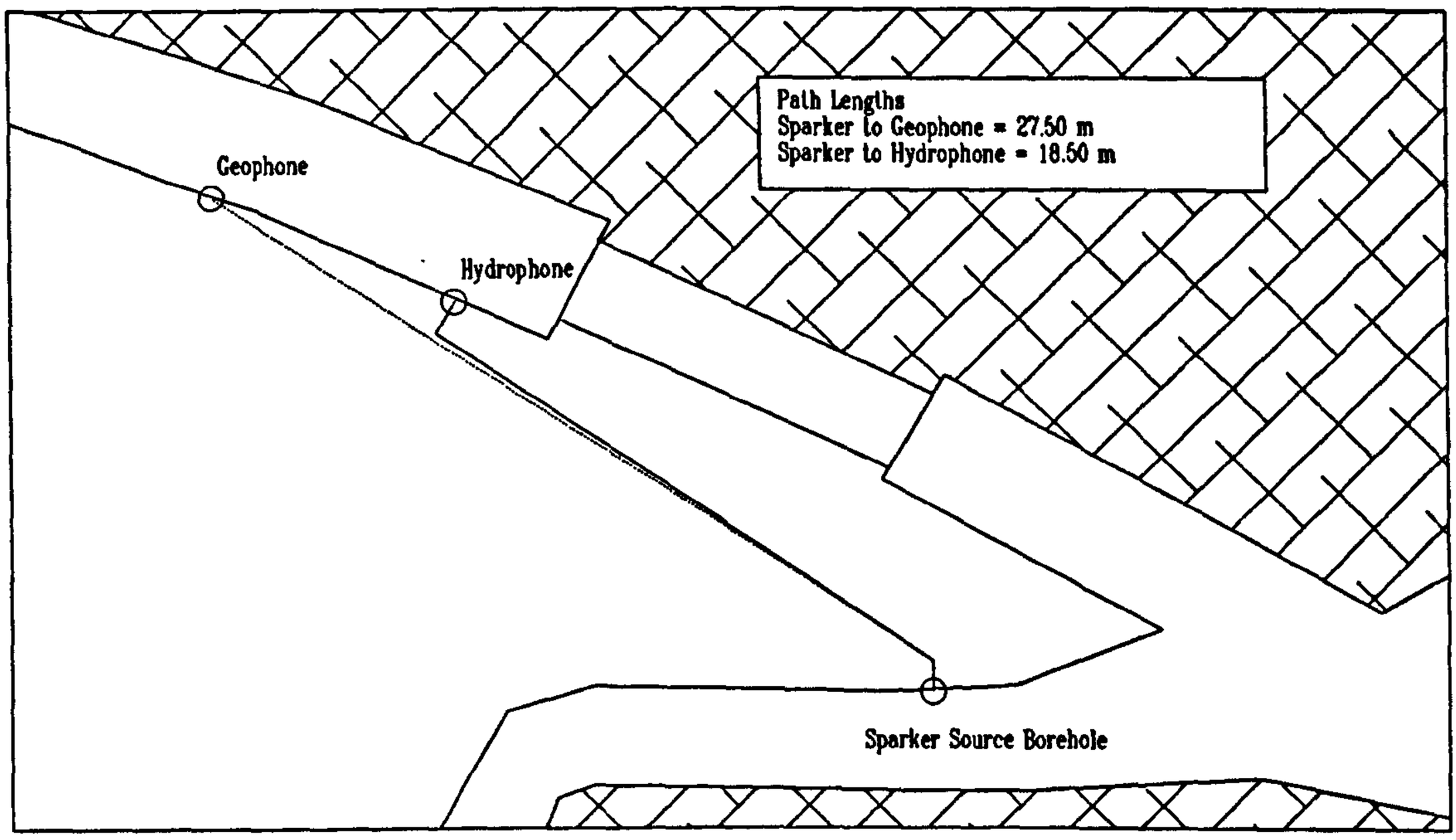

FIGURE 8.4 Plan view of site for sparker source calibration test, showing location of sparker horizontal borehole, hydrophone borehole and geophone mounting.

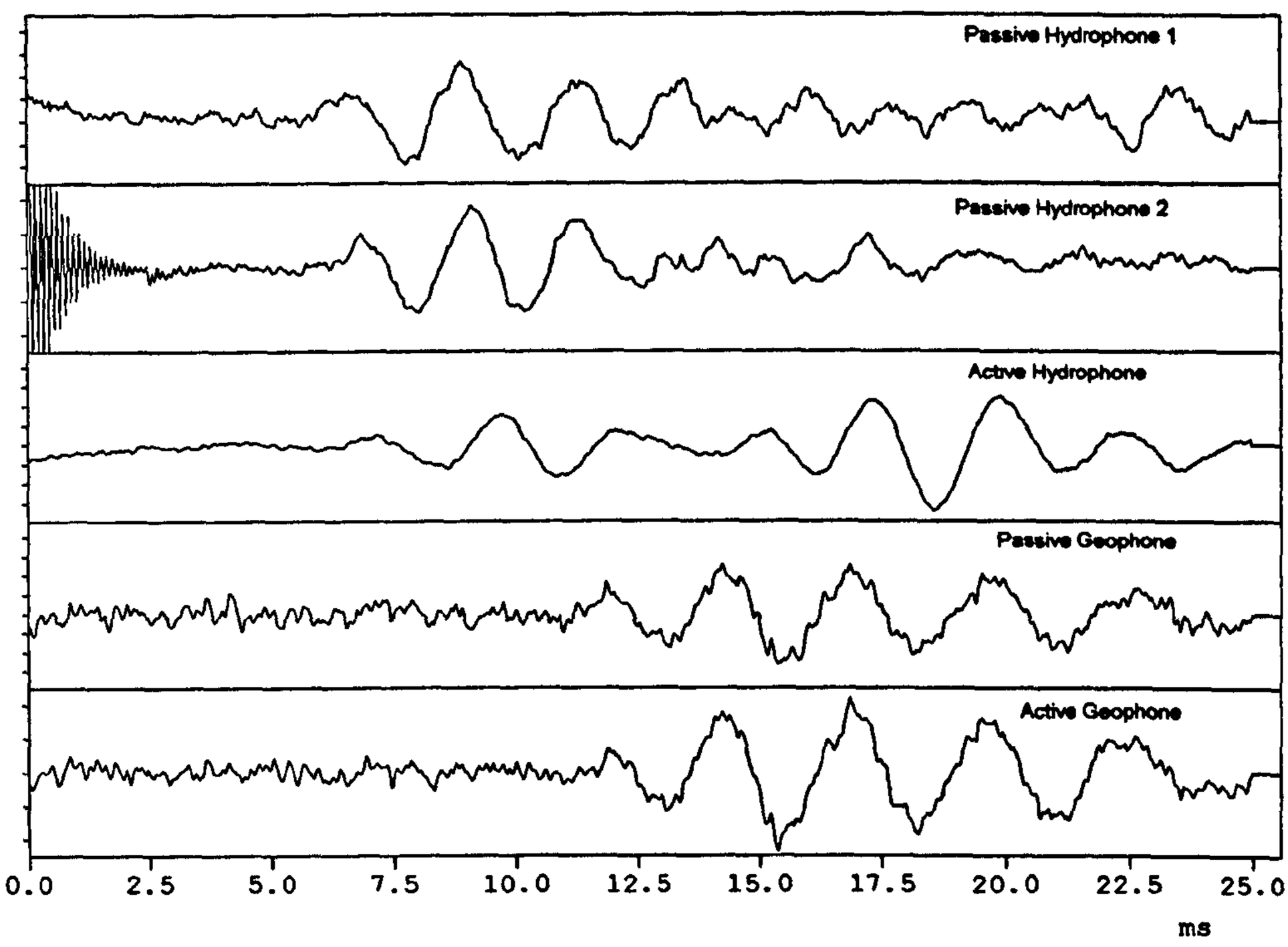

FIGURE 8.5 Raw seismic data from BGS sparker source calibration test.

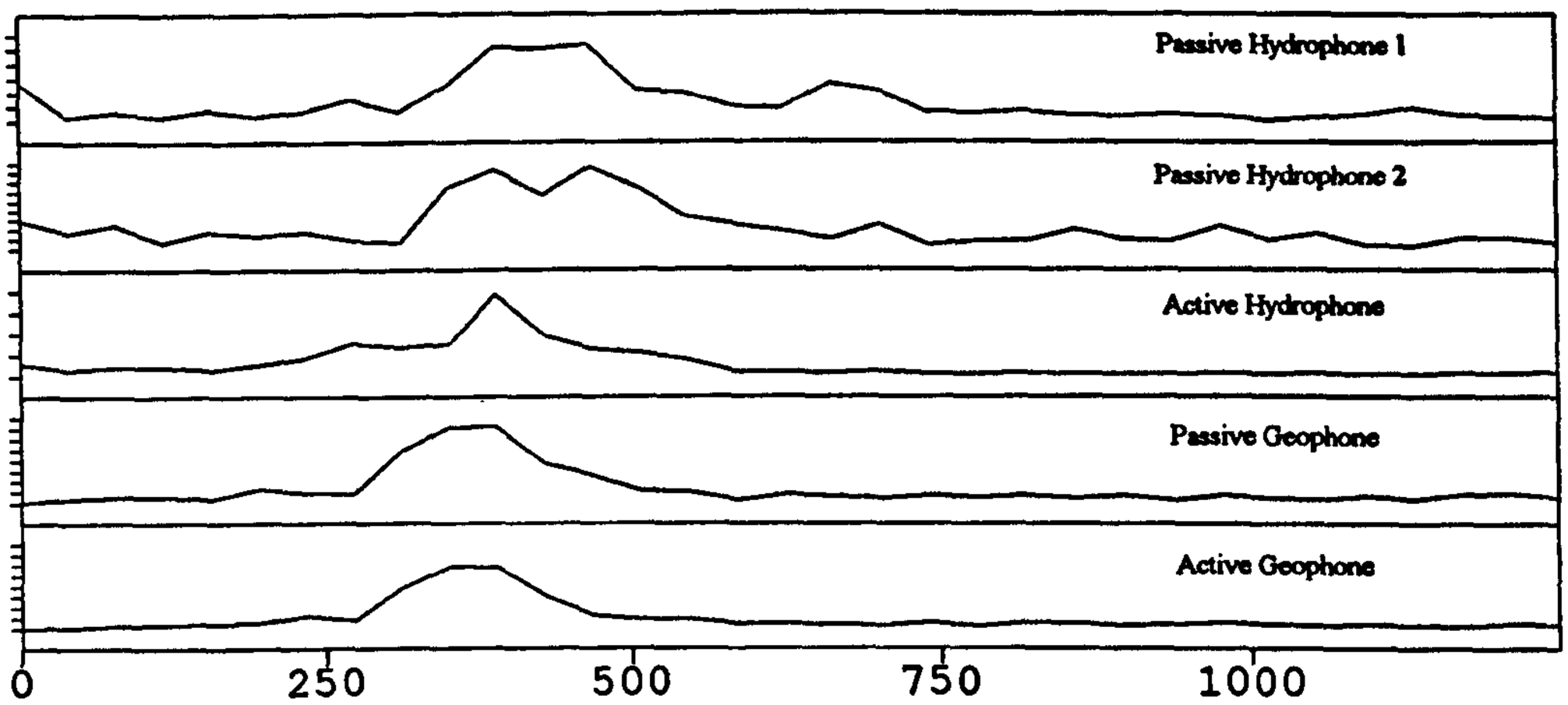

FIGURE 8.6 Raw frequency response for traces in figure 8.5.

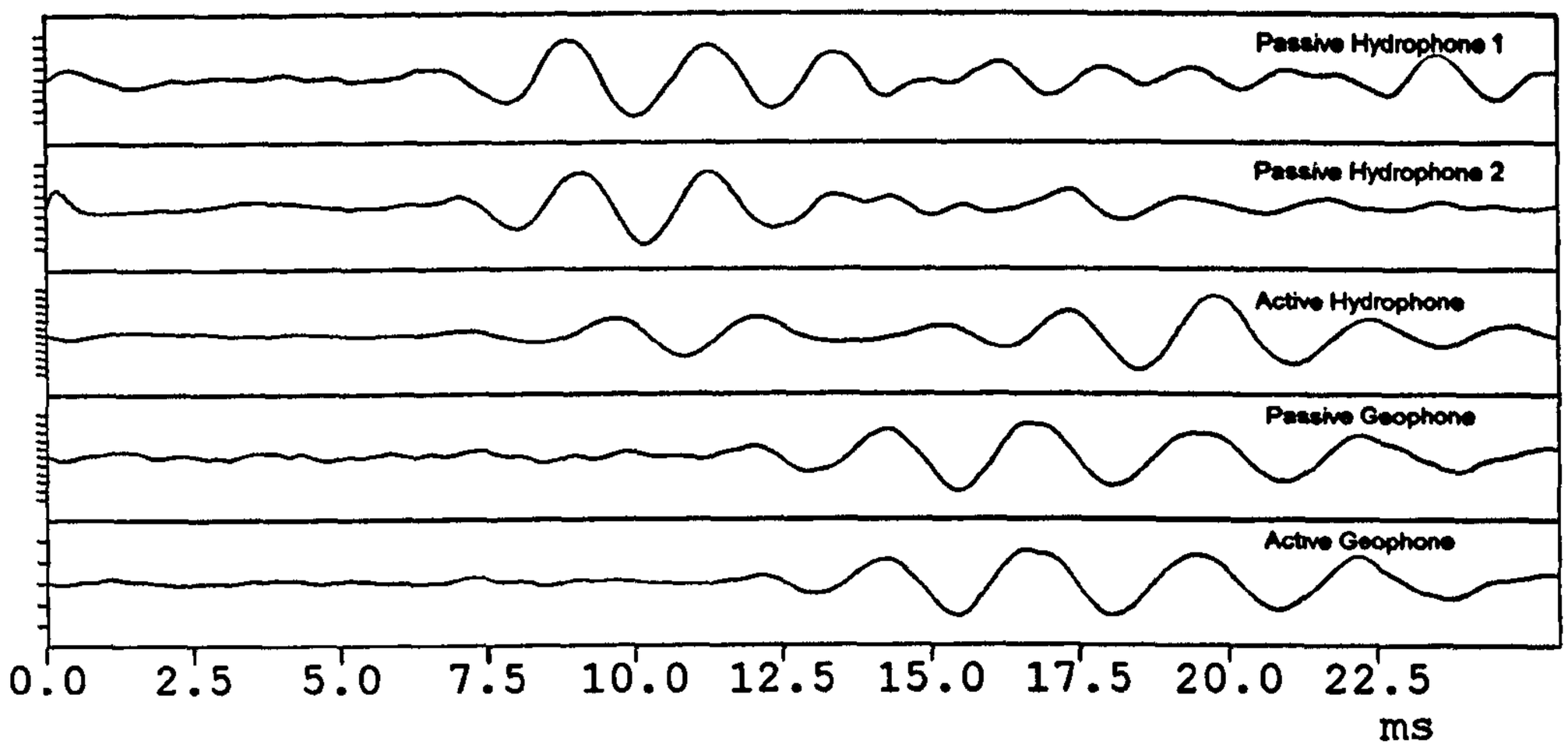

FIGURE 8.7 Second order Butterworth bandpass filter between 250 and 750 Hz applied to data in figure 8.6.

Receiver Type	Path Length (m)	Direct Arrival Time (ms)	Velocity (m/s)
Passive Hydrophone 1	18.50	5.90	3135
Passive Hydrophone 2	18.50	5.95	3109
Active Hydrophone	18.50	6.40	2890
Passive Geophone	27.50	11.35	2423
Active Geophone	27.50	11.475	2397

TABLE 8.1 Data from sparker source calibration test.

with the calculated velocities assuming straight raypaths. The calculated values for velocity give average velocities as follows,

Source to Hydrophone Raypath : 3045 m/s

Source to Geophone Raypath : 2410 m/s

The apparent discrepancy in the two values can be explained by the experimental setup. Some difficulty was experienced in fixing the geophone spikes into the solid limestone and therefore the geophones were not ideally placed and orientated. Hydrophones were arranged nearly horizontally and geophones were arranged vertically. This orientation means that it is most likely that the direct arrival reaching the hydrophones was a P-wave whilst that arriving at the geophones was an S-wave. However, the P/S wave ratio calculates out at 1.26 which is very unrealistic for a carbonate rock (normally 1.7 to 2). Errors may have been introduced due to poor measurement of hydrophone, geophone and sparker borehole locations as well as the calculation being based on limited data.

Laboratory data for saturated, intact samples of limestone taken from the same site yielded velocity values of between 5.45 and 6.20 km/s (see chapter 4) whereas saturated, intensely fractured samples yielded values in the range 3.00 to 4.90 km/s depending on the confining stress conditions. The in-situ P-wave result suggests that the calibration site was fully destressed and fractured due to tunnel blasting. Pusch & Stanfors (1992) investigated the depth of the zone of disturbance around blasted tunnels in granite rock. They concluded that even in strong granite rock at depths of 360m, using careful blasting procedure, the zone of intense fracturing extended at least 1.7 m into the floor and roof and 1 or 2 meters into the sidewall. Beyond this zone, the rock mass was less fractured by extension and opening of existing fractures depending on the original stress regime. In the case of the calibration site, with weaker limestone rock, reduced in-situ stress and with no special blasting processes in use, it is appropriate to assume that a fractured zone existed around all roadways for at least 1 times the roadway diameter or around 3.5 m into the sidewalls. This means that within the survey area, the fractured zones and the destressed area surrounding both roadways probably almost coalesced and at least 50% of the two raypaths passed through fractured rock resulting in the apparently low velocities. Chapter 4 showed that fracturing imparts considerable attenuation to the propagating wave. This would explain the disappointing frequency results obtained where only the dominant sparker frequencies reached the receiver points (400 - 500 Hz, Baria et al, 1989). Previous use of the source in various rock types had propagated frequencies up to 3000 Hz over similar distances, Jackson (1996). In this case, however, the fracturing process

drastically reduced Q values and attenuated any original high frequency components emitted by the source over a short distance.

The site was chosen because it reflected the conditions within a stope block such as localised fracturing and faulting, especially in the transition zone between competent limestone and the vein. In conclusion the test indicated that the sparker source was capable of propagating frequencies of up to 650 Hz. With an average P-wave velocity at the site of 3045 m/s, this frequency of propagation equates to an average wavelength of 4.68 m.

8.3.3 Hammer and explosive source trials.

The mine provided a second location for the trial of an explosive source and a hammer source in an area which had previously been mined out. It was not possible to conduct a second trial of the sparker source at the same site due to the removal of mine services from this area and the inability to drill source boreholes. A representation of the site is shown in figure 8.8 and it provided a good opportunity to test both source types and conduct a simple 2-D tomographic cross-section survey between two levels in the limestone footwall of a worked out stope.

8.3.3.1 Experimental Setup.

Six passive vertical P-wave geophones were positioned in the sidewall on C-drive by mounting vertically on horizontal 16 mm steel bar hammered into small drill holes. The seismograph was located at the bottom of the raise which allowed for easy access between the two levels. A trigger cable was run up the raise to A-drive. Three detonator holes were drilled into the sidewall on A-drive and one hole was charged with a single detonator, the second with a single detonator and a small pill of gelignite (approx. 20 grams), and the third with a single detonator and two small pills of gelignite. The detonators were electrically initiated and therefore subject to at least a one millisecond delay between the electric pulse from the shot firer's battery and the actual detonation. Two techniques could have been used to trigger the seismograph, either the electric pulse from the shot firer's battery, or a break wire trigger. A break wire trigger consists of a small piece of shot firer's wire taped to the detonator and connected across the trigger terminals of the seismograph. When fired, the detonator breaks the wire and the circuit, and triggers the seismograph. The break wire trigger was selected here since it commenced the seismograph recording at the instant the detonator was exploded and was not subjected to the variable delay associated with electric initiation of the detonator. The hammer shot positions are also shown in figure

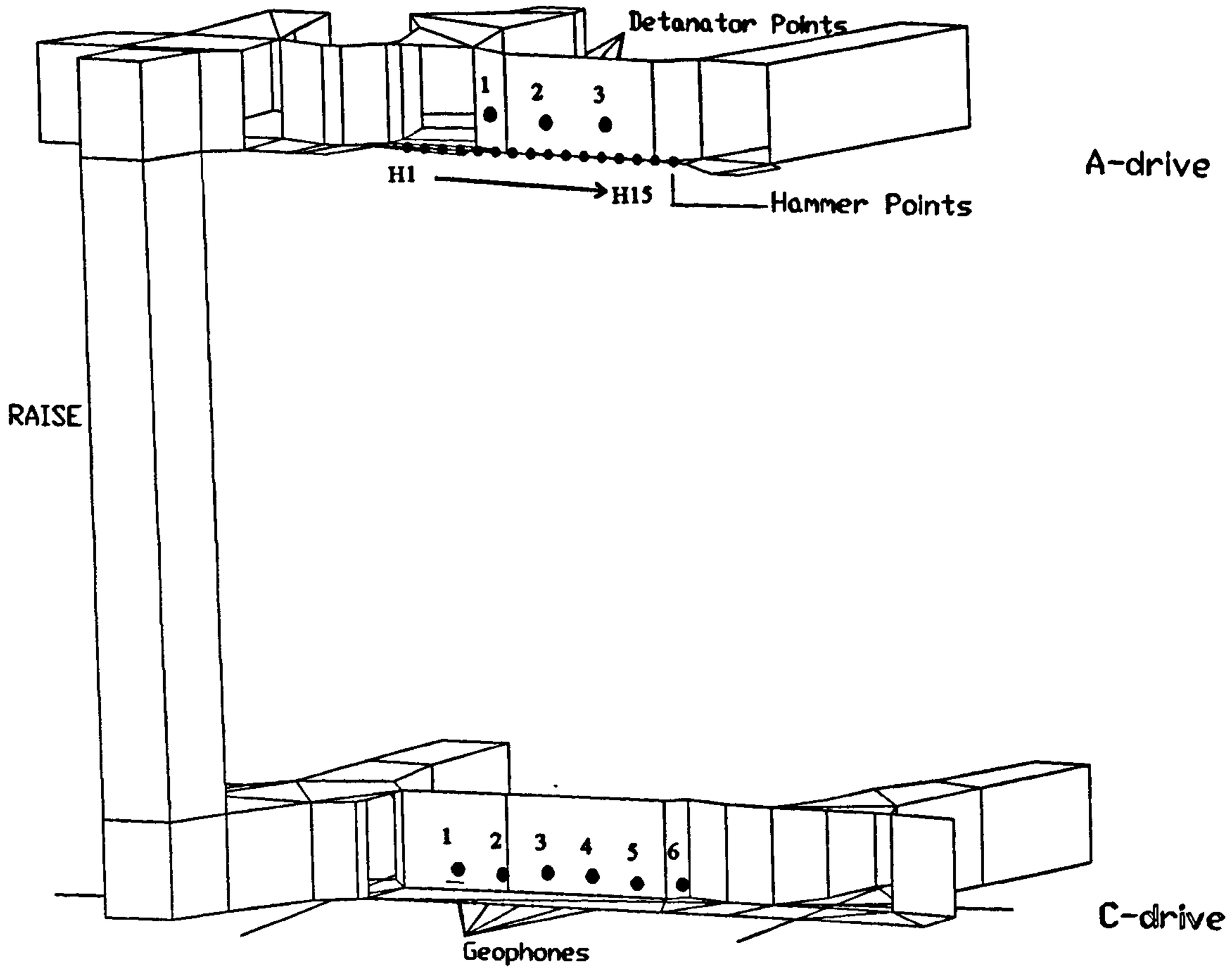

FIGURE 8.8 Inter-level site for investigation of explosive and hammer source properties in the footwall of a worked out stope. Hammer points are labelled H1 to H15. Geophones are labelled 1 to 6.

8.8 and consisted of 15 locations, at one metre intervals, directly above the geophone positions.

8.3.3.2 Explosive test results.

Figure 8.9 shows the seismic traces acquired by geophones directly below each of the three explosive source positions and the corresponding frequency domain characteristics are depicted in figure 8.10. In all three cases, the P-wave arrival is very easy to identify. Table 8.2 compares the properties of each of the different explosive charges. The following trends are apparent from this test,

- In all three cases, the dominant frequency (peak frequency) lies between 850 and 925 Hz.
- The First Peak Amplitude (time domain) and the Peak Frequency Amplitude increase with increasing explosive charge.
- The rise times defined by Blair & Spathis (1982) (chapter 3 section 3.2.1.1) in all three cases are identical (within one sample point) indicating that attenuation imparted to the three raypaths was very similar.

In the case of the detonator only, although a distinct peak exists at 922 Hz, there is also significant energy at other frequencies between 250 and 1250 Hz. However, when all three frequency spectra are plotted on the same chart (figure 8.11) it becomes apparent that this energy is most likely background noise sourced from working mine machinery. A single detonator therefore produced a trace with a signal to noise ratio of 3.7, whereas the use of a small amount of explosive dramatically improved the S/N ratio to 9.5 and 13.3 for one and two additional charges respectively.

8.3.3.3 Hammer test results.

Figure 8.12 depicts trace results from the 6 geophones for a hammer source initiated directly above each of the geophones. The hammer source was stacked five times in each case. The corresponding frequency spectra plots are shown in figure 8.13 and the properties of the traces are tabulated in table 8.3. At first glance, it is obvious that there is greater variability in the results in comparison to the explosives test. This is to be expected, since a hammer source is non-repeatable. In all cases, the P-wave arrival is easy to identify. The calculated velocities in table 8.3, for assumed straight raypaths, vary across the geophone array and this is most likely a reflection of the quality of the limestone footwall. A high velocity area appears to exist in the centre of the footwall between the two cross-cuts and the velocity reduces away from the centre. The same is true for the peak frequency, indicating that the footwall is more competent

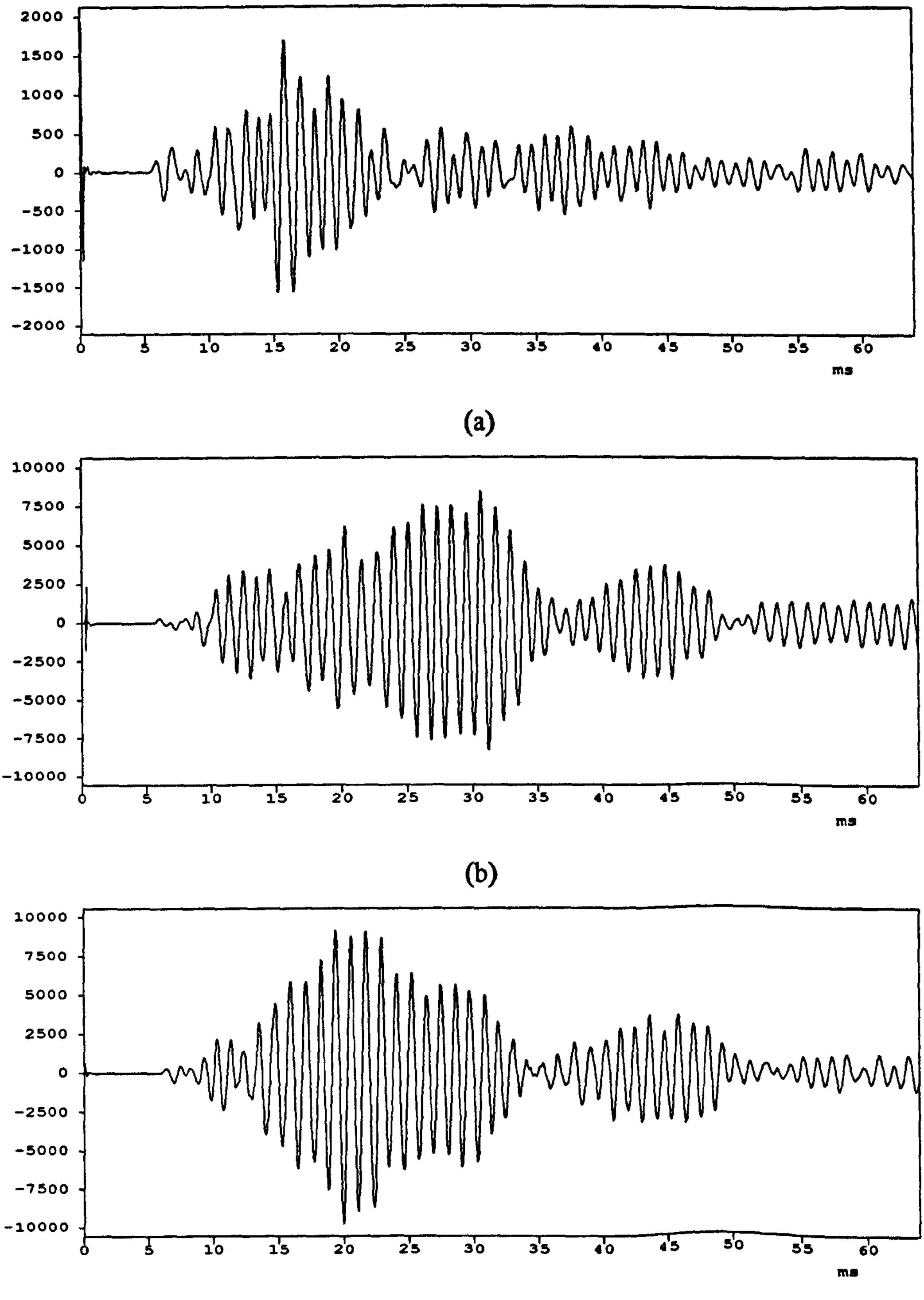

FIGURE 8.9 Comparison of traces acquired directly below three different explosive charges, (a) detonator only (source = detonator point 1, receiver = geophone 2), (b) detonator plus one small pill of gelignite (source = detonator point 2, receiver = geophone 3), (c) detonator plus two small pills of gelignite (source = detonator point 3, receiver = geophone 5). See figure 8.8 for source and receiver locations.

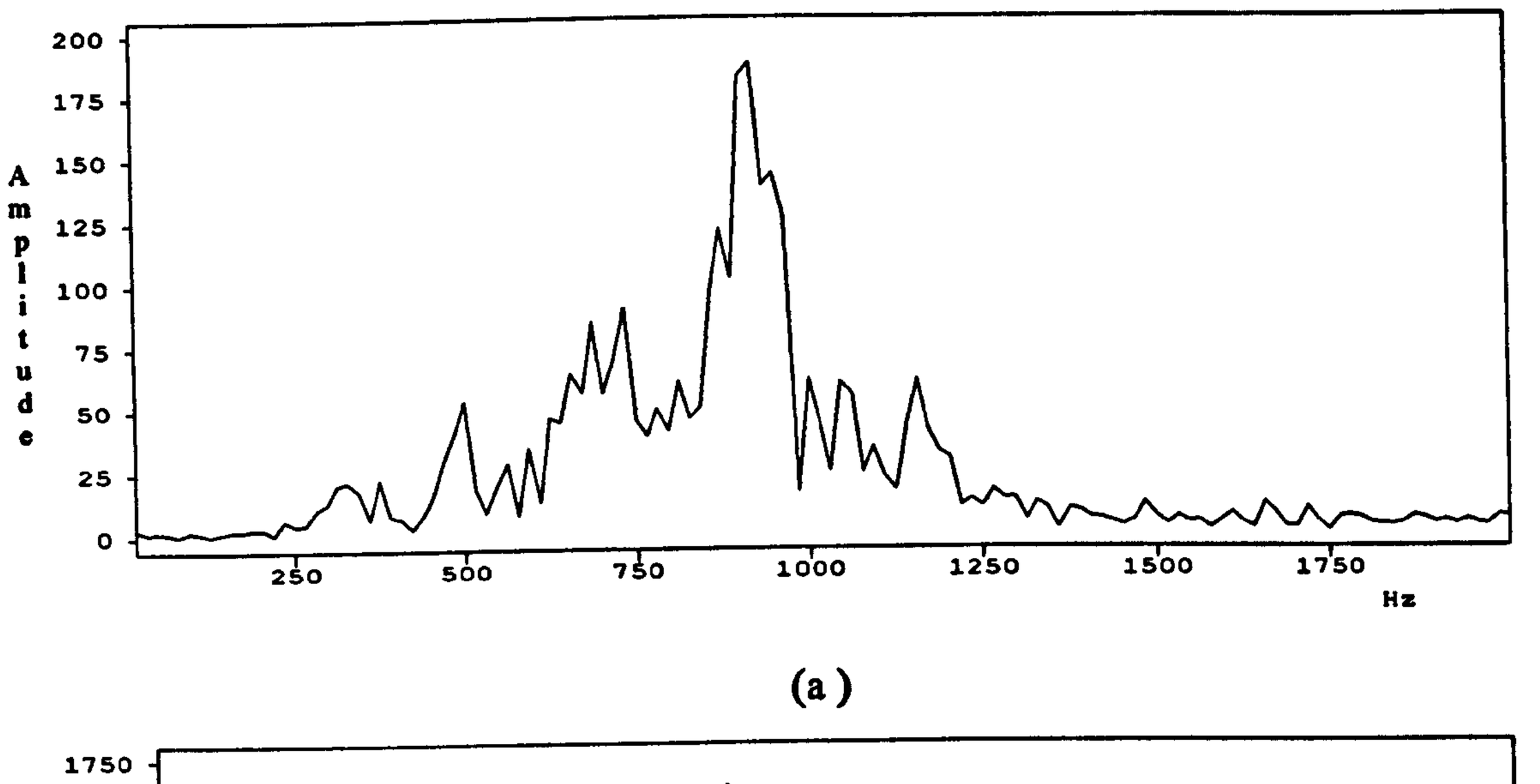

(a)

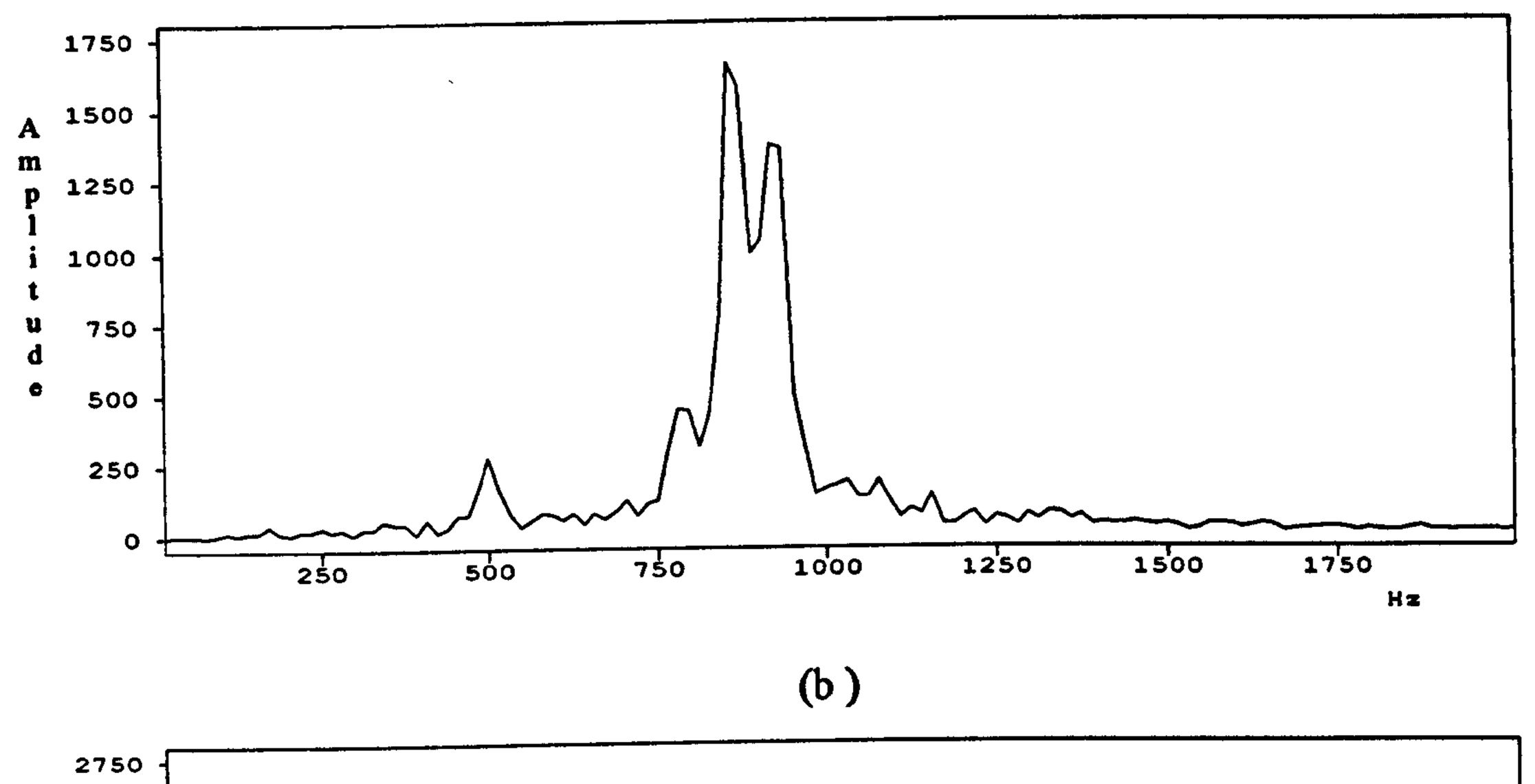

(b)

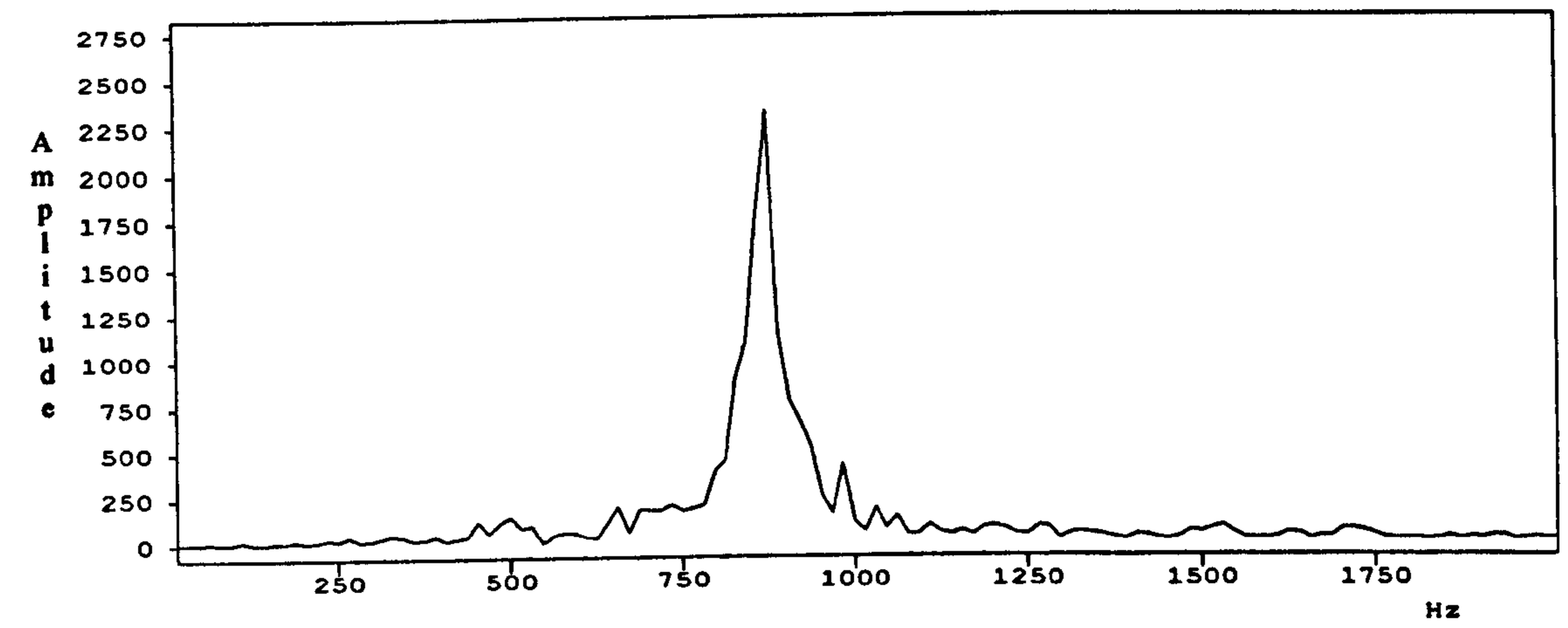

(c)

FIGURE 8.10 Frequency domain characteristics for the traces in figure 8.9 for (a) detonator only, (b) detonator plus one small pill of gelignite, (c) detonator plus two small pills of gelignite.

Source	Travel-time (ms)	First Peak Amplitude	Rise Time (ms)	Peak Frequency (Hz)	Peak Frequency Amplitude
Detonator Only	5.531	155	0.3504	922	188
Det + one charge	5.625	227	0.3504	859	1655
Det + two charges	5.656	267	0.3256	875	2322

TABLE 8.2 Explosive source properties

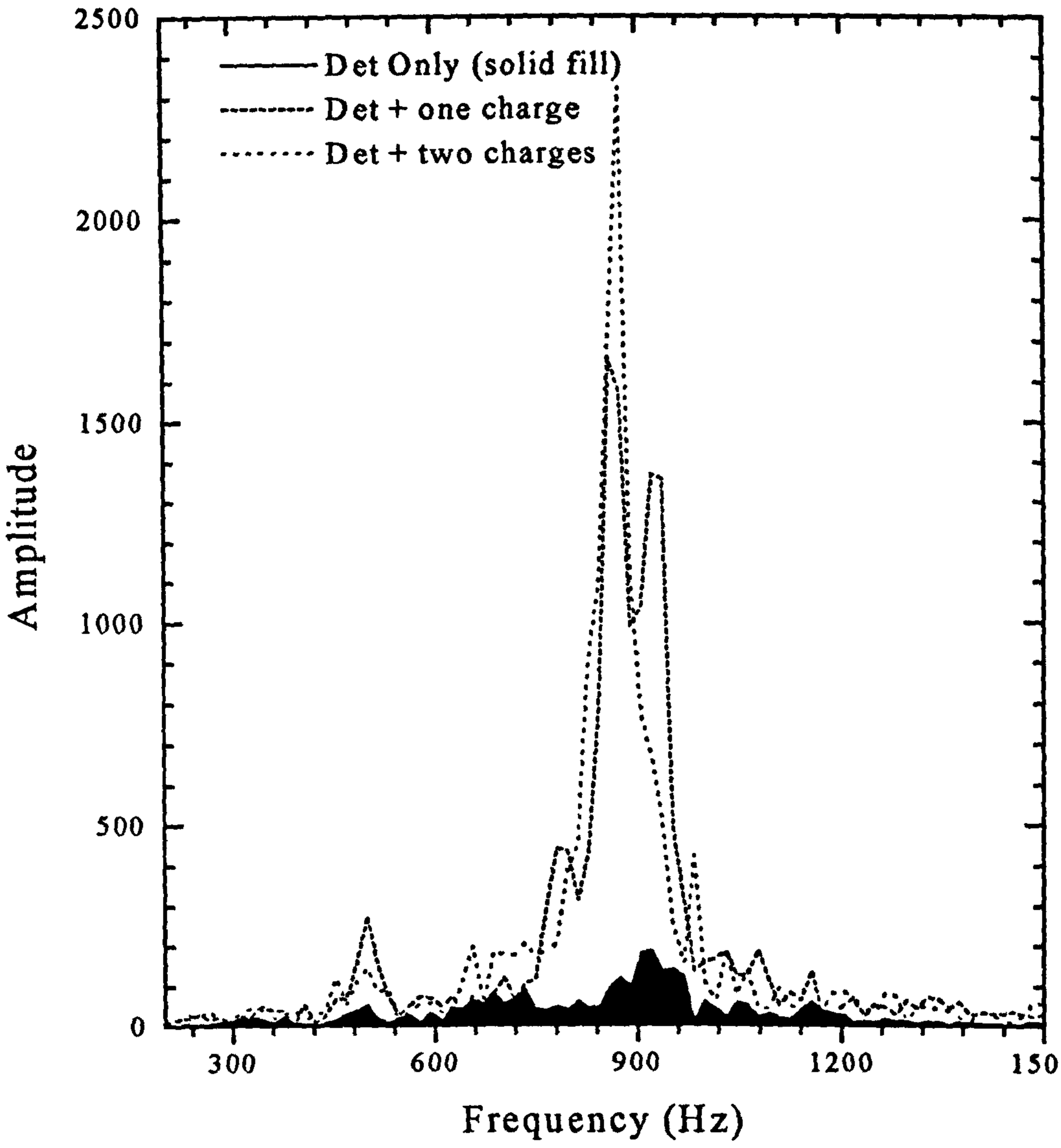

FIGURE 8.11 Amplitude comparison of the three different explosive charge frequency spectra.

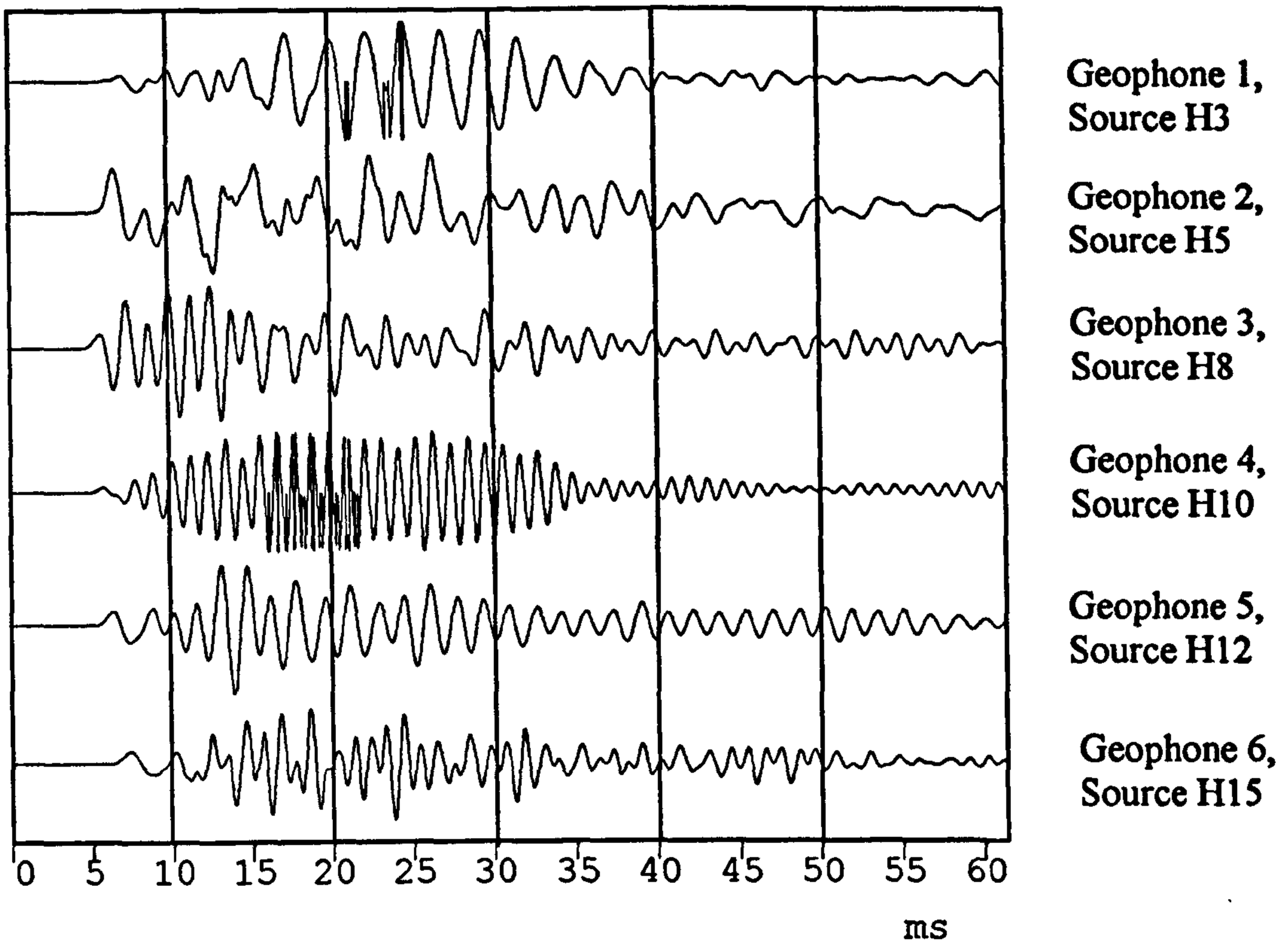

FIGURE 8.12 Traces at each of the 6 geophones for 5 stacked hammer shots directly above.

Geophone Number	Dist. (m)	Travel-time (ms)	Vel. (m/s)	First Peak Ampl.	Rise Time (ms)	Peak Freq (Hz)	Peak Freq Ampl.
1	32.70	5.844	5595	3077	1.2752	406.25	7030
2	32.73	5.500	5951	1487	1.1248	531.25	332
3	32.48	4.719	6883	445	0.9752	765.62	3114
4	32.42	5.125	6326	2947	0.7504	890.62	8389
5	32.57	5.469	5955	2109	0.9496	593.75	2561
6	32.41	6.6563	4869	1349	0.8750	875	644

TABLE 8.3 Hammer source properties

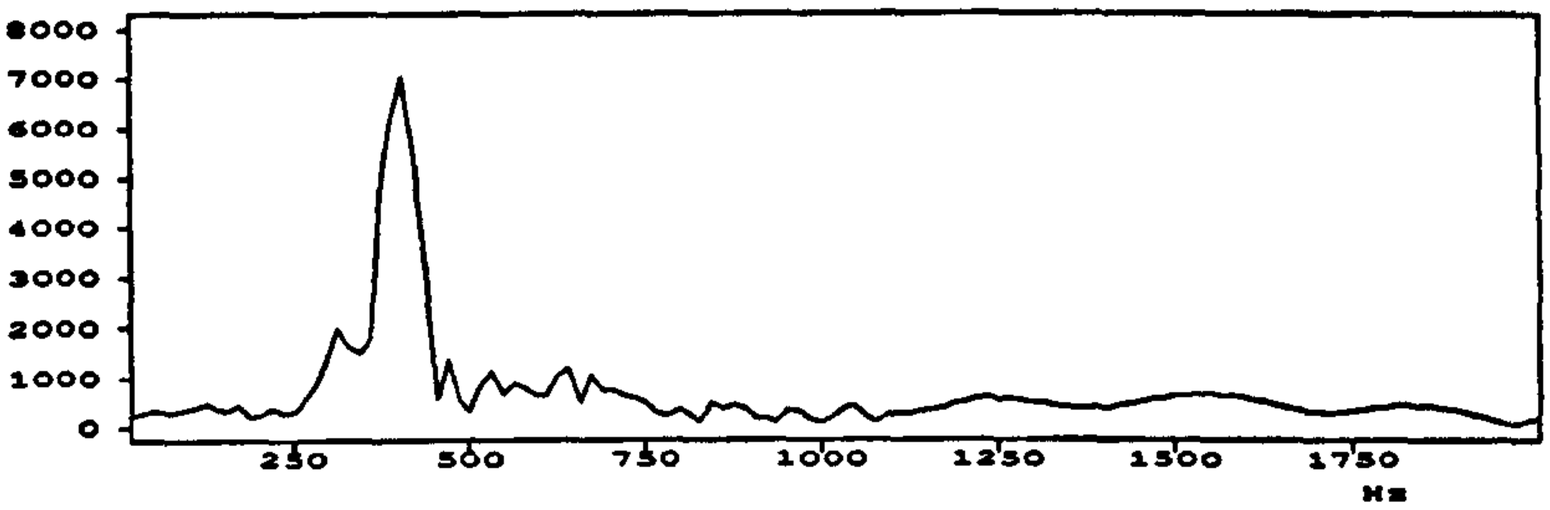

Geophone 1

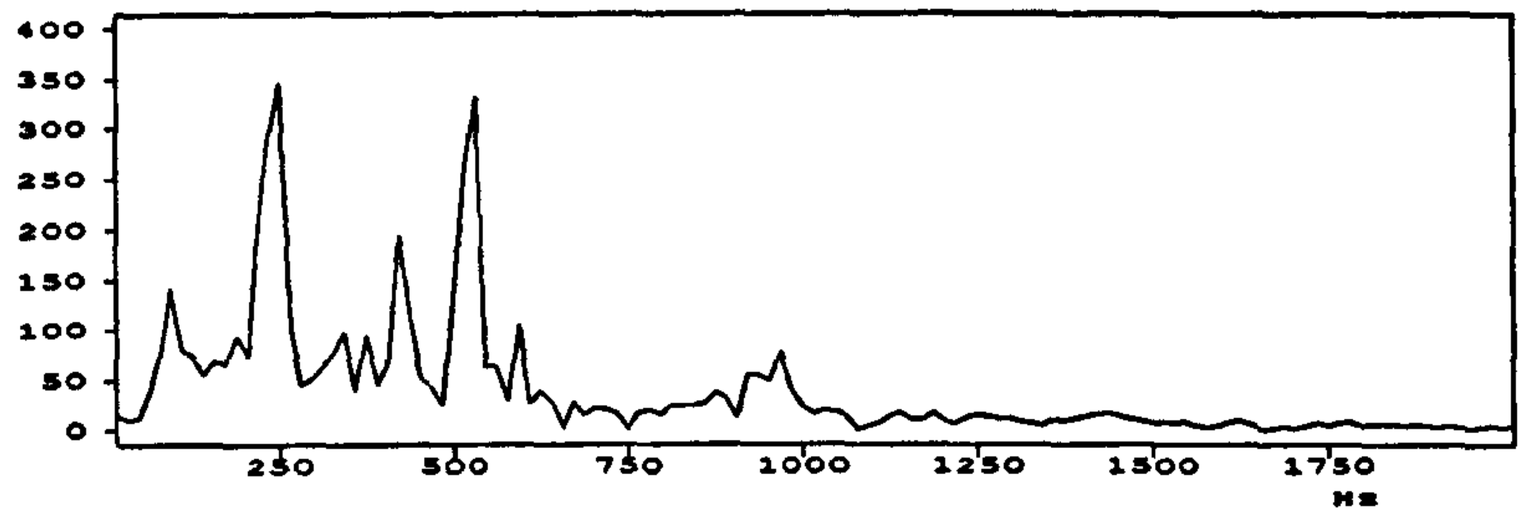

Geophone 2

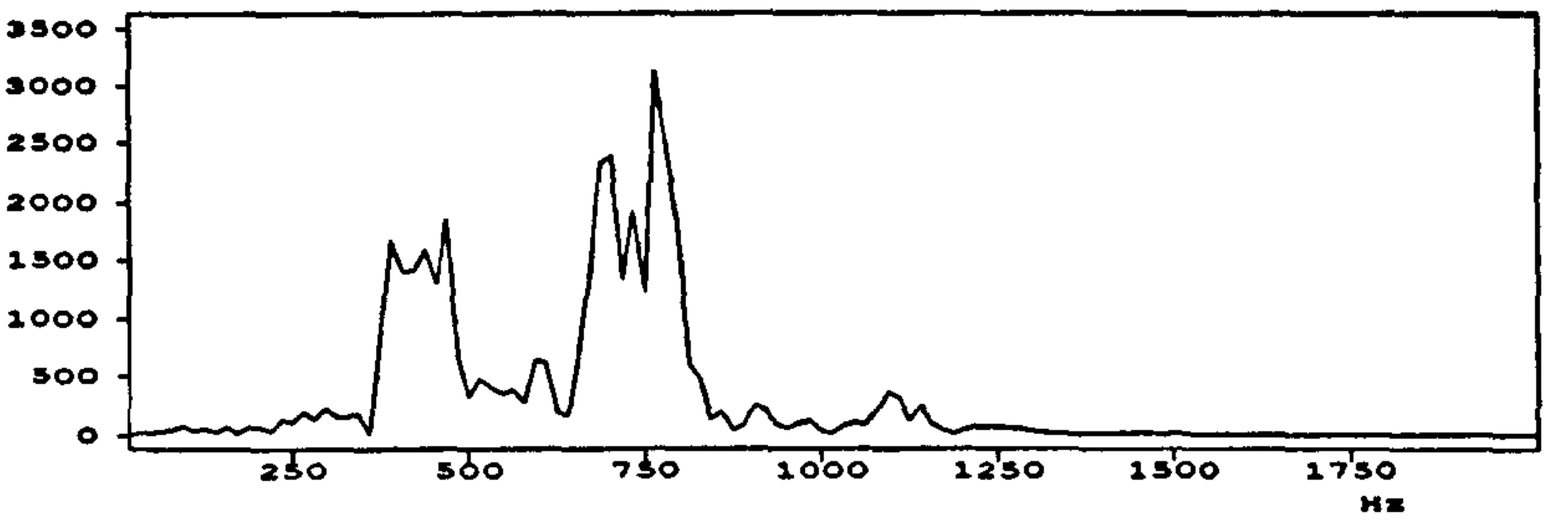

Geophone 3

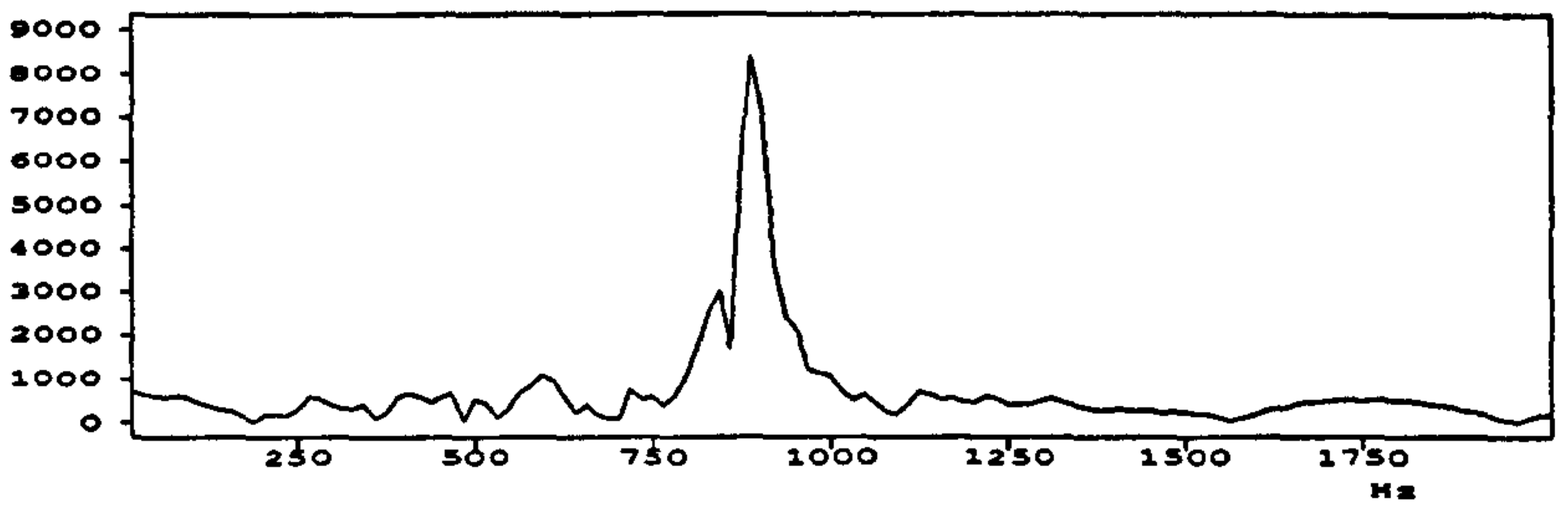

Geophone 4

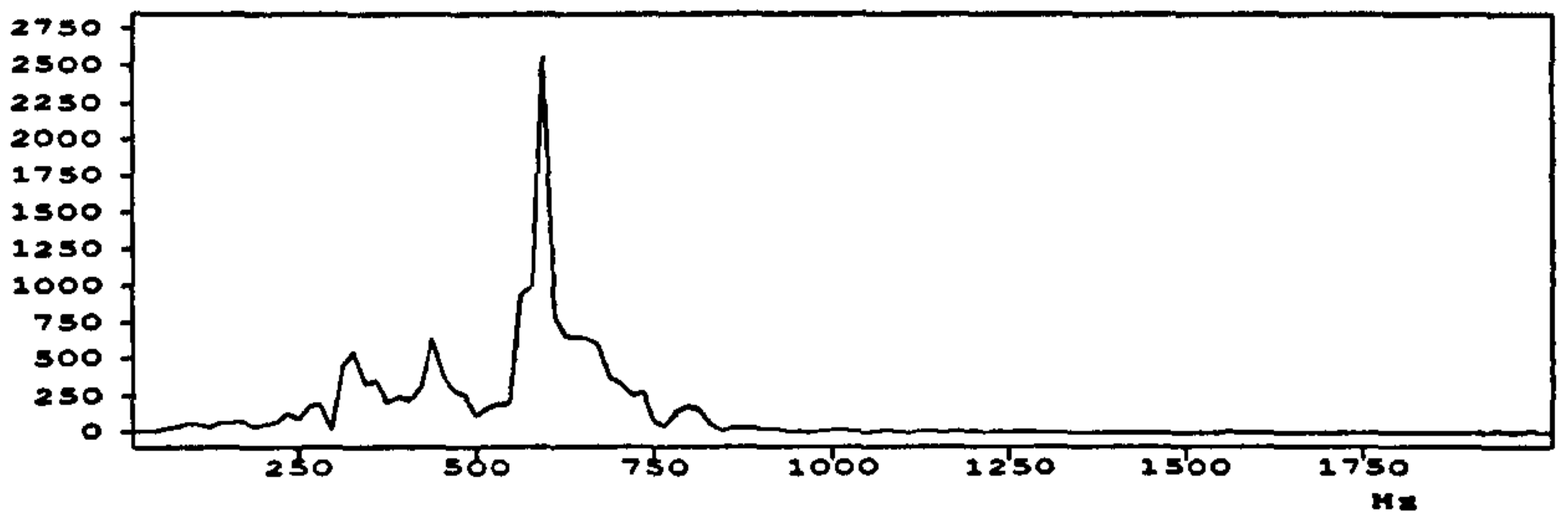

Geophone 5

Geophone 6

FIGURE 8.13 Frequency domain spectra for hammer shot traces in figure 8.12

in the centre than at the sides between the cross-cuts (see figure 8.8). The increase in rise time (increase in attenuation) would tend to confirm this conclusion. Drivage of the cross-cuts and subsequent removal of the vein has destressed the footwall between the levels, particularly around and between the cross-cuts. For highly competent limestone rock, a hammer source can propagate energy with a dominant frequency range of 700 to 900 Hz, whereas in less competent rock, it is still possible to propagate seismic energy at 400 to 600 Hz. In terms of seismic resolution these relate to wavelengths of between 7 and 8 meters.

8.3.3.4 Inter-level 2-D tomography.

The traveltime data collected from the hammer and explosive calibration tests were inverted to produce a P-wave velocity tomogram cross section of the footwall at the test site. This was done to investigate the typical velocities encountered in the footwall area and to confirm some of the conclusions drawn from the hammer source data in the previous section. The combined tests produced a total of 114 raypaths for the inversion procedure, enough data to produce the simple tomogram shown in figure 8.14. The plot reveals the higher velocity zone within the centre of the footwall between the cross-cuts suggesting more competent limestone in this area.

8.4 First Stope Trial

8.4.1 Experimental Setup

It was arranged with the mine to conduct a time-lapse tomographic survey of the footwall of a working stope. The experiment has already been documented by Donnelley & Pearce, 1996. A 3-D view of the site is depicted in figure 8.15. The plan view of the layout is shown in figure 8.16. A week before the stope was due to start production, a number of geophone points were sited on the upper B-West level and dryhole sparker holes drilled in the lower C-West level drive. Mountings for geophones consisted of drilled and tapped small diameter brass bar, grouted into small drill holes in the floor at the side of the upper roadway. Sparker holes were drilled, 3 inch diameter, 2 meters deep, horizontally into the sidewall on C-West level using a boom drill rig available at the site. Ground conditions were particularly poor on B-West level and whilst driving the first cross-cut, the mine encountered running ground associated with the vein which halted development progress. At the proposed site of the second cross-cut on B-West level, an exploratory borehole indicated an identical scenario, and it was decided to mine the block without this development. In terms of the seismic survey, this

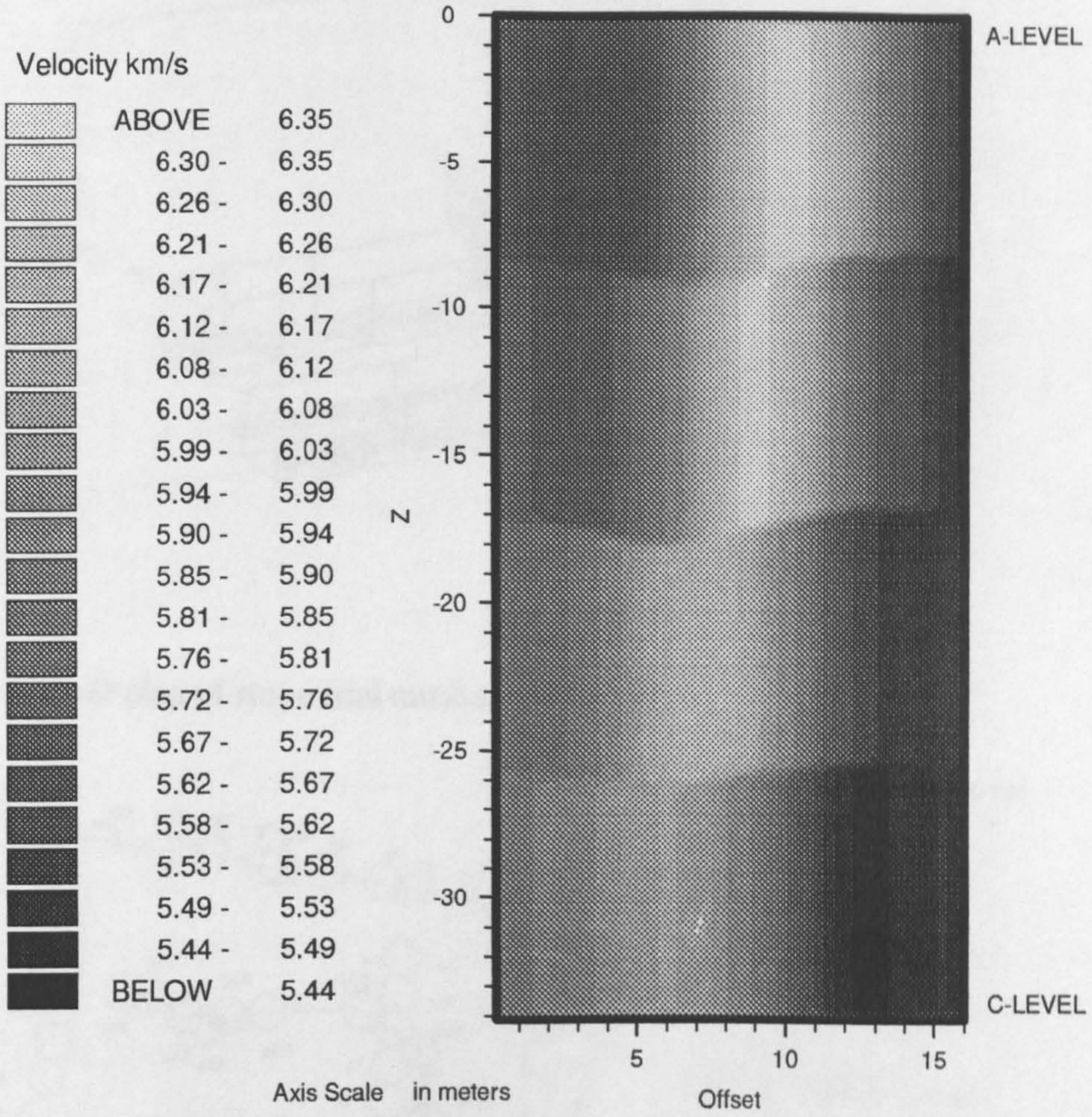

FIGURE 8.14 P-wave velocity inter-level tomogram calculated from the inversion of the combined explosive and hammer source traveltime test data.

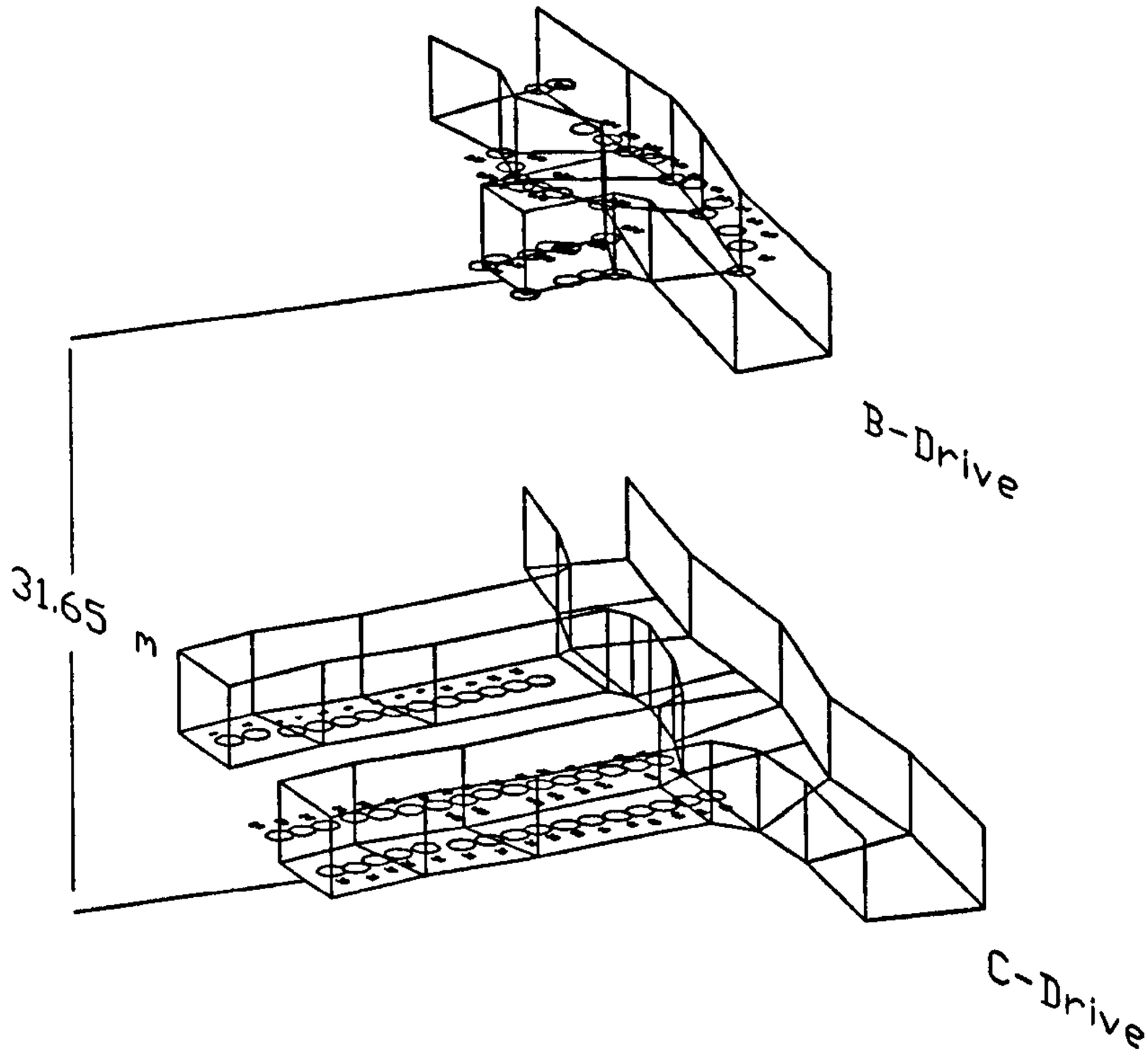

FIGURE 8.15 3-D plan of stope trial number 1 field site.

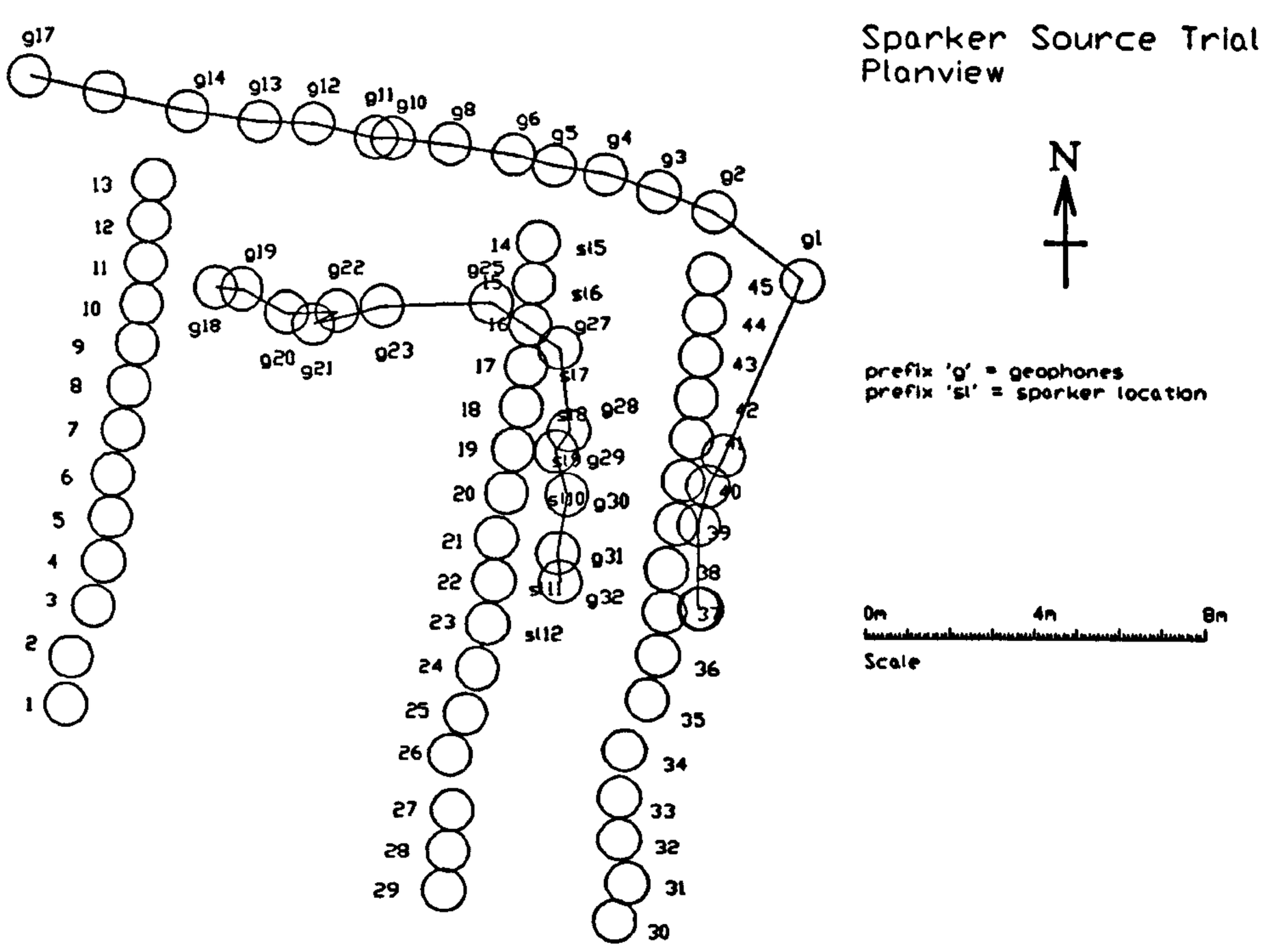

FIGURE 8.16 Plan view of the same site, showing geophone locations (prefix 'g') on B-West drive in relation to the sparker source locations (prefix 'sl') on C-West drive.

posed geometry problems for seismic coverage of the footwall region near the vein. To achieve better angular coverage of the survey area it was decided to place geophones along B-West drive. In all, 38 geophone points were sited, with 45 source holes on the lower level, making a total of 1710 measurable transmission raypaths.

The site was mapped on both levels for the change from competent limestone, through the mineralised zone to the actual vein itself. A number of small faults and joint sets with clay infill were noted running vertically parallel with the vein on the upper B-West level. The geological structure for the site, inferred between the two levels, is shown in figure 8.17

The first survey was carried out during the night shift at which time no production took place as the shift was normally devoted to longhole production drilling, development drilling or roadway maintenance.

Equipment for the test consisted of two ABEM Terraloc seismographs, 38 active geophones and associated cables, a 500m trigger cable run between the two levels, the sparker probe, salt solution supply and power source.

8.4.2 Results

It was realised at the time of the test that the received seismic data was of poor quality. The entire dataset was afflicted by a very poor signal to noise ratio and no seismic signal was discernible for at least a third of the geophones. The signal to noise ratio was not improved after repeated stacking of the source. A characteristic dataset which has been stacked 32 times is shown in figure 8.18 for the sparker source located at position 5. In general,

- Geophones 1 to 24 show evidence of seismic energy, although repeated stacking of shots and data filtering could not accurately identify the first break P-wave arrival. However, the traces show similar frequency characteristics to those recorded in the calibration test (figure 8.5) with respect to the dominant 500 Hz component (see especially geophones 2,7,8,11 and 12). These geophones correspond to receiver positions located in the competent limestone region of B-West drive.
- Geophones 25 to 38 show no seismic energy other than background noise. The signal to noise ratio is too poor to discern any seismic signal. These geophones were located in the cross-cut development on B-West drive (with the exception of geophones 25 to 27 which were located along a small fault line right on the edge of the transition zone) and were sited in the mineralised

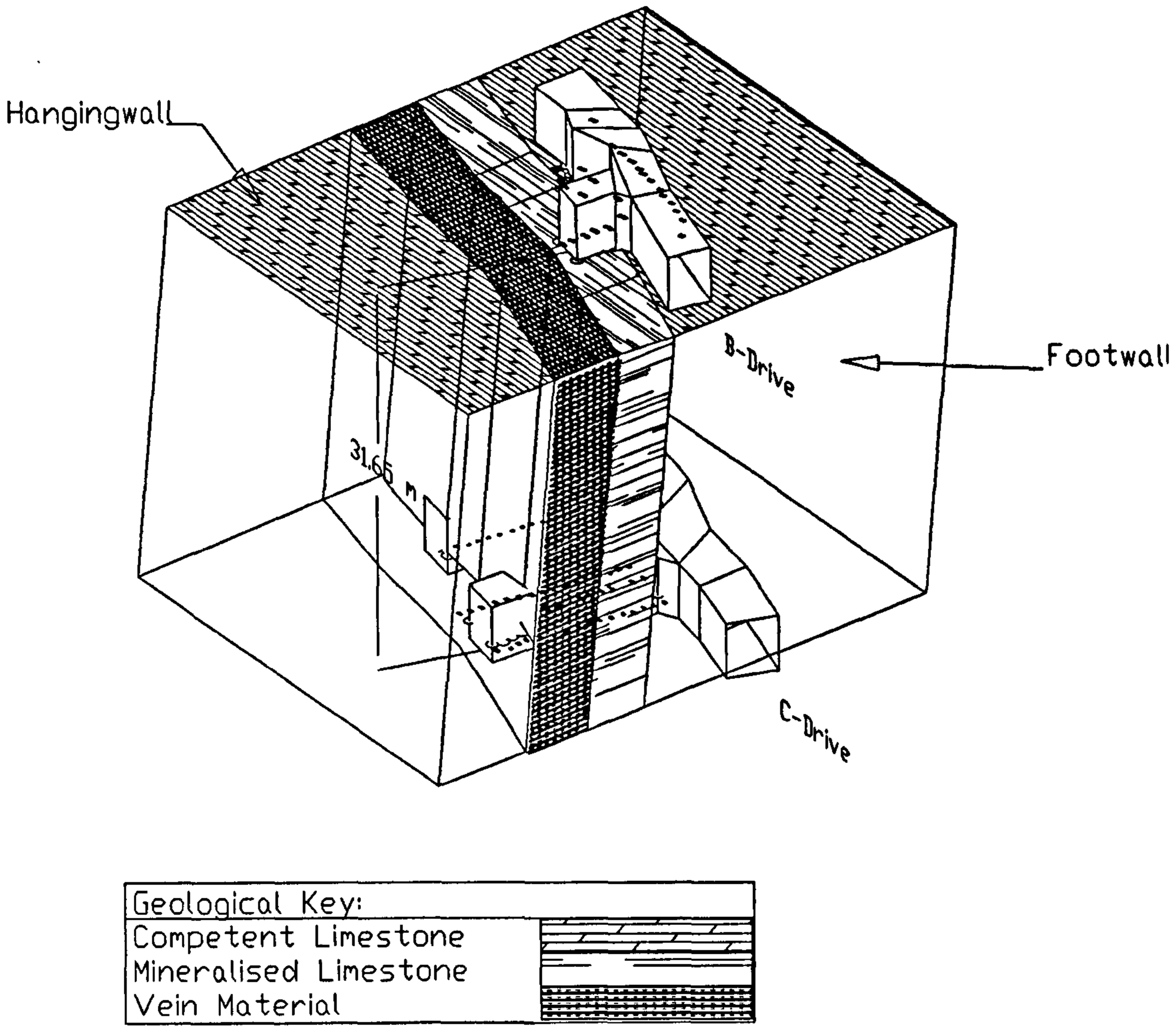

FIGURE 8.17 Geological structure inferred from mapping at the sparker source trial site.

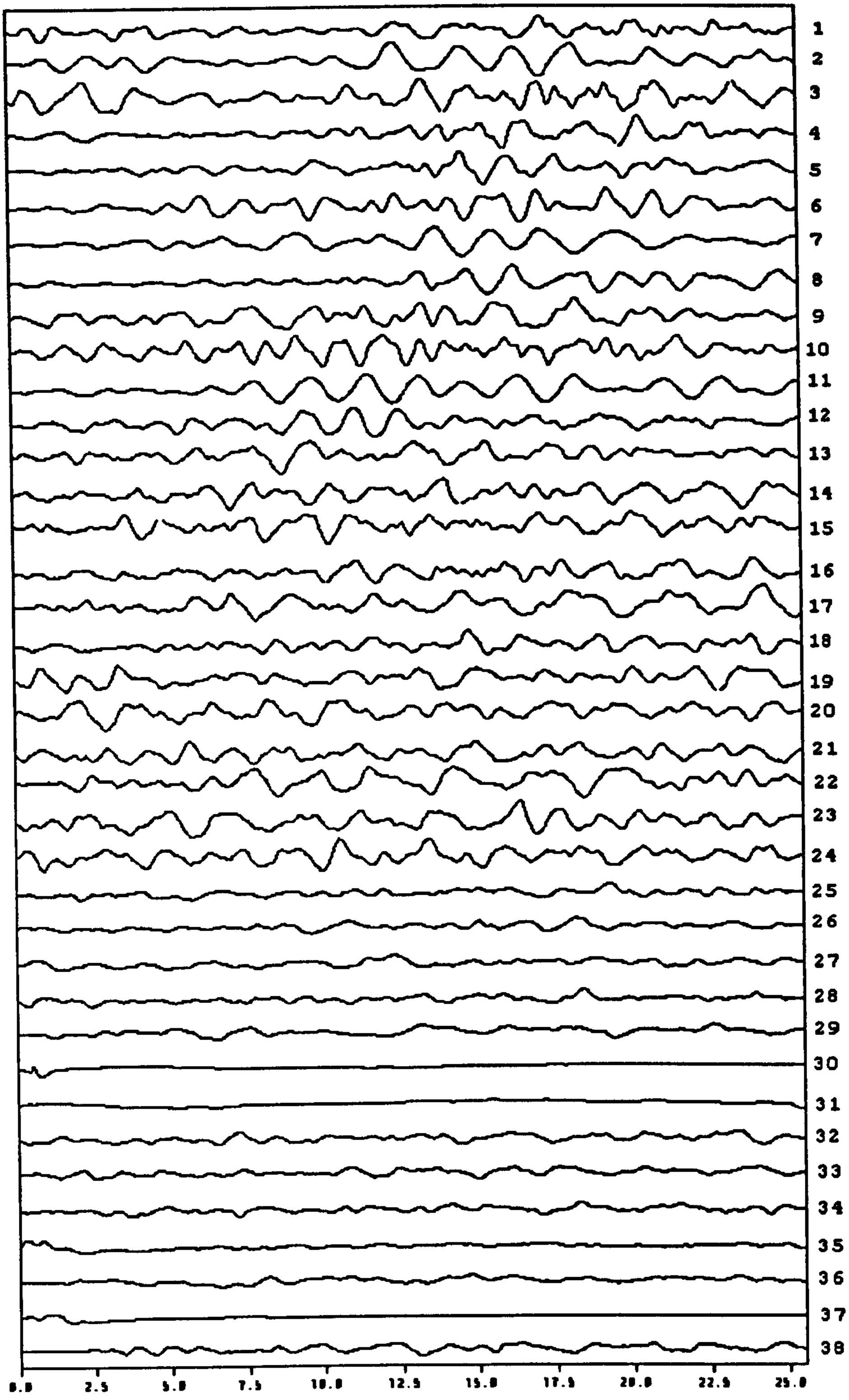

FIGURE 8.18 Typical seismic dataset for source at sparker location number 5 received across the entire 38 geophone array. Data is 2nd order Butterworth Bandpass filtered between 300 and 750 Hz.

limestone zone. The vein was not directly accessible on this level (as shown in figure 8.17).

8.4.3 Analysis

Because of the apparently poor data acquired at the time of the test, a complete survey was not carried out. Therefore it was not possible to measure traveltimes for direct and reflected raypaths for input into the 3-D inversion routine. However, at the time of the test, it was decided to investigate the characteristic seismic change from competent through mineralised limestone to the vein itself. Data was acquired starting at sparker source location 5 in the competent limestone. The source was then progressively moved into the mineralised zone towards the vein until no seismic signal could be discerned arriving at any of the geophones. This occurred at sparker location number 13.

8.4.3.1 First Peak Amplitudes of the Direct Wave

As first arrival times of the direct wave could not be accurately identified it was not possible to determine the velocity between the two levels. Neither therefore was it possible to measure the rise times of the first peak arrival. However, it was possible to investigate the change occurring from sparker source location 5 through to 12 by looking at the first peak amplitudes for a specific geophone or geophones. This is in effect was still a measure of the attenuation imparted to the raypath by the intervening rock mass and should give an indication of the location of the change from competent to mineralised limestone between the two levels. Note that the use of the first peak amplitude is only possible because the sparker source can be considered to be repeatable. This type of analysis would not be appropriate for a hammer or explosive type source.

Geophone 11 gave the best traces across the experimental dataset. These traces are reproduced in figure 8.19 for sparker source positions 5 to 12, plotted with the same y axis to show the deterioration in amplitude across the source positions. The graph in figure 8.20 is a plot of the normalised first peak amplitude at geophone 11 versus the sparker source position. The locations of the geological boundaries mapped on the C-West level development are marked. Figure 8.20 would suggest that the transition from competent to mineralised zone is not clearly defined but gradually changes from sparker location 8 to 10. This might be expected from this type of vein deposit, where the mineralised zone is basically a hydrothermal fluids encroachment area. Raypath diagrams for the source-receiver arrangements are shown in figure 8.22. Geophone 11 is located in the competent limestone, and therefore seismic raypaths

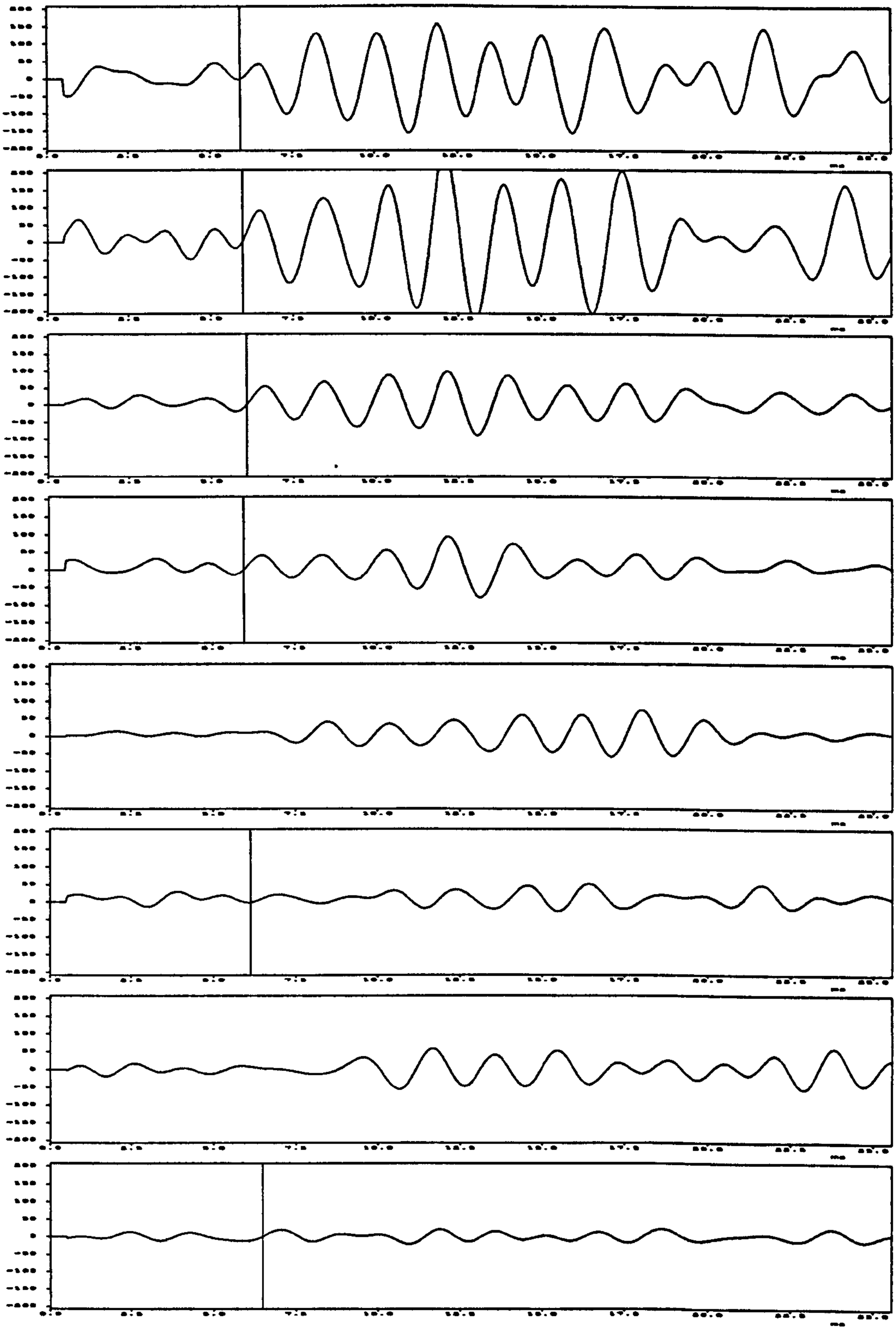

FIGURE 8.19 Seismic traces acquired at geophone 11 from sparker source point 5 through to 12.

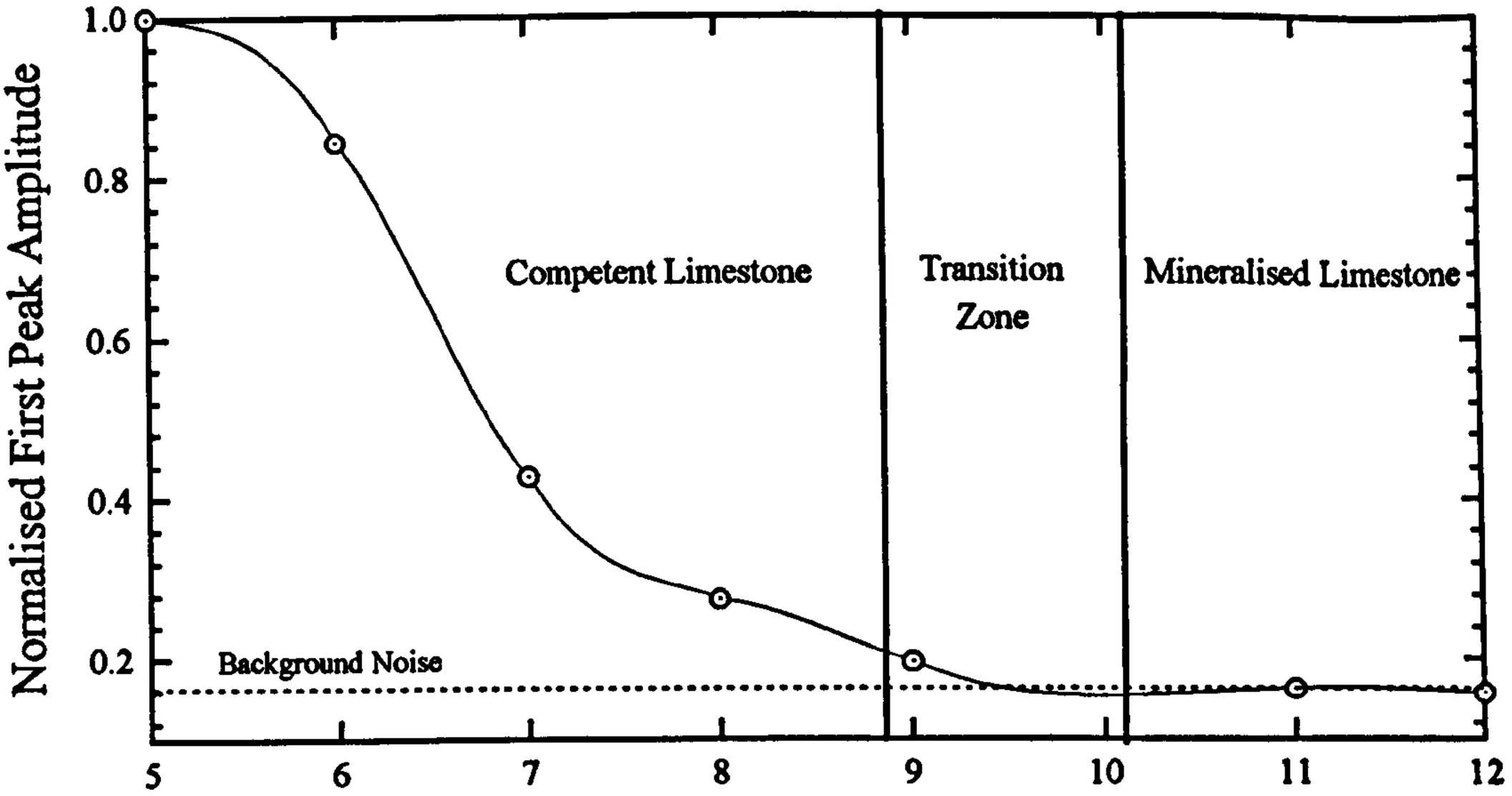

FIGURE 8.20 Normalised first peak amplitude versus sparker source location for geophone 11. The competent limestone - transition zone - mineralised limestone locations are marked according to the positions on the C-West development.

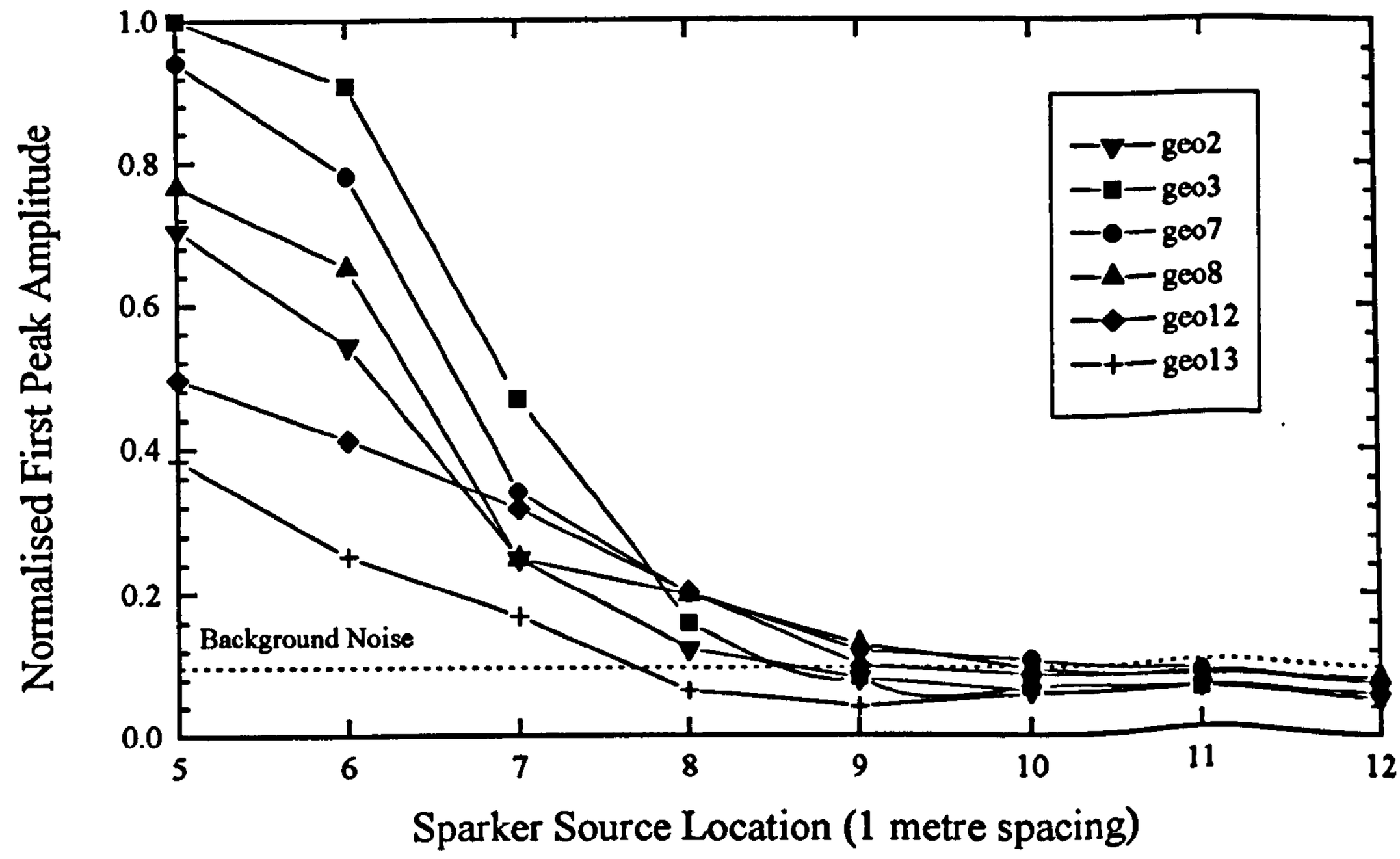

FIGURE 8.21 Normalised first peak amplitude versus sparker source location at geophones 2,3,7,8,12 and 13.

from all the sparker source positions at some point must pass through this competent zone. The maximum first peak arrivals occur along raypaths received from source location 5 and 6. A marked 50 % decrease occurs in the first peak amplitude at location 7 within the competent limestone zone and thereafter for the next two source locations a further reduction of 25% is observed. For the source at subsequent locations from 9 to 12, no further decrease is observed, and the first peak amplitudes remain just detectable above the general background noise. This same trend is observed for other geophones (see figure 8.21) where the signal to noise ratio is poor and the first peak arrivals are more difficult to identify. Typically, percentage drops of between 30 % and 60 % occurred between source locations 6 and 7.

8.4.3.2 Raypath considerations

To understand what was happening in terms of the attenuation imparted to raypaths between the two levels it is easier to consider the paths in three dimensions. Figure 8.22 shows the straight ray approximation for paths between geophones 5 and 11 and all the sparker source locations in this test. The planar boundary marked on this plot joins the location of the competent-replacement interface on both the B-West and C-West cross-cuts. Raypaths from source points 10, 11 and 12 all travel up to a third of their propagation distance within the mineralised or transition zones and are therefore greatly attenuated. Raypaths from source points 5 and 6 only travel through the competent limestone zone and therefore have the greatest first peak amplitudes or the lowest attenuation. By the same token, raypaths from source points 7 to 9 should be similar to 5 and 6. However, a large drop in first peak amplitude is observed for raypaths originating from source point 7 as compared to source point 6. The most likely cause for this discrepancy is that a disturbance zone exists between the two levels within the competent limestone, probably directly above sparker source location 7. This zone may consist of weak or fractured ground, or a series of faults with clay infill which are characteristic of the area. Other evidence for this disturbance zone is the exposure of vertical fault planes running parallel along the south wall of the B-West drive. Presumably these faults extend some distance between the two levels. Seismic energy reaching geophones 18 to 24 is much less coherent and greatly attenuated in comparison to energy received by geophones 1 to 13. In particular, geophones 25 to 27 which were located right along the line of an obvious fault received no seismic energy at all.

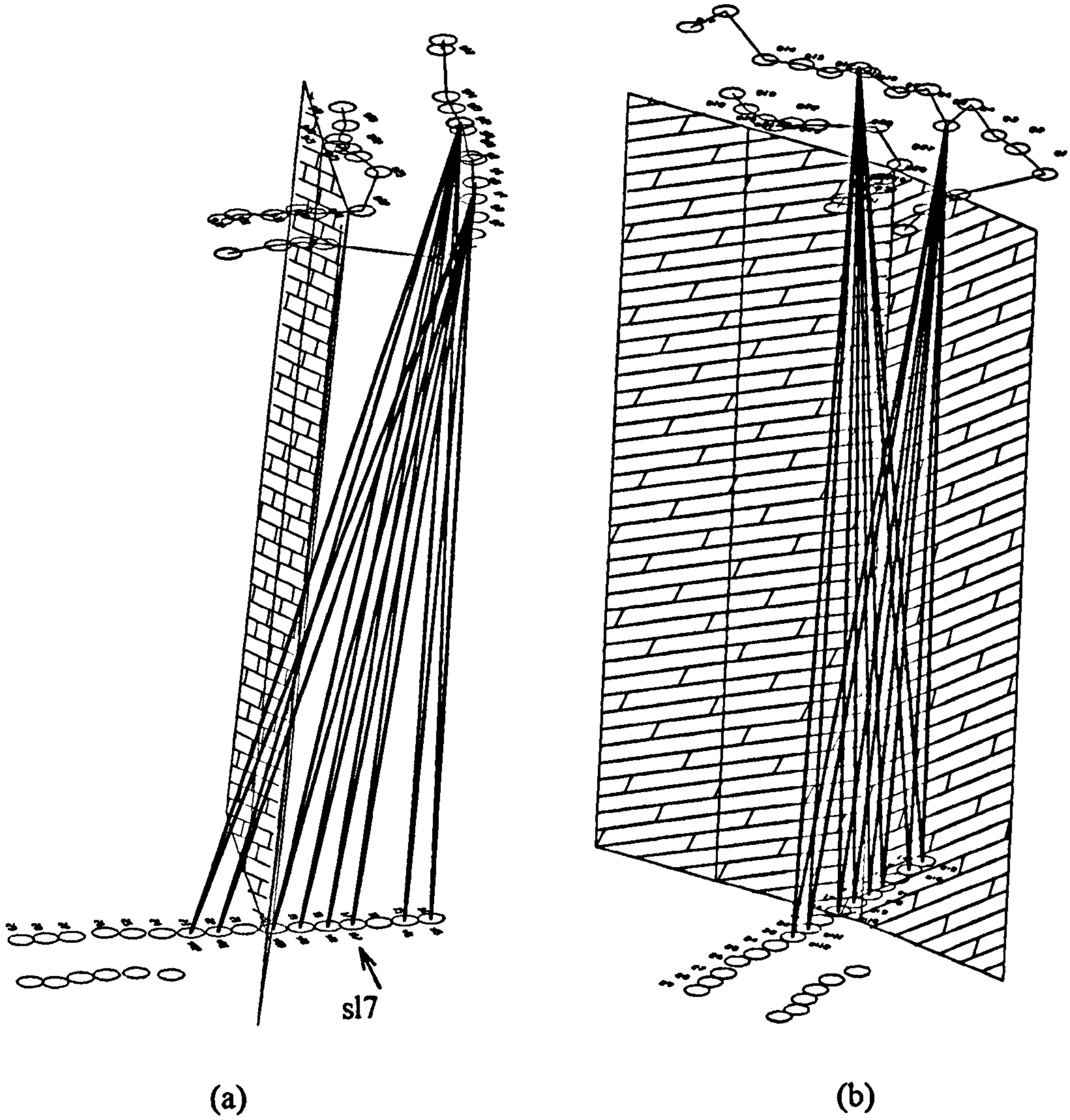

(a) (b)

FIGURE 8.22 3-D views of straight raypath approximations for source locations 5 to 12 to geophones 5 and 11. (a) side view, looking from the east ('sl7' = sparker location 7), (b) front view, looking from the south. The planar structure represents the mineralised limestone - transition zone boundary.

8.4.3.3 Stope collapse

The final piece of evidence for this disturbance zone within the competent limestone was revealed in subsequent stope footwall movement. Approximately 2 weeks after the test was conducted, there was substantial movement in the footwall along the fault lines described in the previous section. This occurred after the first production blast in the stope and the removal of some 2000 tonnes of vein material. Movement of the footwall, most probably due to slippage of these vertical faults along clay infill zones (White, 1996), resulted in the loss of the lower cross-cut located off C-West drive and the loss of the stope. In effect the footwall block cantilevered into the void created by the production blast, with the fault planes providing the pivot or point of weakness. Movement resulted in the need for extensive rock bolting and meshing on B-West drive to prevent loss of this access road. Subsequently, the block was still subsiding for more than 6 months after the initial movement and has caused a major obstruction to production schedules, with B-West drive being off limits for this time period. Extensive ring and chock support work has been carried out in B-West drive in an attempt to prevent further damage.

In retrospect, the first peak amplitude measurements provided a good indication that a major disturbance zone existed in the competent limestone. The large drop in the first peak amplitude between source locations 6 and 7 was not to be expected based on the geological mapping alone or the decrease in amplitude due to the increase in the distance of propagation. A large drop would have been expected to occur between source points 9 and 10, or 10 and 11, corresponding to the transition to mineralised limestone. The overall poor quality of the data was an indication of the poor ground in this area. The sparker source calibration test (section 8.3.2) showed that even through fractured ground, a reasonable first arrival could still be identified. However, this test has shown that even where data is so poor that first arrivals could not be identified and therefore velocities could not be determined, the simple property of first peak amplitude may still have been able to identify a potential area of disturbance, and alerted the need for extra ground reinforcement before the first production blast. This hypothesis needs further clarification, by comparing this data acquired for the worst case scenario with data acquired for a stable stope. This will be considered in the next section documenting the second stope trial.

8.5 Second Stope Trial.

8.5.1 Site Description and Experimental Setup

The mine provided another production stope for a further field study site. The stope was located approximately 70 m west of the first trial site along the parallel footwall drives, i.e. about 7 cross-cuts west on strike. The development stage completed, the stope was awaiting the start of production. Being at the lowest point in the current mine workings, it was temporarily being used as a pump housing in an attempt to de-water the vein ahead of the production stopes. The water inflow into the bottom access drive was noticeably greater than in the previous stope study, which had remained virtually dry. Conversely, the upper level of this current stope was virtually dry. The increase in the water was attributed to an increase in old workings in the area which acted as water stores. Seasonal variation may also have increased the volume of water entering the workings. Only one cross-cut had been developed into the vein on both B-West and C-West levels, but this allowed for a good 2-D cross-section survey of the vein, the mineralised zone and the competent limestone footwall. A 3-D plan of the site, showing source point and geophone locations is shown in figure 8.23. A plan view of the same site is shown in figure 8.24. The vertical distance between the two levels was 30 m.

8.5.1.1 Geology

The stope geology was almost identical to the first field site. A geological cross-section along the line of the two cross-cuts is shown in figure 8.25 (White, 1996). The section consisted of a competent limestone zone, next to a faulted replacement limestone zone, which adjoined the vein itself. Both B-West and C-West drives were located further away from the replacement zone than in the first case, for their improved protection. Exploratory boreholes provided information on the location of the replacement / competent limestone interface between the two levels. The cross-cut on the B-West horizon intersected some open old workings within the vein.

8.5.1.2 Choice of Source

Due to the disappointing performance of the sparker source in the first stope trial it was decided to opt for a different source type. The ideal alternative would have been the explosive source. However, the use of explosives would have damaged the roadway, especially in the relatively fragile mineralised zone and was therefore discounted. The cost of explosives was also a preventative factor. This left only the option of a hammer source, which had produced good results in the calibration trial.

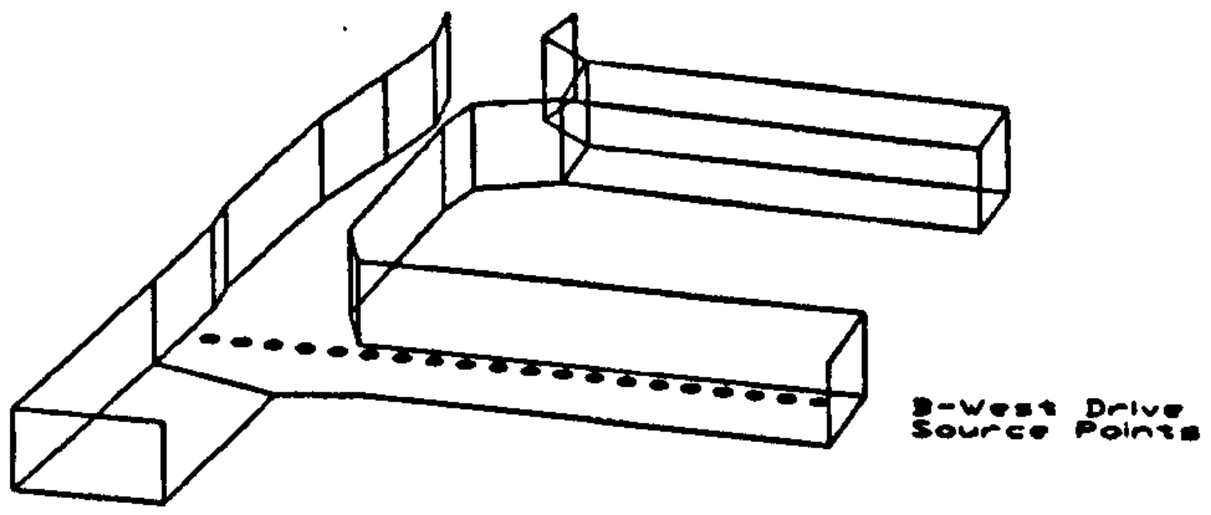

FIGURE 8.23 3-D view of the second stope site.

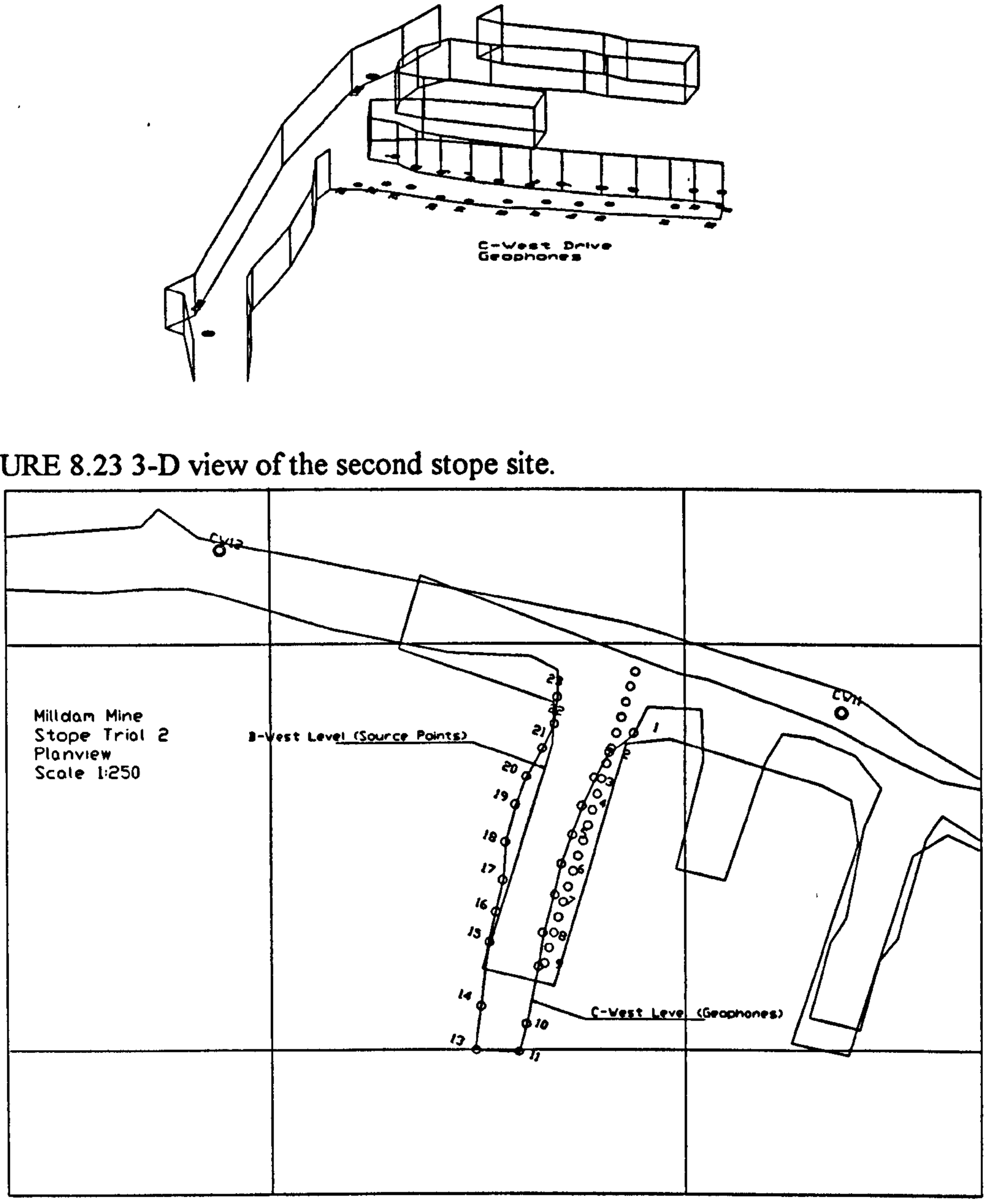

FIGURE 8.24 Planview of the second stope trial site, showing the relative locations of B-West and C-West horizons. CW11 and CW12 are mine survey points on the C-West horizon.

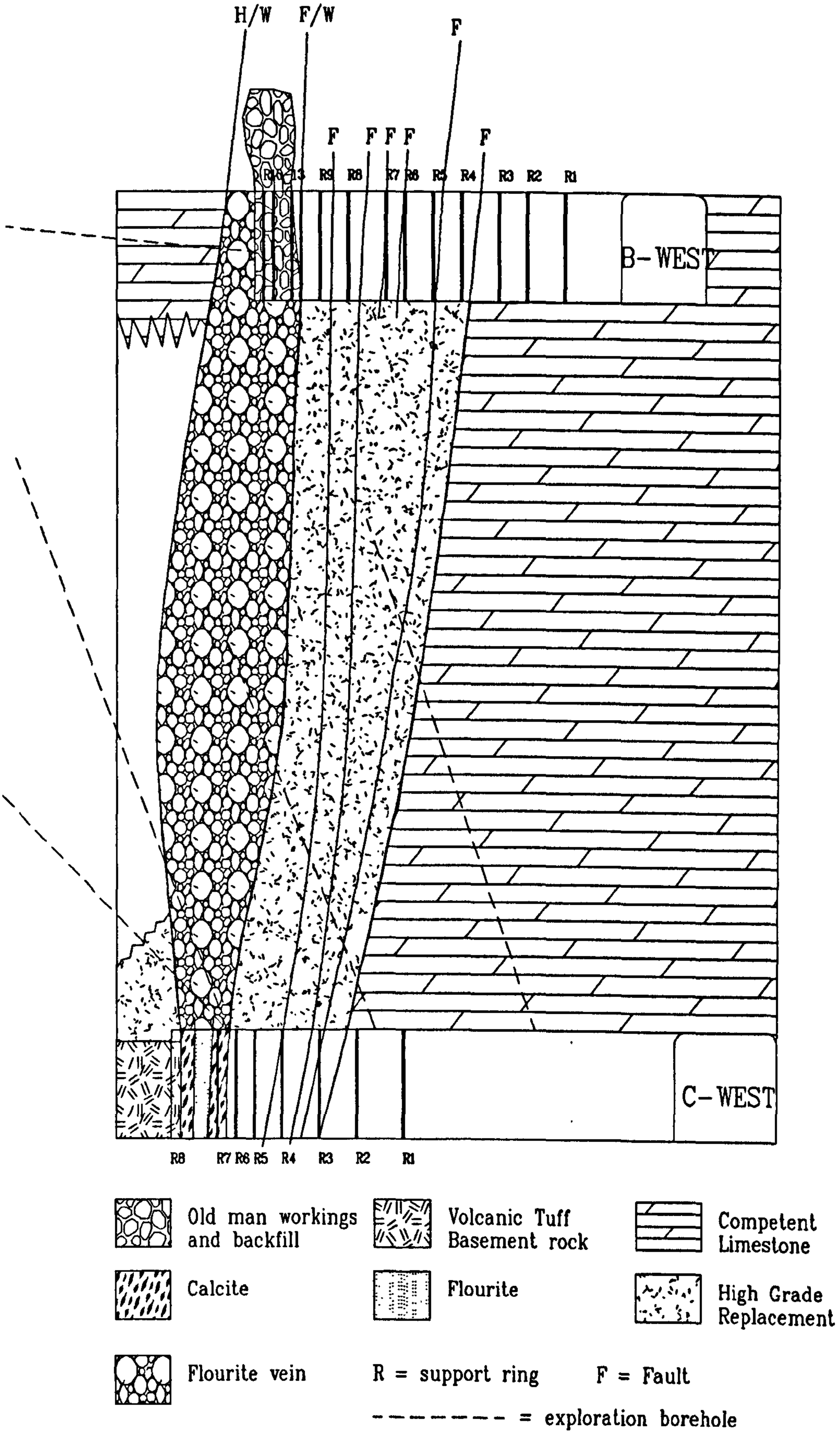

FIGURE 8.25 Geology at the second stope site (White, 1996)

8.5.1.3 Experimental Setup.

24 geophones were sited in the sidewalls of the cross-cut on C-West level, 12 down either side and accurately surveyed in. A line of source points, 18 in all, at one metre intervals was surveyed along the cross-cut on the upper B-West level. The geometry allowed for two tomographic planes to be imaged across the footwall of the stope, using 216 direct arrival traveltimes in each. Similarly it was expected that the same number of reflection arrival traveltimes should be identifiable for each tomogram plane. The 24 geophones were the passive SM-6 type. The seismograph consisted of a 24 channel, 16 bit floating point EG&G Geometrics Smartseis, and was triggered by a standard EG&G hammer switch, connected by a 500m trigger cable between the two levels. Communication between the two levels was facilitated by the mines two way radio system. All seismic data was acquired using the shortest sampling rate on the seismograph (0.03125 ms per sample) for a record duration of 64 ms or 2048 samples. The survey was conducted twice over a 2 week period. The first survey (referred to as Milldam 3) was incomplete due to a technical equipment fault and only acquired data for the first 12 shot points. The second survey (Milldam 4) acquired data for all the shot points.

8.5.2 Results

The quality of the hammer source data was very good when compared to the data acquired in the first stope trial. A typical common source gather is shown in figure 8.26 for the central source point number 9. First arrivals are very clear and therefore easy to identify even for raypaths passing through the mineralised zone. The time of the first arrival increases dramatically for geophones located in the mineralised replacement zone and more than doubles for those in the vein. This indicates that there is a large velocity drop across the interface between the competent and replacement limestones. As well as the increase in arrival time, the dominant frequency received by the same geophones is reduced due to the attenuation of higher frequencies that are able to propagate through the competent limestone zone but not through the replacement and vein.

8.5.2.1 Velocity Tomograms

8.5.2.1.1 Initial Velocity Model

Given the geometry of the stope survey, for the purposes of initial velocity model definition and tomographic inversion it was simplest to consider the stope as a cross-hole survey by turning it through 90 degrees and assuming the B-West and C-West cross-cuts to be boreholes. The resulting initial velocity model is shown in figure 8.27

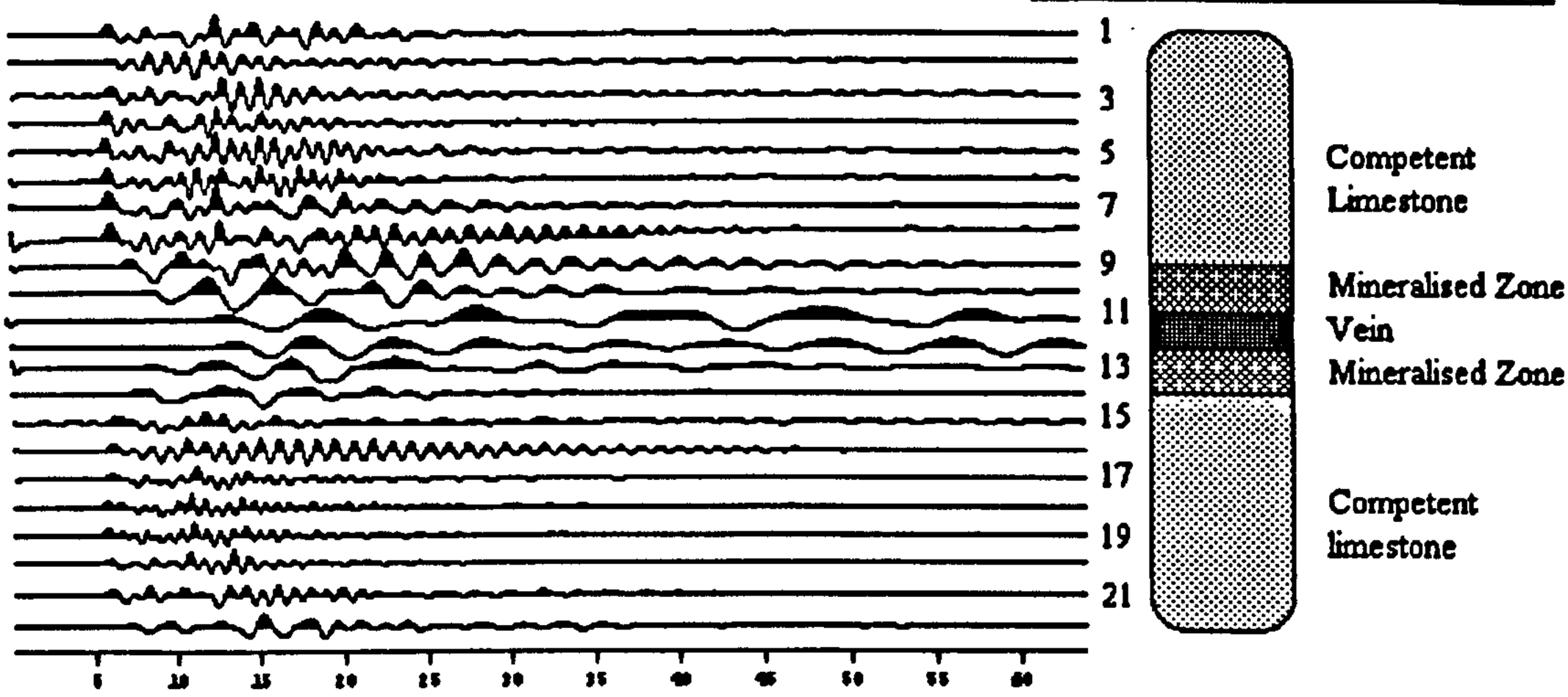

FIGURE 8.26 Typical seismic result set from Milldam Mine stope trial number 2, showing the lithology for the geophone positions. The x-axis scale is the time in milliseconds after the source initiation.

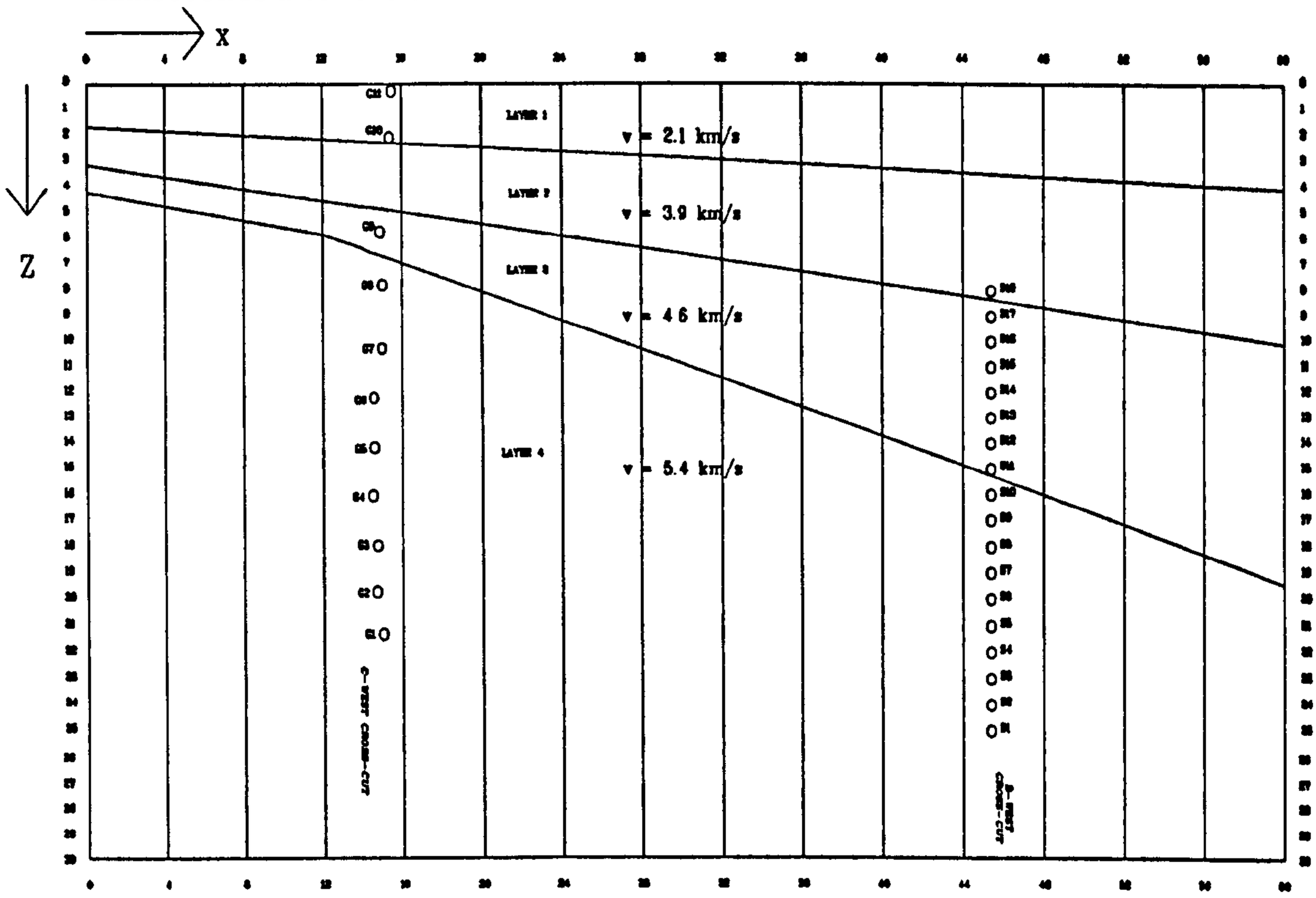

FIGURE 8.27 Initial velocity model for the second stope site. The model was made easier by considering the stope as a cross-hole survey. Velocities were based on single raypath measurements within each of the layers.

and consisted of 4 layers, where layer 1 was the vein, layers 2 and 3 the replacement zone and layer 4 the competent limestone. Given the limited number of transmission raypaths, the size and resolution of the model was restricted to 4 metre spaced x-lines. The velocity values assigned to layers 3 and 4 were the lowest values determined from single traveltime measurements between geophones and source points located in the same layer. Velocities for layers 1 and 2 were estimated from traveltime measurements between source point S18 to geophones G10 and G11 (see figure 8.27).

8.5.2.1.2 Inversion.

Due to the large velocity contrast across the small section, the inversion procedure took longer than expected. The large contrast increased the sensitivity of the raytracing process, where a small change in the source take-off angle caused a large deviation in the eventual detector arrival point (see chapter 5, section 5.3.2). A good result was achieved after 7 iterations with a total CPU time of 756 seconds on a Sun Sparc 10 work station. In keeping with the other inversion results documented in this thesis, the cut-off for the observed deviation of the theoretical model from the true model was set at 0.38 ms and monitored using the χ^2 calculation (see chapter 6 section 6.2.4.3). The interface perturbations were heavily damped in relation to the velocity, since the location of the vein and replacement-competent contact were accurately known along both of the cross-cuts. Therefore the inversion process was forced to change velocity with only minimum adjustment of the interface locations. The change in observed deviation which each iteration is shown in figure 8.28 and shows that the inversion process easily converged on the final result.

8.5.2.1.3 Transmission Tomogram

Velocity tomograms were produced for the two planes through the footwall and only that for plane 1 is reproduced in figure 8.29, the tomogram for plane 2 being virtually identical. The geological zones varying along the cross-section are immediately obvious from figure 8.29. The red zone, or high velocity zone of layer 4 corresponds to the competent limestone, where there is a small variation from 5.0 to 6.0 km/s between the two levels. The contact between this competent zone and the replacement limestone is extremely well defined, with a velocity change across this boundary typically of the order of 1.5 km/s. Within the replacement zone velocities vary between 2.5 and 4.5 km/s. The overall lower velocities in the replacement when compared to the competent limestone, reflect the much weaker and faulted nature of this zone. The contact between the vein and the replacement zone is also well defined with a typical drop in velocity across this boundary of 1 to 1.5 km/s.

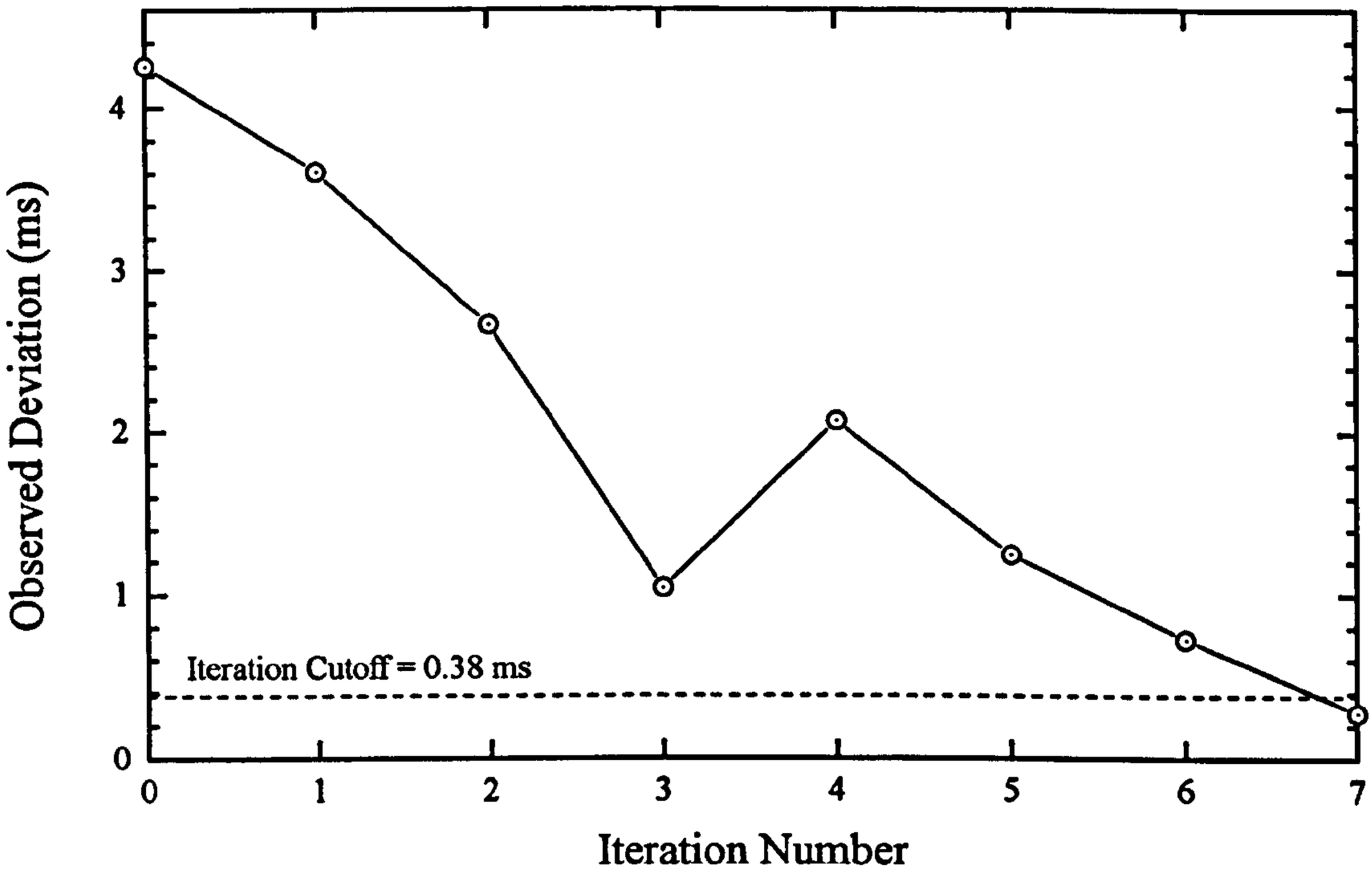

FIGURE 8.28 Observed deviation versus iteration number for the transmission traveltime inversion in the second stope trial.

With respect to the original aims outlined in section 8.2.3, the inversion process has successfully identified the competent-replacement boundary between the two levels. The raytracing diagram in figure 8.30 gives some insight into this process. Longer raypaths between source points 16 to 18 to geophones 1 to 7 with relatively fast traveltimes have forced the inversion process to change the shape of the replacement-competent boundary and extend the competent limestone layer at an inter-level distance of 20 to 30 m. Raypaths within the replacement and vein are less in number and limited in their coverage due to the slowness of these layers. Only the lower portion of the vein receives ray coverage and therefore only velocities and the interface in this area are accurate. Outside the area of ray-coverage the tomogram is just a reflection of the original velocity model. The replacement zone receives good ray-coverage over the whole area except in the top portion near the vein. Therefore the most accurate areas of the model are the competent zone, layer 4, the replacement-competent contact and the layer 3 portion of the replacement zone.

8.5.2.1.4 Forward modelling and combined inversion

Forward modelling of the transmission traveltime model showed that due to the angle of the replacement - competent interface, no reflections were expected from this boundary. Inspection of the seismic field data showed this to be the case with no

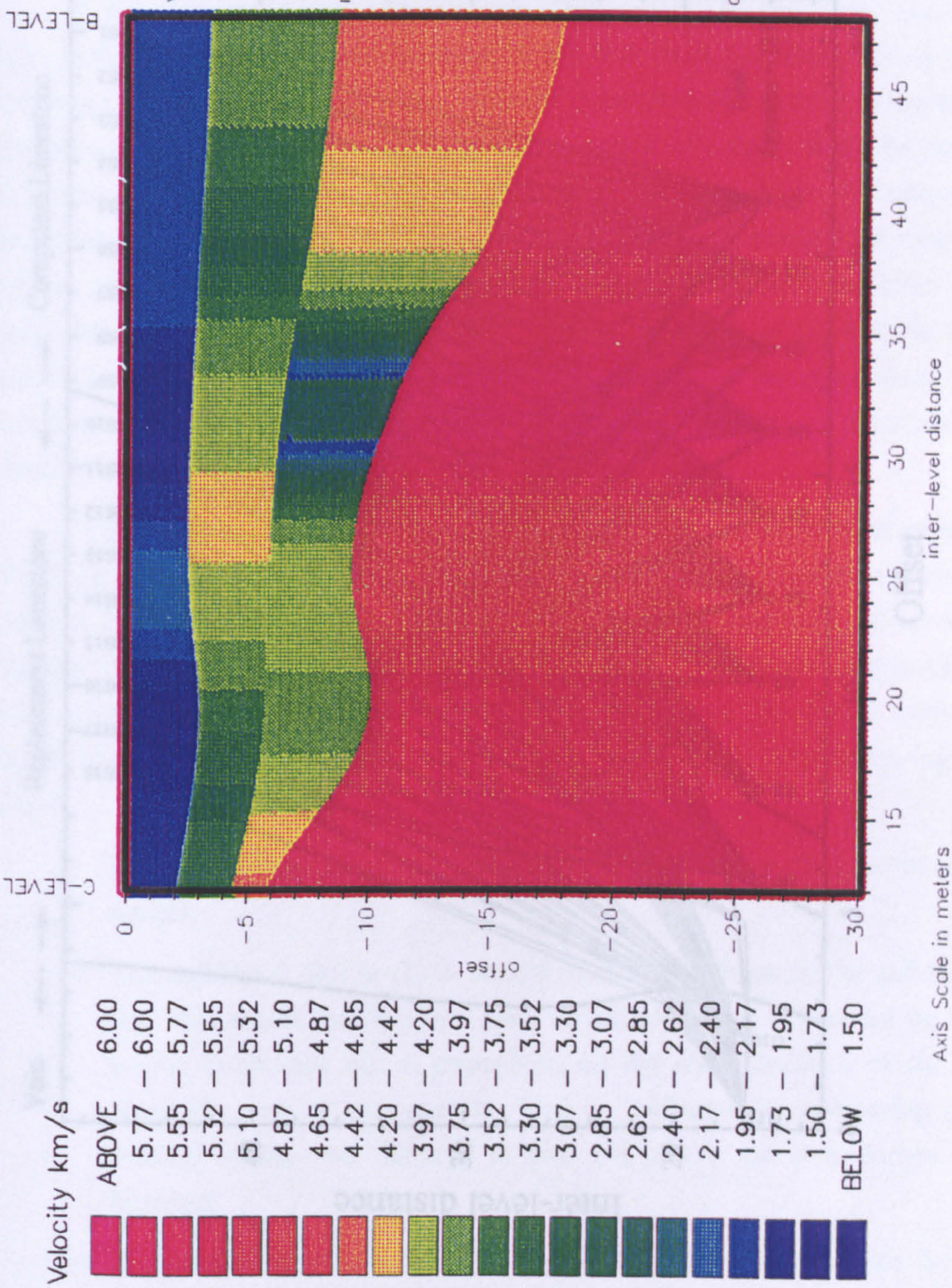

FIGURE 8.29 Transmission traveltime tomogram for plane 1 of the second stope trial.

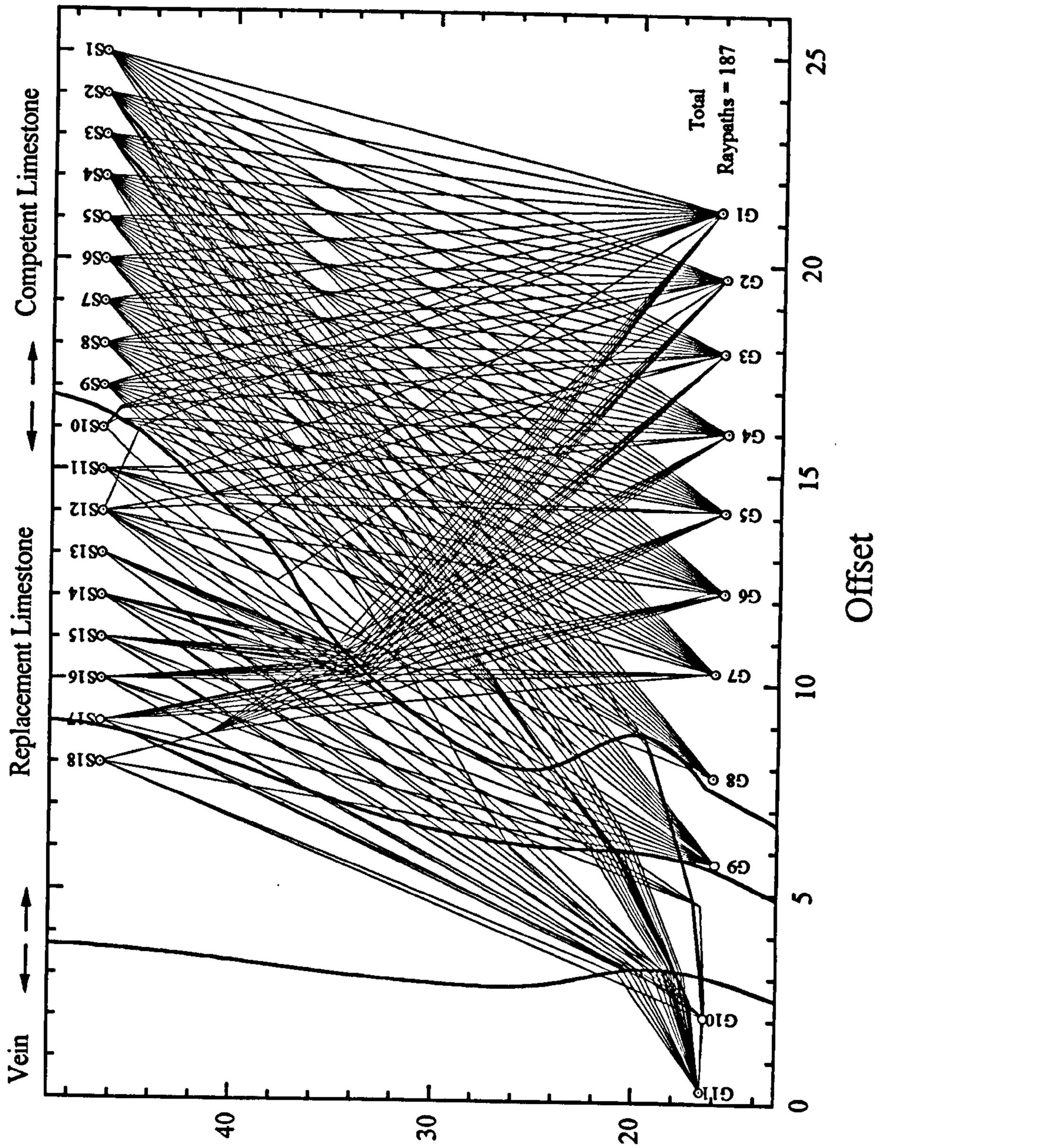

FIGURE 8.30 Transmission raytracing for the tomogram in figure 8.29.

obvious reflection patterns discernible. Therefore, for this field configuration the further step of the CTRT process could not be carried out and no further improvement in the transmission traveltime tomogram was possible.

8.5.2.2 Seismic Profiles

In the first stope trial, despite the poor quality of the data, the use of the repeatable source allowed measurement of the first peak amplitude across a profile of the competent and mineralised zone, with the prediction that a drop in the amplitude in the competent limestone zone indicated the presence of a fault. With the two data sets available for the second stope, each acquired on different dates, the unique situation arose where it was possible to check whether first peak amplitudes measured from traces acquired using a non-repeatable hammer source were suitable for similar predictions. By comparing the first peak amplitude profiles of the two datasets it was possible to check consistency between the two results and therefore show whether or not the amplitudes were a reflection of the rock mass condition, or the variability of the amplitude of the source.

Figure 8.31 shows the normalised first peak amplitudes arriving at geophones 1 to 9 from sources 1 to 12 for (a) Milldam Mine survey number 3 (the first survey on stope number 2) and (b) Milldam Mine survey number 4 (the second identical survey on stope number 2, carried out two weeks later). Figure 8.31 (c) compares the results from the two surveys by taking an average of the two sets of curves. The traces were normalised by dividing by the maximum amplitude along each profile. The following points are clear,

- For each survey, after normalisation, the profiles for each geophone are very similar.
- The milldam 4 plot in (b) is almost identical in shape to the milldam 3 plot in (a). This shows that the first peak amplitude is not dependent on the original source conditions but is dependent on the characteristics of the rock mass along the path of propagation. This is confirmed by comparing the average profiles of the two surveys in plot (c) where the two curves are almost identical.
- The profile curves are not those that would be expected given the geological interpretation in figure 8.25. The competent limestone zone was expected to impart relatively small attenuation to the propagating wave yet low first peak amplitudes are received at geophones sited in this zone for raypaths that have travelled exclusively through this zone. In particular, small amplitudes are

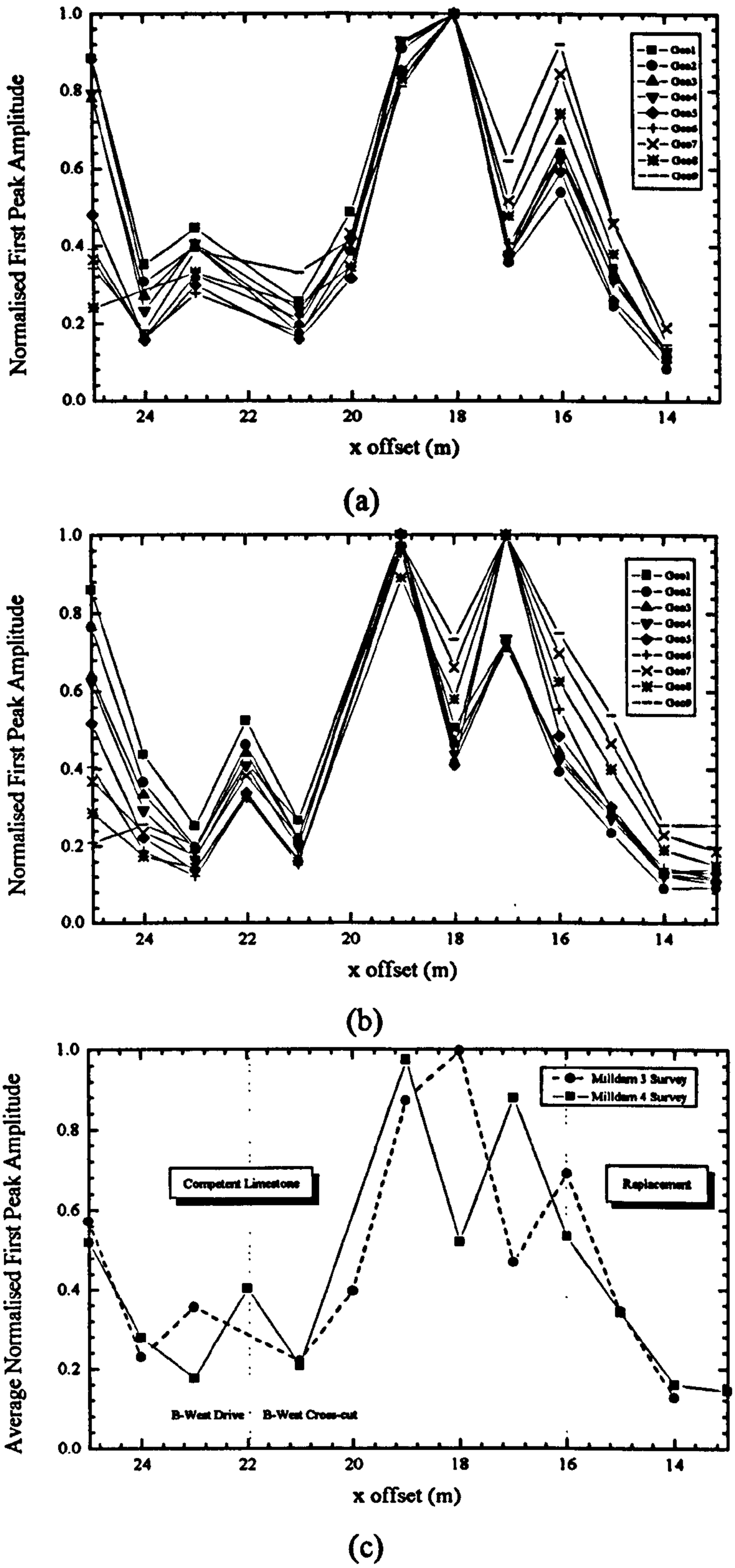

FIGURE 8.31 (a) Normalised first peak amplitudes with x offset for geophones 1 to 9 from Milldam survey number 3 (b) the corresponding normalised first peak amplitudes for Milldam survey number 4. (c) comparison of the average curves from plots (a) and (b).

received at offsets of 23 and 21 metres directly below the B-West drive and at an offset of 18 m directly below the entrance of the B-West cross-cut. The drop off in amplitude from an offset of 16 m and below corresponds to the replacement zone. The anomaly at 18 m corresponds to a clay feature in the floor of the B-West cross-cut roadway which may extend between the two levels. The other anomalies occur in apparently competent limestone, but in the same relative location as a low peak anomaly in stope 1. Therefore, the anomaly may be an indication of a fault or fracture zone between the two levels directly below the B-West drive.

Because the quality of the data in surveys 3 and 4 was much higher than data from the first stope trial it was possible to produce Q and velocity profiles for the same offsets. Q was calculated from the rise time of the first peak using equation 3.1, where the source rise time was assumed to be 0.3 ms and the constant C was set at 0.485 after Kjartansson's (1979a) theoretical constant Q determination of the value. The aim was not to produce absolute values of Q, but to look at the relative changes in Q along the profile. The average Q and velocity profiles are reproduced in figure 8.32 (a) and (b) respectively. Profiles determined from both surveys are almost identical for both Q and velocity. The Q profile follows the same general trend as that observed in the first peak amplitude profile. Low Q values are observed at x offsets of 22 m and 21 m and correspond with reduced first peak amplitudes at these points. The Milldam Survey number 4 also reveals a low Q value at 18 m offset which corresponds with the same low first peak amplitude anomaly. The same trough does not appear in the Milldam Survey 3 and could be attributed to the slightly poorer quality of data collected in this survey in comparison to survey 4. Velocity profiles between the two surveys are virtually identical with velocity varying slightly between 6.0 and 6.6 km/s in the competent limestone and dropping to a value of less than 4.5 km/s in the replacement zone. In particular, there is no significant reduction in velocity at x offsets of 21 to 23 m where low amplitude anomalies were present for the first peak amplitudes and Q profiles.

8.5.2.3 Discussion

The greatest area of interest along the profile is the reduced amplitude anomalies at offsets of between 21 and 23 m for both the normalised first peak amplitude and Q profiles. By assuming that the most competent part of the stope footwall corresponds to the point where these two parameters reach maximum values along the profiles it is possible to calculate percentage changes that occur away from this competent zone in the anomalous low value zones. Some of the results from chapter 4 can then be used to

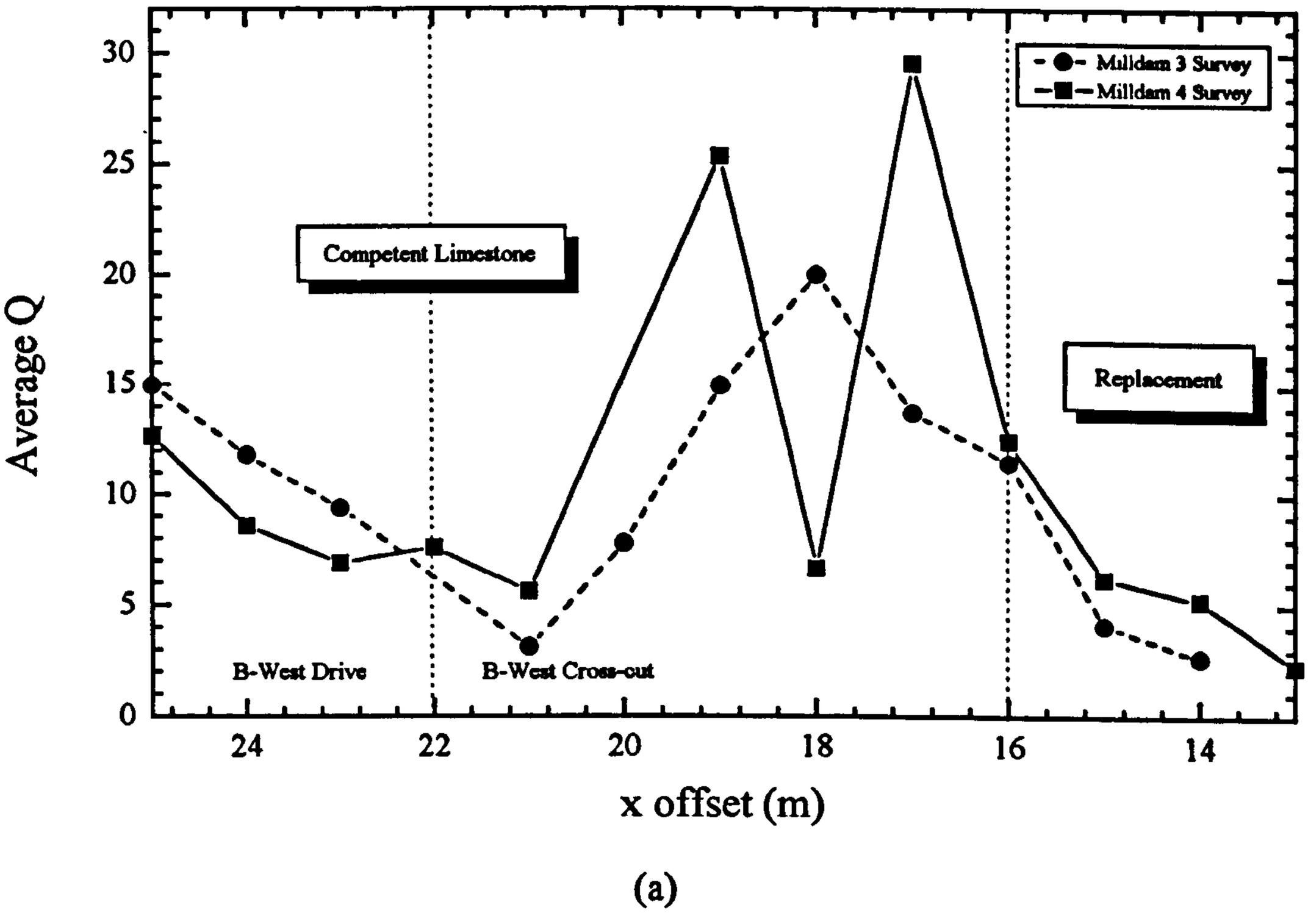

(a)

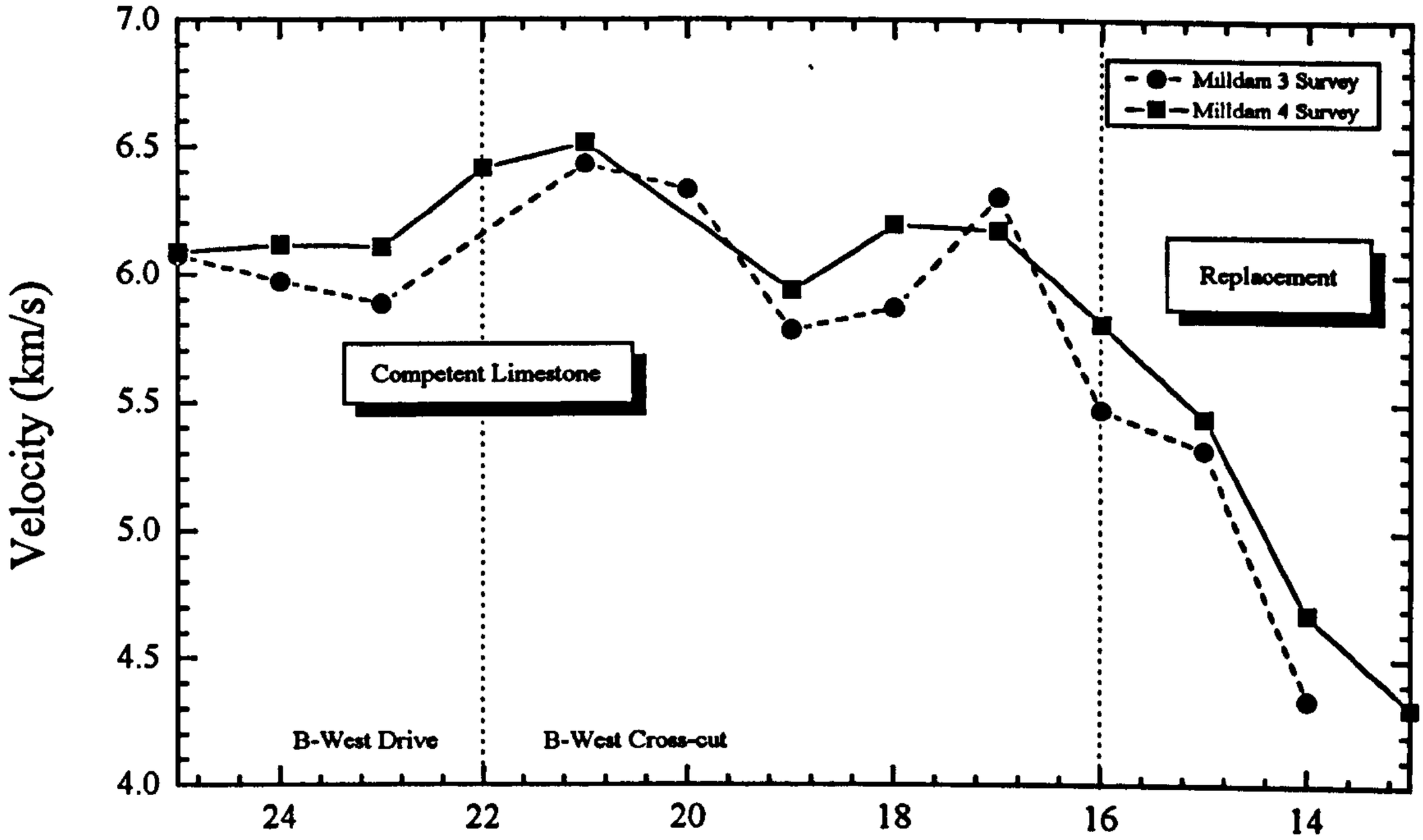

(b)

FIGURE 8.32 Comparison between seismic profiles for Milldam 3 and Milldam 4 surveys for (a) Q, and (b) Velocity

help interpret these percentage changes in terms of the possible rock mass conditions that could be responsible for the anomalous low values. A summary of the calculated percentage changes is given in table 8.4

Seismic Parameter	Survey Number	Profile Maximum	Maximum Position	Profile Minimum	Minimum Position	% Change
Velocity	Milldam 3	6.435	20	5.899	23	8.5
	Milldam 4	6.518	20	6.109	23	6.3
NFPA	Milldam 3	0.873	19	0.291	23	66.7
	Milldam 4	0.973	19	0.262	23	73.1
Q	Milldam 3	20.04	18	6.26	21	68.8
	Milldam 4	29.54	17	6.70	21	77.3

TABLE 8.4 Comparison of profile maxima and minima determined for the seismic properties of velocity (values given in km/s), Normalised first peak amplitude (NFPA) and Q.

From table 8.4 it is obvious that the characteristic of the competent zone anomaly is a slightly reduced velocity (average 7.4% reduction across the two surveys) and a large reduction in both first peak amplitude and Q. Referring to chapter 4, table 4.4, a similar case was documented for a laboratory sample before and after failure by a single fracture at a constant hydrostatic stress of 15 MPa. After the failure, the velocity reduced by 2.59% from the original intact sample value and Q reduced by 51.21%. Based on this laboratory finding and experience from the first stope trial, which was located 70 m away on strike, it seems sensible to assume that this velocity, Q, NFPA (normalised first peak amplitude) pattern is the signature of an isolated fault or fracture zone located between the two levels between an offset of 21 to 23 m.

8.5.2.4 Stope Inspection

To confirm these findings the stope was revisited when half the vein and replacement zone between the two levels had been extracted. On first inspection the stope looked to be in good condition, and no ground control problems had been experienced over the stope's lifespan to that date. The various portions of the stope were carefully inspected with respect to the location of the exposed replacement-competent contact between the two levels and the suspected location of a fault zone along the south wall of B-West drive.

8.5.2.4.1 Replacement-Competent contact

The curved nature of this interface in the tomogram in figure 8.29 suggests that two washout areas exist at interlevel distances of 20 m and 40 m. Within these washouts, the more reactive competent limestone has been dissolved by water action in preference to the less reactive replacement material and the remaining void infilled by clay, (White, 1996). Inspection of the bottom section of the stope, at the end of the C-West crosscut, showed clear evidence of the lower washout zone at 20 m and this had resulted in a steeply back angled north wall. The stope was unusually wet, with water literally pouring down the north wall and therefore the loose material from within the washout zone had been eroded away. The inspection confidently showed that the interface predicted by the simultaneous inversion procedure was, indeed, correctly placed.

8.5.2.4.2 Fault zone

The south wall of B-West drive at the entrance to the cross-cut on this level was inspected at the point corresponding to the low value NFPA and Q anomalies in figures 8.31(c) and 8.32(a) respectively. A fault zone was identified at this point consisting of a series of vertical faults with clay infill varying in thickness between 1 and 3 cms. One of the vertical faults had an East-West orientation which cut directly across the entrance of the cross-cut in line with the south wall of B-West drive corresponding to an offset of 22 m on the aforementioned plots. A second fault was identified running vertically but offset by around 15 to 20 degrees from the East-West direction next to the first fault. The region was unfractured and dry suggesting that it remained competent.

The same area was inspected at the entrance of the corresponding C-West crosscut. The rock mass had changed considerably since the Milldam 3 and 4 surveys were carried out. Since stope production had started, the entrance to C-West crosscut had experienced some roof control problems resulting in the need for mesh and strap support. A fracture zone and vertically inclined East-West fault was identified in this area and was most likely a continuation of the same zone identified at the entrance to the B-West crosscut. With the onset of stope extraction some movement must have occurred along this fault or fracture feature. Tell tale signs of this movement were the damage to the roof and also some seepage of water from cracks where prior to mining activity it had been dry. Conversely, the competent limestone zone corresponding to the high values of Q and NFPA, at x offsets of 18 to 20 m, remained dry and unfractured.

When the cross-cuts were inspected at the time of surveys 3 and 4, no fault zone was identified at the entrance to either the B-West or C-West cross-cuts. Therefore, the

data from these surveys had predicted the presence of a fracture/fault zone correctly to within 1 or 2 metres. This zone only revealed itself with subsequent destressing of the footwall associated with mineral extraction and the influx of water into the area. The danger associated with this zone is that the increased flow of water could start to loosen and wash away the clay infill within the faults, therefore weakening the area and increasing the risk of movement. In retrospect, the use of the combined velocity and attenuation profiles successfully identified this potential weakness point.

At the time of writing, the stope remains half finished and the mine has been alerted to a potential problem which, at worst, could result in the loss of the stope and further damage to B-West drive.

8.5.2.4.3 Re-inspection of Stope 1

The area around stope 1 had continued to move for at least a year since its initial collapse and was still moving at the time of writing. Large cracks had appeared with displacements of up to 10 cm along a fault which runs parallel with the south wall of B-West drive and corresponds precisely to the location of the low NFPA anomaly values in figures 8.20 and 8.21 to within 0.5 m.

8.6 Conclusions

This chapter has considered field examples from an active mining environment. A number of calibration tests have been conducted to determine the different types of seismic source and receiver properties. It was recognised that, because of the small scale of the field sites, tomographic imaging would require high frequency data to achieve good resolution. Three source types were investigated and compared for their principal frequencies of propagation and associated wavelengths dependent on the velocity structure. In conclusion, for similar limestone rock conditions, a dryhole sparker source propagated at between 400 and 650 Hz, a hammer source at between 400 and 900 Hz and an explosive charge at 850 to 950 Hz. Therefore, for the given geological conditions and for an ideal tomographic survey the explosive source offered the best characteristics. However, cost and potential roadway damage precluded the use of explosives and the ensuing field trials used both the sparker and hammer sources.

The first stope trial involving the sparker source produced poor quality data. However, some analysis was possible based on normalised first arrival peak amplitudes in the time domain and this identified an unexpected low value anomaly within the apparently competent limestone zone. Proof of a connection between this anomalous

low first peak amplitude region and a suspected fracture or fault zone within the footwall competent zone came when the footwall failed along a fault line in the same area resulting in the loss of the stope.

The second stope trial involving a hammer source produced excellent seismic data with clearly defined transmission arrivals. A velocity tomogram was produced which clearly identified the competent-replacement interface between the two levels and predicted the mineable volume of the replacement and vein material. The tomogram did not however reveal any low velocity anomalies within the competent limestone indicating that this area should remain stable with mining extraction of the vein. Two surveys were carried out and this gave the opportunity of determining whether normalised first peak amplitudes from hammer source data could be used to determine rock mass condition, or whether the data would be purely dependent on the energy at the source. First peak amplitude profiles from the two surveys were almost identical, showing that they were not dependent on the source strength and were indeed a reflection of the rock mass condition. An anomalously low value zone occurred along the profile at an x offset of 21 to 23 m. A calculated Q profile based on rise times and traveltimes also showed an anomalous low value zone in the same region. A velocity profile revealed only a marginal reduction in the same area. Based on laboratory findings in samples with a single fracture, this result was most likely the signature of a single isolated fault plane or fracture zone. This prediction was confirmed during inspection of the stope after mining had commenced where a fault zone was identified at the precise location that low value Q and NFPA anomalies occurred in the original surveys before mining commenced.

This successful conclusion shows that the simple plotting of a seismic profile cross-sections for both velocity and attenuation can be used to characterise the rock mass between two levels. This simple tool can provide predictive information about rock mass behaviour with the onset of mining and with further development could be employed to predict support requirements necessary to prevent potentially destructive events such as stope collapse.

CHAPTER 9

9. Conclusion and Suggestions for Further Work

9.1 Conclusion

The aim of this thesis has been to show that it is possible to non-destructively characterise an in-situ rock mass by taking seismic velocity and attenuation measurements. As well as characterisation, this thesis has gone one step further and introduced the concept of rock mass behaviour prediction using the same seismic measurements. This conclusion will summarise how the field examples in this thesis have achieved this aim, and how these results have been helped by the comprehensive laboratory study.

9.1.1 Seismic tomography in rock mass characterisation

The most powerful interpretation technique applied throughout this thesis has been seismic tomography. The technique has been around for a number of years but has still to gain general acceptance for routine site investigation in the mining and civil engineering industries. It is more usually applied in specialist cases where a high degree of detail is required. It is for this reason that this work has introduced a new variant of tomography, taken from the field of reflection seismics where it has been used successfully to solve depth-velocity ambiguity problems, and applied the technique to the imaging of small scale survey areas. The introduction of this new technique to the areas of engineering or site-investigation geophysics is a natural continuation of the further development of tomographic techniques and aims to make the process more accessible to industry. The method is more flexible than simple transmission traveltime tomography and this thesis has shown this through a number of examples of the imaging of inaccessible areas of small scale geological structure in great detail. For example, in chapter 6 the technique was successfully applied to image a square survey area which was only accessible from two adjacent sides. The use of the CTRT method in this case clearly improved the tomogram image from that which would have been possible with transmission tomography alone, and as a result identified the location of suspected old workings, shale partitions and a change in limestone type. In chapter 8, the same inversion method (though without reflection traveltime data) was successfully used to identify the boundary between competent and replacement limestone in a stope footwall therefore allowing accurate predictions of stope volumes and indicating where weak washout zones existed along the line of the interface. The potential for other

applications where the location of geological interfaces, boundaries, faults, fissures or other anomalous interfaces must be correctly identified is enormous.

Chapter 7 provided the opportunity to compare the CTRT technique with other more popular tomography algebraic reconstruction methods. For the transmission traveltime models, little difference was observed between the techniques. The advantage of the CTRT method over the other techniques is that the further processing step can be carried out in terms of forward modelling of the transmission model to identify reflections in the seismic data field set. Although this process was not carried out in the example in chapter 7, because of time restrictions, similar improvements would be expected to occur as with the CTRT tomogram in chapter 6, due to the increased raypath coverage of the model.

Therefore, the CTRT method offers a more flexible variant of seismic tomography which can be used in inaccessible survey areas without the need for expensive longhole drilling or roadway development to site seismic source and receiver points in more favourable locations.

9.1.2 Seismic measurements in rock mass behaviour prediction

Chapter 2 examined current experimental knowledge and theoretical descriptions of the large number of factors that affect the propagation of seismic waves. The chapter showed that many of these factors were closely interrelated making the job of interpretation of changes in seismic data difficult. A large focus of this thesis has been to examine the use of P-wave attenuation in rock mass characterisation and to determine the advantages and disadvantages of using this parameter as an added interpretative aid in addition to the more often used P-wave velocity. For this reason a comprehensive laboratory study has been documented in chapter 4 for measurements of seismic velocity and attenuation in rock core samples under conditions of simulated varying triaxial stress. This study has pushed the boundaries of previous investigations of stress-induced anisotropy where, in particular, little or no investigation has been previously documented in the literature concerning the phenomenon of P-wave stress-induced attenuation anisotropy. As well as the important work of studying the phenomenon in intact samples, the chapter documented a previously untried study of the same phenomenon in three samples which had been subjected to varying degrees of fracturing by sample failure. This work highlighted how velocity and attenuation measurements should not be considered as separate parameters which provide separate rock mass interpretations. They are in fact closely interrelated and should be combined to provide better interpretations such that the relative changes in both attenuation and

velocity are indicators of the type of change occurring in the rockmass. For example, a change in axial stress of the order of 5 MPa within a laboratory sample brings different amounts of change in velocity and attenuation. Chapter 4 outlined a method for quantitatively defining this change as a percentage per MPa change in the stress in the direction of propagation and suggested that intact sample values determined in the laboratory could be used for predicting stress change in-situ for a reasonably homogenous rock mass with isolated fractures.

Experiments which measured velocity and attenuation through confined samples which were loaded to failure showed that a small change in velocity accompanied by a larger drop in Q was an indicator that stress levels had reached 80% of the failure load, and that the rock mass was experiencing progressive microcrack and macrocrack damage.

In chapter 8, the work was directed at determining ways in which seismic measurements on an un-mined block of ground could help predict how that rock mass would behave when mining commenced. The initial approach was to comprehensively survey the rock mass to image the entire area. The problem with most field work of this type is that as a method increases in complexity, so it becomes more difficult to carry out successfully, especially in the environment of a working underground mine. With the failure of the tomographic survey on the first stope trial in chapter 8 it was decided to use the data to produce simple seismic profiles. The results were clear, and revealed that the measurement of a simple parameter such as the amplitude of the first peak arrival could be used to successfully predict the presence of a large fault or fracture zone in the footwall between two levels. Whilst this initial result was somewhat tenuous, the application of the same method on a second stope survey revealed the presence of a similar fault zone and proved that this simple method worked. This was truly confirmed when mining commenced in the second stope and the fault revealed itself by reactivation and an influx of water. The laboratory analysis of a sample with a simple fracture had been the key to identifying that the fault zone existed where a very small change in velocity was accompanied by a large change in Q or the first peak amplitude. Interestingly, had the stope footwall only been tomographically imaged for its velocity structure, the location of the fault would never have been identified. The production of simple seismic profiles could provide a working tool for Milldam Mine which is very simple to conduct in the field, easy to process and yet shows within the nearest metre where problem areas occur within the stope footwall. The same technique could be applied to mining operations all over the world to provide an easy working method without having to resort to the complexities of tomography.

Whilst this simple method proved very effective, the same fault zone would have been identified by using a combination of velocity and attenuation tomograms. The development of this fault zone could also have been monitored over time by using a sequence of successive surveys. This time lapse tomographic method is one of the suggestions for further work described in the next section and is surely the natural progression of the seismic profile principle.

In conclusion this thesis has comprehensively described how seismic measurements can be used to characterise a rock mass and has laid the foundations for using the same measurements for monitoring changes and predicting rock mass behaviour in active environments.

9.2 Further Work

Whilst this thesis has been comprehensive in its coverage of many aspects of the use of velocity and attenuation measurement in rock mass characterisation, a number of areas have been identified which deserve further attention.

One of the original aims of the work was to produce attenuation tomograms along with the velocity tomograms in this thesis. However, time was not available to pursue this, and the CTRT method needs further development to incorporate attenuation. The complexity of the calculation process increases because of the need for full waveform viscoelastic modelling for a combined transmission and reflection amplitude algorithm. However, the process would rely on the fact that the velocity structure will have already have been pre-determined as the first step in the process. This velocity structure would then be forward modelled for amplitudes and the calculation of reflection constants at boundaries and the results iteratively adjusted so that they match the real dataset. Other methods exist for creating attenuation tomograms more simply by using amplitude ratios, spectral ratios or rise time measurements and these could be considered. Having a spatial distribution plot of the attenuating properties of a rock mass can only help to improve the accuracy of rock mass interpretation and would allow for better analysis of the interrelation between velocity and this parameter.

Another of the aims in the area of rock mass behaviour prediction was the repeated surveying of a mine stope to observe how the velocity changed with time. Time pressures and field work difficulties due to the instability of the sites did not allow this phase to be carried out. The laboratory proof of using velocity and attenuation measurements as a stress change indicator has already been presented. Therefore the

author suggests that a time lapse tomography experiment be conducted where it can be determined whether difference tomograms can be used to predict stress change. To aid this process, it would help to have a secondary way of measuring stress changes by the use of devices such as commercially available borehole methods. Difference tomograms are easy to produce and could accurately locate exactly where stress change or fracturing is occurring. To produce such plots, the author suggests the use of cross-correlation techniques to accurately identify traveltime differences between seismic datasets. Other techniques such as automatic waveform matching could give even better results and speed the process considerably.

Further to the findings of the laboratory study in chapter 4, the author suggests that many aspects of this work could be pursued further, particularly with measuring and quantifying stress-induced velocity and attenuation anisotropy in fractured samples. Experiments of this type can help to improve interpretation in-situ and can identify unique situations where certain ratios of velocity and attenuation might indicate the presence of faults or fractures.

References

Aki, K. & Lee, W. H. K. (1976) Determination of three dimensional velocity anomalies under a seismic array using P wave arrival times from local earthquakes, 1. A homogenous model, Journal of Geophysical Research, Vol. 81, pp. 4381-4399.

Aki, K. & Richards, P. G. (1980) Quantitative Seismology, theory and methods, W. H. Freeman, San Francisco.

Almossawi, H. I. H (1988) Ultrasonic spectroscopy in rocks: An experimental study of highly porous synthetic sandstones, Geophysical Prospecting, Vol. 36, pp. 700-718.

Attewell, R. P. & Ramana, Y. V. (1966) Wave attenuation and internal friction as functions of frequency in rocks, Geophysics, Vol. 31, pp. 1049-1056.

Baria, R., Jackson, P. D. & McCann, D. M. (1989) Further development of a high-frequency seismic source for use in boreholes, Geophysical Prospecting, Vol. 37, pp 31-52.

Batzle, M. L., Simmons, G. & Siegfried, R. W. (1980) Microcrack closure in rocks under stress: direct observation, Journal of Geophysical Research, Vol. 85, pp. 7072-7090.

Biot, M. A. (1956a) Theory of propagation of elastic waves in a fluid saturated porous solid, I: Low frequency range, Journal of the Acoustic Society of America, Vol. 28, pp. 168-178.

Biot, M. A. (1956b) Theory of propagation of elastic waves in a fluid saturated porous solid, II: High frequency range, Journal of the Acoustic Society of America, Vol. 28, pp. 179-191.

Birch, F. (1960) The velocity of compressional waves in rocks to 10 kilobars, 1., Journal of Geophysical Research, Vol. 65, pp. 1083.

Birch, F. (1961) The velocity of compressional waves in rocks to 10 kilobars, 2., Journal of Geophysical Research, Vol. 66, pp. 2199.

Blair, D. P. (1982) Measurements of rise times of seismic pulses in rock, Geophysics, Vol. 47, pp. 1047-1058.

Blair, D. P. & Spathis, A. T. (1982) Attenuation of explosion - generated pulse in rock masses, Journal of Geophysical Research, Vol. 87, pp. 3885-3892.

Blair, D. P. & Spathis, A. T. (1984) Seismic source influence in pulse attenuation studies, Journal of Geophysical Research, Vol. 89, pp. 9253-9258.

Blair, D. P. (1990) A direct comparison between vibrational resonance and pulse transmission data for assessment of seismic attenuation in rock, Geophysics, Vol. 53, pp. 51-60.

Carabelli, E. (1988) Sonic velocity tomography in concrete and earth dams evaluation, SEG expanded abstracts, 58th SEG Annual Meeting, Anakeim, California, pp. 328-330.

Chow, T. M., Melgis, I. L. & Young, R. P. (1995) Progressive microcrack development in tests on Lac du Bonnet Granite - II. Ultrasonic tomographic imaging, International Journal of Rock Mechanics, Mineral Science and Geomechanical Abstracts, Vol. 32, pp. 751-761.

Christensen, N. I. (1965) Compressional wave velocities in metamorphic rocks at pressures to 10 kilobars, Journal of Geophysical Research, Vol. 70, pp. 6147.

Cottin, J. F., Deletie, P., Jacquet-Francillon, H., Lakshamanan, J., Lemoine, Y. & Sanchez, M. (1986) Curved ray seismic tomography application to the Grand Etang Dam (Reunion Island), First Break, Vol. 4, pp. 25-30.

Dasgupta, R. (1994) Seismic wave attenuation with respect to reflection seismology, PhD Thesis, Department of Earth Sciences, Leeds University.

De-Boor, C. (1978) A practical guide to splines, Springer - Verlag.

Domenico, S. N. (1976) Effect of brine-gas mixture on velocity in an unconsolidated sand reservoir, Geophysics, Vol. 41, pp. 882-894.

Donnelly, L. J. & Pearce, D. R. (1996) A 4-D seismic tomography investigation at Laportes Milldam Mine, Derbyshire : A strata control investigation to locate sedimentary horizons associated with the orebody and fault zones, British Geological Survey, Engineering Geology & Geophysics Group, Report WN/96/37.

Dunham, K. C. & Stubblefield, C. J. (1944) The stratigraphy, structure and mineralisation of the Greenhow mining area, Yorkshire, Quarterly Journal of the Geological Society of London, Vol. 100, pp. 209-268.

Dutta, N. C. & Seriff, A. J. (1979) On White's model of attenuation in rocks with partial gas saturation, Geophysics, Vol. 44, pp. 1806-1812.

Dvorkin, J., Nolen-Hoeksema, R. & Nur, A. (1994) The squirt flow mechanism: Macroscopic description, Geophysics, Vol. 59, pp. 428-438.

Endres, A. Z. & Knight, R. (1991) The effects of pore scale fluid distribution on the physical properties of partially saturated tight sandstones, Journal of Applied Physics, Vol. 69, pp. 1091-1098.

Evans, A. M., Ford, T. D. & Allen, J. R. L. (1968) Geology of the East Midlands, Chapter 1, Precambrian Rocks, pp. 1-12.

Fletcher, R. (1987) Practical methods for optimisation, John & Willey.

Friedel, M. J., Jackson, M. J., Scott, D. F., Williams, T. J. and Olson, M. S. (1995) 3-D tomographic imaging of anomalous conditions in a deep silver mine, Journal of Applied Geophysics, Vol. 34, pp. 1-21.

Freidel, M. J., Jackson, M. J., Williams, E. M., Olson, M. S. & Westman, E. (1996) Tomographic Imaging of Coal Pillar Conditions : Observations and Implications, International Journal of Rock Mechanics, Mineral Science and Geomechanical Abstracts, Vol. 33, pp. 279-290.

Futterman, W. I. (1962) Dispersive body waves, Journal of Geophysical Research, Vol. 67, pp. 5279-5291.

Ganley, D. C. & Kanasewich E. R. (1980) Measurement of absorption and dispersion from check shot surveys, Journal of Geophysical Research, Vol. 85, pp. 5219-5226.

Gassmann, F. (1951) Elastic waves through a packing of spheres, Geophysics, Vol. 16, pp. 673-685.

Gill, P. E., Murray, W. & Wright, M. H. (1981) Practical optimisation, Academic Press.

Gladwin, M. T. & Stacey, F. (1974) Anelastic degradation of acoustic pulses in rock, Physics of the Earth & Planetary Interiors, Vol. 8, pp. 332-336.

Gordon, R. B. & Davis, L. A. (1968) Velocity and attenuation of seismic waves in imperfectly elastic rock, Journal of Geophysical Research, Vol. 73, pp. 3917-3935.

Goulty, N. R., Thatcher, J. S. And Findlay, M. J. (1990) Experimental investigation of crosshole seismic techniques for shallow coal exploration, Quarterly Journal of Engineering Geology, Vol. 23, pp. 217-228.

Goulty, N. R. (1993) Controlled-source tomography for mining and engineering applications, Seismic Tomography: Theory and Practice, Ed's. Iyer, H. M. & Hirahara, K., Chapman and Hall, London, pp. 797-813.

Green, D. H., Wang, H. F. and Bonner, B. P. (1993) Shear wave attenuation in dry and saturated sandstone at seismic to ultrasonic frequencies, International Journal of Rock Mechanics, Mineral Science and Geomechanical Abstracts, Vol. 30, pp. 755-761.

Gustavsson, M. Ivansson, S., Moren, P. and Pihl, J. L. (1986) Borehole tomography - measurement system and field studies, Proc. IEEE, Vol. 74, pp. 339-346.

Han, D. H., Nur, A. & Morgan, D. (1986) Effects of porosity and clay content on wave velocities in sandstones, Geophysics, Vol. 51, pp. 2093-2107.

Hawley, B. W., Zandt, G. & Smith, R. B. (1981) Inversion for lateral velocity variations: an iterative solution with a layered model, Journal of Geophysical Research, Vol. 86, pp. 7073-7076

Jackson, P. D. (1996) Engineering Geophysicist, BGS Engineering Geology and Geophysics Group, Personal Communication.

Jackson, P. D. & McCann, D. M. (1990) New seismic system for P-wave transmission tomography in between dry near-horizontal boreholes : test results from the Channel Tunnel site - Shakespeare Cliffs, Chalk, Thomas Telford, London, pp. 477-484.

Johnston, D. H., Toksov, M. N. & Timur, A. (1979) Attenuation of seismic waves in dry and saturated rocks : II. Mechanisms, Geophysics, Vol. 44, pp. 691-711.

Johnston, D. H. & Toksov, M. N. (1980) Ultrasonic P and S wave attenuation in dry and saturated rocks under pressure, Journal of Geophysical Research, Vol. 85, pp. 925.

Jones, T. D. (1986) Pore fluids and frequency dependant wave propagation in rocks, Geophysics, Vol. 51, pp. 1939-1953.

Jones, T. D. & Nur, A. (1983) Velocity and attenuation in sandstones at elevated temperatures and pressures, Geophysical Research Letters, Vol. 10, pp. 140-143.

Kan, T. K., Batzle, M. L. & Gaiser, J. E. (1983) Attenuation measured from VSP : Evidence of frequency dependent Q, abstracts, 53rd Annual International Meeting of the Society of Exploration Geophysicists, pp. 589-590.

Kavetsky, A., Chitombo, G. P. F. and McKenzie, C. K. (1990) A model of acoustic pulse propagation and its application to determine Q for a rock mass, International Journal of Rock Mechanics, Mineral Science and Geomechanical Abstracts, Vol. 27, pp. 33-41.

King, M. S. (1966) Wave velocities in rocks as a function of changes in overburden pressure and pore fluid saturants, Geophysics, Vol. 31, pp. 50-73.

King, M. S. (1969) Ultrasonic compressional and shear wave velocities of confined rock samples, Proceedings 5th Canadian Rock Mechanics Symposium, pp. 127-156.

Kjartansson, E. (1979a) Constant Q-wave propagation and attenuation, Journal of Geophysical Research, Vol. 84, pp 4737-4748.

Kjartansson, E. (1979b) Attenuation due to thermal relaxation in porous rocks, Abstracts, Society of Exploration Geophysicists International Meeting 49, pp. 163-164.

Klimentos, T. (1988) Seismic and petrophysical properties of porous rocks, PhD Thesis, University of Reading.

Klimentos, T. & McCann, C. (1990) Relationships among compressional wave attenuation, porosity, clay content and permeability in sandstones, Geophysics, Vol. 55, pp. 998-1014.

Klimentos, T. (1991) The effects of porosity-permeability-clay content on the velocity of compressional waves, Geophysics, Vol. 56, pp. 1930-1939.

Kowalis, B. J., Jones, L. E. A. & Wang, H. F. (1984) Velocity-porosity-clay content systematics of poorly consolidated sandstone, Journal of Geophysical Research, Vol. 89, pp. 10355-10364.

Kormendi, A., Bodoky, L., Herman, L., Dianski, L. and Kalman, T. (1986) Seismic measurements for safety in mines, Geophysical Prospecting, Vol. 34, pp. 1022-1037.

Kuster, G. T. & Toksov, M. N, (1974) Velocity and attenuation of seismic waves in 2 phase media, I. Theoretical formulations, Geophysics, Vol. 39, pp. 607-618.

Lee, W. H. K. & Pereyra, V. (1993) Mathematical introduction to seismic tomography, Seismic Tomography: Theory and Practice, Ed's. Iyer, H. M. & Hirahara, K., Chapman and Hall, London, pp. 9-21.

Leung, L. , Downey, M., Herman, P. (1988) Cross-hole seismic tomography for mineral exploration and mine planning, SEG expanded abstracts, 58th SEG Annual Meeting, Anaheim, California, pp. 328-330.

Li, W & Norlund, A (1993) Technical Note : Effects of couplants on acoustic transmission, Rock Mechanics and Rock Engineering, Vol. 26, pp. 63-69.

Lockner, D. A., Walsh, J. B. & Byerlee, J. D. (1977) Changes in seismic velocity and attenuation during deformation of granite, Journal of Geophysical Research, Vol. 82, pp. 5374-5378.

Lucet, N. Zinszner, B. (1992) Effects of heterogeneities and anisotropy on sonic and ultrasonic attenuation in rocks, Geophysics, Vol. 57, pp. 1018-1026.

Mao, W. & Gubbins, D. (1995) Simultaneous determination of time delays and stacking weights in seismic array beamforming, Geophysics, Vol. 60, pp. 491-502.

Mao, W. & Stuart, G. W. (1995) Transmission-reflection tomography : application to reverse VSP data, Geophysics, in press.

Mao, W. & Stuart, G. W. (1996) Rapid multi-wavetype ray tracing in complex 2-D and 3-D isotropic media, Geophysics, in press.

Martin, C. D. & Read, R. S. Strength of massive granite around underground excavations. Proceedings of the 16th Canadian Rock mechanics Conference, Sudbury.

Mavko, G. M. & Nur, A. (1975) Melt squirt in the asthenosphere, Journal of Geophysical Research, Vol. 80, pp. 1444-1448.

Mavko, G. M. (1979) Frictional attenuation : an inherent amplitude dependence, Journal of Geophysical Research, Vol. 84, pp. 4769-4776.

Mavko, G. M. & Nur, A. (1979) Wave attenuation in partially saturated rocks, Geophysics, Vol. 44, pp. 161-178.

Mavko, G. M. & Nolen-Hoeksema, R. (1994) Estimating seismic wave velocities at ultrasonic frequencies in partially saturated rocks, Geophysics, Vol. 59, pp. 252-258.

Maxwell, S. C. & Young, R. P. (1994) Application of seismic tomography to induced seismicity investigations, Eurock '94, pp. 597-604.

Molina, J. P. & Wack, B. (1982) Crack field characterisation by ultrasonic attenuation - preliminary studies on rocks, International Journal of Rock Mechanics, Mineral Science & Geomechanical Abstracts, Vol. 19, pp. 267-278.

Murphy, W. F. (1982) Effects of partial water saturation on attenuation in Massilon sandstone and vycor porous glass, Journal of the Acoustic Society of America, Vol. 71, pp. 1458-1468.

Nur, A. & Simmons, G. (1969) Stress induced velocity anisotropy in rock : An experimental study, Journal of Geophysical Research, Vol. 74, pp. 6667-6674.

O'Connell, R. J. & Budiansky, B. (1977) Viscoelastic properties of fluid saturated cracked solids, Journal of Geophysical Research, Vol. 82, 5719-5736.

Oliver, J. S. (1992) Robust P-wave attenuation estimates from VSP first arrivals, Extended Abstracts, 54th Meeting European Association of Exploration Geophysicists, paper P067

Palmer, I. D. & Traviola, M. L. (1980) Attenuation by squirt flow in undersaturated gas sands., Geophysics, Vol. 45, pp. 1780-1792.

Pandit, B. I. & King, M. S. (1979) The variation of elastic wave velocities and quality factor of a sandstone with moisture content, Canadian Journal of Earth Science, Vol. 16, pp. 2187.

Papadakis, E. P., Fowler, K. A. & Lynworth, L. C. (1973) Ultrasonic attenuation by spectrum analysis of pulses in buffer rods : method and diffraction corrections, Journal of the Acoustic Society of America, Vol. 53, pp. 1336-1343.

Papadakis, E. P. (1976) Ultrasonic diffraction from single apertures with application to pulse measurement and crystal physics, Physical Acoustics, Principles and Methods, Vol. XI, pp. 151-211.

Peacock, S., McCann, C., Sothcott, J., Astin, T. R. (1994) Experimental measurements of seismic attenuation in microfractured sedimentary rock, Geophysics, Vol. 59, pp. 1342-1351.

Pearce, D. R. & Wade, L. (1995) Rock mass characterisation through the velocity and attenuation of seismic waves - a project overview, LUMA, pp. 13-22.

Pearce, D. R. & Wade, L. (1996a) Laboratory and in-situ assessment of rock mass quality, APCOM '96, Penn State University.

Pearce, D. R. & Wade, L. (1996b) The application of seismic velocity and attenuation tomography in mining, Int. Conf. Mining Science & Technology, Xuzhou, China.

Peselnick, L. & Outerbridge, W. F. (1961) Internal friction in shear and shear modulus of Solenhofen limestone over a frequency range of 10^7 cycles per second, Journal of Geophysical Research, Vol. 66, pp. 581-588.

Pusch, R. & Stanfors, R. (1992) the zone of disturbance around blasted tunnels at depth, International Journal of Rock Mechanics, Mineral Science and Geomechanical Abstracts, Vol. 29, pp. 447-456.

Radon, J. (1917) Uber die Bestimmung von Funktion dirch ihre Integralwerk langs gewisser Mannigfaltigkeiten, Ber. Verh. Saechs. Akad. Wiss. Leipzig. Math. Phys. Kl., Vol. 69, pp. 262-277.

Raymer, L., Hunt, E. R., & Gardner, J. S. (1980) An improved sonic transit time-to-porosity transform, presented at the 21st Annual International Meeting, Society of Professional Well Log Analysts.

Remy, J-M., Bellanger, M., Homand-Etienne, F. (1994) Laboratory velocities and attenuation of P-waves in limestones during freeze thaw cycles, Geophysics, Vol. 59, pp. 245-251.

Sayers, C. M., Van Munster, J. G. & King, M. S. (1990) Stress induced ultrasonic anisotropy in Berea sandstone, International Journal of Rock Mechanics, Mineral Science & Geomechanical Abstracts, Vol. 27, pp. 429-436.

Sears, E. M. & Bonner, B. P. (1981) Ultrasonic attenuation measurement by spectral ratio utilising signal processing techniques, IEEE, Trans. Geosci. Remote Sensing, Vol. 19, pp. 95-99.

Simmons, G. & Brace, W. F. (1965) Comparison of static and dynamic measurements of compressibility of rocks, Journal of Geophysical Research, Vol. 70, pp. 5649.

Spencer, J. W. (1981) Stress relaxations at low frequencies in fluid saturated rocks : Attenuation and modulus dispersion, Journal of Geophysical Research, Vol. 86, pp. 1803-1812.

Spencer, J. W., Sonnad, J. R. & Butler, T. M. (1982) Seismic Q - Stratigraphy or dissipation, Geophysics, Vol. 47, pp. 16-24.

Tarif, P. & Bourbie, T. (1987) Experimental comparison between spectral ratio and rise time techniques for attenuation measurement, Geophysical Prospecting, Vol. 35, pp. 668-680.

Tittmann, B. R., Nadler, H., Clark, V. A. & Ahlberg, L. A. (1981) Frequency dependence of seismic dissipation in saturated rocks, Geophysical Research Letters, Vol. 8, pp. 36-38.

Tocher, D. (1957) Anisotropy in rocks under simple compression, Transactions American Geophysical Union, Vol. 38, pp. 89-94.

Tonn, R. (1991) The determination of the seismic quality factor Q from VSP data : A comparison of different computational methods, Geophysical Prospecting, Vol. 39, pp. 1-27.

Toksov, M. N., Johnston, D. H. & Timur, A. (1979) Attenuation of seismic waves in dry and saturated rocks : I. Laboratory measurements, Geophysics, Vol. 44, pp. 681-690.

Tosaya, C. & Nur, A. (1982) Effect of diagenesis and clays on compressional wave velocities in rocks, Geophysical Research Letters, Vol. 9, pp 5-8.

Tutuncu, N., Podio, A. L. & Sharma, M. M. (1994) An experimental investigation of factors influencing compressional and shear wave velocities and attenuations in tight gas sandstones, Geophysics, Vol. 59, pp. 77-86.

Walsh, J. B. (1965) The effect of cracks on the compressibility of rock, Journal of Geophysical Research, Vol. 70, pp. 381-389.

Walsh, J. B. (1966) Seismic wave attenuation in rocks due to friction, Journal of Geophysical Research, Vol. 71, pp. 2591-2599.

Walsh, J. B. (1995) Seismic attenuation in partially saturated rock, Journal of Geophysical Research, Vol. 100, pp. 15407-15424.

White, C. (1996) Chief Geologist, Laporte Minerals, Personal Communication.

White, J. E. (1975) Computed speeds and attenuation in rocks with partial gas saturation, Geophysics, Vol. 40, pp. 224-232.

Wiggins, R. A. (1972) General linear inverse problem - implication of surface waves and free oscillation for earth structure, Rev. Geophys. Space. Phys., Vol. 10, pp. 251-285.

Williamson, S (1969) Least Squares Fitting of a straight line, Canadian Journal of Physics, Vol. 46, pp. 1845-1847.

Williamson, P. R. (1991) A guide to the limits of resolution imposed by scattering in ray tomography, Geophysics, Vol. 56, pp. 202-207.

Winkler, K. W., Nur, A. & Gladwin, M. (1979) Friction and seismic attenuation in rocks, Nature, Vol. 227, pp. 528.

Winkler, K. W., & Nur, A. (1982) Seismic attenuation: Effects of pore fluids and frictional sliding, Geophysics, Vol. 47, pp. 1-15.

Winkler, K. W. & Plona, T. J. (1982) Technique for measuring ultrasonic velocity and attenuation spectra in rocks under pressure, Journal of Geophysical Research, Vol. 87, pp. 10776-10780.

Winkler, K. W. (1985) Dispersion analysis of velocity and attenuation in Berea sandstone, Journal of Geophysical Research, Vol. 90, pp. 6793-6800.

Wu, B., King, M. S., & Hudson, J. A. (1991) Stress induced ultrasonic wave velocity anisotropy in a sandstone, International Journal of Rock Mechanics, Mineral Science & Geomechanical Abstracts, Vol. 28, pp. 101-107.

Wyllie, M. R. J., Gregory, A. R., Gardner, G. H. F. (1958) An experimental investigation of factors affecting elastic wave velocities in porous media, Geophysics, Vol. 23, pp. 459-493.

Zamanek, J. Jr. & Rudnick, J. (1961) Attenuation and dispersion of elastic waves in a cylindrical bar, Journal of the Acoustic Society of America, Vol. 33, pp. 1283-1288.

A1. Appendix A : AUTOQ Program Listing

A1.1 Overview

AUTOQ is written in C++ and takes advantage of the complex number facilities in this language. The program listing given here will calculate velocity values, Q values and attenuation spectra for a complete experimental set-up.

A1.1.1 Program Arguments

Syntax is as follows :

AUTOQ [int bottom] [int top] [ini filename] [flag int 0,1,2 or 3]

where,

bottom = lower range frequency value (integer = frequency(Hz) / (sampling rate (Hz)/number of samples per trace)

top = upper range frequency value (integer = frequency(Hz) / (sampling rate (Hz)/number of samples per trace)

ini filename = name of file containing program set-up (see section A1.1.2 for format)

flag int 0,1,2 or 3 (optional)

case 0 : use range file (RANGE.DAT) to supply lower and upper frequency range values for each experimental trace

case 1: use range file and output ASCII format attenuation spectra files for each trace

case 2: only output ASCII format attenuation spectra files

case 3: use intact sample traces as reference traces for fractured sample traces and output fracture attenuation spectra

case : no flag, no range file or ASCII outputs.

A1.1.2 Ini File

AUTOQ requires an input file to initiate the program containing the sample filenames, traveltimes and rectangular window locations. The **space delimited** ASCII file format is as follows,

*.INI File format:

LINE	DESCRIPTION
1	Sample Name
2	Sample State
3	Aluminium Filename
4	Sample Diameter (m)
5	Sample Mass (kg)
6	Sample Length (m)
7	Acquisition Sampling Rate (MHz) (float)
8	Number of samples per trace (integer)
9	Number of sample traces, or stress regimes, n (integer)
10	Aluminium Window Location 1 (integer)
11	Aluminium Window Location 2 (integer)
12	Transducer Face Plate Traveltime (microsecs) (float)

13 ↓ 13+n	Filename (sample) (trace)	Axial Stress (kN)	Horiz Stress (MPa)	Traveltime (microsecs)	Window 1	Window 2
	12c	%10f	%10f	%10f	%10i	%10i

where,

12c = 12 character filename

%10f = 10 character float

%10i = 10 character integer

A1.1.3 Program output

AUTOQ produces a number of output files with results from the calculations as follows for each sample trace,

Filename	Description
DATASET.DAT	Complete program results including sample details, velocities and errors, Robust calculated Q and Least Squares calculated Q with associated errors
ATT18KHZ.DAT	Attenuation coefficient at 18kHz (Low freq. case) in dB/cm
ATT29KHZ.DAT	Attenuation coefficient at 29kHz (Low freq. Case) in dB/cm
ATT49KHZ.DAT	Attenuation coefficient at 49kHz (Low freq. Case) in dB/cm
AT500KHZ.DAT	Attenuation coefficient at 500kHz (High freq. Case) in dB/cm
AT800KHZ.DAT	Attenuation coefficient at 800kHz (High freq. Case) in dB/cm
*.ASC	One file for each trace (optional), the trace filename with the suffix *.ASC, contains the frequency spectra for the sample and aluminium reference and the corresponding attenuation spectra in dB/cm.
VELOCITY.DAT	Velocity values for each trace and errors
ROBUSTQ.DAT	File contains robustly calculated Q values for each trace and associated errors

Filename	Description
LEASTQ.DAT	File contains Least Squares calculated Q values for each trace and associated errors
ROBQL5PC.DAT	Robust Q values with errors less than 5 percent
ROBQL3PC.DAT	Robust Q values with errors less than 3 percent
LEAQL5PC.DAT	Least Squares Q values with errors less than 5 percent
LEAQL3PC.DAT	Least Squares Q values with errors less than 3 percent

A1.2 Program Listing

A1.2.1 Program Functions

Program functions are as follows,

cliptrace(int c1,int c2,float cliparray[])

Applies rectangular window the cliparray[] between points c1 and c2. Outside this range cliparray[] is set to zero.

data_out(void)

Writes complete calculation results to the filenames defined in section A1.1.3

fft(char fiflag, float realarray[], float imagarray[])

Calculates fast fourier transform coefficients of real array realarray[]. Fiflag is set to 'F' for forward transform and 'I' for inverse transform. Result replaces values in real array for the real coefficients and places the imaginary coefficients in imagarray. Realarray[] must be of length of a power of 2, and the function does not check this

file_subloop(void)

Organises the files and loops through the calculations until all samples have been completed

fit(float fitarray[])

Organises data in fitarray[] ready for fitting by least_fit() or robust_fit()

least_fit(float x[],float y[], int ndata)

Calculates the least squares linear fit of data of length ndata in arrays x[] and y[] and returns answer via global variables

load_aluminium(int alflag)

Reads aluminium trace and puts it in to the globally defined aluminium array

Qcalc(float qarray[],float qerrarray[],float grad)

Calculates Q value and associated error for the current sample using the globally returned answers from the previous two functions and places the answers in qarray[] and qerrarray[]

ratio(complex ratarray[])

Calculates the spectral ratio from globally defined aluminium and sample frequency spectra and places it in the complex array, ratarray[]

read_range(void)

Reads optional range file RANGE.DAT which supplies individual frequency range values for each trace for the fit() function

read_trace(void)

Reads sample trace, file name is set by reading init file, and puts it in to globally defined sample array

read_visq(void)

Reads init file

robust_fit(float x[],float y[],int ndata)

Calculates the robust linear fit of data of length ndata in arrays x[] and [y] and returns answer to global variables

savedata(void)

Saves all currently calculated data to dataset.dat and therefore allows review of the partial results even if the program fails to finish

A1.2.2 Full Listing

Program notes are written in *//italics*

```
#include <stdio.h>
#include <dir.h>
#include <stdlib.h>
#include <conio.h>
#include <dos.h>
#include <math.h>
#include <ctype.h>
#include <complex.h>
#include <bios.h>
#include <string.h>
#include <malloc.h>
#define SWAP(a,b) temp = (a); (a)=(b);(b)= temp;                    //macros
#define EPS 1.0e-7

int clip[9][2],specflag[3],attflag,ascflag=5,alflag=0;              // program flags
char alumfile[12], sname[8], sstate[8],filename[11],initfile[12],fileout[12];   //sample details & locations
char linereturn[2],instring[10],rangefile[12],intactdir[64];
char string[12],intactfile[12];
int  i,j,k,l,ndata,bottom,top,window1,window2,alumwin1,alumwin2,range[100][2];
int  dirnum,pvept,sampnum;
float alum[2049],sigr[2049],sigi[2049],platens,density,mass,diameter,smplength;   // trace stores
float travelt[100], velad[100], vel[100];                           //velocity and traveltime
float traveltint[100], velsdint[100], velint[100];                  //velocity and traveltime for intact sample (option ascflag = 3)
float astress[100], hstress[100];                                   // sample stress states
complex freqstore[160],rat[160],alumstore[160];                     //complex spectral ratio and frequency stores
float freq.[160], sample_rate, x[160], y[160], a, al, b, bl, abdev, sumyy, sumy, sumxy, sumysx, meanx, sumxxm;//robust estimation variables
float spec[160];                                                    //real spectral ratio store
float Q[100], Qerr[100], Ql[100], Qlerr[100], att29khz[100], att18khz[100], att49khz[100];   //Q values
FILE *f1,*f2,*fracfile;                                             //file pointers
FILE *eventlog;                                                     //eventlog file pointer

void read_visq(void);                                               //see descriptions above for functions
void load_aluminium(int alflag);
void read_trace(void);
void fft(char fiflag,float realarray[], float imagarray[]);
void savedata(void);
void file_subloop(void);
void cliptrace(int c1,int c2,float cliparray[]);
void ratio(complex ratarray[]);
```

```
void robust_fit(float x[],float y[],int ndata);
void least_fit(float x[],float y[], int ndata);
void Qcalc(float qarray[],float qerrarray[],float grad);
void data_out(void);
void fit(float fitarray[]);
void read_range(void);

int main(int argc,char *argv[])
{
        if(argc<4||argc>5)                                              //program arguments
        {
                printf("AUTOQ D. Pearce, Last modified 5/6/96, ver 2.12");
                printf("\nUsage 1: AUTOQ [int bottom] [int top] [ini filename]");
                printf("\n      2: AUTOQ [int bottom] [int top] [ini filename]\n      [range (0) *.asc & range (1) *.asc (2) *.asc
+ sing-als (3)]");
                return(0);
        }
bottom = atoi(argv[1]); top = atoi(argv[2]); sprintf(initfile,"%s",argv[3]);
eventlog = fopen("eventlog.dat","wt");                                  //file to log calculation progress
if (argc==5)ascflag = atoi(argv[4]);
if (ascflag ==3) alflag =1;                                             //tells program to use intact sample traces as reference
printf("\n*****************************************");
printf("\n* AUTOQ (LF) & (HF)                     *");
printf("\n* Calc Q and velocity for stress        *");
printf("\n* regimes, a.                           *");
printf("\n* D. R. Pearce 1995                     *");
printf("\n* ver 2.12                              *");
printf("\n* Last modified 5/6/96                  *");
printf("\n*****************************************");
switch(ascflag)
{
        case 0:printf("\nRange option selected");break;
        case 1:printf("\nRange and *.asc file option selected");break;
        case 2:printf("\n*.asc file option selected");break;
        case 3:printf("\n*.asc file and intact / fracture spectral ratio");break;
        default:printf("\nNo range/*.asc options selected");break;
}
read_visq();                                                            //data input
if (ascflag==0||ascflag==1)
        read_range();                                                   // read frequency range file
sample_rate = ((sample_rate*1000000)/2)/(sampnum/2);                    // calculates data sampling rate
for (i=1;i<160;i++)
        freq[i] = i*sample_rate;                                        //frequency array
for (j=0;j<dimnum;j++)                                                  //main file loop
{
        for (i=1;i<160;i++)
                rat[i] = complex(0.00,0.00);                            //resets ratio
        clrscr();
        file_subloop();                                                 //load files and calculate spectral ratio
        switch(attflag)
        {
        case 0:                                         // low frequency range attenuation coefficient calculation
        att29khz[j]=0.2*real((log10(alumstore[24]/freqstore[24]))/smplength);
        att18khz[j]=0.2*real((log10(alumstore[15]/freqstore[15]))/smplength);
        att49khz[j]=0.2*real((log10(alumstore[40]/freqstore[40]))/smplength);
        break;
        case 1:                                         //high frequency range attenuation coefficient calculation
        att29khz[j]=0.2*real((log10(alumstore[41]/freqstore[41]))/smplength);
        att18khz[j]=0.2*real((log10(alumstore[66]/freqstore[66]))/smplength);
        att49khz[j]=0.2*real((log10(alumstore[82]/freqstore[82]))/smplength);
        break;
        }
        strncpy(string,filename,4);
        string[4] = '\0';
        if (ascflag == 1||ascflag == 2||ascflag==3)
        {
        sprintf(fileout,"%s_%1.0f.asc",string,hstress[j]);
        printf("\nWriting Attenuation Spectra File (ASC FORMAT) for %s",filename); //output attenuation spectra file
        f2 = fopen(fileout,"wt");
        for(i=1;i<160;i++)
        fprintf(f2,"%1.0f;%1.6f;%1.6f;%1.6f;\n", freq[i], 0.2*real((log10 (alumstore[i] / freqstore[i]))/smplength),
sigr[i],alum[i]);
        fclose(f2);
        }
        fit(spec);                                      //robust fit to spectral ratio between user defined limits
        Qcalc(Q,Qerr,b);                                //calculate robust Q
        Qcalc(Ql,Qlerr,bl);                             //calculate least squares Q
```

```
                savedata();                                   // save dataset file
        }                                                     //end main dir loop
        data_out();                                           // save velocity, Q and attenuation coefficient data to file
        fclose(eventlog);                                     //close eventfile
        printf("\n\nProgram completed successfully!");
        return(0);
}                                                             // end main

void file_subloop(void)
{
        for (i=1;i<160;i++)
        {
                freqstore[i] = complex(0.0,0.0);              //reset freqstore to zero
                alumstore[i] = complex(0.0,0.0);
        }
        fread(instring,12,1,f1);
        sprintf(filename,"%s",instring);                      //read initfile to get filename
        fread(instring,10,1,f1);
        astress[j] = atof(instring);                          //read initfile to get axial stress
        fread(instring,10,1,f1);
        hstress[j] = atof(instring);                          //read initfile to get horiz stress
        fread(instring,10,1,f1);
        travelt[j] = atof(instring);                          //read initfile to get traveltime
        fread(instring,10,1,f1);
        window1 = atoi(instring);                             //read initfile to get first window point
        fread(instring,10,1,f1);
        window2 = atoi(instring);                             //read initfile to get second window point
        switch(ascflag)
        {
        default:                                              // defaults to aluminium waveform file
                fread(linereturn,1,1,f1);
                load_aluminium(0);
                break;
        case 3 :                                              // special case for intact sample as reference
                fread(instring,1,1,f1);
                fread(instring,12,1,f1);
                sprintf(intactfile,"%s",instring);            //read initfile to get intact trace filename
                fread(instring,10,1,f1);
                traveltint[j] = atof(instring);               //read intact trace traveltime
                fread(instring,10,1,f1);
                alumwin1 = atoi(instring);                    //read initfile to get first intact trace window point
                fread(instring,9,1,f1);
                alumwin2 = atoi(instring);                    //read initfile to get second intact trace window point
                fread(linereturn,1,1,f1);
                load_aluminium(1);                            //read intact file trace in to aluminium array
                velint[j] = smplength/((traveltint[j]-platens)/1000000);  //work out intact velocity & store
                velsdint[j] = 0.800166649 * (velint[j] - (smplength/(((traveltint[j]-platens)+0.02)/1000000)));
                                                              //work out intact velocity error & store
                break;
        }
        astress[j] = (astress[j]/((M_PI*(diameter*diameter))/4))/1000;// work out axial stress in MPa and store
        vel[j] = smplength/((travelt[j]-platens)/1000000);    //work out velocity & store
        velsd[j] = 0.800166649 * (vel[j] - (smplength/(((travelt[j]-platens) + 0.02) /        1000000)));
                                                              //work out velocity error & store
        read_trace();                                         //load trace 1 in to sigr[i]
        cliptrace(window1,window2, sigr);                     //clip trace at window values
        cliptrace(alumwin1,alumwin2,alum);                    //clip aluminium at window value
        printf("\nCalculating 2 way FFT");
        fft(F,sigr,sigi);                                     //calculate fast fourier transform of sample trace
        for(i=1;i<160;i++)
                freqstore[i] = complex(sigr[i],sigi[i]);      //store frequency result
        for(i=1;i<2048;i++)
                sigi[i] = 0.0;                                //reset imaginary array
        fft(F,alum,sigi);                                     //calculate fast fourier transform of aluminium trace
        for(i=1;i<160;i++)
                alumstore[i] = complex(alum[i],sigi[i]);      //store result
        printf("\nCalculating Spectral Ratio");
        ratio(rat);                                           //calculate ln spectral ratio
        for(i=1;i<160;i++)
                spec[i] = real(rat[i]);                       //extract spectral ratio data
}

void data_out(void)
{
char results_dir[8];
        switch(attflag)
        {
```

```
                case 0: sprintf(results_dir,"%i-%i",bottom,top);break;
                case 1: sprintf(results_dir,"%i-%i",bottom,top);break;
                default : sprintf(results_dir,"results");break;
}
f2 = fopen("velocity.dat","wt");
fprintf(f2,"%s, %s, Velocity data file\n",sname,sstate);
fprintf(f2,"   Axial   Horiz  Velocity\n");
for (i=0;i<dirnum;i++)
                fprintf(f2,"%10.2f%10.2f%10.2f\n",astress[i],hstress[i],vel[i]);
fclose(f2);
if(ascflag ==3)
{
f2 = fopen("velcomp.dat","wt");
fprintf(f2,"%s, %s, Velocity Comparison data file\n",sname,sstate);
fprintf(f2,"   Axial   Horiz  FracVel  FVelErr  IntVel  IVelErr IVel-FVel Perchange\n");
for (i=0;i<dirnum;i++)
                fprintf(f2,"%10.2f%10.2f%10.2f%10.2f%10.2f%10.2f%10.5f\n",astress[i],hstress[i],vel[i],velsd[i],velint[i],velsdint[i],v
elint[i]-vel[i],(1-(velint[i]/vel[i]))*100);
                fclose(f2);
                }
                switch(attflag)
                {
                        case 0 :
                                f2 = fopen("att29kHz.dat","wt");
                                fprintf(f2,"%s, %s, Attenuation Coefficient at 29kHz\n", sname, sstate);
                                fprintf(f2,"   Axial   Horiz  AttCoef   CalcQ\n");
                                for (i=0;i<dirnum;i++)
                                fprintf(f2, "%10.2f%10.2f%10.6f%10.2f\n", astress[i], hstress[i], att29khz[i],
                                (M_PI*sample_rate*24) / (vel[i] * att29khz[i] ));
                                fclose(f2);
                                f2 = fopen("att18kHz.dat","wt");
                                fprintf(f2,"%s, %s, Attenuation Coefficient at 18kHz\n", sname, sstate);
                                fprintf(f2,"   Axial   Horiz  AttCoef          CalcQ\n");
                                for (i=0;i<dirnum;i++)
                                        fprintf(f2, "%10.2f%10.2f%10.6f%10.2f\n", astress[i], hstress[i],
                                        att18khz[i],(M_PI*sample_rate*15)/(vel[i]*att18khz[i]));
                                fclose(f2);
                                f2 = fopen("att49kHz.dat","wt");
                                fprintf(f2,"%s, %s, Attenuation Coefficient at 49kHz\n", sname, sstate);
                                fprintf(f2,"   Axial   Horiz  AttCoef          CalcQ\n");
                                for (i=0;i<dirnum;i++)
                                        fprintf(f2, "%10.2f%10.2f%10.6f%10.2f\n", astress[i], hstress[i],
                                        att49khz[i],(M_PI*sample_rate*40)/(vel[i]*att49khz[i]));
                                fclose(f2);
                                break;
        case 1 :
                                f2 = fopen("at500kHz.dat","wt");
                                fprintf(f2,"%s, %s, Attenuation Coefficient at 500kHz\n", sname, sstate);
                                fprintf(f2,"   Axial   Horiz  AttCoef          CalcQ\n");
                                for (i=0;i<dirnum;i++)
                                        fprintf(f2, "%10.2f%10.2f%10.6f%10.2f\n", astress[i], hstress[i],
                                        att29khz[i],(M_PI*sample_rate*41)/(vel[i]*att29khz[i]));
                                fclose(f2);
                                f2 = fopen("at800kHz.dat","wt");
                                fprintf(f2,"%s, %s, Attenuation Coefficient at 800kHz\n", sname, sstate);
                                fprintf(f2,"   Axial   Horiz  AttCoef          CalcQ\n");
                                for (i=0;i<dirnum;i++)
                                        fprintf(f2, "%10.2f%10.2f%10.6f%10.2f\n", astress[i], hstress[i],
                                        att18khz[i],(M_PI*sample_rate*66)/(vel[i]*att18khz[i]));
                                fclose(f2);
                                f2 = fopen("att1MHz.dat","wt");
                                fprintf(f2,"%s, %s, Attenuation Coefficient at 1 MHz\n", sname, sstate);
                                fprintf(f2,"   Axial   Horiz  AttCoef          CalcQ\n");
                                for (i=0;i<dirnum;i++)
                                        fprintf(f2, "%10.2f%10.2f%10.6f%10.2f\n", astress[i], hstress[i],
                                        att49khz[i],(M_PI*sample_rate*82)/(vel[i]*att49khz[i]));
                                fclose(f2);
                                break;
                }
mkdir(results_dir);
chdir(results_dir);
f2 = fopen("robustQ.dat","wt");
for (i=0;i<dirnum;i++)
                fprintf(f2, "%10.2f%10.2f%10.2f%10.2f\n", astress[i], hstress[i], Q[i], Qerr[i]);
fclose(f2);
f2 = fopen("robQ15pc.dat","wt");                                        //Robust Q datafile, Q<5% error
for (i=0;i<dirnum;i++)
                if(((Qerr[i]/Q[i])*100)<5.0)
```

```
                        fprintf(f2,"%10.2f%10.2f%10.2f\n",astress[i],hstress[i],Q[i]);
fclose(f2);
f2 = fopen("robQl3pc.dat","wt");                        //Robust Q datafile, Q<3% error
for (i=0;i<dirnum;i++)
        if(((Qerr[i]/Q[i])*100)<3.0)
                fprintf(f2,"%10.2f%10.2f%10.2f\n",astress[i],hstress[i],Q[i]);
fclose(f2);
f2 = fopen("leastQ.dat","wt");
for (i=0;i<dirnum;i++)
        fprintf(f2 ,"%10.2f%10.2f%10.2f%10.2f\n", astress[i], hstress[i], Ql[i], Qlerr[i]);
fclose(f2);
f2 = fopen("leaQl5pc.dat","wt");                        //Least Q datafile, Q<5% error
for (i=0;i<dirnum;i++)
        if(((Qlerr[i]/Ql[i])*100)<5.0)
                fprintf(f2,"%10.2f%10.2f%10.2f\n",astress[i],hstress[i],Ql[i]);
fclose(f2);
        f2 = fopen("leaQl3pc.dat","wt");                //Least Q datafile, Q<3% error
        for (i=0;i<dirnum;i++)
                if(((Qlerr[i]/Ql[i])*100)<3.0)
                        fprintf(f2,"%10.2f%10.2f%10.2f\n",astress[i],hstress[i],Ql[i]);
        fclose(f2);
}

void savedata(void)
{
struct date d;
char dataout[20];
float bf,tf;
 getdate(&d);
 printf("\nSaving data to dataset.dat");
 sprintf(dataout,"dat%i-%i.dat",bottom,top );
 f2 = fopen(dataout,"wt");
 fprintf(f2,"SAMPLE %s Results from AUTOQLF run %d/%d/%d",sname,d.da_day,d.da_mon,d.da_year);

fprintf(f2,"\n==========================================================================================
==========");
 fprintf(f2,"\n\nSAMPLE NAME : %s\tSAMPLE STATE : %s", sname, sstate);
 fprintf(f2,"\nLENGTH : %1.5fm\tMASS : %1.5fkg\tDIAMETER : %1.5fm\tDENSITY : %4.2fkg/m2", smplength,mass,diameter,density);
 fprintf(f2,"\n\nTRAVELTIMES / VELOCITIES");
fprintf(f2,"\n==========================================================================================
==========");
 fprintf(f2,"\nAXIAL\tHORIZ\tTRAVL\tVELOC\tVLerr\tVLerr");
 fprintf(f2,"\n(MPa)\t(MPa)\t(mis)\t(m/s)\t(m/s) \t  %\n");
 for (i=0;i<=j;i++)
        fprintf(f2,"\n%2.2f\t%2.0f\t%2.2f\t%4.1f\t%2.1f\t%2.2f",astress[i],hstress[i],travelt[i],vel[i],velsd[i],(velsd[i]/vel[i])*100);
fprintf(f2,"\n==========================================================================================
==========");
 fprintf(f2,"\nQ Values          ");

fprintf(f2,"\n==========================================================================================
==========");
 fprintf(f2,"\n AXIAL    HORIZ    Q(Robust)  Qerr(Rob) Qerr%(R)  Q(Least)  Qerr(Lst)  Qerr%(L)     From       To");
 fprintf(f2,"\n (MPa)    (MPa)                                                (kHz)    (kHz)\n");
 for (i=0;i<=j;i++)
 {
        if(ascflag==0||ascflag==1)
        {
                switch(attflag)
                {
                        case 0: bf = 1.221 * range[i][0]; tf = 1.221 * range[i][1];break;
                        case 1: bf = 12.207 * range[i][0]; tf = 12.207 * range[i][1];break;
                }
        }
        else
        {
                switch(attflag)
                {
                        case 0: bf = 1.221 * bottom; tf = 1.221 * top;break;
                        case 1: bf = 12.207 * bottom; tf = 12.207 * top;break;
                }
        }

        fprintf(f2,"\n%10.2f%10.2f%10.2f%10.2f%10.2f%10.2f%10.2f%10.2f%10.0f%10.0f",astress[i],hstress[i],Q[i],Qerr[i],(Qerr[
        i]/Q[i])*100,Ql[i],Qlerr[i],(Qlerr[i]/Ql[i])*100,bf,tf);
 }
fprintf(f2,"\n==========================================================================================
==========");
 fclose(f2);
```

```
}

void read_range(void)
{
        f1 = fopen("range.dat","rt");
        if (f1==NULL) printf("\n\nFILE ERROR :: range file required and not found (RANGE.DAT)"), exit(0);
        printf("\nReading range.dat");
        for (i=0;i<dirnum;i++)
        {
                fread(instring,10,1,f1);
                range[i][0] = atoi(instring);
                if (attflag == 0)
                        range[i][0] = (range[i][0]*1000)/1221;
                fread(instring,10,1,f1);
                range[i][1] = atoi(instring);
                if (attflag == 0)
                        range[i][1] = (range[i][1]*1000)/1221;
                fread(linereturn,1,1,f1);
        }
        fclose(f1);
}

void read_visq(void)
{
char qu;
        f1 = fopen(initfile,"rt");
        if (f1==NULL) printf("\n\nFILE ERROR :: %s does not exist",initfile), exit(0);
        printf("\nReading %s",initfile);
        fscanf(f1,"%s\n",&sname);                       //samplename
        printf("\nSample Name : %s",sname);
        fscanf(f1,"%s\n",&sstate);                      //samplestate
        printf("\nSample State = %s",sstate);
        fscanf(f1,"%s\n",&alumfile);                    //alumintum filename
        printf("\nAluminium Filename = %s",alumfile);
        fscanf(f1,"%f\n",&diameter);                    //sample diameter
        printf("\nDiameter = %1.5f", diameter);
        fscanf(f1,"%f\n",&mass);                        //sample mass
        printf("\nMass = %1.5f", mass);
        fscanf(f1,"%f\n",&smplength);                   //sample length
        printf("\nLength = %1.5f",smplength);
        density = mass / ((M_PI *(diameter*diameter)/4)*smplength);   //calculate density
        printf("\nDensity = %4.2f", density);
        fscanf(f1,"%f\n",&sample_rate);                 //sampling rate for acquisition
        printf("\nSample Rate = %2.1f MHz",sample_rate);
        if (sample_rate == 2.5) attflag = 0; else attflag = 1;
        switch(attflag)
        {
                case 0 : printf("\nLow frequency range, freq/sample = 1221 Hz");break;
                case 1 : printf("\nHigh frequency range, freq/sample = 12207 Hz"); break;
                default : printf("\n Frequency Range error, Program Terminated"); exit(0); break;
        }
        fscanf(f1,"%d\n",&sampnum);                     //number of samples per trace
        printf("\nSamples per trace = %d",sampnum);
        fscanf(f1,"%d",&dirnum);                        //number of sample states
        printf("\nNumber of directories = %i",dirnum);
        fscanf(f1,"%d",&alumwin1);                      //aluminium window 1 location
        fscanf(f1,"%d",&alumwin2);                      //aluminium window 2 location
        fscanf(f1,"%f",&platens);
        printf("\nPlatens Face Traveltime = %f",platens);
        if(ascflag==3)
                fscanf(f1,"%s",&intactdir);
                fread(linereturn,1,1,f1);
}

void fit(float fitarray[])
{
int i;
        ndata=0;                                        //reset number of data points
        sumyy=0.0;sumy=0.0;sumxy=0.0;sumysx=0.0,sumxxm=0.0;
        if (ascflag == 0||ascflag ==1)                  //case for range file specified
        {
                bottom = range[j][0];
                top = range[j][1];
        }
        for(i=bottom;i<=top;i++)
        {
                x[i-bottom]=freq[i];                    //put variables in to x and y for
```

```
                y[i-bottom]=fitarray[i];                    //robust estimation
                ndata++;                                    //calculates number of points
}
least_fit(x,y,ndata);                                       //calculate least squares fit
robust_fit(x,y,ndata);                                      //calculate robust fit
for(i=0;i<ndata;i++)
{
                sumyy += (y[i]*y[i]);                       //sum y squared
                sumy += y[i];                               //sum y
                sumxy += (y[i]*x[i]);                       //sum x * y
                sumxxm += x[i];                             //sum x
                y[i]=a+b*x[i];                              //calculate fit line values
}
meanx=sumxxm/ndata;                                         //average x
sumysx = sqrt(fabs(((sumyy-(a*sumy)-(b*sumxy))/ndata-2)));
                for(i=0;i<ndata;i++)
                        sumxxm += sqrt(((x[i]-meanx))*((x[i]-meanx)));
}

void least_fit(float x[],float y[],int ndata)
{
float sumx,sumy,sumx2,sumxy,meanx,meany;
                printf("\nCalculating Least Squares Fit");
                for(i=0;i<ndata;i++)
                {
                        sumy += y[i];                       //sum y
                        sumxy += (y[i]*x[i]);               //sum x * y
                        sumx += x[i];                       //sum x
                        sumx2 += x[i]*x[i];                 //sum x squared
                }
                meanx = sumx/ndata;
                meany = sumy/ndata;
                bl = ((ndata*sumxy) - (sumy*sumx))/((ndata*sumx2) - (sumx*sumx));
                al = meany - (bl * meanx);
}

void cliptrace(int c1,int c2, float cliparray[])
{
int i;
                printf("\nApplying Rectangular Window across %i to %i",c1,c2);
                fprintf(eventlog,"\nApplying Rectangular Window across %i to %i",c1,c2);
                for (i=1;i<(c1);i++)
                        cliparray[i]=0.00;
                for (i=c2;i<2048;i++)
                        cliparray[i]=0.00;
}

void Qcalc(float qarray[],float qerrarray[],float grad)
{
int i;
float tdist[60]={0.0,12.71,4.303,3.182,2.776,2.571,2.447,2.365,2.306,2.262,2.228,2.201,2.179,2.160,2.145,2.131,2.120,2.110,2.101,
2.093,2.086,2.080,2.074,2.069,2.064,2.060,2.056,2.052,2.048,2.045,2.042,2.040,2.037,2.035,2.032,2.030,2.028,2.026,2.024,2.0225,
2.021,2.020,2.019,2.018,2.017,2.015,2.014,2.013,2.012,2.011,2.010,2.009,2.009,2.008,2.007,2.007,2.006,};
                                                            //t-distribution values for calculating confidence limits
float berr;

                qarray[j] = fabs(M_PI / (grad * vel[j]));
                berr = tdist[ndata-2] * (sumysx/sumxxm);
                qerrarray[j] = fabs(qarray[j] - (M_PI/((grad-berr)*(vel[j]-velsd[j]))));
                printf("\nQ = %10.2f     error = %10.2f",qarray[j],qerrarray[j]);
                fprintf(eventlog,"\nQ = %10.2f       error = %10.2f",qarray[j],qerrarray[j]);
}

void ratio(complex ratarray[])
{
                int i;
                printf("\nCalculating Spectral Ratio");
                for(i=1;i<160;i++)
                        ratarray[i] = log((alumstore[i]/freqstore[i]))/smplength ;
}

void read_trace(void)
{
                strncpy(string,filename,11);
                string[11] = '\0';
                printf("\nReading file %s",string);
                fprintf(eventlog,"\nReading file %s",string);
```

```
		f2 = fopen(string,"rt");
		if (f2==NULL)
		{
			printf("\n\nFILE ERROR :: File %s not found", string);
			exit(0);
		}
		for (i=1;i<2049;i++)
		{
			fscanf(f2,"%f\n",&sigr[i]);
			sigi[i] = 0.0;
		}
		fclose(f2);
}

void load_aluminium(int alflag)
{
int i;
char homedir[64];
FILE *f2;
switch(alflag)
 {
 case 0:
		strncpy(string,alumfile,12);
		string[13] = '\0';
		printf("\nReading Aluminium waveform %s",string);
		if ((f2 = fopen(string,"rt"))==NULL)
		{
			printf("\n\nFILE ERROR :: Check aluminium files");
			exit(0);
		}
		for (i=1;i<2049;i++)
			fscanf(f2,"%f\n",&alum[i]);
		fclose(f2);
		break;
 case 1:                                        //special case for intact samples as reference traces
		getcurdir(0,homedir);
		chdir(intactdir);
		printf("\nReading Aluminium waveform %s",intactfile);
		if ((f2 = fopen(intactfile,"rt"))==NULL)
		{
			printf("\n\nFILE ERROR :: Check intact files, %s",intactfile);
			exit(0);
		}
		for (i=1;i<2049;i++)
			fscanf(f2,"%f\n",&alum[i]);
		fclose(f2);
		chdir("\\");
		chdir(homedir);
		break;
 }
}

float *vector(int nl,int nh)
{
		float *v;
		v=(float *)malloc((unsigned) (nh-nl+1)*sizeof(float));
		return v-nl;
}
void free_vector(float *v,int nl,int nh)
{
		free((char*) (v+nl));
}

void fft(char fiflag,float realarray[], float imagarray[])          //Thanks to Rob Farnfield !!
{
div_t x;
int i,j,k,l,m,n,n1,d2,m1,lpk,me;
double q1,t1,t2,u1,u2,w1,w2;
		n=2048;
		n1=11;
		d2=1024;
		m1=n-1;
		j=1;
		for(l=1;l<=m1;l++,j+=k)
		{
			if(l<j)
			{
				t1=realarray[j];
```

```
                        t2=imagarray[j];
                        realarray[j]=realarray[l];
                        imagarray[j]=imagarray[l];
                        realarray[l]=t1;
                        imagarray[l]=t2;
                }
                k=d2;
                while(k<j)
                {
                        j=j-k;
                        x=div(k,2);
                        k=x.quot;
                }
        }
        for(m=1;m<=n1;m++)
        {
                u1=1.0;
                u2=0.0;
                me=pow(2,m);
                x=div(me,2);
                k=x.quot;
                w1=cos(M_PI/k);
                if(fiflag == 'F')
                        w2= -sin(M_PI/k);
                else
                        w2=sin(M_PI/k);
                for(j=1;j<=k;j++)
                {
                        l=j;
                        while(l<=n)
                        {
                                lpk=l+k;
                                t1=realarray[lpk]*u1-imagarray[lpk]*u2;
                                t2=realarray[lpk]*u2+imagarray[lpk]*u1;
                                realarray[lpk]=realarray[l]-t1;
                                imagarray[lpk]=imagarray[l]-t2;
                                realarray[l]=realarray[l]+t1;
                                imagarray[l]=imagarray[l]+t2;
                                l+=me;
                        }
                        q1=u1;
                        u1=u1*w1-u2*w2;
                        u2=q1*w2+w1*u2;
                }
        }
        if(fiflag == 'F')
        {
                for(i=1;i<=n;i++)
                {
                        realarray[i]=realarray[i]/n;
                        imagarray[i]=imagarray[i]/n;
                }
        }
}

/*****************************************************
* Routine for robust estimation of linear trends     *
* Global variables are aa & b as in y = a+bx         *
* also abdevt, the absolute mean deviation in y       *
* and ndatat, the number of data points              *
* and x[] amd y[]                                    *
*****************************************************/

int ndatat;
float *xt,*yt,aa,abdevt;
extern float a,b,abdev;
float rofunc(float b);
float select(unsigned long k, unsigned long n,float arr[]);

void robust_fit(float x[],float y[],int ndata)
{
int j;
float sy=0.0,sxy=0.0,sxx=0.0,sx=0.0,sigb,f2,f1,f;
float del,chisq=0.0,bb,b2,b1,abdevt,temp;

        printf("\nCalculating Robust Fit");
        ndatat=ndata;
        xt = x;
```

```
yt = y;
for (j=1;j<=ndata;j++)
{
        sx += x[j];                                  //first guess for a and b, use least squares
        sy += y[j];
        sxy += x[j] * y[j];
        sxx += x[j] * x[j];
}
del = ndata*sxx-sx*sx;
aa = (sxx*sy-sx*sxy)/del;                            // least squares solution.
bb = (ndata*sxy-sx*sy)/del;
for (j=1;j<=ndata;j++)
        chisq += (temp=y[j]-(aa+bb*x[j]),temp*temp);
sigb = sqrt(chisq/del);                              //standard deviation gives a clue
b1 = bb;                                             // to how big an iteration step to take.
f1 = rofunc(b1);
b2 = bb+(f1>0.0 ? fabs(3.0*sigb) : -fabs(3.0*sigb)); // Guess bracket as 3 -s.d. away, in
f2 = rofunc(b2);                                     // downhill direction known from f1
while (f1*f2 > 0.0)      {
        bb = 2.0*b2-b1;
        b1 = b2;
        f1 = f2;
        b2 = bb;
        f2 = rofunc(b2);
}
sigb = 0.01*sigb;
while(abs(b2-b1)>sigb) {
        bb = 0.5*(b1+b2);
        if((bb==b1)||(bb == b2)) break;
        f = rofunc(bb);
        if (f*f1 >=0.0)
        {
                f1 = f;
                b1 = bb;
        }
        else
        {
                f2 = f;
                b2 = bb;
        }
        }
        a = aa;
        b = bb;
        abdev = abdevt/ndata;
}

float rofunc(float b)
{
int j;
float *arr, d, sum=0.0;

        arr = vector(1,ndatat);
        for (j=1;j<=ndatat;j++)
                arr[j] = yt[j]-b*xt[j];
        if (ndatat & 1)
                aa = select((ndatat+1)>>1,ndatat,arr);
        else
        {
                j = ndatat >>1;
                aa = 0.5 * (select(j,ndatat,arr)+select(j+1,ndatat,arr));
        }
        abdevt = 0.0;
        for (j=1;j<=ndatat;j++)
        {
                d = yt[j]-(b*xt[j]+aa);
                abdevt += fabs(d);
                if (yt[j] != 0.0) d/=fabs(yt[j]);
                if (fabs(d) > EPS) sum += d >0.0 ? xt[j] : -xt[j];
        }
        free_vector(arr,1,ndatat);
        return(sum);
}


float select(unsigned long k, unsigned long n,float arr[])
{
unsigned long i,ir,j,l,mid;
float a,temp;
```

```
l = 1;
ir = n;
for (;;)
{
        if (ir<= l+1)
        {
                if (ir == l+1 && arr[ir] < arr[l])
                {
                        SWAP(arr[l],arr[ir])
                }
                return arr[k];
        }
        else
        {
mid=(l+ir) >> 1;
SWAP(arr[mid],arr[l+1])
if (arr[l]>arr[ir])
{
        SWAP(arr[l],arr[ir])
}
if (arr[l+1] > arr[l])
{
        SWAP(arr[l+1],arr[l])
}
i = l+1;
j = ir;
a = arr[l];
for (;;)
{
        do i++; while (arr[i] <a);
        do j--; while (arr[j] >a);
        if (j<i) break;
        SWAP(arr[i],arr[j])
}
arr[l]=arr[j];
arr[j]=a;
                if (j >= k) ir=j-1;
                if (j <= k) l =i;
        }
    }
}
```